Modeling of Gas-Liquid and Liquid-Liquid Taylor Flow in Mini- and Microchannels

BY

© AMIN ETMINAN

A Thesis submitted to the School of Graduate Studies in partial fulfillment of the requirements for the degree of
Doctor of Philosophy

Department of Mechanical Engineering
Faculty of Engineering and Applied Science
Memorial University of Newfoundland

October 2022
St. John's, Newfoundland and Labrador
Canada

Abstract

An experimental and numerical study of viscous Taylor flow through capillaries is performed to investigate the effects of viscosity, superficial phase velocity ratio, channel diameter, channel diameter expansion, and gas holdup on the hydrodynamic and heat transfer. Through millimetric and microfluidic devices, two-phase Taylor flows have been a significant drive in almost all energy-related industrial applications to reduce the size and enhance heat and mass transport phenomena. A topical and comprehensive review of the hydrodynamic of Taylor flow and liquid film surrounding the slugs is conducted to shed more light on gas-liquid, and liquid-liquid Taylor flows better. An in-detailed step-by-step numerical method solves such flows in a two-dimensional axisymmetric plan of a circular tube which can be extended to mass transfer applications. The validity of the experimental setup is greatly appreciated by benchmarking of single-phase theory and the empirical/analytical correlations reported in the literature.

The numerical study differentiates flow characteristics of slug flow under two flow conditions: developing and fully developed. The slug profile, slug length, liquid film thickness, and pressure drop are compared to show the influence of slug breakup on these flow parameters as the slug moves downstream. The effects of the dynamic viscosity ratio of phases of gas-liquid and liquid-liquid Taylor flows are studied to display a five-stage slug formation process: introducing, expanding, contracting, necking, and breakup. A new linear logarithmic correlation is proposed to compute the gas holdup in terms of the superficial phase velocity ratio. Another correlation is also developed to predict the liquid film thickness using liquid and gas Weber numbers and gas holdup for such Taylor flows in tubes with only a 1.42% discrepancy.

In the experiments, the hydrodynamic and thermal analyses of Taylor flow are examined by the flow visualization, pressure drop, and heat transfer measurements which are accompanied by CFD results. The impact of interfacial pressure drop on the total pressure loss and isothermal bath temperature on the thermal performance is investigated over a wide range of volumetric flow rate ratios. The flow patterns inside and outside Taylor slugs are visualized, indicating a significant change in recirculation regions as the volumetric flow rate ratio increases. It is found, in good agreement with the literature, that the pressure drop generated by the interface increases the total pressure loss up to 200% compared to the single-phase flow. The influence of interfacial pressure drop decreased as the dimensionless length of the channel approached beyond 0.1, resulting in concise water slugs and long oil plugs.

General Summary

Two-phase flow refers to the interactive flow of two components, called dispersed and continuous, commonly occurring in channels. Superficial phase velocity ratio, phase viscosity, and channel diameter characterize the pattern of the two-phase flow by the terminology of bubbly, Taylor/slug, churn, and annular. Mainly, gas-liquid and liquid-liquid Taylor flows consist of a train of equal-length bubbles/slugs with the same diameter as that of the tube, where the slugs are surrounded by a thin layer of carrying phase and are separated by carrying phase plugs.

Energy dissipation, heat and mass transfers, and material consumption are critical factors in energy-related and process applications. Utilizing the Taylor flow in such applications can aim for more compact heat exchangers and optimal operational conditions, which is in line with sustainable development. Understanding Taylor flow's hydrodynamic characteristics and thermal behaviours are of interest to meet this achievement.

Taylor flow increases the mass transfer rate in the radial direction which is desired while decreasing the axial transport. There are two different two-phase slug flows called a traditional plug or slug flow and a segmented or Taylor flow. Traditional two-phase slug flow includes a range of lengths, shapes, and distributions of dispersed phase slugs in the carrier phase, making the analysis much more complicated. Conversely, Taylor flow that shows a uniform distribution of same-sized dispersed slugs, called a train, is more applicable to theoretical analysis. In addition to the geometrical features and thermophysical properties, flow circulation within the Taylor slugs, the hydrodynamic and thermal boundary conditions introduce more complexities for analyzing such flows.

This study is focused upon the Taylor flow in capillaries through experiments and computational fluid dynamics simulations. Different geometries and operational conditions are examined to find the influence of viscosity, superficial phase velocity ratio, channel diameter, channel diameter expansion, and gas holdup on the flow and thermal characteristics. There is a paucity of research exploring the effects of the channel's diameter, superficial velocities ratio, and viscosity on slug curvature and film thickness in gas-liquid and liquid-liquid flows. Therefore, our experiments and numerical simulations are aimed at addressing this deficit in the literature by analyzing velocity field, flow pattern, pressure drop, and heat transfer rate qualitatively and quantitatively.

In our experimental setup a pair of high-precision Harvard PHD 2000 programmable syringe pumps are used as a fluid supplying unit. The tubing system consists of a tee junction and a set of straight transparent mini-channels with inner diameters of 1.42, 1.52, and 1.65 mm. An Omega pressure transmitter, model PX409-001DWU5V, with a pressure range of 0–1 psi measures the pressure drop over a length of 200 mm. The flow pattern is visualized to measure slug length, liquid film thickness, and slug curvature prior to entering the thermal section. A high-speed Phantom camera v611 controlled by a computer captures the images of the two-phase slug flow. The camera has a resolution of 1280 × 800, a pixel size of 20 μm, and a 12-bit depth, providing high-quality images of flow patterns to predict slug shape, curvature, and liquid film thickness. A unique manual-focus Canon MP-E 65 mm f/2.8 1-5x lens captures micro shots and close-ups of slugs. Two T-type Omega thermocouples are also employed to measure the inlet and outlet bulk temperatures of the flow at the test section located inside an isothermal bath manufactured by Fisher Scientific Co.

Co-Authorship Statements

This Ph.D. thesis has been prepared in a manuscript style, including a series of chapters appearing in peer-reviewed publications. All the chapters are collaborative and frequently involve the contributions of my supervisor, Dr. Yuri S. Muzychka, and co-supervisor, Dr. Kevin Pope. Chapter 2 is a peer-reviewed journal publication with *Processes*. I made a significant contribution to the study and reviewed relevant articles. My supervisor advised me how to organize the paper and what concepts must be covered. Dr. Pope helped with technical writing and proofreading. Dr. Muzychka recommended that I focus on the liquid film thickness and compare all the reported correlations for measuring film thickness plus experimental data in the literature. It has resulted in another peer-reviewed journal paper published in the *Canadian Journal of Chemical Engineering*, which is presented in Chapter 3. Dr. Pope significantly improved the structure of this manuscript and helped with proofreading. Chapter 4 has been prepared based on a conference and a peer-reviewed journal paper presented at the *5th World Congress on Momentum, Heat and Mass Transfer (MHMT'20)* and the *Journal of Fluid Flow, Heat and Mass Transfer*, respectively. Dr. Muzychka and Dr. Pope helped acquire funds and supervised the research. Both co-authors also revised the papers and approved the final versions. Chapter 5 is another conference paper presented at the *ASME Fluids Engineering Division Summer Meeting*. Dr. Pope helped with the final version of the manuscript, and Dr. Muzychka helped with the technical structure. Dr. Muzychka administrated both conference presentations that were held virtually due to the COVID19 global pandemic. Chapter 6 has been published in the *Canadian Journal of Chemical Engineering*. I designed the study and made the idea of diameter expansion effects on flow patterns that my co-authors greatly appreciated. Then, I revised the text after my supervisors' comments on the draft version. Chapter 7 has been intended to be submitted to the *Journal of Heat Transfer*. The general research questions were proposed by Dr. Muzychka, who also helped with the experimental setup and carried out the experiments. Dr. Pope contributed to technical writing support and proofreading. During all chapters, I conducted the literature review and the general introduction, which were furnished by the comments/feedback from my supervisory team. Their technical support was extended to all parts of the chapters to approve the final version of the manuscript.

Acknowledgments

I would like to express my gratitude to my Ph.D. supervisor, Prof. Y.S. Muzychka. Working with him has shown me how to work efficiently and accurately. His experience regarding my experimental analysis has greatly helped me to figure out how to design and operate an experiment correctly and safely. I also like to thank my co-supervisor, Prof. K. Pope, who has always encouraged me to look forward and do my best. He has supported me with his careful reviews of my Ph.D. research proposal, publications, and thesis and provided fruitful comments/feedback.

Thanks are extended to the supervisory committee: Prof. Kevin Pope and Prof Xili Duan, and also to examining members: Prof. Satish G. Kandlikar, Prof. Sohrab Zendehboudi, and Prof. Baafour Nyantekyi-Kwakye, for their valuable suggestions.

I gratefully acknowledge my friends, Wesam and Mahmoud, for their technical tips in helping me with the experiments. Last but not least, Farzan has always supported me and has been by my side as a brother.

Finally, I would express my heartfelt thanks to my lovely wife, Fatemeh. She made the finishing of this work possible and did an excellent job of taking care of our kids, Nafas and Johnmehr, along with her honorable achievements over two highly challenging years due to the COVID19 global pandemic.

Table of Contents

List of Figures

List of Tables

Nomenclature and Acronyms

Dimensionless Numbers		
Ar		Archimedes number
Bo		Bond number
Ca		Capillary number
Cn		Cahn number
Co		Confinement number Courant number
Eo		Eötvös number
Fr		Froude number
La		Laplace number
N		viscosity number
Nu		Nusselt number
Oh		Ohnesorge number
Pe		Peclet number
Pr		Prandtl number
Re		Reynolds number
Su		Suratman number
We		Weber number
English Letters		
A	[m^2] [micron]	area of the channel microreactor oscillation in Eq. (2.9)
B	[$kg\ m^{-2}\ s^{-1}$]	mass velocity of the liquid phase (mass flux)
C	[–] [$J\ kg^{-1}K^{-1}$]	Chisholm constant (5, 10, 15, and 20 for different flow regimes) specific heat
d, D	[m]	tube diameter
E		flow parameter
f	[–]	apparent friction factor and a function defined by Wang et al. (2012)
F	[s^{-1}] [N]	frequency of gas bubbles force
f_0	[kHz]	constant vibrating frequency
f_α	[–]	a function defined by Wang et al. (2012)
g	[$m\ s^{-2}$]	gravity acceleration
G	[$kg\ m^{-2}\ s^{-1}$]	mass velocity of the gas phase (mass flux)
h	[mm] [$W\ m^{-2}\ K^{-1}$] [m]	the height of the rectangular cross-sectional area channel convective heat transfer coefficient film thickness in Figure 3.6
H	[m]	Kelvin-Helmholtz instability index
k	[$W\ m^{-1}\ K^{-1}$]	conductive heat transfer coefficient
K	[–]	end effect of a bubble
j	[$m\ s^{-1}$]	superficial phase velocity in Figures 1.5 and 2.6

J	[–]	coefficient matrix
L	[m] [–]	length Laplace constant
m	[–]	true index of the velocity of flow
M	[kg]	mass
$\dot{m}$	[kg s^{-1}]	mass flow rate
n	[–]	number of slugs unit normal vector on the interface line
N	[–]	number of nodes
P	[N m^{-2}] [m]	pressure the perimeter of the channel
$\bar{q}$	[J m^{-2}]	mean wall heat flux
Q	[ml s^{-1}] [J s^{-1}]	volumetric flow rate convective heat transfer
r	[m]	radial distance from the axis of the tube
R	[m]	radius of channel, equivalent radius in Eq. (2.6)
s	[–]	channel gap
S	[–]	slip ratio
t	[s] [–]	time tangential unit vector on the interface line
T	[°C or K]	temperature
u, U	[m s^{-1}]	average velocity
v	[volt]	voltage
V	[m s^{-1}]	superficial velocity
w	[mm] [–]	the width of the rectangular channel uncertainty
W	[–]	potential error
x	[–]	the mass quality or the dryness fraction
X	[–]	Lockhart-Martinelli parameter
y		measured variable
z	[m]	axial length
Z	[m]	height

Greek Letters

α	[–] [m^2 s^{-1}]	void fraction thermal diffusivity
β	[–]	the volumetric quality
γ	[–] [s^{-1}]	the ratio between dynamic viscosity of droplet to carrying phase shear rate
δ	[m] [–]	liquid film thickness Dirac delta function
ε	[–]	the gas phase holdup
η	[–]	non-dimensional radial coordinate axis
θ	[degree]	contact angle
κ	[m^{-1}]	radius of the curvature
λ		$= \left(\frac{\rho_g}{0.075}\frac{62.3}{\rho_l}\right)^{0.5}$
μ	[Pa s]	dynamic viscosity
ν	[m^3]	the volume of liquid flowing per bubble and slug
ξ	[–] [m]	non-dimensional axial coordinate axis interface width
ρ	[kg m^{-3}]	density
σ	[N m^{-1}]	surface tension
τ	[N m^{-2}]	shear stress
υ	[m^2 s^{-1}]	kinematic viscosity
ω_0	[s^{-1}]	angular frequency
∀	[mm^3]	volume of the dispersed phase cell volume

φ	[–]	two-phase friction multiplier amount of property
ψ		$= \frac{73}{\sigma}\left[\mu_l + \left(\frac{62.3}{\rho_l}\right)^2\right]^{\frac{1}{3}}$
Δ	[–]	gradient operator

Subscripts and Superscripts

*	minimum or maximum, and dimensionless parameters
⋆	dimensionless wall heat transfer and length scale
0	initial
3D	droplet at the junction
a	aqueous phase air advancing
adv	advancing
b	the equivalent diameter of a sphere bubble
c	continuous
ca	capillary
cap	head or rear meniscuses of the gas bubble
CH1	the first detection point
CH2	the second detection point
cn	surrounding cell centre
co	cell centre
cr	critical
d	dispersed dodecane
D	diagonal direction in Figure 2.10
e	extension effective
f	film face centre
Fr,c	frictional, continuous
Fr,d	frictional, dispersed
g, G	gas
GL	gas-liquid
GS	gas superficial
h, H	hydraulic
i Int	interfacial
l, L	liquid
L	lateral direction in Figure 2.10
LL	liquid-liquid
lm	logarithmic mean temperature difference
LS	liquid superficial
ks	kerosene-superficial
m	mixture or mean
max	maximum
mf	moving film
min	minimum
n	node
o	organic phase
p	constant pressure process plug selected phase
rec r	receding

s	slug inner surface area of the copper tube section
sf	stagnant film
su	surface
s∞	the radius of the gas bubble in the uniform film thickness region
t T	total
th	macro-to-micro-scale threshold
tp	two-phase velocity
uc	unit cell
w	wall
ws	water-superficial

Acronyms

2D	two-dimensional
3D	three-dimensional
ALE	arbitrary Lagrangian-Eulerian
BTB	bromothymol blue
cSt	centistoke
CBC	convective boundedness criterion
CFD	computational fluid dynamics
CFL	courant-Friedrichs-Lewy
CICSAM	compressive interface capturing scheme for arbitrary meshes
CP	central part of plug
CS	central part of slug
CSF	continuum surface force
CSS	continuum surface stress
DEA	diethanolamine
DNA	deoxyribonucleic acid
FEP	fluorinated ethylene propylene
FV	finite volume
FVM	finite volume method
GGCB	green-gauss cell-based
GGNB	green-gauss node-based
GL	gas-liquid
GS	gas-solid
HFM	homogeneous flow model
HRIC	high-resolution interface capturing
IL	ionic liquid
IPA	isopropyl alcohol
LBM	lattice Boltzmann method
LL	liquid-liquid
LS	liquid-solid
MAD	mean absolute deviation
MCR	micro- or mini-channel reactors
ME	microfluidic extractors
MEMS	microelectromechanical systems
MPLSM	multivariable power least squares method
NITA	non-iterative time advancement
PBM	population balance model
PDF	probability density function
PIV	particle image velocimetry
QUICK	quadratic upstream interpolation for convective kinematics
RMSE	root mean square errors
SDS	sodium dodecyl sulfate
SFM	separated flow model
SIMPLEC	semi-implicit method for pressure linked equations-consistent
SRC	scale-resolving simulation

SSE	sum of squared errors
TBP	tributylphosphate
TS	tip of slug
VoF	volume of fluid
VTC	viscosity-temperature coefficient
XFVM	extended finite volume method
μ-PIV	micro-particle image velocimetry

Chapter 1

Introduction

1.1 Overview

Many engineering applications deal with the momentum and thermal energy transport phenomena that specifically benefit from two immiscible phases: gas and liquid. This research investigates the hydrodynamics and heat transfer of viscous gas-liquid (GL) and liquid-liquid (LL) Taylor flows in mini- and microchannels with a circular cross-sectional area. Taylor flow consists of a steady chain of gas bubbles or liquid slugs with equivalent diameters of microtubes, capillaries, or microchannels in a gas-liquid or liquid-liquid two-phase flow that is mostly surrounded by a thin film of the liquid carrying phase and also is separated by the liquid plugs. Figure 1.1 shows a train of Taylor droplets of distilled water / silicone oil (1 cSt) flow in a mini-channel with an inner diameter of 1.65 mm. The lengths of slugs and plugs remain constant, and a uniform film region is established to separate the slugs and inner surface of the channels. The water slugs form two semi-hemispherical curvatures at two ends and an elongated capsular shape between them.

A broad spectrum of technological contexts encompasses multiphase flows dealing with a wide range of scales varying between nano- and meter-engineering disciplines (Figure 1.2). Multiphase flow in micro-sized structures refers to a microflow in which two or more distinct phases are recognizable, i.e., a carrying or continuous phase and one or more dispersed phases. A two-phase flow denotes a combination of two different matters, including gas, liquid, and solid particles. The GL and LL are two common types of multiphase flows in microchannels encountered

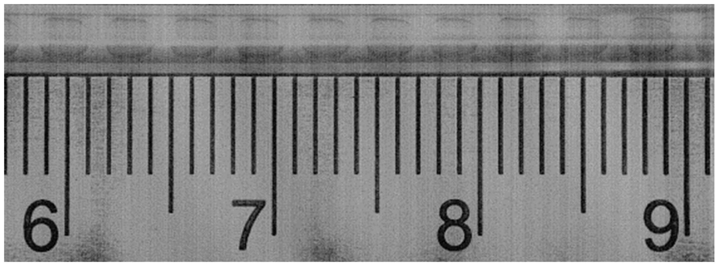

FIGURE 1.1: Fully developed water / silicone oil two-phase Taylor flow in a mini-channel with an inner diameter of 1.65 mm. Volumetric flow rates of the dispersed phase (distilled water) and continuous phase (1 cSt silicone oil) are 10 ml/min (a snapshot of the current study)

in various practical applications, such as biomedical, pharmacological, engineering, and commercial. Immiscible LL two-phase flows can also be observed in many industrial applications, where the dispersive liquid flow is introduced as droplets into the liquid carrying phase. Intensified LL extraction as a separation process is another application of two-phase flow in oil and gas industries. Most energy-related engineering applications involve two-phase flows, while three-phase flows can also be observed in some special industrial applications, such as a typical oil and gas reservoir, which simultaneously includes oil, gas, and water. These flows can also involve phase changes, such as evaporation, boiling, condensation, melting, and freezing, causing the matter to change from one state to another.

The interactions between the different phases, flow rates, thermophysical properties, and geometrical details of the channel characterize the flow pattern, liquid film thickness, gas bubble or droplet shape, pressure drop, heat, and mass transfer rates. Knowledge of two-phase flow characteristics enables researchers and designers to optimize channel size and operating conditions. For example, minimizing the pressure drop can reduce corrosion and erosion while providing a high heat transfer

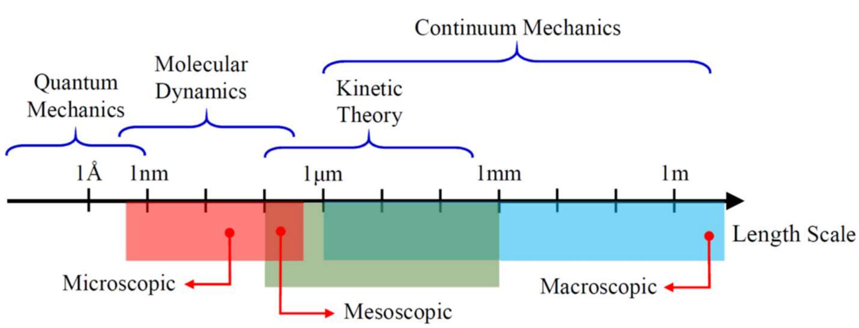

FIGURE 1.2: Theories and different spatial scales in multiscale flows

rate, as Angeli and Gavriilidis (2008) demonstrated. An essential feature of Taylor flow is the flow pattern in the liquid slug, which can also be classified in recirculation flow and bypass flow (Awad and Muzychka, 2008 and 2010). Therefore, knowledge of hydrodynamic properties of Taylor flow is undoubtedly required to understand transport phenomena characteristics for improving the performance of microchannels and enabling operational conditions to be well-controlled.

Chemical reactions on the microscale are often performed in monolith reactors functioning as catalyst support. The catalytically active site of reactors should be reached by chemical reactants, not products, emphasizing the critical role of the diffusion phenomenon in catalysts. For example, in monolith reactors, many parallel channels with hexagonal or square cross-sections offer a particular reaction area for wall-mounted catalysts at places where the wall is thin. This results in better heat transfer through the walls and better mechanical stability than circular capillaries (Gascon et al., 2015). Knowledge of the underlying fluidics is crucial for process control, stabilization, and precise reactor design. The high grade of parallel micochannels complicates the prediction of hydrodynamics and pressure drop (Kreutzer et al., 2005a; Huerre et al., 2014).

Besides the importance of dispersing phase distribution and slug formation frequency, the actual droplet velocity is also essential for the reactor's droplet residence time. It determines the contact time and influences the pressure drop of the reactor (Fu and Ma, 2015; Ładosz and von Rohr, 2018). In parallel reactors, the exact knowledge of the pressure drop is essential since a steady supply for every single reactor is required to ensure stable and efficient working conditions. The hydrodynamic supreme of monolith reactors is the ability to carry a high volumetric flow rate with low pressure loss (Schubert et al., 2016).

The slug formation process is governed by two mechanisms: shear and wetting. The first mechanism is characterized by a thin film of carrying phase between a growing bubble and the inner surface of the microtube. While, the latter mechanism shows no film layer surrounding the slugs and three-phase contact lines are in effect. The interaction between capillary force and shear stresses characterizes the bubble expansion (growth) and breakup (detachment) stages (Wang, 2015; Svetlov and

Abiev, 2018). Svetlov and Abiev (2018) introduced a unique coaxial-spherical junction for generating a slug flow regime over a wide range of volumetric flow rates to improve the efficiency of such channels to maintain Taylor flow in mini- and microchannels (Figure 1.3). Theirs results showed considerably longer slugs in low gas and liquid flow rates using a coaxial mixer compared to a coaxial-spherical mixer. At even lower gas flow rate, the flow pattern was changed from slug to slug-annular using the coaxial mixer. In contrast, the coaxial-spherical mixer kept Taylor flow regime due to additional force applied to the dispersed gas flow. They also correlated the length of the bubbles to geometric dimensions, features of the mixer shape, and phase superficial velocity ratio. Svetlov and Abiev (2021) mathematically analyzed a significant role of the continuous phase flow rate on the hydrodynamic characteristics and droplet formation in a mixer of coaxial and T-shaped junction. A force balance includes Archimedes, surface tension, resistance, dynamic pressure, and inertia components, in which the relative velocity of the dispersed phase can be less or greater than the carrying phase velocity that controls the slug formation process. After simplifying and applying boundary conditions, they obtained an expression that describes the velocity at the phase boundary. As a result, they showed a weaker effect of the dispersed phase flow rate compared to the continuous phase on the length of the slugs; conversely, the dispersed phase flow rate significantly governed the critical diameter of the slugs.

The Hagen-Poiseuille equation is a physical law to compute a Newtonian and incompressible pressure drop through a long circular tube with a constant cross-sectional area (White, 2016). The flow regime remained laminar due to the low Reynolds number of the microflows, where the fanning friction factor becomes $\mathrm{f} = 16/\mathrm{Re}$ for round tubes. The hydrodynamics of single-phase flow in microchannels shows similarities to a conventional channel with a larger diameter (Herwig and Hausner, 2003; Sharp and Adrian, 2004; Hetsroni et al., 2005; Kohl et al., 2005; Morini et al., 2007; Park and Punch, 2008). However, due to the increased effects of surface tension compared to inertial forces in milli- and microchannels, such flow regimes and transport phenomena differ from those investigated by scholars over the last few decades. Even with the simplicity of two-phase flow formation, the hydrodynamics of such flows is complex due to the interaction between phases. The momentum, heat,

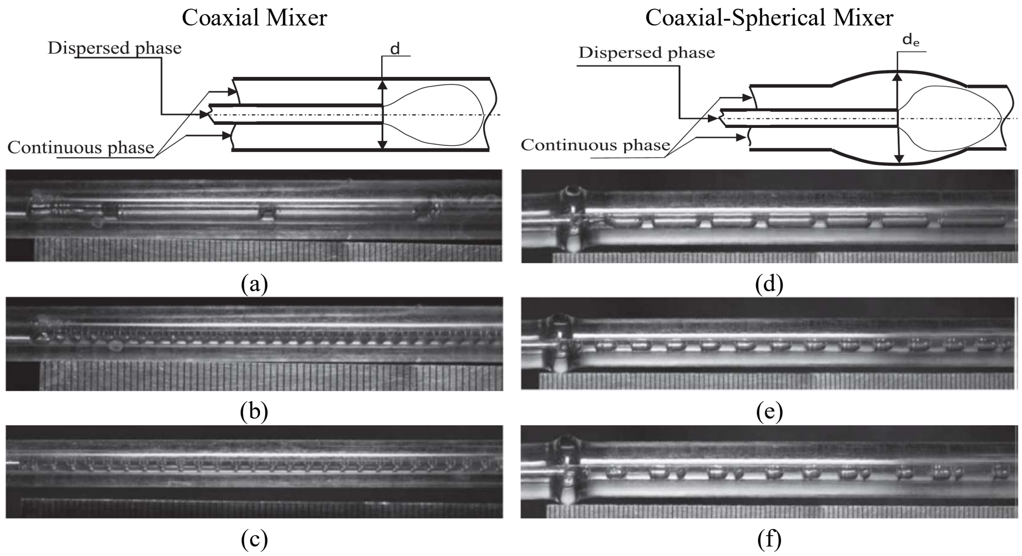

FIGURE 1.3: Schematics of coaxial and coaxial-spherical mixers and snapshots of gas-liquid Taylor flow through a straight microchannel and a nozzle with inner diameters of 2 and 0.51 mm, respectively. Superficial velocities of gas and liquid phases are (a) 0.087 and 0.18 m s^{-1}, (b) 0.284 and 0.83 m s^{-1}, (c) 0.31 and 0.37 m s^{-1}, (d) 0.09 and 0.15 m s^{-1}, (e) 0.03 and 0.3 m s^{-1}, and (f) 0.316 and 0.34 m s^{-1}, Svetlov and Abiev (2018)

and mass transfer rates in Taylor flow are essentially dependent on the pattern of slug train and their subsequent motion through the capillaries. The comparison between the same length of tubes involving single-phase and two-phase flows showed the enhanced rates of heat and mass transfer and pressure drops (Jakiela et al., 2012; Yao et al., 2019; Alrbee et al., 2019, 2020, and 2021).

1.2 Motivations

Bubbles and droplets are widely encountered in nature, biological environments, and many human-made products. The complex hydrodynamics of GL and LL flows have been twisted with the ecological features of our surroundings and greatly influence the behaviour of systems. Surface tension has a critical role in the interaction between bubbles and microorganisms in natural and artificial ecosystems. Bubbles and droplets are being desired in the oxygenation processes, bio- and microreactors. The complexity of multiphase flow lies in its transient nature and unpredictable transitions between various flow patterns. From an engineering point of view, energy dissipation and transport phenomena in multiphase flow devices are two key concerns to be analyzed carefully to understand problems that can be potentially led to sustainable development.

As mentioned earlier, two-phase Taylor flow usually consists of a train of dispersed bubbles or droplets carried by a continuous phase, potentially enhancing heat and mass transfer rates in industrial applications. Figure 1.4 presents a series of schematics and experimental snapshots of GL flow patterns in capillaries. The geometrical details of the channel, configuration of the channel, properties of phases, superficial velocities of phases, and types of junctions are the predominant factors to determine flow patterns in microchannels. Each phase's wetting or drainage effects are responsible for at least part of the flow regime in multiphase flows. In a bubbly flow regime (Figure 1.4a), the individual bubbles move through the liquid phase at very low liquid superficial velocities, i.e., 100% of surviving small bubbles. When the bubble size is small, the interaction between bubbles is negligible.

Conversely, increasing the gas-to-liquid volumetric flow rate causes the bubbles to coalesce, and a breakup occurs (Figure 1.4b). Bubble coalescence becomes more potent as the gas-to-liquid volumetric fraction increases to make large long bubbles with a rounded front that spans the cross-sectional area of the channel (Figure 1.4b). Characteristics of the bullet-shaped bubbles, most often called Taylor or slug flow, in which the Taylor bubbles are surrounded by a thin layer of the carrier liquid phase (Figure 1.4c). Some small-dispersed bubbles are between the Taylor bubbles as the gas-to-liquid volumetric ratio is enhanced to transition from slug to churn patterns (Figure 1.4c). In slug / semi-annular transition flow (i.e., a transition from slug to churn flow pattern also called unstable slug flow pattern), neither dispersed nor carrier phases are continuous and irregular plugs of gas flow through the liquid phase, and a wide variety of bubble lengths can be observed. This chaotic flow pattern occurs when the velocity increases (Figure 1.4d). An oscillating chaotic flow in large-diameter tubes is much more remarkable than in small-diameter tubes. In an annular flow pattern, liquid slugs are nonexistent, and a very thin thickness of the liquid phase remains on the walls of the channel for two flow conditions: the gas-to-liquid volumetric flow rate increases and the velocities of phases rise at low liquid volume fraction (Figure 1.4e). While very small-diameter droplets of the liquid phase are in the core of the gas phase, the flow pattern is annular (Figure 1.4f).

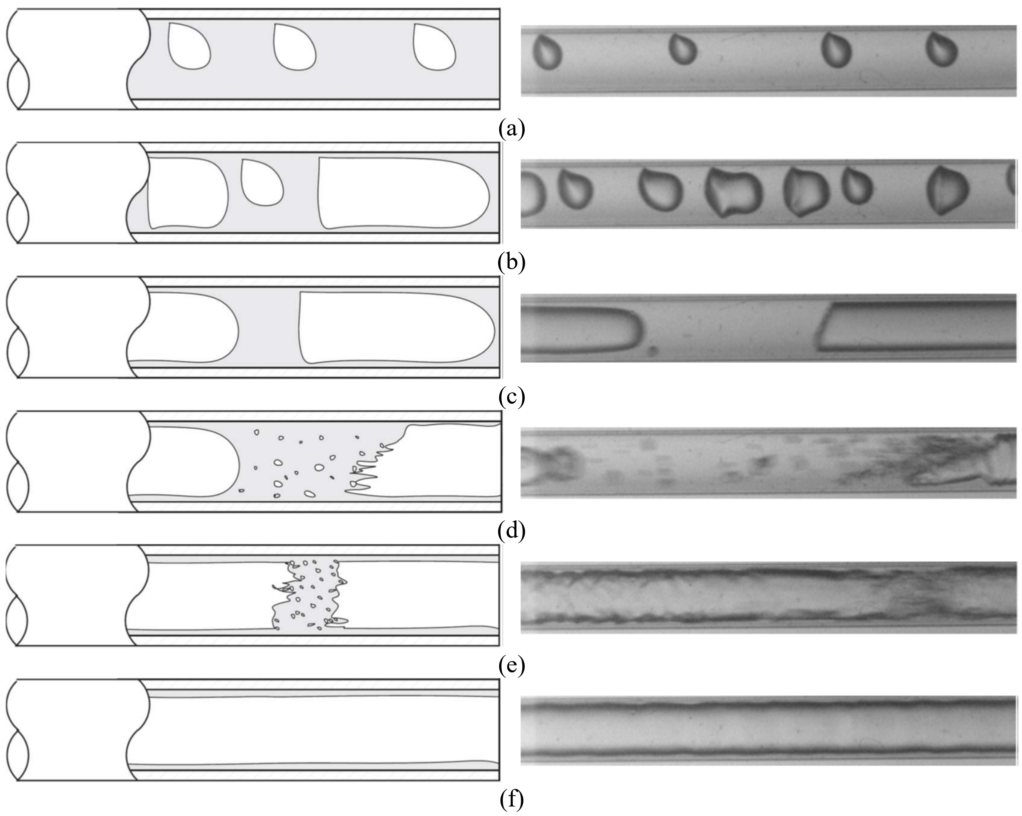

FIGURE 1.4: The schematic flow patterns (left column) and experimental snapshots (right column) of observed flow patterns and transitions for R-134a flow through a tube with an inner diameter of 0.509 mm and the length of 70.70 mm in the horizontal configurations; (a) bubbly flow, (b) bubbly / slug or segmented flow, (c) slug or Taylor flow, (d) slug / semi-annular flow, (e) semi-annular flow, (f) annular flow, Revellin (2005)

Although the flow patterns in microchannels and large-diameter channels show similarities, there are several differences. As the channel diameter increases, the laminar flow regime starts to be unstable due to the inertial effects. Kawaji and Chung (2003) and Akbar et al. (2002 and 2003) indicated flow patterns in micro and minichannels, where the stratified flow regime was not present for larger channels. Kreutzer et al. (2005b) numerically and experimentally discussed the effects of increasing the Reynolds number on the bubble profile. Their results indicated a more elongated nose and flattened tail due to the lack of large enough interfacial forces to keep the hemispherical shape of the bubble caps as Reynolds number increased.

A graphical representation called phase-mapped diagram is a common way to predict the local flow pattern of two-phase flow through a capillary and explain flow characteristics qualitatively. This diagram is to identify the influences of two-phase flow on the structure of analytical, experimental, or numerical models. A phase-mapped diagram is generally in terms of superficial phase velocities, including the transition lines in such maps to specify the criterion of a transition from one flow regime to another. Figure 1.5 shows two log-log flow maps in circular and square microchannels developed by Kawaji and Chung (2003). They used different terminology to classify the provided maps based on the shape of the gas-liquid interface around the gas bubbles (refer to the legend in Figure 1.5). Their horizontal microchannel apparatus utilized a pneumatic pump to establish air / water flow.

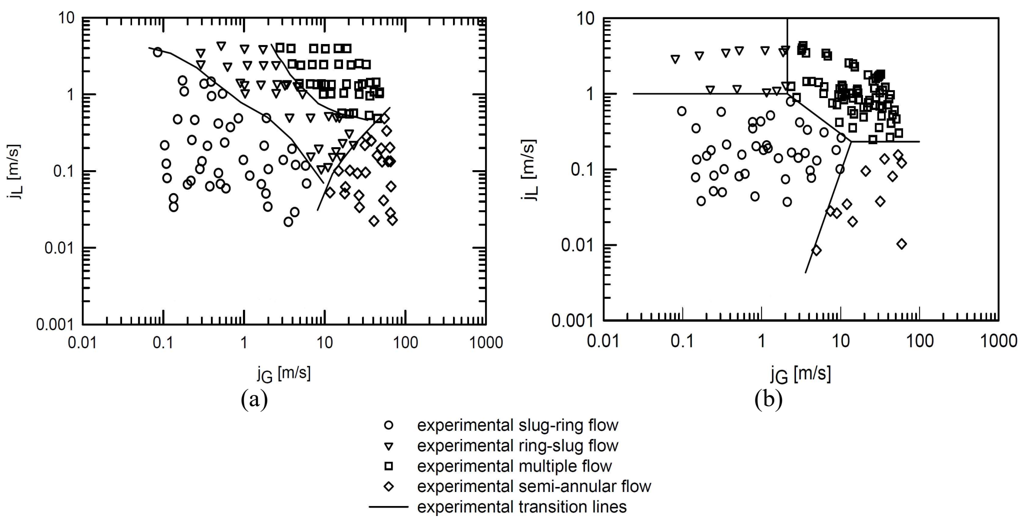

FIGURE 1.5: Gas-liquid two-phase flow regime maps in terms of superficial phase velocities for (a) a circular microchannel with an inner diameter of 100 μm and (b) a square microchannel with a hydraulic diameter of 96 μm. A linear pressure drop distribution was assumed between the inlet and outlet of channels to evaluate flow parameters, such as phase velocity at the observation window of the microchannels. The slug-ring flow regime occurred when the void fraction was less than 0.8, and the ring-slug flow regime occurred when the averaged void fraction was greater than 0.8, Kawaji and Chung (2003)

Energy dissipation, heat and mass transfers, and material consumption are critical factors in energy-related and process applications. Utilizing Taylor flow in such applications can aim for more compact heat exchangers and optimal operational conditions, which is in line with sustainable development. Understanding Taylor flow's hydrodynamic characteristics and thermal behaviour are of interest to meet this achievement. Several microchannel heat exchangers have been designed to enhance heat transfer rate, such as diverging, converging, and wall-mounted vortex generators. All the designs can increase convective surface area and flow circulation (Zhang et al., 2021). Due to dominant surface tension and viscous effects in such channels, any change in flow structure may lead to significant variations in pressure drop, wall-to-bulk flow temperature difference, and phase concentration throughout the channels. Therefore, dispersed bubble / slug formation, slug breakup, liquid film thickness, slug length, slug velocity, pressure drop, and heat and transfer coefficients are of interest to be addressed. The interactions of convection and advection either inside or outside of bubble / droplet Taylor flow throughout the capillaries are responsible for providing sustainable optimal flow conditions where the pressure drop is low, and heat and mass transfer are high. To sum up, a superior comprehension of Taylor flow hydrodynamics and heat and mass transfer mechanisms enable us to attain these targets.

1.3 Objectives and Scopes of the Present Work

Taylor flow through mini- and microchannel modeling for numerical simulations or establishing for experimental works most often requires a clear and in-depth understanding of the hydrodynamics of Taylor flows in those geometries. Two-dimensional (2D), three-dimensional (3D), and axisymmetric channels can be considered for numerical simulations. Each one takes the analysis forward differently and necessarily needs a meaningful discussion by the designer. The realization of Taylor flow in microtubes or microfluidic chips is integrated with careful image acquisition, image processing, and reconstruction of the z-component velocity perpendicular to the light sheet in the particle image velocimetry (PIV) method (Mießner et al., 2020 and 2021). A train of slugs in segmented flows accumulates a total pressure drop throughout the channel, breaking down into pressure drops over a unit cell. Technically, a unit cell can consist of two halves of subsequent slugs and a full plug or two halves of subsequent plugs and a full slug. The latter, which is displayed in Figure 1.6 by a dashed outline, has been employed by researchers to show the variations of flow parameters (e.g., Gupta et al., 2009 and 2013; Talimi et al., 2012; Sontti and Atta, 2017). As is also seen in Figure 1.6, the slug curvatures at two ends follow an approximate semi-hemispherical profile connected to a flat film region by transition regions. This semi-hemispherical curvature is demonstrated in experimental and analytical data (e.g., Bretherton, 1961; Aussillous and Quéré, 2000; Han and Shikazono, 2009).

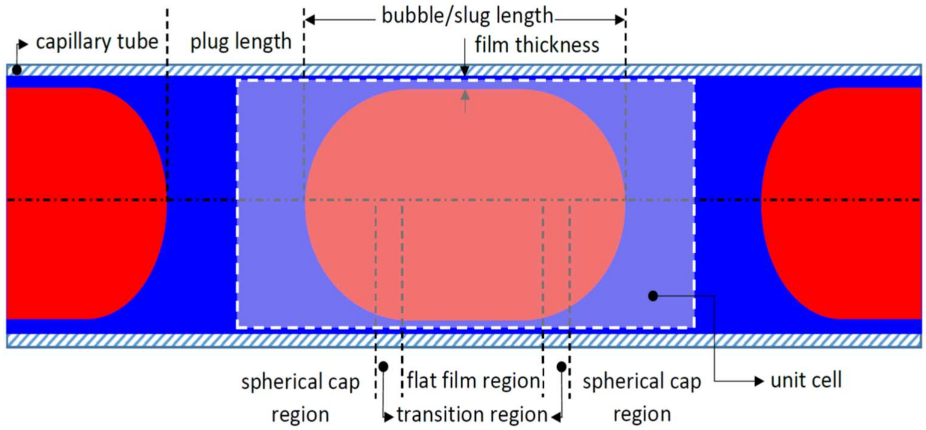

FIGURE 1.6: Different regions of a typical Taylor flow (dispersed slugs are coloured red and carrying flow is coloured blue)

Due to the presence of a film region in a typical Taylor flow and the predominant impact of the boundary layer, surface tension, and shear stress compared to the inertia forces within the film region, bypass flow can be observed as the droplets / slugs move downstream. Taylor (1961) presumed the possibility of a thin layer of carrying flow around the slugs where the recirculating vortex was plotted in Figure 1.7. Later studies confirmed the structure of the GL and LL Taylor flows by numerical simulations and experimental methods using PIV compared to Taylor's findings (Cox, 1963 and 1964; Thulasidas et al., 1997; Günther et al., 2004; Fukagata et al., 2007; Meyer et al., 2014; Helmers et al., 2019; Mießner et al., 2020). The film region's surface tension and viscous effects decelerate the bypass flow and enhance the circulation inside the droplets / slugs. In addition, due to the very small diameter of microchannels, the inertia and gravity effects are in the order of d^3 while viscous, and surface tension effects are in the order of d^2 (Abiev, 2011 and 2012). The impacts of bypass flow on a growing bubble in a microfluidic T-junction were studied by van Steijn et al. (2007 and 2009) experimentally by means of the µPIV technique. Their accumulated findings are summarized below:

- About one-quarter of the liquid phase passes the gas bubble
- The gas bubble formation process includes three steps:
    - The gas bubble grows until occupying the junction
    - Gas bubble development decreases as the liquid phase passes the bubbles, and the bubble neck is tightened

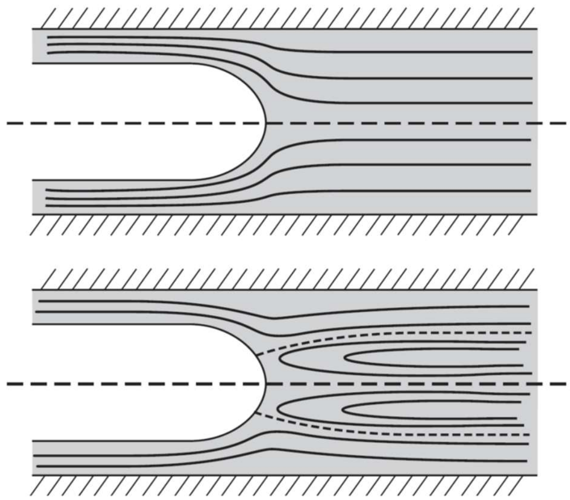

FIGURE 1.7: Rough sketches of the two simplest possible flow patterns and recirculating vortex in the liquid plugs between elongated air bubbles in Taylor flow in capillaries. The upper pattern shows complete bypass flow without any stagnation region at the nose of the bubble for $m > 0.5$. In this case, the central streamlines are moved towards the nose meniscus of the bubble, and only one stagnation point is possible. This situation can be created when the flow reaches a steady-state motion by superposing a mean velocity of –U in the reverse direction of the main flow. The bottom pattern occurs for $m < 0.5$, when the central streamlines are moved away from the bubble nose and form a stagnation point on the vortex and a stagnation ring on the meniscus. A true index of the velocity of flow (m) also called '*droplet mobility*', is the ratio of the velocity difference between a bubble and mean flow ahead of the bubble to the bubble flow velocity, which Taylor (1961) introduced in his pioneering work on Taylor flow

  - Gas bubble neck rapidly decreases until approaching one-quarter of original diameter before breaking up

- The breakup is initiated, not by a Plateau-Rayleigh instability (Papageorgiou, 1995), but by the liquid flow that passes the tip of the thread to the neck where pinch-off occurs

In noncircular channels with sharp corners, droplets / slugs do not entirely occupy the cross-sectional area and the film thickness is not uniform. In this case, bypass flow becomes stronger, and the relative velocity of droplets / slugs must be taken into account. The operational conditions, transport phenomena, and hydrodynamic features cause the non-equality of slug and mean velocities up to 30% deviation (e.g., Wong et al., 1995; Fuerstman et al., 2007; Parthiban and Khan, 2013). The droplets / slugs velocity is always less than the mean velocity of flow behaving from a leaky piston in the fully-wetted regime to a fitted piston as the capillary number increases (Jose and Cubaud, 2014; Kreutzer et al., 2018; Helmers et al., 2019). A reversed local pressure gradient in respect to the overall flow direction speeds up droplets / slugs to move faster than the averaged velocity of the flow. In this case, the carrying flow is moved from the frontal plug of the droplets / slugs to the plug on the back (Abiev, 2017). This reversed pressure gradient can also reshape the droplets / slugs in micro-sized channels by exerting forces on the interface. The dynamic of droplets / slugs deformation was experimentally conducted by Sauzade and Cubaud (2013) and Ładosz and van Rohr (2018), for example, to show a significant effect of liquid film thickness on the accuracy of pressure drops. The latter study proposed two models called moving film and no-film; their inaccuracies are attributed to the viscosity ratio of phases involved. The first model estimates the liquid film thickness by treating it as the fitting parameter. Table 1.1 presents the averaged deviation between the first two models and the other models in literature to predict pressure drop experimentally.

TABLE 1.1: Comparison of the average error between the calculated and measured values of pressure drop for the four models: moving film, no-film, no-film and gutters, and mechanistic. The first two models are proposed by Ładosz and von Rohr (2018) by treating the droplet body as an annular flow which allows to predict the velocity distribution in the film layer in the first model and neglecting the film layer in the second model. The third model considers the main contribution of liquid droplets and not thin-film and gutters towards pressure drop proposed by Yue et al. (2014). Garimella et al. (2003) developed the last model for vapour / liquid slug flow in noncircular microchannels solves the Couette flow problem for annular flow between the tube wall and the liquid / bubble interface. The absolute difference between the first two models and the others is taken to calculate the error values

Experimental Series	**Channel Size** (μm)	**Models** Ładosz and von Rohr (2018) (1)	(2)	Yue et al. (2014) (3)	Gari et al. (2003) (4)
Water / Toluene	200	14.3%	14.9%	23.8%	40.1%
Water / Toluene	400	19.9%	19.9%	37.9%	52.3%
Water / SiO	200	31.4%	39.4%	19.9%	56.4%
Water / SiO	400	29.3%	41.3%	14.6%	57.1%

Model (1)
$$\frac{\Delta P}{L} = \alpha \frac{\mu_c U}{A}\left(1 - \frac{A}{A_d}\frac{U_d}{u_d}\right) + \alpha \frac{A}{A_d}\frac{U_d}{u_d}\frac{U}{\left(\frac{1}{\mu_d} - \frac{1}{\mu_c}\right)\frac{A_d^2}{A} + \frac{A}{\mu_c}} + \sigma \frac{w+h}{A}\frac{f_d}{u_d} c_1 Ca_d^{2/3}$$

Model (2)
$$\frac{\Delta P}{L} = \alpha \frac{\mu_c U_c}{A}\left(1 + \frac{\mu_d}{\mu_c}\frac{U_d}{U_c} + \frac{w+h}{\alpha}\frac{f_d}{U_c} c_1 Ca_d^{-1/3}\right)$$

Model (3)
$$\frac{\Delta P}{L} = \frac{1}{L_s + L_d}\left(\frac{C\mu_c L_s U + C\mu_d (L_d - D_H) u_d}{A} + c_1 Ca^{2/3}\frac{2\sigma}{D_h}\right)$$

Model (4)
$$\frac{\Delta P}{L} = \frac{1}{L_s + L_d}\left(\frac{32\mu_c U L_s}{D_h^2} + \frac{32\mu_d (u_d - 2u_f) L_d}{D_d^2} + \rho_c\left(1 - \frac{D_d^2}{D_h^2}\right)\frac{(U - u_d)(u_d - u_f)}{2}\right)$$

This thesis presents an in-depth discussion of the governing forces and the fluid dynamics of Taylor flow in microchannels. Hydrodynamics of Taylor flow in mini and micro capillaries is presented in Chapter 2 highlighting state-of-the-art experimental and numerical methods, flow transitions, slug length correlations, and pressure drops. Chapter 3 discusses the prediction of liquid film thickness in Taylor flows through mini- and microchannels with different cross-sectional geometry. The variations of liquid film thickness are shown over a wide range of capillary numbers for both experimental and computational studies. The literature review shows the depth of research conducted in the field of multiphase Taylor flows that are of interest for mechanical and chemical engineers dealing with transport phenomena. Even though most studies have adequately discussed the momentum, heat, and mass transfer in microchannels, there are still vague aspects of numerical discretization approaches, numerical methods, liquid film thickness, interface region, and heat transfer performance.

Chapter 4 develops a method to establish a step-by-step analysis and provide detailed reference data for the fluid dynamics of gas-liquid and liquid-liquid Taylor flows through tubular capillaries. The volume of fluid (VoF) method is employed to simulate the interface between two phases, i.e., air and water. The numerical results lets us quantify flow patterns, slug lengths, slug curvatures, film thickness, and pressure drop. In Chapter 5, a systematic analysis is conducted by exploring the effects of different superficial velocities and apparent viscosities on the hydrodynamics of a slug flow regime. A concentric junction is employed to make bubbles of air in a continuous flow of water and slugs of water in a continuous flow of dodecane oil. Two models are proposed to describe bubble velocity and film thickness in terms of Weber number, gas holdup, and channel diameter. The singularity of a sudden expansion's influence on the GL and LL two-phase flow behaviour is also accessed in Chapter 6. The air-bubble and water-slug evolution processes, slug breakup, and slug expansion are investigated. In all cases, the lengths of air bubbles and water slugs increase with increasing superficial velocity ratio, particularly before the expansion. The methodology and results throughout Chapters 4–6 are validated by available experimental and numerical data in literature.

Chapter 7 presents an experimental setup to predict pressure drop and heat transfer rate using an open-loop water / oil two-phase non-boiling flow through mini-scale tubing with sizes of 1.42, 1.52, and 1.65 mm in which LL Taylor flow is heated under a constant wall temperature. Two silicone oils with 1 and 5 cSt at several volumetric flow rates are used to establish segmented flow. The impacts of the channel diameter, viscosity, and volumetric flow rate ratio on the flow patterns, pressure drop, film thickness, and heat transfer rate are investigated. The results reveal that slug length affects pressure drop and heat transfer rate significantly.

Chapter 8 summarizes the main findings of the present study, conclusions and reviews a few observations found during this research that future researchers might explore. The accumulated results provide deep insight in the physics of Taylor flows in circular capillaries, and the methodology reported herein can also be extended to mass transfer for improving the reactor design and microfluidics devices.

Figure 1.8 shows a summary of some critical parameters in Taylor flow analysis. They are classified into three interdependent categories: hydrodynamics, heat, and mass transfer.

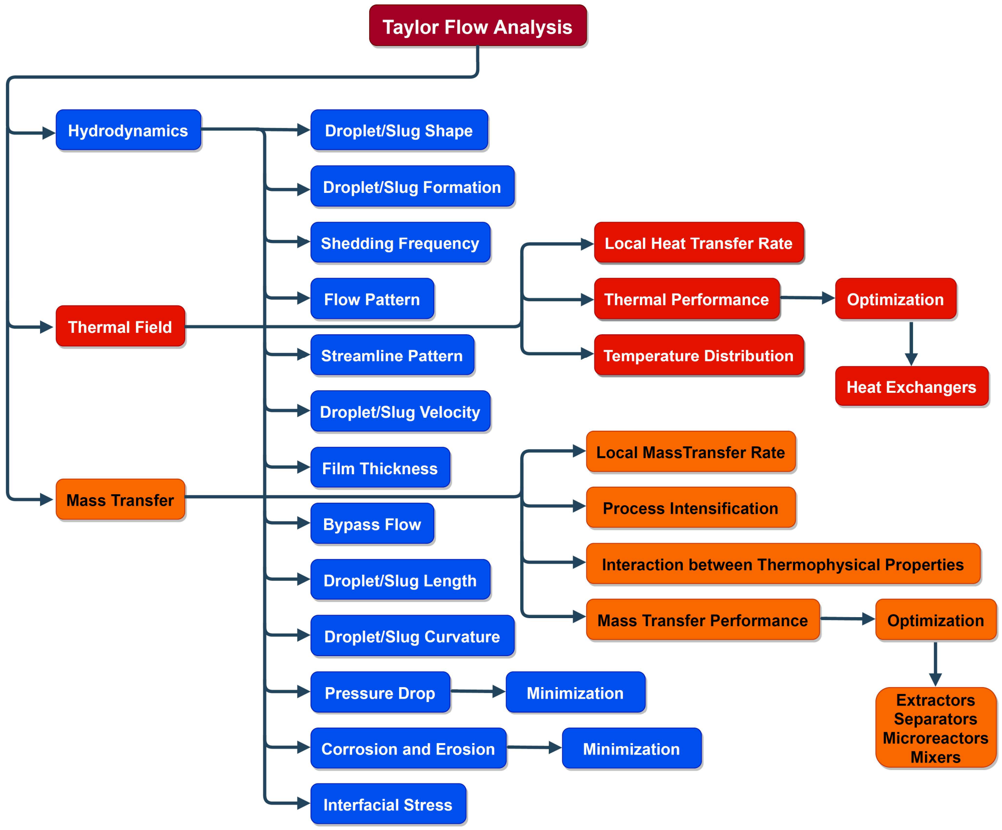

FIGURE 1.8: A summary of Taylor flow analysis including three main categories: hydrodynamics (flow field), heat, and mass transfer. Each category involves the prediction / determination of many key parameters, which explain the behaviour of droplets / slugs in a segmented flow. Controlling a typical Taylor flow can aim to understand the physics and optimize the performance of such flows. The flow field and geometrical parameters are interdependent and need to be analyzed through the microchannel and the individual Taylor droplet / slug

Chapter 2

Basics, Identification, and Hydrodynamics of Taylor Flow in Microchannels[1]

2.1 Overview

Taylor flow is a strategy-aimed flow to transfer conventional single-phase into a more efficient two-phase flow resulting in an enhanced momentum / heat / mass transfer rate, as well as a multitude of other advantages. To date, Taylor flow has focused on the processes involving gas-liquid and liquid-liquid two-phase systems in microchannels over a wide range of applications in biomedical, pharmaceutical, industrial, and commercial sectors. Appropriately micro-structured design is, therefore, a key consideration for equipment dealing with transport phenomena. This chapter highlights the hydrodynamic aspects of gas-liquid and liquid-liquid two-phase flows in microchannels. It covers state-of-the-art experimental and numerical methods in the literature for analyzing and simulating slug flows in circular and noncircular microchannels. This chapter's main objective is to identify the considerable opportunity for further development of microflows and provide suggestions for researchers in the field. Available correlations proposed for the transition of flow patterns are presented. A review of the literature of flow regime, slug length, and pressure drop is also carried out.

[1] This chapter is written based on:
Etminan, A., Muzychka, Y.S., Pope, K. (2021a) A review on the hydrodynamics of Taylor flow in microchannels: experimental and computational studies. Processes. 9, 870.
DOI: 10.3390/pr9050870

2.2 Introduction

Multiphase flow in micro-sized structures refers to a microflow in which two or more distinct phases are recognizable, i.e., a carrying or continuous phase and one or more dispersed phases. A two-phase flow denotes a combination of two distinct phases, including gas, liquid, and solid particles. Gas-liquid (GL) and liquid-liquid (LL) are two common types of multiphase flows in microchannels encountered in various practical applications, such as biomedical, pharmacological, engineering, and commercial purposes. Immiscible LL two-phase flows can also be observed in many industrial applications, where the dispersive liquid flow is introduced as droplets into the carrying liquid flow. Intensified liquid-liquid extraction as a separation process is another application for two-phase flow in oil and gas industries. The gas bubbles with equivalent diameters of the microchannel diameter in a GL Taylor flow are surrounded by a thin liquid film of the continuous flow and separated by the liquid slugs (Angeli and Gavriilidis, 2008). The interaction between the different phases, flow rates, thermophysical properties, and geometrical details of the channel characterizes the flow pattern, liquid film thickness, gas bubble or droplet shape, pressure drop, heat, and mass transfer rates. Knowledge of two-phase flow characteristics enables researchers and designers to optimize channel size and operating conditions. Minimizing the pressure drop can reduce corrosion and erosion while providing a high heat transfer rate (Angeli and Gavriilidis, 2008; Awad and Muzychka, 2010). An essential feature of Taylor flow is the flow pattern in the liquid slug, which can also be classified in recirculation flow and bypass flow (Awad and Muzychka, 2008 and 2010). Therefore, knowledge of hydrodynamic properties of Taylor flow is certainly required to understand transport phenomena characteristics for improving the performance of microchannels and enabling operational conditions to be optimized.

Angeli and Gavriilidis (2008) conducted a review on the hydrodynamic characteristics of Taylor flow for circular and noncircular small channels. Correlations for film thickness measurements were summarized and the key effects of capillary number (Ca) on film thickness were discussed in detail. Recently, Etminan et al. (2022a) presented all of the correlations proposed for film thickness measuring in the literature. They found the best-fitted correlation between some experimental data and a wide range of Ca. It can be concluded that there is still a lack of certainties for the gradient of surface tension at the interfacial region resulting in discrepancies between experimental predictions and numerical / theoretical findings. Moreover, more attempts should be devoted to finding specific flow and operational conditions for enhancing the performance of microchannels.

For multiphase flows, it is necessary to predict the transport phenomena in terms of flow parameters, i.e., superficial flow velocity components, slug length, liquid film thickness, and the flow rates of each phase. Multiphase flow is valid as long as the separation between phases is recognizable at a scale greater than the molecular level. The ability to describe the behaviour of multiphase flow requires a set of basic definitions and assumptions. The following subsections have been designed to represent the importance of these basic definitions and the role of dimensionless groups in describing the two-phase flows' behaviour. This chapter is aimed to review two-phase flows in microchannels, with a particular focus on the hydrodynamic aspects. Fundamentals of multiphase flows, such as basic definitions and dimensionless parameters are studied. Identification of flow pattern and bubble / droplet formation are discussed in experimental investigations, numerical simulations, and flow regime transitions. Correlations of slug lengths and pressure drop are presented and classified in terms of cross-sectional areas of microchannels.

2.3 Basic Definitions in Two-Phase Flows

The capillary length has been used to identify the compaction in micro-sized applications, such as microchannels in heat exchangers. A micro-sized channel can be adequately assumed when the hydraulic diameter of the channel is less than the capillary length. In contrast, for large-diameter channels, the Laplace number (La) can be properly considered as a suitable length scale for calculations instead of the bubble or droplet diameter. Many other definitions have been developed to describe the characteristics of multiphase flows, including fluid flow, and heat and mass transfers, which are presented in Table 2.1. It should be noted that due to the presence of more than one phase and the interaction between all phases involved in multiphase flow, the thermophysical properties have been expressed differently compared to those of a single-phase flow (Awad and Muzychka, 2008; Awad, 2012; Etminan et al., 2022a).

TABLE 2.1: Important definitions for multiphase flows

Name	Symbol	Definition	Description
Total mass flow rate	$\dot{m}_t$	$\dot{m}_l + \dot{m}_g$	The sum of mass flow rate of the liquid and the gas phases
Total volumetric flow rate	Q_t	$Q_l + Q_g$	The sum of volumetric flow rate of the liquid and gas phases
Total mass flux	G_t	$\dot{m}_t/A$	The total mass flow rate by cross-sectional area of the tube
Capillary length	L_{ca}	$\left[\frac{\sigma}{g(\rho_l\text{-}\rho_g)}\right]^{0.5}$	The ratio between interfacial and gravitational (buoyancy) effects
Slip ratio	S	U_g/U_l	The ratio of average real velocity of the gas and liquid phases
Average velocity of gas phase	U_g	$\frac{Q_g}{A_g} = \frac{Q_g}{\alpha A} = \frac{V_g}{\alpha}$	The ratio of volumetric flow rate of the gas phase to tube cross-sectional area occupied by the gas phase flow
Average velocity of liquid phase	U_l	$\frac{Q_l}{A_l} = \frac{Q_l}{(1\text{-}\alpha)A} = \frac{V_l}{(1\text{-}\alpha)}$	The ratio of volumetric flow rate of the liquid phase to tube cross-sectional area occupied by the liquid phase flow
Superficial velocity of gas phase	V_g	Q_g/A	The velocity of the gas phase if it flows alone in the tube or the ratio of the volumetric flow rate of the gas phase and the cross-sectional area of the tube
Superficial velocity of liquid phase	V_l	Q_l/A	The velocity of the liquid phase if it flows alone in the tube or the ratio of the volumetric flow rate of the liquid phase and the cross-sectional area of the tube
Mixture velocity	V_m	$\frac{Q_t}{A} = V_l + V_g$	The sum of the superficial velocities of two phases
Quality or dryness fraction	x	$\dot{m}_g/\dot{m}_t$	The ratio of the mass flow rate of the gas phase to the total mass flow rate
Void fraction	α	A_g/A	The ratio of the tube cross-sectional area (or volume) occupied by the gas phase to the tube cross-sectional area (or volume)
Volumetric quality (dynamic holdup)	β	Q_g/Q_t	The ratio of the volumetric flow rate of the gas phase to the total volumetric flow rate
Two-phase friction multiplier	φ	$\left(1 + \frac{C}{X} + \frac{1}{X^2}\right)^{0.5}$	A function of the Lockhart–Martinelli parameter (X) and the Chisholm constant (C)

2.4 Dimensionless Parameters

A dimensionless number can represent the ratio of two different forces or physical quantities, which play a significant role in the flow pattern and interaction between phases (Table 2.2). The length scale of a channel, which appears for the majority of dimensionless numbers, is often defined as the diameter of tubes or the hydraulic diameter of ducts.

TABLE 2.2: The most common non-dimensional numbers in multiphase flow

Name	Symbol	Definition	Description
Archimedes	Ar	$\frac{\rho_l(\rho_l\text{-}\rho_g)gd^3}{{\mu_l}^2}$	The ratio of the gravitational to the viscous effects
Bond or Eötvös	Bo Eo	$\frac{gd^2(\rho_l\text{-}\rho_g)}{4\sigma}$	The ratio of the gravitational (buoyancy) and the capillary force scales
Cahn	Cn	ξ/d	The ratio of the interface width and the tube diameter or any other length scale
Capillary	Ca	$\mu U/\sigma$	The ratio of the viscous forces and the capillary forces
Ca/Re	Ca/Re	$\mu^2/(\rho d\sigma)$	(N/A)
Froude	Fr	$U/\sqrt{gd}$	The ratio between the flow inertia and the external field
Laplace	La	$\left[\frac{\sigma}{gd^2(\rho_l\text{-}\rho_g)}\right]^{0.5}$	The ratio of the capillary and the gravitational (buoyancy) effects
Ohnesorge	Oh	$\frac{\sqrt{We}}{Re}=\frac{\mu}{\sqrt{\sigma\rho d}}$	The ratio of the viscous force to the inertia and the surface tension forces
Reynolds	Re	$\rho Ud/\mu$	The ratio between the inertia and the viscous forces
Suratman	Su	$\frac{Re^2}{We}=\frac{1}{Oh^2}=\frac{\sigma\rho d}{\mu^2}$	The ratio of the surface tension to the viscous forces
Weber	We	$CaRe=\frac{\rho U^2 d}{\sigma}$	The ratio of the inertial forces to the interfacial forces

The relation of gravitational to viscous forces is Archimedes number (Ar) that the formal definition is given in Table 2.2. This number frequently appears in tube-shaped chemical process reactor designs, which describe the motion of fluids caused by the difference in densities. The Ar was linked to the Reynolds number (Re) as an explicit iterative correlation (Turton and Clark, 1987):

$$\mathrm{Re} = \frac{\mathrm{Ar}}{18}\left(1 + 0.579\ \mathrm{Ar}^{0.412}\right)^{-1.214} \tag{2.1}$$

Hua et al. (2009) found that ellipsoidal gas bubbles were produced as the Ar and Bond (Bo) numbers were gradually increased. In solid particle multiphase flows, the Ar has also been related to the drag force coefficient and the Re (Yin and Koch, 2007; Zhang and Prosperetti, 2010; Zhan et al., 2014) and the wind threshold velocities of particles in GL flow (Rabinovich and Kalman, 2007). The Ar number was also correlated with the inverse viscosity number (N) by Quan (2011) in an upward or downward co-current Taylor flow,

$$\mathrm{N} = \mathrm{Ar}^{0.5} = \left(\frac{\rho_l\left(\rho_l - \rho_g\right) g d^3}{{\mu_l}^2}\right)^{0.5} \tag{2.2}$$

For a large N, the tail of the elongated bubbles was oscillated for the upward co-current flow, and the tail of the bubbles was shortened and even deformed to a round shape for downward co-current flow. The Bond number (Bo), also called Eötvös number (Eo), is the inverse of the Ar number and denotes the ratio between the gravitational and capillary effects. Since the Bond number varies with the square of length-scale, each change, even small, in channel diameter causes significant variation in the Bo. For air-water two-phase flow in channels of a diameter less than 1 mm, which are very common in micro-sized applications, the Bo number is approximately in the order of 0.1 and the importance of viscous effects is predominant. Therefore, the gravitational effects can be negligible in most GL flows in microchannels. Table 2.3 presents the remarkable effects for the specific range of Bo. Some other specific regions of Bo and $\mathrm{BoRe}_l^{0.5}$ numbers have been proposed by investigators to categorize the behaviour of multiphase flows. The absorption of CO_2 in micro-scale reactors where the Chisholm parameter was correlated with the Bo number was studied by Ganapathy et al. (2014). Prajapati and Bhandari (2017) quantified the instability increase of boiling flow in a microchannel for the region of $\mathrm{Bo} < 1$.

TABLE 2.3: Remarkable effects in different Bo numbers in multiphase flow

Range	Remarks	Ref.
$\mathrm{Bo} > 50$	significant wall effects elongated bubbles with spherical caps	Uno and Kintner (1956) and Hua et al. (2009)
$\mathrm{Bo} > 11$	negligible surface tension effects	Wu (2010a and 2010b) Wu and Li (2010) Wu et al. (2011)
$1.5 < \mathrm{Bo} \leq 11$	non-negligible inertia, surface tension, and viscous effects	
$\mathrm{Bo} \leq 1.5$	dominant surface tension	

The Cahn number (Cn) is defined as the ratio of the interface width (ξ) and the tube diameter or any other length scale (d),

$$\mathrm{Cn} = \xi / d \tag{2.3}$$

Cahn and Hilliard (1958 and 1959) and Cahn (1959) focused their studies on the free energy of the volume of an isotropic system, where the densities of components involved are non-uniform. The concept of the Cahn number was introduced by them when they found an increase in the thickness with temperature. Soon after, the efforts to obtain the governing equation in a non-equilibrium situation led to a well-known Cahn-Hilliard equation involving the Cahn number for the first time (Cahn, 1961; Langer, 1975; Anderson and McFadden, 1998; He et al., 2010). For example, Choi and Anderson (2011) coupled the Cahn-Hilliard theory with the extended finite volume method (XFVM) for the dynamic modeling of suspended particles in two-phase flows. The importance of viscous and capillary effects in two-phase flow in microchannels has been correlated by the capillary number based on the liquid slug velocity,

$$\mathrm{Ca} = \mu U / \sigma \tag{2.4}$$

The capillary number is a dimensionless group to explain how viscous and surface tension forces affect the interface between the gas and liquid phases, and also between two immiscible liquids. Although, the length-scale does not appear in the capillary number, surface tension forces become more significant relative to gravity as the cross-sectional area of the channel is decreased. For most microflow applications, the approximate values of superficial velocity range from 10 μms^{-1} to 1 ms^{-1}, when the viscosity is 10^{-3} $kgm^{-1}s^{-1}$, and the surface tension can be reasonably considered at 0.05 Nm^{-1}. These flow conditions cause the Ca to range from 2×10^{-7} to 2×10^{-2}. For high viscosity liquids, such as silicone oil at a mixture velocity of 1 ms^{-1}, the Ca becomes ~1. The Ca frequently appears in correlations measuring liquid film thickness (Fairbrother and Stubbs, 1935; Marchessault and Mason, 1960; Bretherton, 1961; Taylor, 1961; Schwartz et al., 1986; Teletzke et al., 1988; Irandoust and Andersson, 1989; Ratulowski and Chang, 1989; Giavedoni and Saita, 1997; Thulasidas et al., 1997; Giavedoni and Saita, 1999; Heiszwolf et al., 2001; Aussillous and Quéré, 2000; Bico and Quéré; 2000; Kreutzer et al., 2001; Heil, 2001; Kreutzer et al., 2005a; Grimes et al., 2006; Han and Shikazono, 2009; Eain et al., 2013; Gupta et al., 2013; Klaseboer et al., 2014; Huang et al., 2017; Ni et al., 2017; Patel et al., 2017), pressure drop (Bretherton, 1961; Ratulowski and Chang, 1989; Kreutzer et al., 2005a; Gupta et al., 2013; Kreutzer et al., 2005b; Walsh et al., 2009; Warnier et al., 2010; Jovanović et al., 2011; Eain et al., 2015), and slug length (Qian and Lawal, 2006; Tan et al., 2008; Fries and von Rohr, 2009; Steegmans et al., 2009) in multiphase flows. Recently, the poor accuracy of classical pressure drop correlations with an increase of the Ca was emphasized by Ni et al. (2017). This was due to the presence of waves around the tail of the bubble, change of the semi-spherical head of the bubble, and powerful circulation inside the liquid slugs. Patel et al. (2017) indicated that the film thickness at the corner of a square microchannel decreased with an increase of Ca, where a linear expression was derived for the film thickness in terms of Ca. Several other researchers showed an increasing trend in film thickness with Ca. These hydrodynamic features will be discussed in the following sections. The Re expresses the ratio of inertial to viscous effects and predicts the flow pattern in different situations:

$$\mathrm{Re} = \rho U d / \mu \tag{2.5}$$

where ρ, μ and U are the density, dynamic viscosity of the continuous phase fluid, and the velocity of flow, respectively. The thermophysical properties of a multiphase flow are different from a single-phase flow, which has been discussed by Awad (2012) in detail. Regarding the value of the inertia forces, the flow regime remained laminar for the Re numbers less than ~2300 (White, 2006 and 2016). Since the cross-sectional area of a microchannel often has a diameter of 1 mm or smaller and the liquid velocity is less than 1 ms^{-1}, the Re for water as the continuous phase is ~1000 or less. This means that the flow regime in the microchannel applications is normally laminar and the predominant effects of the viscous forces must be taken into account. Because more than one phase is involved, different approaches have been used by researchers to determine the value of Re and the thermophysical properties in the multiphase flows. To realize the importance of the Re definition, consider two following cases: first, the inertia effects of the gas phase are insignificant, when the gas and the liquid superficial velocities are in the same order. For instance, the air to water density ratio in two-phase flow is around 1.225×10^{-3}, which indicates the dominant role of the liquid phase density in defining the Re. This situation can be recognized in a bubbly flow pattern. Second, the inertia effects of both phases are important when the gas superficial velocity is relatively high compared with the liquid superficial velocity. The friction factor is necessarily calculated for the pressure drop calculation, while the Re appears in other correlations of hydrodynamic concepts, refer to section 2.7 for further information. The Re is in the correlations for liquid film thickness and pressure drop obtained by Heiszwolf et al. (2001) and Han and Shikazono (2009). The product of the Re and the We numbers was introduced as a transition criterion from slug to slug-bubbly regimes by Suo and Griffith (1964). Jayawardena et al. (1997) proposed the ratio of liquid phase to gas phase the Re numbers to identify the transitions from bubbly to slug and from slug to annular patterns. Several other non-dimensional numbers in multiphase flows have been gathered and discussed by Awad (2012).

As the diameter of the channel and the velocity of flow decrease, the inertial, and gravitational effects become negligible, while the surface tension becomes a predominant factor. The knowledge of the hydrodynamics of multiphase flow is strictly intertwined with the dimensionless numbers presented in Table 2.4. According to this table, an accurate description of the flow map, bubble or droplet formation, and transition from one flow regime to another are highly depended on Bo or Eo, Ca, Re, We, Su, and Fr. While, Bo, Ca, and Re have appeared in the pressure drop correlations so far, the friction factor is only governed by the Re. The liquid film thickness has been correlated or described with Re, Ca, and We numbers. Finally, the slug length has only included the Re and the Ca numbers.

TABLE 2.4: Dependency of hydrodynamic aspects and the dimensionless numbers

Hydrodynamic Aspects	**Dimensionless Numbers**					
	Bo (Eo)	Ca	Fr	Re	Su	We
film thickness		✓		✓		✓
pressure drop	✓	✓		✓		
slug length		✓		✓		
friction factor				✓		
flow map, slug profile	✓	✓	✓	✓	✓	✓
flow regime transition	✓	✓	✓	✓	✓	✓

A graphical flow map, which displays the specific region for each flow regime along with their transition lines, uses a few important characteristics of multiphase flow, such as superficial velocity, Re, Ca, and We. Table 2.5 summarizes the non-dimensional numbers and other flow parameters that use the x- and y-axis coordinates for quantitative-based flow map diagrams.

As a guide to reading this table; the kinetic energy of flow (ρV^2) was used by the author's group of 7 which its row and column are colored red. The first effort to display a flow pattern diagram dates back to 1953 when Baker computed the mass velocity of each phase and two other expressions involving the viscosity and densities (G/λ and $B\lambda\psi/G$) of both phases (refer to '5' in Table 2.5). These dimensional terms were not chosen by others afterward. In contrast, it is the interfacial velocities of the phases that have frequently been selected by scholars for more than half a century (refer to '1' in Table 2.5). After velocity, it seems that Re, We, and Ca numbers have the highest use by researchers for showing the flow pattern clearly and more understandably.

TABLE 2.5: Non-dimensional numbers and thermophysical properties selected by authors for displaying flow maps

		Dispersed Liquid or Gas Phase, #2									
		V	Re	Ca	Re_2/Re_1	We	We Oh	$Q_l/(Q_l+Q_g)$	ρV^2	G/λ	X	Quality
Continuous Liquid Phase, #1	V	(1)										
	Re		(13)									
	Ca			(11)		(15)		(6)				
	Re/Ca		(3)									
	We			(15)		(2)	(14)					
	Su		(9)		(10)							
	We Oh					(14)	(4)					
	ρV^2								(7)			
	$B\lambda\psi/G$									(5)		
	Flow Rate											(8)
	Force										(12)	

The list of authors: (1) Ganapathy et al. (2014), Patel et al. (2017), Hewitt and Roberts (1969), Fukano and Kariyasaki (1993), Triplett et al. (1999), Zhao and Bi (2001), Akbar et al. (2002), Kawaji and Chung (2003), Cubaud and Ho (2004), Günther et al. (2004), Yue et al. (2007), Kirpalani et al. (2008), Yue et al. (2008), Dessimoz et al. (2010), Roudet et al. (2011), Deendarlianto et al. (2019), Wu and Sundén (2019), Farokhpoor et al. (2020) (2) Akbar et al. (2002), Yue et al. (2008), Zhao et al. (2006), Yagodnitsyna et al. (2016), (3) Jayawardena et al. (1997), Dessimoz et al. (2010), (4) Wu and Sundén (2019), Yagodnitsyna et al. (2016), (5) Baker (1953), (6) Suo and Griffith (1964), (7) Hewitt and Roberts (1969), (8) Sato et al. (1972), (9) Jayawardena et al. (1997), (10) Jayawardena et al. (1997), (11) Cubaud and Mason (2008), (12) Kirpalani et al. (2008), (13) Dessimoz et al. (2010), (14) Yagodnitsyna et al. (2016), (15) Wu and Sundén (2019).

2.5 Identification of Flow Patterns and Bubble / Slug Formation

The first step of transport phenomena analysis of multiphase flows is to explain the flow characteristics in a phase-mapped diagram. The transition lines in such maps specify the criterion of a transition from one flow regime to another. A two-phase flow usually consists of a train of dispersed bubbles or droplets carried by a continuous phase, which potentially enhances the rates of heat and mass transfers in industrial applications. Although the flow patterns in microchannels and large-diameter channels show similarities, there are several differences. As the channel diameter increases, the laminar flow regime starts to be unstable due to the inertial effects. Kawaji and Chung

(2003) and Akbar et al. (2002 and 2003) indicated flow patterns in micro and minichannels, where the stratified flow regime was not present for larger channels. The effects of increasing the Reynolds number on the bubble profile were numerically and experimentally discussed by Kreutzer et al. (2005c). Their results indicated a more elongated nose and flattened tail due to the lack of large enough interfacial forces to keep the hemispherical shape of the bubble caps as Reynolds number increased.

Figure 2.1 presents a schematic of GL flow patterns in capillaries. The geometrical details of the channel, configuration of the channel, properties of phases, superficial velocities of phases, and types of junctions are the predominant factors to determine flow patterns in microchannels. The wetting or drainage effects of each phase are responsible for at least part of the flow maps in multiphase flows. In a bubbly flow regime, the individual bubbles move through the continuous liquid phase at very low liquid superficial velocities. When the bubble size is small, the interaction between bubbles is negligible. Conversely, increasing the gas-to-liquid volumetric flow rate causes the bubbles to coalesce and a breakup occurs (Figure 2.1). Bubble coalescence becomes stronger as the gas-to-liquid volumetric flow rate is increased, to make large long bubbles with a rounded front that spans the cross-sectional area of the channel. Characteristics of the bullet-shaped bubbles most often called Taylor or slug flow in which the Taylor bubbles are surrounded by a thin layer of the carrier liquid phase, Figure 2.1. Some small dispersed bubbles are between the Taylor bubbles as the gas-to-liquid volumetric flow rate is enhanced to make a transition from slug to churn patterns (Figure 2.1e). In a churn flow pattern, neither dispersed nor carrier phases are continuous and irregular plugs of gas flow through the liquid phase and a wide variety of bubble lengths can be observed. This chaotic flow pattern occurs when the velocity is increased (Figure 2.1f). In large-diameter tubes, an oscillating chaotic flow is much more remarkable than that in small-diameter tubes. This flow regime is also named a semi-annular or unstable-slug flow pattern. In an annular flow pattern, a very thin thickness of the liquid phase remains on the walls of the channel for two flow conditions: the gas-to-liquid volumetric flow rate increases and the velocities of phases rise at low liquid volume fraction (Figure 2.1g). While very small-diameter droplets of the liquid phase are in the core of the gas phase, the flow pattern is mist (Figure 2.1h).

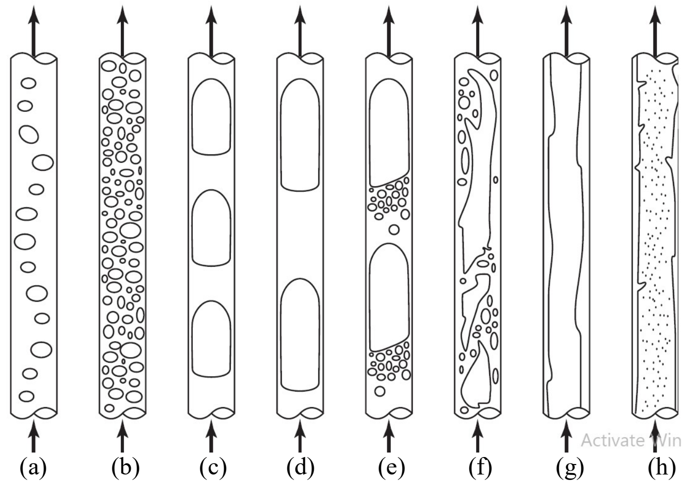

FIGURE 2.1: The schematic of observed flow regimes in the vertical microchannels; (a,b) bubbly flow, (c,d) Taylor or segmented flow, (e) transitional flow from slug to churn, (f) churn flow, (g) annular-film flow, (h) mist-annular or wispy-annular flow, Kreutzer et al. (2005a)

An experimental study of a hydrophobic ionic / water two-phase flow in two T and Y inlet junctions on the flow patterns was carried out by Tsaoulidis et al. (2013), resulting in a negligible impact of the inlet configuration. They also investigated the effects of capillaries' materials made of glass, fluorinated ethylene propylene (FEP), and Tefzel on flow patterns illustrated in Figure 2.2. Although the boundaries of the FEP and Tefzel are similar, the plug flow regime occupies a larger area in the flow map compared to the FEP capillary, and an annular pattern is observed in higher mixture velocities and lower ionic volume fraction. They did not observe annular and drop patterns in the glass capillary when the continuous phase was water.

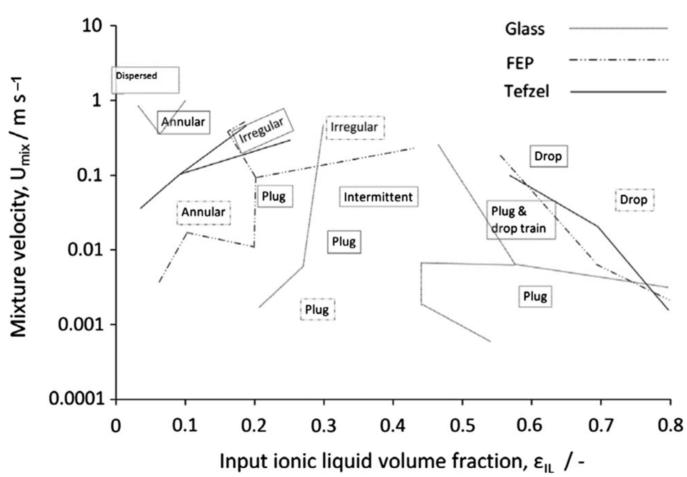

FIGURE 2.2: Flow map boundaries observed in three different glass, FEP, and Tefzel microchannels with a T-junction, Tsaoulidis et al. (2013)

2.5.1 Experimental Investigations

Transport phenomena for multiphase flows in capillary passages involve the behaviour of each phase individually, the mutual interactions of phases, and the interactions between phases and solid boundaries. The presence of gas bubbles in a multiphase flow can be considered as an obstacle to the liquid phase flow, which is known as the Jamin's effect (Wright, 1934). This phenomenon is prominent enough to decrease the productions of the petroleum industry due to the high-pressure drop and the flow pattern transition. At the interface between two components of a GL two-phase flow, the surface tension gradient is substantial, which affects the interaction between phases and other transport phenomena. Historically, this effect is known as the Marangoni effect, which pushes the liquid phase to flow away from low surface tension regions and was first explained by Gibbs (1878).

A comprehensive experimental study on the flow maps by means of high-speed X-ray photography and flash methods simultaneously was reported by Hewitt and Roberts (1969), which recognized the previous correlations for each flow pattern proposed by Baker (1953) and Wallis (1962). A rough sketch of streamlines in the slug region of a GL flow was experimentally obtained by Taylor (1961), where a stagnation point on the vortex and a stagnation ring on the curvature of the bubble were observed for two extreme cases of velocity fraction, $(V_g - V_m)/V_g$, greater and less than 0.5. The high-speed photography was compared with X-ray technology to provide clear images of air-water flow regimes through a capillary (Hewitt and Roberts, 1969). Irandoust and Andersson (1989) experimentally depicted Taylor's bubble profile, where the film thickness remained constant in the middle of the gas bubble. They also confirmed that the gas bubble was elongated in the front and squeezed in the rear parts. The effects of bubble and slug lengths on the mass transfer in a GL flow was experimentally studied by Berčič and Pintar (1997). Their results revealed that the amount of nitrite transported was independent of the gas bubble length and primarily depended on the liquid slug length. A review study on the flow maps was conducted by Akbar et al. (2002) to show the dominant effects in each flow regime using available experimental data. They proposed a hydraulic diameter of 1 mm as a criterion for classifying the previous studies into the five regions: bubbly, plug or slug (surface tension dominated), annular (inertia dominated), dispersed, and transition zones regarding the amounts of superficial velocities and the Weber numbers. Micro-particle image velocimetry (μ-PIV) and fluorescence microscopy techniques were used by Günther et al. (2004) to recognize a micro-segmented GL flow in a rectangular cross-section area channel. They showed that the roughness of the inner side of the channel and compressibility of the gas bubbles induce an imbalance into the flow field and accelerate the mixing rate accordingly. The periodic switching of recirculation regions in the liquid slugs caused a higher mixing rate in a meandering channel compared with a straight channel (Figure 2.3). Dore et al. (2012a) investigated the dynamics of water / ionic two-phase flow by exploring slug formation and recirculation flow in fluid segments at T-junction, straight and curved microchannel employing μ-PIV. As shown in Figure 2.4, the circulation patterns in water plug consisted of two main mirrored and counter rotating vortices for low mixture velocity. As the mixture velocity increased, two secondary vortices arose at the nose cap of water plug.

The flow patterns of an LL two-phase flow in a rectangular cross-section duct were experimentally investigated by Zhao et al. (2006). The flow maps and the flow transitions were correlated by the inertia forces of each phase and the interfacial forces. They realized six distinctive flow maps in terms of dispersed phase droplet formation process at a T-junction as follows:

- Slug regime; when the interfacial tension is greater than inertial forces, and Weber numbers are $7.61 \times 10^{-6} < \mathrm{We_{ws}} < 4.87 \times 10^{-2}$ and $5.94 \times 10^{-6} < \mathrm{We_{ks}} < 5.94 \times 10^{-4}$.
- Monodispersed droplet regime; when the carrier phase flow rate is increased, and the Weber numbers are $7.61 \times 10^{-2} < \mathrm{We_{ws}} < 0.78$ and $2.38 \times 10^{-5} < \mathrm{We_{ks}} < 5.94 \times 10^{-4}$.
- The droplet population regime; when $1.07 < \mathrm{We_{ws}} < 30.43$ and $3.8 \times 10^{-4} < \mathrm{We_{ks}} < 2.38 \times 10^{-1}$. This flow regime is observed at the centre of the channel where the inertial effects of the continuous phase are significantly greater than the interfacial tension.
- Chaotic thin striations regime; when both flow rates are increased the We numbers are in a range of $0.17 < \mathrm{We_{ws}} < 30.43$ and $4.29 < \mathrm{We_{ks}} < 53.5$. This flow map will be eventually changed into annular due to the instability of the flow.

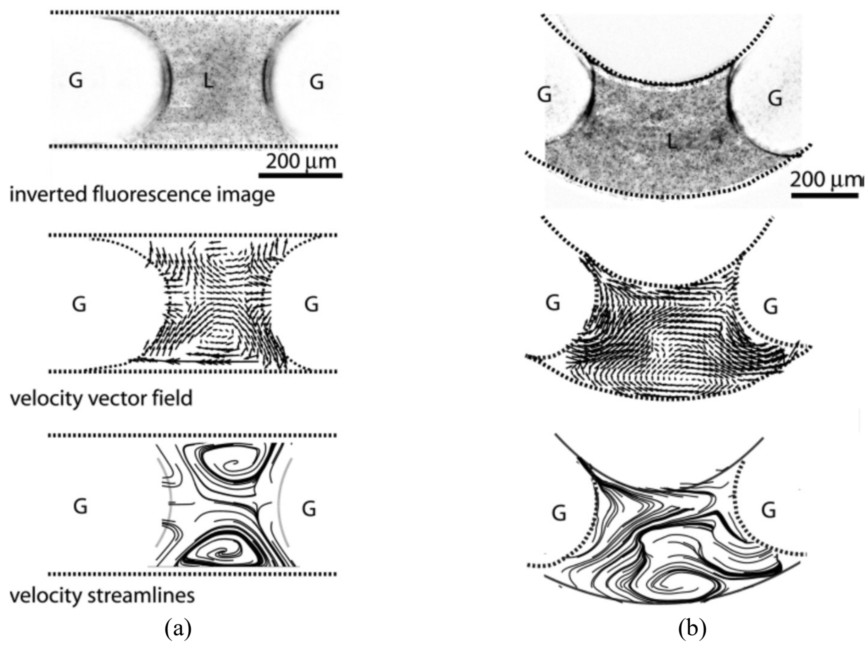

FIGURE 2.3: The sketch of fluorescent micrographs for, (a) straight channel, and (b) meandering channel, Günther et al. (2004)

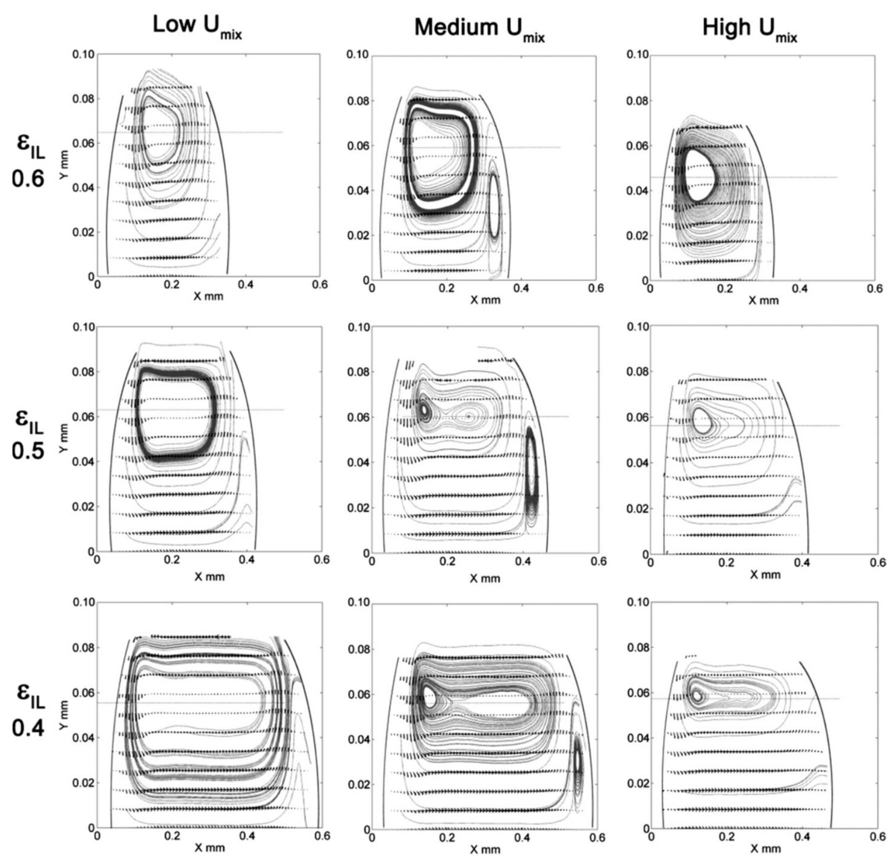

FIGURE 2.4: Schematic representative of circulation patterns within water plugs for three different water holdups and mixture velocities, Dore et al. (2012a)

A combination of experimental observations and numerical simulations was employed by Meyer et al. (2014) to show velocity profile, flow patterns in a 2 mm × 2 mm vertical channel, Figure 2.5. Both methods predicted a Couette velocity distribution within the liquid film region, a mirrored main recirculating region, and two small vortices in the nose and rear caps with a direction of opposite. They also realized some differences between the results of the two methods as shown previously by Aland et al. (2013).

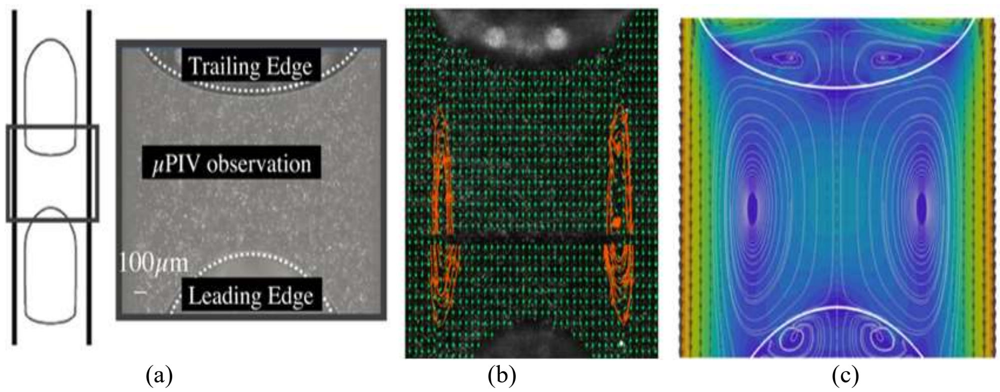

FIGURE 2.5: Flow patterns and streamlines within the Taylor bubble and liquid plug predicted by (a,b) μ-PIV, and (c) numerical simulation, Meyer et al. (2014)

Experimental analysis by Zhao et al. (2006) revealed that the volume of dispersed flow was significantly affected by interfacial forces, inertia force, and the volumetric ratio of dispersed phase, which correlated by the multivariable least squares method,

$$\frac{R}{d_H} = -0.1276 \ \ln\left[\frac{We_{ws}\ (1\text{-}\varepsilon)}{(We_{ks}\varepsilon)^{0.15}}\right] + 0.5595 \tag{2.6}$$

where the dynamic hold-up fraction (ε) and equivalent radius (R) in terms of the volume of dispersed phase (V_d) are,

$$\varepsilon = Q_k/(Q_w + Q_k) \tag{2.7}$$

$$R = \sqrt[3]{3\forall_d/4\pi} \times 10^{-3} \tag{2.8}$$

The diameter of the channel has a major role in the measured void fraction and a flow pattern which is shown in Figure 2.6 for the small diameter tube of 38.1 mm (upper row) and large diameter tube of 101.6 mm (lower row). An increase in tube diameter resulted in more compressed gas bubbles toward the top wall and occupied a smaller region of the cross-sectional area (Kong et al., 2018). The measurement also showed that a further increase in superficial velocity ratio makes a more uniform gas phase distribution realized by a smaller portion of gas volume in the top region of the tube. As a consequence, the bubbly to plug / slug transition occurs at lower superficial velocity as the channel's diameter increases (i.e., j_g =0.51 ms^{-1} for the smaller pipe and j_g =0.25 ms^{-1} for the larger pipe).

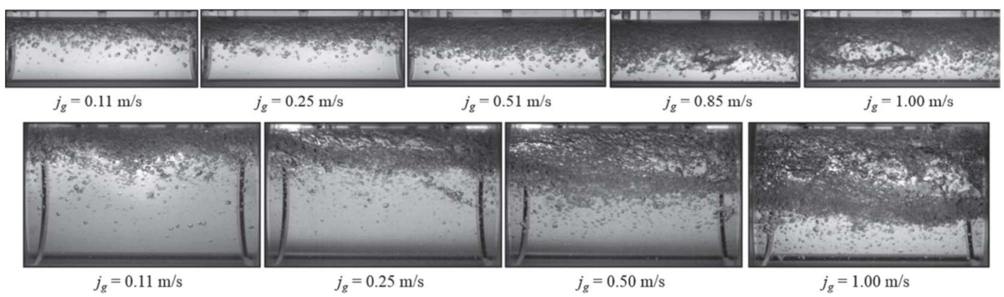

FIGURE 2.6: Snapshot images to highlight the effects of channel's diameter increase from 38.1 mm (upper row) to 101.6 mm (lower row) on bubbly to plug / slug transition regimes for different superficial velocities, Kong et al. (2018)

A critical Reynolds number of ~300 was found by Butler et al. (2018), where the time-averaged gas phase volume fraction showed a significant difference by means of the PIV measurements in capillaries with a T-junction. As shown in Figure 2.7, a large mirrored recirculation region was observed between two consecutive O_2 bubbles with a relative velocity of $2V_{tp} - V_g$ resulting in the most efficient convective transport (regimes 1, 2, 11, and 13 in Figure 2.7). They also revealed the key role of the recirculating motion in the liquid plug on the dynamics of mass transfer and its dependency on the bubble velocity.

Two different structures named high-concentrated and low-concentrated were observed by Yao et al. (2020) to characterize the mass transfer and flow patterns of liquid-liquid slug flow at the bend region of a rectangular meandering microchannel. As is shown in Figure 2.8a, lower flow rates created a non-crossing evolution pattern where the red filaments occupied the outer and inner layers when moving through the

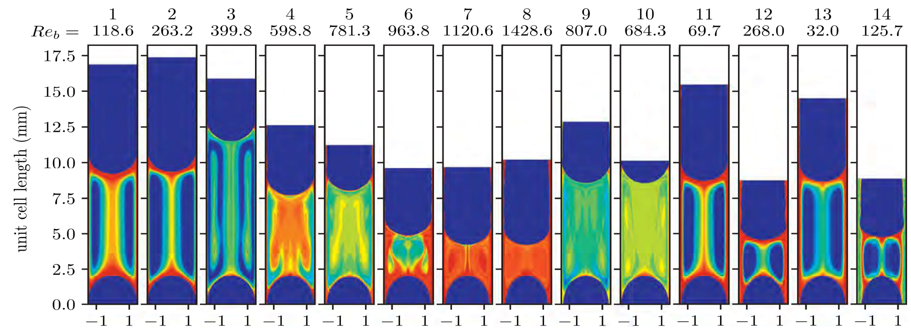

FIGURE 2.7: Time-averaged O_2 volume fraction plots for 14 different flow regimes in terms of Re_b in the liquid plug regions between two consecutive gas bubbles, Butler et al. (2018)

bend. Conversely, when the flow rates were increased, Figure 2.8b, the outer red filament was shifted to the central region of the bend. Asano et al. (2020) verified the possibility of contactless mass transfer between subsequent aqueous slugs / droplets separated by oil experimentally. Bromothymol blue (BTB) was used to show the BTB transportation between slugs. Table 2.6 presents selected experimental studies on the flow patterns of two-phase flows in tubular and non-tubular microchannels and gas bubble or droplet formation. Etminan et al. (2022c) have recently studied state-of-the-art development of μPIV for visualization of microfluidics and nanofluidics.

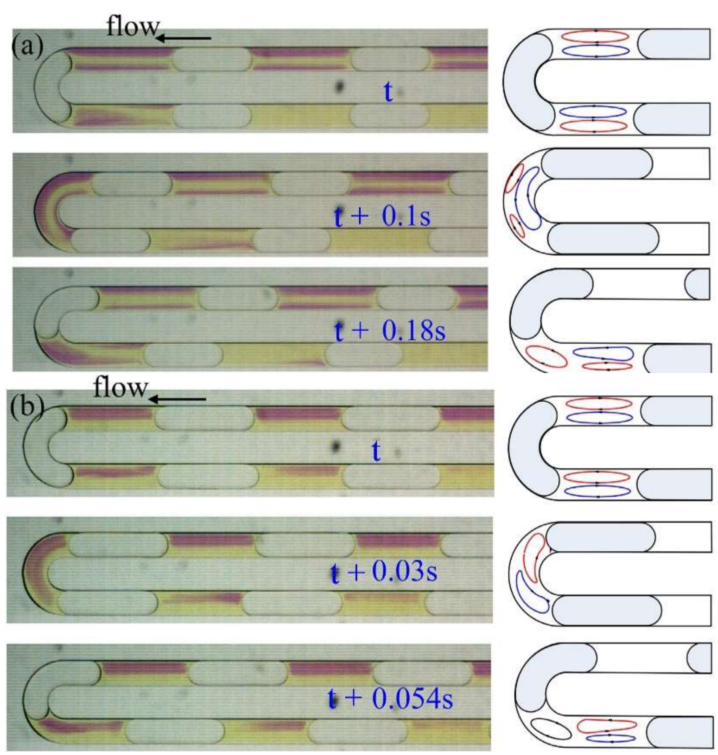

FIGURE 2.8: The evolution patterns of a typical water / toluene two-phase flow at the bend of microchannel for (a) non-crossing pattern and (b) crossing pattern, Yao et al. (2020)

TABLE 2.6: Selected experimental studies on the flow pattern maps and bubble or droplet formation

Comment(s)	Cross-Section	Phases	Ref.
Several correlations as the function of velocity and pressure drop in each phase were suggested for different flow regimes	Circular	GL	Baker (1953)
Combination of X-ray and high speed flash photography technique High liquid flow rates	Circular	GL	Hewitt and Roberts (1969)
The influence of velocity on the mass transport phenomenon The effects of liquid slug lengths on flow parameters	Circular	GL	Berčič and Pintar (1997)
Recognizing a novel flow map using Su number for microgravity two-phase flow	Circular	GL	Jayawardena et al. (1997)
Boiling heat transfer of R141b Heat transfer coefficient correlations Different flow regime in small- and large-diameter tubes Observation of local dry-out on the channel wall	Circular	GL (single phase)	Kew and Cornwell (1997)
Using particle image velocimetry Recirculation flow pattern with a high degree of mixing Counter-rotating vortices were observed inside the liquid slugs Velocity profile inside the slugs	Circular Square	GL	Thulasidas et al. (1997)
Increasing gas superficial velocity led to the development of the slug flow Low liquid superficial velocity made longer bubbles, shorter liquid slugs profile Slug and annular patterns At high liquid superficial velocity, churn flow was established	Circular Semi-Triangular	GL	Triplett et al. (1999)
Five flow regimes were observed including bubbly, wedging, slug, bubbly, and dry flow for moderate void fraction The classification of patterns regarding liquid fraction The effect of a sharp return of the channel Void fraction measurement The gravitational effects were taken into account for a bubbly pattern with a spherical gas bubble Liquid droplets may be observable on the walls in wedging pattern	Square	GL	Cubaud and Ho (2004)
Using µ-PIV and fluorescent microscopy imaging The liquid phase segments were attached at the corners of the cross-section Gas phase flow improved the mixing and the residence time features	Rectangular	GL	Günther et al. (2004)

The hemispherical ends of gas bubbles were not maintained as the Ca increases The nose and the tail of the bubble elongated and flattened as the Re increased The Marangoni effect was observed in experiment efforts and was not taken into account in the numerical simulations	Circular	GL	Kreutzer et al. (2005a)
Surface modifications Contact angle measurements Meandering microchannel When the length of the bubble was equal to the channel diameter, the flow map was annular At low void fraction when the surface energy was low, the isolated symmetric bubble patterns were observed At moderate void fractions, the flow pattern was asymmetric	Square	GL	Cubaud et al. (2006)
Discussed in the text	Rectangular	LL	Zhao et al. (2006)
An increase in Ca changes the droplet profile Development of droplet formation with the increase in Ca The significant deviation between the measured film thickness and the Bretherton and Taylor predictions	Circular	LL	Grimes et al. (2006)
At relatively low flow rates, the slug pattern was established with the length equal to the inner diameter of the tube At high volumetric flow rate, the deformed interface regime was made with long water slugs and small cyclohexane droplets	Circular	LL	Kashid and Agar (2007) Kashid et al. (2007)
Using a μ-PIV technique to capture bubble formation in a T-junction About 25% of the liquid phase passed the gas bubble The gas bubble formation process was included in three steps: Gas bubble growing until occupied the junction Gas bubble developing was decreased as the liquid phase passes the bubbles and the bubble neck was tightened Gas bubble neck was rapidly decreased until approached one-quarter of the diameter before breaking up	Square	GL	Steijn et al. (2007)
An empirical correlation for a transition from Taylor to unstable slug flow regimes At lower superficial velocities, the Taylor regime was established At higher superficial velocities, the Taylor flow was transited into the dripping flow pattern	Circular	GL	Yue et al. (2007 and 2008)
Boiling heat transfer of Fluorinert FC-77 As the heat flux enhanced, the bubble generation rate increased along with an increase of bubble length At moderate heat flux, flow pattern went back and forth between churn and wispy-annular flow regimes	Rectangular	GL (single phase)	Harirchian and Garimella (2009)

Bubbly flow regime was found at a low gas superficial velocity and a high liquid superficial velocity An increase in gas superficial velocity generated slug regime, where the gas-bubble length was longer than the diameter High liquid velocity and moderated gas superficial velocity produced churn flow map Low liquid superficial velocity and high gas superficial velocity transited the churn to the slug-annular	Circular	GL	Niu et al. (2009)
PIV measurements were taken into account Backflow around the liquid slugs were observed The liquid slugs moved faster than that of average flow due to the lubricating effects	Circular	LL	Kashid et al. (2008)
Using a μ-PIV technique to capture flow structure Slug or Taylor pattern was observed for low superficial velocities As the superficial velocities increased, the lengths of bubbles, and slugs became more variable At high enough gas velocity, the gas phase penetrates the liquid and the length of slugs became shorter	Circular	GL	Fouilland et al. (2010)
Using a laser signal system to provide flow pattern images The channel diameter affects the flow pattern and transition conditions In the bubbly flow regime, the size of the bubbles was approximately was the same as channel diameter	Circular	GL	Ong and Thome (2011)
A model of mass and momentum balance Stratified flow regime was observed for low oil to gas superficial velocity ratios An increase in the velocity of the gas phase makes the interface to be wavy	Circular	GL	Khaledi et al. (2014)
The number of small bubbles in liquid plug / slug was significantly increased with increasing V_g The size of small bubbles was decreased with increasing V_g or increasing V_l Increasing V_g or decreasing V_l slightly increased the depth of the plug / slug bubble Increasing pipe size enhanced the contribution from large bubbles to a total void fraction Large bubble was accelerated due to small bubble coalescence as flow developed, leading to α decreases	Circular	GL	Kong et al. (2018)
Indicating of wave growth and coalescence during slug flow formation For low superficial velocities, the flow pattern remained stratified smooth By an increase of superficial gas velocity, the flow pattern was changed to wavy	Circular	GL	Deendarlianto et al. (2019)
The transition from slug to continuous flow regimes was conducted using non-Newtonian dispersed phase The effects of shear-thinning dispersed phase flow on the slug length and formation process were revealed	Rectangular	LL	Yagodnitsyna et al. (2021)

2.5.2 Numerical Simulations

Numerical modeling methods can be categorized into four main groups; electronic, atomistic, mesoscale, and continuum (Gubbins and Moore, 2010). In the following, we only review some of the widely-used numerical methods in the modeling of Taylor flows, and more in-depth reviews on the rest of numerical studies can be found in literature (e.g., Wörner, 2012).

Two different methods may be considered in numerical analysis when describing the motions of fluids in two-phase flows: continuous fluid (Eulerian) and discrete particle (Lagrangian). The first method solves the governing partial differential equations to predict the motion of the continuum-based fluid flow, while the second method follows the movement of fluid particles or molecules to predict fluid flow and heat transfer. The interaction between different phases is calculated by both methods to determine the coalescence and interference of interfacial forces (Keyes et al., 2013). Hashim et al. (2012) simulated transport phenomena and biological components, such as proteins, DNA, and cells using the Eulerian method. The innovative aspect of their simulation was to describe the mixing concentration distribution at the interaction of biological components. Apte et al. (2003) numerically investigated the liquid fuel spray from a nozzle using the Eulerian-Lagrangian approach with a point-particle approximation for the liquid droplets. Their results revealed that the droplets cannot be considered point-particles due to the high-density spray in the region close to the injector. Ni et al. (2017) investigated numerical study of the GL and LL Taylor flows on an arbitrary Lagrangian-Eulerian (ALE) formulation to track interfacial and curvatures of slugs. They showed the predominant roles of the viscosity ratio and density ratio of continuous phase to the disperse phase for quite large Ca causing a non-stagnant liquid film region. The Lagrangian approach was also used by Trapp and Mortensen (1993), Delnoij et al. (1997), Ye et al. (2005), Pepiot and Desjardins (2012) and Barbosa et al. (2019), but not limited to. Therefore, these methods can be widely employed in applications concerning fluid motion.

The lattice Boltzmann method (LBM) is a computational fluid dynamics (CFD) method that simulates a fluid density on a lattice framework with streaming and collision (relaxation) processes instead of solving the Navier-Stokes equation directly

(Chen and Doolen, 1998). This method is an efficient tool for modeling complex fluid systems that include complex boundaries, microscopic interactions, propagations, and the collusions of particles (Frisch et al., 1986; McNamara and Zanetti, 1988; Chen et al., 1991; Gunstensen and Rothman, 1991; Grunau et al., 1993; Shan and Chen, 1993; Takada et al., 2000; Inamuro et al., 2001). The LBM in a GL two-phase flow modeling was proposed by Seta and Kono (2004), based on a particle velocity-dependent forcing scheme. Their results revealed that the effects of high potential caused instability in a three-dimensional model. A diffuse interface free energy LBM was utilized by Komrakova et al. (2014) to study the behaviour of a single liquid-droplet suspended in another liquid. They found that for droplets with a radius of less than 30 lattice units, a smaller interface thickness is required. Li et al. (2016) comprehensively reviewed different uses of LBM proposed by others for simulating thermal boundary treatments, interaction forces between two different phases, mechanical stability conditions, liquid vapour phase changes, fuel cells, droplet collisions, and energy storage systems. Recently, Fei et al. (2019) developed a three-dimensional, multiple-relaxation-time LBM based on a set of non-orthogonal vectors for modeling realistic multiphase flows. Some other uses of the LBM have also been developed by many investigators (e.g., Qin et al., 2018; Shi et al., 2019; Cui et al., 2019).

Another widely used method for modeling two-phase flows is the volume of fluid (VoF), which is a numerical technique that determines the location of a free surface, GL, and LL interface by following the Eulerian approach. This numerical method is a powerful tool for modeling the interfaces of incompressible and immiscible two-phase flows because it is able to predict the interface between two phases even though the interface is becoming too weak to capture the curvature of the interfacial line (Katopodes, 2018). Ketabdari (2016) discussed VoF regarding the governing equations, as well as its advantages and capabilities predicting the interface line between two phases with large deformation. Osher and Sethian (1988) devised a new numerical algorithm to realize and determine the propagation of curvature dependent speed, which can be combined with VoF. This algorithm approximates the equations of motion by using hyperbolic conversation laws. Many investigators employed this method when simulating a two-phase flow's interface, e.g., Fukagata et al. (2007), Adalsteinsson and Sethian (1995 and 1999), Mahady et al. (2015). The general applications of this method and a comprehensive review were conducted by Osher and Fedkiw (2001), which discusses the variants and extension methods, such as fast methods for steady-state problems, diffusion generated motion and the variation level set approach. The growth of liquid film thickness was governed by one equation (Thomas et al., 2010). They assumed a constant pressure gradient in the channel direction and a linear velocity distribution over the liquid film thickness, emphasizing that the model was valid only for a film thickness less than near-wall grid size.

An effort to predict the bubble profile was analytically conducted by Bretherton (1961), where he found that considering gravitation as a buoyancy force produced nonsensical results in the vertical configuration of a capillary tube. A critical value ($\rho g R^2/\sigma$) of 0.842 was introduced to show no upward movement of the bubble for the amount less than the critical value. Kolb and Cerro (1993) found an axisymmetric bubble profile for the Ca greater than 0.1, where the lubrication's law predicts the interface profiles and the flow patterns adequately. The flow field predictions were numerically obtained by Giavedoni and Saita (1997), who illustrate the streamlines for showing the bubble profiles and the slug region. They found that with an increase in the Ca, the recirculation flow disconnected the GL interface and moved downstream. Brauner et al. (1998) followed an exact analytical solution to model the interface curvature of two-dimensional stratified flow.

Heil (2001) numerically simulated the influence of fluid inertia, Re, on the flow patterns and the propagation of an air bubble on two flexible and rigid walls of a GL flow in a two dimensional channel. Fujioka and Grotberg (2005) numerically analyzed the propagation of liquid plugs inside a two-dimensional channel using a finite volume method. They showed that as the liquid plug grew, the frontal part swept the interfacial surfactant from the precursor liquid film. A pair of recirculation regions was found inside the liquid plug shortening as the magnitude of the velocity decreased. They also noted that micelle production and its transport process must be added to the numerical model when plug propagation occurs with a much higher concentration. Their results revealed that as the Re increases, a recirculation flow appears inside the plug core and is then skewed toward the rear part of the bubble. Kreutzer et al. (2005a) denoted that the inertia effects due to an increase in the Reynolds number elongated the nose and flattened the rear menisci of the gas bubble profile.

The influence of pressure gradient on the flow patterns and bubble profile were illustrated in Figure 2.9. According to this figure, as the pressure gradient increases, the elongated gas bubble is stretched along the tube axis and the impact of the no-slip conditions at the walls becomes weaker on the bubble shape. Strong, and clockwise circulation is predicted next to the head cap of the bubble resulted in bubble elongation when the pressure is intermediate.

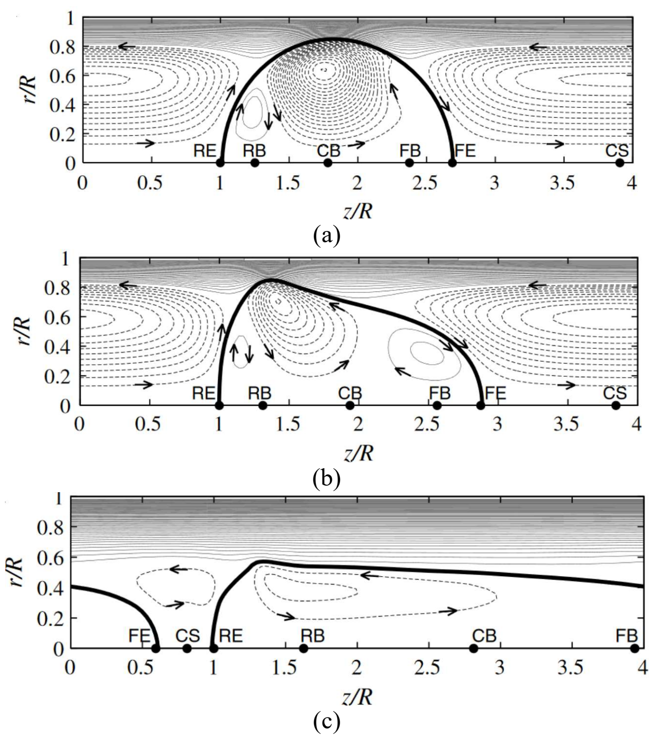

FIGURE 2.9: The streamlines inside and outside the bubbles for different pressure gradients (a) 85 MPa.m^{-1}, (b) 850 MPa.m^{-1}, and (c) 3000 MPa.m^{-1}, Fukagata et al. (2007)

Falconi et al. (2016) numerically and experimentally studied a vertical-upward three-dimensional Taylor flow in a square milli-channel using the VoF in-house finite volume code and μ-PIV measurements, respectively, Figure 2.10a. Instantaneous streamlines in Figure 2.10b show three vortices within the bubble; a large central vortex, two small toroidal vortices at the caps of the bubble. The main central vortex represents the highest z-component velocity next to the channel axis with the direction of rotation opposite to the smaller vortices. Valizadeh et al. (2020) conducted a

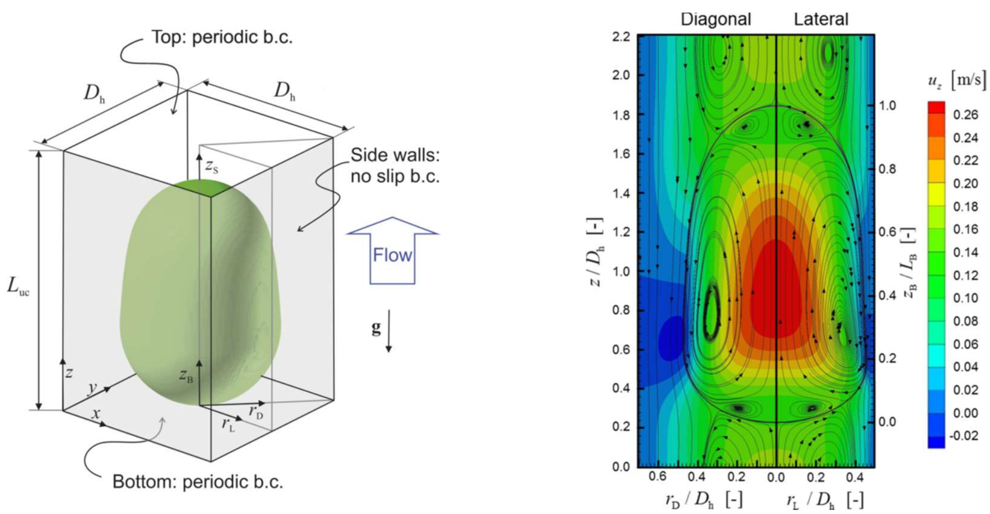

(a) (b)

FIGURE 2.10: (a) The schematic of computational setup and coordinate system, and (b) instantaneous streamlines in the moving frame with the bubble and z-component velocity contour-plot in a fixed frame of reference, Falconi et al. (2016)

numerical parametric study of non-Newtonian turbulent flow in a spiral duct by investigating the effects of geometry, consistency index, and power-law index values of viscosity. Their study dealt with a wide range of large Reynolds numbers in spiral milli-channel, indicating much higher friction coefficient due to the secondary flow effects compared to straight tube.

Both experimental and 3D numerical simulations were carried out by Abdollahi et al. (2020) for liquid-liquid Taylor flow in a square channel with hydraulic diameters of 1 and 2 mm. Figure 2.11 displays the non-dimensional contour of the radial velocity component highlighting its key effects on heat transfer enhancement and recirculating flow within the slugs and the carrying phase. The highest radial velocity occurred at the nose and rear of the slug to make two vortices rotating in the opposite direction of the main recirculation zone in the middle of the slugs as observed by Fukagata et al. (2007) and Falconi et al. (2016). In a constant length unit cell, as the dispersed phase volume fraction increased, the liquid film thickness remained constant. The large recirculating zone in the middle of the slug show less axial flow and more radial flow as the droplet length was decreased. Their results also showed a huge increase of heat transfer rate up to 700% compared to single-phase flow indicating more effectiveness of short slugs on the heat transfer rate.

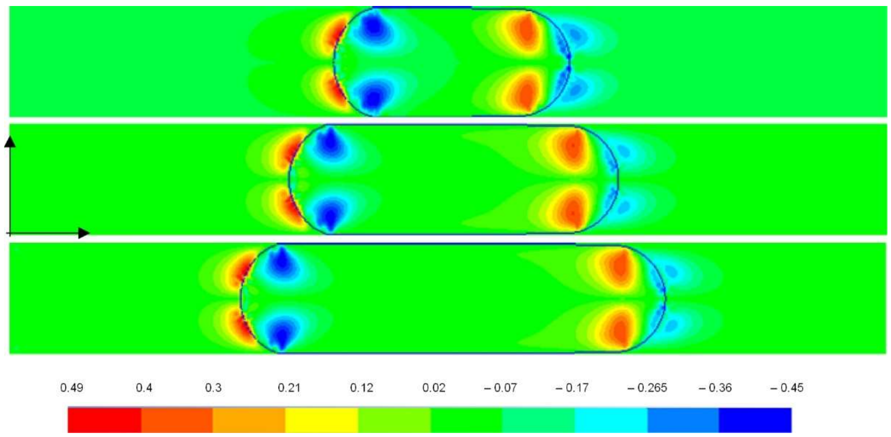

FIGURE 2.11: Radial velocity component contours with different dispersed phase volume fraction in a fixed unit cell length, Abdollahi et al. (2020)

Xu et al. (2021) numerically simulated 3D Taylor flow in a microchannel with a square cross-section under ultrasonic oscillation. A harmonic, vertical, and ultrasonic oscillating applied to microreactor as,

$$d_y = A\cos(\omega_0 t) \tag{2.9}$$

where the amplitude of the microreactor oscillation (A) is in the order of 2–8 microns and the angular frequency as a function of a constant vibrating frequency of $f_0 = 20$ kHz is

$$\omega_0 = 2\pi f_0 \tag{2.10}$$

They found the channel oscillation affected the flow pattern and hydrodynamic characteristics in both liquid slugs and bubbles as shown in Figure 2.12 for Taylor flow in bends and oscillating bubbly flows, for example. Twisted flow structure in the liquid slugs improved mixing rate and transport phenomena. Wavy interface of bubble enhanced the interfacial area accelerating the mass transfer rate across the channel and improved the performance of microreactor. The sub-harmonic bubble surface wave was also created by the pressure pulsation in the parallel direction of the oscillation.

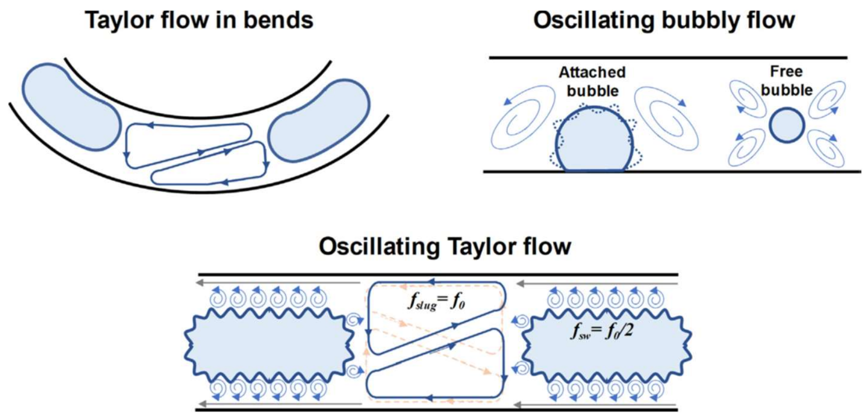

FIGURE 2.12: Schematic of different gas-liquid Taylor flow in microchannel; Taylor flow in bends, oscillating bubbly flow, and oscillating Taylor flow, Xu et al. (2021)

A summary of analytical and numerical investigations on the flow patterns and the formations of the gas / liquid slugs is presented in Table 2.7.

TABLE 2.7: Selected numerical and analytical studies on the flow patterns and the bubble or the droplet formation

Comment(s)	Cross-Section	Phases	Ref.
The film thickness at the advance of the rear meniscus oscillated The front and rear menisci were slightly different in curvatures Equilibrium bubble profile under surface tension and gravitational effects in a vertical tube	Circular	GL	Bretherton (1961)
The film thickness The profiles of front and rear film thickness The film thickness for very elongated gas bubbles	Circular and Square	GL	Ratulowski and Chang (1989)
Bubble profile Flow fields around and between bubbles The motion of a bubble	Square	GL	Kolb and Cerro (1993)
The influence of velocity on the mass transport phenomenon The effects of liquid slug lengths on flow parameters	Circular	GL	Berčič and Pintar (1997)
Stronger recirculating flow region as the Ca decreased A liquid backflow was appeared at non-dimensional liquid thickness less than 1/3 Single stagnation point at the vertex of bubble curvature for no-recirculating flow conditions A decrease in the Ca made recirculating flow and moved the stagnation point further the vertex	Parallel plates and Circular	GL	Giavedoni and Saita (1997)
The effects of flow rates on the interface curvature The influence of Eo and wall adhesion on the interface curvature	Circular	Two-phase (parametric)	Brauner et al. (1998)
The rear profile of bubble meniscus versus Ca and Re The effect of Re on the free surface undulations Gas bubble profile The curvature of the gas bubble	Circular	GL	Giavedoni and Saita (1999)

The flow inertia effect was more significant even for deformable wall channels Flexible wall channels were more sensitive than rigid wall channels to the propagation of air bubbles into the walls at low Re and Re/Ca situations The pressure gradient in faraway positions of the tip of the air bubble was generated by Poiseuille flow	2D	GL	Heil (2001)
The propagation of liquid plug The adsorption/desorption process of the surfactant was modeled The Marangoni stress results in nearly zero surface velocity at the front meniscus	2D	GL	Fujioka and Grotberg (2005)
Refer to Table 2.6	Circular	GL	Kreutzer et al. (2005a)
Slug flow development with time Either uniform or parabolic inlet velocity profile made the same-sized slugs The inlet mixing level influence on the slug lengths	2D	GL	Qian and Lawal (2006)
Bubble shape in slug flow regime The effects of pressure gradient on the bubble profile The presence of gas bubbles made the circulating regions stronger causing a higher momentum transport	2D	GL	Fukagata et al. (2007)
Curved vertical microchannel Slug flow development with time The gas bubbles moved faster than liquid slugs The impact of inlet geometry on the slug development	Circular	GL	Kumar et al. (2007)
The VoF and level-set methods The lack of enough adhesion on wall deformed the rear interface of the slugs	2D	LL	Kashid et al. (2008)
The VoF method Bubble shapes and formation The effects of superficial velocities on the bubble profiles The influence of nozzle diameter on the bubble formation and shapes	2D and 3D	GL	Goel and Buwa (2009)
Structured-square grid minimizes inaccuracies in the surface tension calculation The process of bubble formation was happened periodically	2D	GL	Gupta et al. (2009)
The VoF and level set techniques Two commercial simulating software; Ansys and TransAT Bubble formation and development The effect of mixture velocity on the flow pattern and the bubble shapes	2D	GL	Gupta et al. (2010)
Bubble curvature in slug flow The characteristics of flow were dominantly determined by adherent liquid film thickness An optimized model to minimize the pressure drop and maximize the heat transfer rate	2D	GL	He et al. (2010)

2.6 Flow Regime Transitions

A transition from one flow regime to another often occurs when the flow or boundary conditions are changed. The actual flow maps and the transition conditions specifically depend on a group of effective features during an experiment or the assumptions in numerical simulations (Satterfield and Ózel, 1977; Lowe and Rezkallah, 1999; Kreutzer, 2003; Zhang et al., 2017). For example, Bottin et al. (2014) experimentally obtained various flow regimes for a horizontal two-phase flow in a pipe with an inner diameter of 0.1 m. They attempted to describe different flow regimes regarding the values of superficial velocities of the gas and liquid phases in the earlier experiments (Taitel et al., 1980; Barnea et al., 1982a and 1982b; Dukler and Taitel, 1986; Andreussi et al., 1999; Govier and Aziz, 1972). Some of the transition criteria from a flow regime to another in microchannels are presented in Table 2.8.

Jayawardena et al. (1997) showed the ratio of gas to liquid Reynolds numbers as a function of the Suratman number for recognizing the flow maps. An accurate transitional value of the Su occurs between 10^4 and 10^7 from a bubble to a slug transition. However, the transition from a slug regime to an annular regime has two different criteria regarding the value of Su, greater and less than 10^6. The motion of the gas bubble through a microchannel with a square cross-sectional area was experimentally studied by Cubaud and Ho (2004) and Cubaud et al. (2006). Regarding the liquid fraction, $Q_l/(Q_l + Q_g)$, they classified the flow patterns into several categories: bubbly, wedging, slug, annular, and dry, which are illustrated in Figure 2.13. Their experiments specified some critical liquid fractions for a transition from one flow regime to another, which are ~0.75 from bubbly to wedging, ~0.20 from wedging to slug, ~0.04 from slug to annular, and ~0.005 from annular to dry transitions. They also found that at low liquid velocity, the gas bubbles clogged at the sharp corner of the channel bend before merging and eventually passing the bend. The corner of the channel bend trapped a gas bubble to merge into another upcoming bubble, producing a single larger bubble.

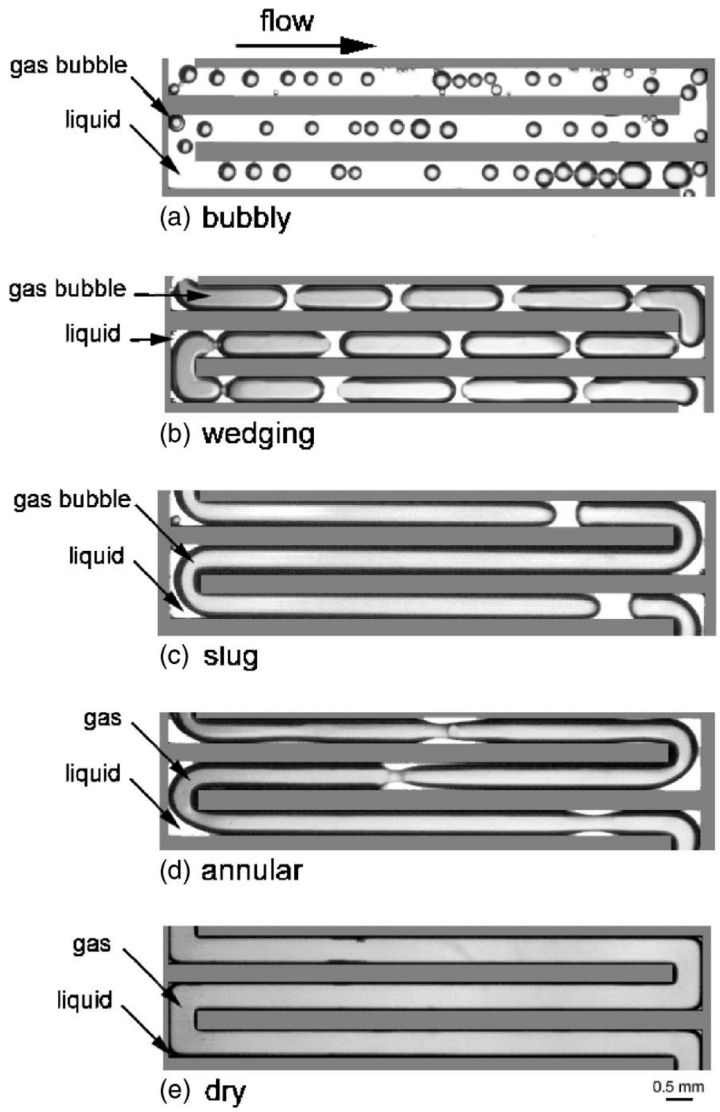

FIGURE 2.13: The different flow patterns from high to low liquid fraction, Cubaud et al. (2006)

Table 2.8: Summary of proposed criteria for the transition of flow pattern

Comment(s)	Criterion	Mechanism	Cross-Section	Phases	Ref.
Bubbly to slug transition The collision frequency was so low when the void fraction was smaller than 10% The collision frequency was rapidly increased at a void fraction above 25% so that transition to slug flow was rapid even in a strongly liquid	When the rate of coalescence was much more than that of break-up and at a void fraction of 0.25 − 0.3	Bubble coalescence and void fraction	Circular	GL	Radovcich and Moissis (1962)
Churn to annular happens at a value of	$\frac{V_g \rho_g^{0.5}}{\left[gd\left(\rho_l - \rho_g\right)\right]^{0.5}}$	Minimum gas and liquid superficial velocities	Circular	GL	Wallis (1962)
Slug to slug-bubbly transition No stratified flow pattern was observed in channels with diameter less than 1 mm it was also verified by Fukano and Kariyasaki (1993)	$ReWe = 2.8 \times 10^5$ where, $Re = \rho_l d V_g / 2\mu_l$ $We = \rho_l d V_g^2 / 2$	The production of Re and the We numbers	Rectangular	GL	Suo and Griffith (1964)
The churn to annular transition occurred at lower in comparison to the flow reversal transition	the same as Wallis (1962)		Circular	GL	Hewitt and Roberts (1969)
Bubbly to slug transition	0.25	Void fraction	Circular	GL	Taitel et al. (1980)
The transition from stratified to slug regimes	$H \geq \left(1 - \frac{\pi}{4}\right) d$ $Bo_{cr} = 4.7$	Kelvin-Helmholtz instability and critical Bond number	Circular	GL	Barnea et al. (1982a)
Upward and vertical flow For several transitions The flowing quality was more suitable than the thermal equilibrium quality to correlate the flow-regime transitions	For bubbly to slug: ~0.3	Void fraction	Circular	GL	Mishima and Ishii (1984)
Concentric and eccentric annuli (eccentricity 50%) Upward and vertical flow Mathematical modeling Insignificant effect of eccentricity on transitions for many transitions	$\frac{V}{V_{max}}$ and $\int PDF\, dv$	Probability Density Function (PDF)	Circular	GL	Kelessidis and Dukler (1989)

The dominant surface tension in stratified flow regime	$\mathrm{Eo} = \frac{(2\pi)^2\sigma}{(\rho_l - \rho_g)d^2 g}$	Linear stability analysis	Circular	GL	Brauner and Maron (1992)
Bubble to slug transition Upward and vertical flow Turbulence-dependent rate processes controlled the transition at a high flow rate	~34%	Average void fraction	Circular	GL	Das and Pattanayak (1994)
Discussed in the text	$\frac{Re_g}{Re_l} = 464.16\ Su^{-\frac{2}{3}}$ $\begin{cases} \frac{Re_g}{Re_l} = 4641.6\ Su^{-\frac{2}{3}} \\ Re_g = 2 \times 10^{-9}\ Su^2 \end{cases}$	Suratman number	Circular	GL	Jayawardena et al. (1997)
Bubble to slug transition Upward and vertical flow	(N/A)	Void fraction	Circular	GL	Cheng et al. (1998)
Bubbly to slug transition The formulation of interfacial transport equations The classification of bubble interactions The categorization of basic mechanisms of bubble coalescence and breakup	(N/A)	Interfacial area concentrations	Circular	GL	Hibiki and Ishii (2000)
Upward and vertical flow for a bubble to slug transition	for $s < d_b$ $\alpha=0.2$ for $d_b \leq s \leq 3d_b$ $\alpha=\frac{s}{20\ d_b} + 0.15$ for $s > 3d_b$ $\alpha = 0.3$	Void fraction	Rectangular	GL	Hibiki and Mishima (2001)
Discussed in the text	Discussed in the text	Liquid fraction	Square	GL	Cubaud and Ho (2004) Cubaud et al. (2006)
The bubble size distribution played a crucial role in the flow regime transition and flow patterns	(N/A)	Population balance model (PBM)	Circular	GL	Wang et al. (2005)

Slug into parallel transition happened at small flow rates and large superficial flow ratio By increasing the flow rate, the chaotic flow was changed into annular Equivalent radius was correlated to the We numbers and holdup fraction	Specific range of We for each flow pattern	Weber number	Rectangular	LL	Zhao et al. (2006)
Slug to deformed interface occurred for $2.5 < Q_c / Q_d < 5$ Slug to drop transition happened in the $3 < Q_d / Q_c < 6$	$\frac{Q_c}{Q_d}$	Volumetric flow rate ratio	Circular	LL	Grimes et al. (2006)
Bubbly to slug transition Vertical and upward configuration Effect of bubble size and diameter on the transition	Maximum bubble size	PBM	Circular	LL	Kashid and Agar (2007)
Bubbly to slug transition The influence of the bubble population at the inlet region on the regime transition An increase in bubble diameter transits the flow map from bubbly to slug A decrease in tube diameter changed the flow patterns from slug to bubbly regimes	Bubble diameter	PBM	Circular	GL	Das et al. (2009a and 2009b)
Stable slug regime in the square duct at $Re_g < 24$ Stable slug regime in the circular duct at $Re_g < 36$ Stable slug regime in the rectangular duct at $Re_g < 40$ Stable slug regime in the trapezoidal duct at $Re_g < 72$ Annular flow regime at $\frac{Re_l}{Ca_l} \leq 24Re_g - 7638$	$\frac{\rho_g V_g d_H}{\mu_g}$	Reynolds number of gas phase	Square and Trapezoidal	GL	Dessimoz et al. (2010)
Slug to churn transition and flow map identification	$\alpha \geq f_\alpha$	Void fraction	Circular	GL	Wang et al. (2012)
A transition on the slug producing from squeezing to dripping occurred at the junction	$Q_g > 20$	Gas volumetric flow rate	Rectangular	GL	Song et al. (2019)
Above the transition value of Ca, an elliptic or oval cross-section area of the gas bubble was observed, and viscous shear overcame the interfacial tension	0.01	Capillary number	Quasi-trapezoidal	GL	Wu and Sundén (2019)

2.7 Slug or Bubble Length

The hydrodynamic characteristics of slug flows are highly dependent on the profile and length of the liquid slug. Bubble length measuring was experimentally conducted by Marchessault and Mason (1960), where the change in the shape of the liquid film thickness around short bubbles was likely caused by end effects, buoyancy, and cylindrical model assumption. According to Schwartz et al. (1986), the liquid film thickness left behind a gas bubble in a capillary was adequately close to the predictions of lubrication theory when the length of bubbles was short. They also found that for the length of bubbles shorter than the tube diameter, the thin film layer region was no longer observed. According to Kashid and Agar (2007) and Kashid et al. (2007), the capillary number and the junction dimensions significantly affect slug length. In a slug flow regime, the lengths of slugs of both phases are greater than their diameters, but at relatively low volumetric flow rates, the slug pattern is established with the length equal to the inner diameter of the tube. In the case of a high volumetric flow rate and surrounded water slugs by cyclohexane, the deformed interface regime is made with long water slugs and small cyclohexane droplets. A few simple linear equations to compute the stable slug lengths were reported by Taitel et al. (1980), Kelessidis and Dukler (1989), Akagawa and Sakaguchi (1966), and Fernandes (1981), which indicated that the ratio of the liquid slug length to the tube diameter remained at a constant value of 16, 20.7, 7.5, and 21.5, respectively.

Table 2.9 presents the correlations for measuring the length of liquid slugs of two-phase flow in a microchannel including the void fractions. Beyond the data provided in Table 2.9, two other recent studies, Han and Chen (2018) and Qian et al. (2019), are concerned with the slug length and its formation, but the correlations of slug length were not proposed by the authors. The first study numerically simulated the droplet formation at a T-junction in a microchannel. The effective diameter of droplets was studied in terms of contact angle, continuous phase viscosity, flow rate ratio, and interfacial tension. The latter experimental investigation considered the influence of flow rate on the liquid slug generation in a microchannel with a square cross-sectional area. They found the slug lengths vary from 0.923 to 1.186 mm based on different flow rates of the continuous and dispersed phases. The distance between subsequent water slugs was also measured.

2.8 Pressure Drop

The interactive structure of different phases and between phases and solid walls represent the predominant parameters to describe the flow pattern of multiphase flow and pressure loss through the channel. Two homogenous and separated flow models have been employed by researchers to predict the frictional pressure drop (White, 2006). The first model postulates the same velocity for both gas and liquid phases, which implies that the slip ratio at the interactive boundaries is equal to one. This model considers two or more different phases as a single phase. The values of the flow properties are dependent on the quality, while the frictional pressure drop can be obtained by single-phase theory (White, 2016):

$$f = \left(\frac{1}{2}\frac{d}{\rho V^2}\right)\left(\frac{dp}{dz}\right)_l \tag{2.11}$$

where z indicates the axial direction of the channel.

The Hagen-Poiseuille equation is a physical law to compute the pressure drop of a Newtonian and incompressible flow through a long and circular tube with a constant cross-section area (White, 2016). The flow regime remained laminar due to the Reynolds number of the microflows, where the friction factor becomes $f = 16/\mathrm{Re}$ for round tubes and the equation above can be rearranged as:

$$\Delta p = \frac{16}{\mathrm{Re}}\left(\frac{1}{2}\rho V^2\right)\frac{4L}{d} \tag{2.12}$$

where L and d are the length and the diameter of the tube, respectively. The presence of the second phase in two-phase flow causes an additional term to the pressure loss of a single-phase flow and does not satisfy Poiseuille's law anymore. Therefore, the total pressure drop (Δp_t) is the sum of the single-phase pressure drop (Δp_s) and the

TABLE 2.9: Previous research on the correlation of the slug length in two-phase flows in circular and noncircular cross-section area microchannels

Correlation	Comment(s)	Flow Parameter	Cross-Section	Phases	Method	Ref.
$\frac{L_g}{d}=\left(\frac{Re}{Eo^2}\right)^{0.63}=0.0878\left(\frac{V_s\rho_l\sigma^2}{\mu_l(\rho_l\text{-}\rho_g)^2 d^3 g^2}\right)^{0.63}$ $\frac{L_l}{d}=\left(\frac{1}{Re\ Eo}\right)^{1.2688}=3451\left(\frac{\mu_l\sigma}{(\rho_l\text{-}\rho_g)\rho_l V_g d^3 g}\right)^{1.2688}$	The gas and liquid slug lengths versus dimensionless numbers The effect of gas superficial velocity on slug lengths	$d \leq 4$ mm $55 \leq Re \leq 2000$ $0.0015 \leq Ca \leq 0.1$	Circular	GL	Experimental	Laborie et al. (1999)
$L_l=\frac{1\text{-}\varepsilon_g}{\varepsilon_g}\frac{\pi}{6}\frac{d_g^3}{d^2}$	The slug length was extensively depended on physical means of the experiment, operational conditions, and delivering system	$d = 50$ mm $0.07 ms^{-1} \leq V_g \leq 0.27\ ms^{-1}$ $0.07\ ms^{-1} \leq V_l \leq 0.27\ ms^{-1}$	Circular	GL	Experimental	Broekhuis et al. (2001)
$\frac{L}{w}=1+\alpha\frac{Q_d}{Q_c}$	The squeezing mechanism affected the size of droplets or bubbles	$w = 0.1$ mm $h = 0.033$ mm $10\ mPas \leq \mu_c \leq 100\ mPas$ $10\ mPas \leq \mu_d \leq 100\ mPas$ $Q_c = 0.00278, 0.0278, 0.278\ \mu Ls^{-1}$	Rectangular	LL GL	Experimental	Garstecki et al. (2006)
$\frac{L_{uc}}{d}=1.637\varepsilon^{-0.893}(1\text{-}\varepsilon)^{-1.05}Re^{-0.075}Ca^{-0.0687}$ $\frac{L_g}{d}=1.637\varepsilon^{0.107}(1\text{-}\varepsilon)^{-1.05}Re^{-0.075}Ca^{-0.0687}$ $\frac{L_l}{d}=1.637\varepsilon^{-0.893}(1\text{-}\varepsilon)^{-0.05}Re^{-0.075}Ca^{-0.0687}$	A decrease in superficial liquid velocity increased the gas slug length An increase in superficial gas velocity enhanced the gas slug length Both slug lengths were moderately affected by the surface tension and wall surface adhesion	$d = 0.25, 0.5, 0.75, 1, 2, 3$ mm $15 \leq Re \leq 1500$ $2.78 \times 10^{-4} \leq Ca \leq 0.01$ $0.09 \leq \varepsilon \leq 0.91$	2D and Circular	GL	Numerical	Qian and Lawal (2006)

	The gravitational effects on the slug lengths can be ignored					
$\frac{L_d}{w} = 1.59\left(\frac{Q_c}{Q_d}\right)^{-0.2} Ca^{-0.2}$	The effects of wettability and the shape of the interface as the volumetric flow rates ratio on the plug length The equilibrium of the shear force and interfacial tension in the form of Ca on the plug length	$w = 0.4$ mm $Ca < 0.1$ $\frac{Q_c}{Q_d} > 1$	Square	GL	Experimental	Tan et al. (2008)
$\frac{L_l}{w} = 0.369 \ln\left[\left(\frac{Re}{Ca}\right)^{0.33} \frac{\frac{V_l}{V_l+V_g}}{509.12}\right] + 3.15$	An increase in superficial velocities enhanced the slug length Larger bend diameter of the meandering channel made longer slugs	$0.2 \text{ mm} \leq w \leq 0.4$ mm $h = 0.15$ mm $4.7 \times 10^{-3} \leq Ca \leq 7.4 \times 10^{-3}$ $11.6 \leq Re \leq 22.6$ $20.4 \times 10^{3} \leq Pe \leq 39.6 \times 10^{3}$ $0.01 \text{ ms}^{-1} \leq V_l \leq 0.07 \text{ ms}^{-1}$ $V_g = 0.08 \text{ ms}^{-1}$	Rectangular	GL	Experimental and Numerical	Fries and von Rohr (2009)
$\frac{L_g}{d} = 2$ $\frac{L_s}{d} = 1.3$	The inlet conditions affect the bubble length significantly The lengths were computed at the centerline of the channel	$d = 0.5$ mm $V_g = 0.245 \text{ ms}^{-1}$ $V_l = 0.255 \text{ ms}^{-1}$ $Re = 280$ $Ca = 0.006$	2D	GL	Numerical	Gupta et al. (2009)
$\frac{d_{3D}}{h} = 0.334\left(\frac{\frac{w}{h}-0.89}{\frac{w}{h}+0.79}\right)^{0.5} Ca_c^{-0.5}$ and at $\frac{w}{h} > 4.5$: $\frac{d_{3D}}{h} = 0.334\, Ca_c^{-0.5}$	Droplet size at the junction The dependency of droplet diameter on the channel width was insignificant at large width to height ratio	$w = 22.6$ and 23.7 µm $h = 5$ µm $0.008 \leq Ca_c \leq 0.2$	Rectangular	LL	Experimental	Steegmans et al. (2009)

$\frac{L_g}{d_H} = 1.3\varepsilon^{0.07}(1\text{-}\varepsilon)^{-1.01}We^{-0.1}$	Variation of slug length with volumetric gas and liquid flow rates	$d_H = 0.15, 0.29$, and 0.4 mm $0.1 \leq We \leq 26$ $0.02\ ms^{-1} \leq V_g \leq 1.2\ ms^{-1}$ $0.004\ ms^{-1} \leq V_l \leq 0.7\ ms^{-1}$ $0.06 \leq \varepsilon \leq 0.85$	Square	GL	Experimental	Sobieszuk et al. (2010)
$\frac{L_g}{w} = \frac{V_g}{V_l}(1 + 1.37\ We^{-0.349})$ $\frac{L_l}{w} = 1.157\left(\frac{V_g}{V_l + V_g}\right)^{-0.365}\left(\frac{V_l}{V_l+V_g}\right)^{-0.373} We^{-0.208}$	The effects of flow rates on the slug lengths	$w = 0.75$ mm $h = 0.28$ mm $0.08\ ms^{-1} \leq V_l \leq 0.5\ ms^{-1}$ $0.155\ ms^{-1} \leq$ $V_g \leq 0.952\ ms^{-1}$	Rectangular	GL	Experimental	Chaoqun et al. (2013)
$L_d = \frac{1 \pm \sqrt{1\text{-}4w\left(0.96\left(\frac{Q_d}{Q_c}\right)^{-1.5}\right)}}{2\left(0.96\left(\frac{Q_d}{Q_c}\right)^{-1.5}\right)}$ $L_c = \frac{0.73w\left(\frac{Q_d}{Q_c}\right)^{-1.1}}{L_d}$	The slug lengths of dispersed and continuous phases The slug formation process was not affected by pressure fluctuations Varying slug lengths	$w = 0.1$ mm $h = 0.095$ mm $4\ \mu lmin^{-1} \leq V_l \leq 44\ \mu lmin^{-1}$ $0.6 \leq \frac{Q_d}{Q_c} \leq 3$ $\mu_d = 1$ cs	Rectangular	LL	Experimental	Miki et al. (2013)
$L_d = 0.0116V_{uc}^{-0.32}d^{1.25}\left(\frac{Q_a}{Q_o}\right)^{0.89}$	The length of dispersed slugs The effects of operational conditions on the slug lengths The influence of slug velocity and flow rate on the slug length	$d = 0.6, 0.8, 1$ mm $0.5 \leq \frac{Q_a}{Q_o} \leq 3$ $0.01\ ms^{-1} \leq V_l \leq 0.03\ ms^{-1}$	Circular	LL	Experimental	Xu et al. (2013)
$L_l = \frac{1}{2}(t_{CH1} + t_{CH2})V_l$	A slug flow in superhydrophobic microchannel An increase in gas flow rate decreased the slug length	$w = 0.8$ mm $h = 0.9$ mm $6 < Re < 40$ $5\ mlmin^{-1} \leq Q_g \leq 30\ mlmin^{-1}$ $2 \leq \frac{Q_g}{Q_l} \leq 300$	Rectangular	GL	Experimental	Song et al. (2019)

interaction pressure drop (Δp_{int}) caused by introducing the secondary phase. These pressure drop components can be shown together as follows:

$$fRe_t = 16 + \frac{\Delta p_{int}^*}{2L^*} \tag{2.13}$$

The non-dimensional pressure drop and length scale in Eq. (2.12) were proposed by Walsh et al. (2009), as below:

$$\Delta p_{int}^* = \frac{\Delta p_{int} d}{\mu V} \tag{2.14}$$

$$L^* = \frac{L_s}{d} \tag{2.15}$$

where μ and L_s denote the dynamic viscosity of the continuous phase and the length of liquid slugs, respectively. The pressure drop over a unit cell can also be described by three components (Kreutzer et al., 2005c; Fouilland et al., 2010; Ni et al., 2017):

$$\Delta p_{uc} = \Delta p_s + \Delta p_f + \Delta p_{cap} \tag{2.16}$$

Furthermore, Abiev (2011) assumed the total pressure losses in the capillary tubes were a summation of two components, named the formation of a new surface during the motion of bubble and the arrangement of a velocity profile in liquid slugs as below (refer to Table 2.9 for further details):

$$\Delta p_t = \Delta p_{\Delta F} + \Delta p_{trans} \tag{2.17}$$

Besides, Song et al. (2019) expressed the total pressure drop considering the total number of water slugs (n), including the pinching off slug,

$$\Delta p_t = \Delta p_g + \Delta p_{cr} + (n - 1)\Delta p_s \quad (2.18)$$

where the first term indicates the pressure drop of single-phase flow of gas, the second term is the critical pressure drop to break up the water slugs, and the last term denotes the pressure drop due to the moving slugs through the capillary. According to the literature, a circular cross-sectional area has been assumed for the gas bubble, where the velocity gradient is limited to the confined liquid region surrounding the bubbles, not inside the bubbles (Marchessault and Mason, 1960). However, the linear ratio between the pressure and velocity fields is valid for a straight tube, independent of the diameter of the channel. Introducing gas bubbles into the continuous phase flow changes the relation to be nonlinear. The moving bubbles in a tube leave a backfill of liquid left behind the bubble, where the volumetric flow rate of this backflow can be calculated by $\pi r \delta V_g$. Marchessault and Mason (1960) also showed the pressure gradient as a function of surface tension, film thickness, and the radius of the tube. They experimentally determined that at high velocities the liquid film thickness increases in the direction of the gas-bubble movement, when the profile of the bubble shows a tendency to be conic at the front.

Table 2.10 presents the correlations to calculate the pressure drop created by bubble / droplet in a microflow. One of the first empirical correlations of pressure loss in a capillary tube for horizontal and vertical configurations was experimentally and analytically obtained by Bretherton (1961). He discovered that the pressure drop was enhanced from a coefficient of 14.894 at the leading to 18.804 at the trailing regions due to the slight difference between the frontal and rear menisci of the bubble. Ratulowski and Chang (1989) proposed a correlation for pressure drop over a finite gas bubble approaching Bretherton's law for low Ca along with two other correlations for a square tube. Using a finite element method (FVM), Giavedoni and Saita (1997) determined the pressure gradient between two specific points; the first at the stagnation point of the gas bubble, and the second in the uniform film thickness region. Their results revealed an increasing trend in pressure gradient with the capillary number. They also found that the backflow region disappears when the capillary number is sufficiently high. Interfacial pressure along the free surface on the rear half of the gas bubble was found by them two years later, where the pressure was significantly decreased because of leaving liquid phase from the uniform film thickness region (Giavedoni and Saita, 1999). Kawaji and Chung (2003) found that the shape of the ducts had an impact on the frictional pressure loss or the void fraction. They showed that the total pressure drop was a summation of pressure loss in the single-phase part and the two-phase part of a unit cell. The size impact of the cross-section area of a rectangular microchannel was experimentally carried out by Harirchian and Garimella (2009) for a boiling heat transfer situation. A slight decrease in pressure drop was found with a heat flux increase caused by liquid viscosity reduction as the liquid phase temperature increased. They also observed an increase in pressure loss as the cross-sectional area decreased. Niu et al. (2009) showed the total pressure drop in a two-phase microflow was the summation of the wall friction and the sudden expansion components showing good agreement when compared with homogenous and separated models.

2.9 Conclusions

In this chapter, the literature of GL and LL two-phase flows through microchannels with different cross-sectional areas were discussed. Key results can be summarized in the following way.

- The maps of Taylor flow and the transition boundaries between each flow regime have been explained by x-y graphs, where the axes are defined by the superficial phase velocities, dimensionless numbers, and volumetric flow rates.
- Most often the gas bubbles and dispersed liquid droplets are surrounded by a thin film of carrying phase, except in noncircular tubes with very high void fraction where the dry-out at the inner surface of the tube has been observed.
- There is still no universal agreement to classify all flow regimes due to the experimental apparatus and capturing equipment, which force investigators to name the flow regimes differently.
- As more efficient numerical solutions and supercomputers emerge, they are used to solve interesting microflow problems with acceptable accuracy. Since the hydrodynamic of the film thickness is crucial and informative, high-resolution

TABLE 2.10: The literature on pressure drop correlations of the two-phase flow in the microchannels

Correlation	Comment(s)	Flow Parameter	Cross-Section	Phases	Method	Ref.
Across a bubble $\Delta p = 14.894 \frac{\sigma}{d} Ca^{\frac{2}{3}}$	Dynamic pressure component was dominantly greater than the static value (lubrication approximation) for small Ca The main pressure drop caused by a slight difference between the head and rear curvatures of the bubble	d=1 mm $1 \times 10^{-3} \leq Ca \leq 0.01$	Circular	GL	Experimental and Analytical	Bretherton (1961)
$\Delta p = \frac{2\mu_l V_g}{d}\left[\frac{64\nu}{\pi d^3} + K\right]$	The end effect (K) of the bubble was shown by a constant value of 45 for $0 < Re < 270$ a function of the Re of $0.163(\rho_l V_g D)/2\mu_l$ for $270 < Re < 360$	$0.5\ mm \leq d \leq 0.8\ mm$ $0.5 \leq U_s/U_b \leq 1$ $23 \leq \frac{\mu_l}{\mu_b} \leq 58$	Circular	GL	Experimental	Jayawardena et al. (1997)
For circular tube: $\Delta p = 9.4\ Ca^{\frac{2}{3}}$-$12.6\ Ca^{0.95}$ For Square tube: axisymmetric bubbles, $\Delta p = 3.14\ Ca^{0.14}$ non-axisymmetric bubbles, $\Delta p = 12.2\ Ca^{0.55}$	Matched Asymptotic Analysis Infinite bubbles, $L > d$ Finite bubbles, $L < d$	$3 \times 10^{-3} \leq Ca \leq 0.01$ $Bo = 4 \times 10^{-4}$	Circular and Square	GL	Numerical and Analytical	Ratulowski and Chang (1989)
$\Delta p = \Delta p_l \varepsilon_l \left[1 + 0.065\left(\frac{L_s}{d\ Re_l}\right)^{-0.66}\right]$	An entry region friction model	(N/A)	Circular	GL	Numerical and Analytical	Heiszwolf et al. (2001)
In uniform film thickness region: $\Delta p = -\frac{1}{R_{s\infty}}$	Bubble profiles For $0.1 < Ca < 0.54$:axisymmetric bubbles, For $Ca > 0.54$: bubbles moved faster than liquid and complete by-pass was realized	$Ca = 0.16, 0.54$, and $We \ll 1.0$	Square	GL	Numerical and Analytical	Kolb and Cerro (1993)

	For Ca < 0.54: bubbles moved slower than liquid and reverse flow occurred For Ca=0.54: bubbles traveled as the same velocity as the liquid and no stagnation pressure					
$\Delta p = \Delta p_l \alpha_l^{-\frac{1}{2}}$	The pressure drop of two-phase flow was greater than single-phase flow The Lockhart and Martinelli model did not adequately predict the pressure drop for the laminar flow regime, Coleman and Garimella (1999) The viscosity of the liquid phase had a key role in the frictional part of the pressure loss	d_H=0.2, 0.525 mm $0.001 \leq Ca \leq 0.2$ $0.004 \leq V_g \leq 11$ $0.001 \leq V_l \leq 0.2$	Square	GL	Experimental	Cubaud and Ho (2004)
$\Delta p = 16\left(1 + 0.17\frac{d}{L_s}\left(\frac{Re}{Ca}\right)^{\frac{1}{3}}\right)$ $\Delta p = 14.2\left(1 + 0.17\frac{d}{L_s}\left(\frac{Re}{Ca}\right)^{\frac{1}{3}}\right)$	Pressure drop over the slugs	d = 2 mm $0.002 \leq Ca \leq 0.04$ $0.04 \leq V_l \leq 0.3$ $Re \leq 900$	Circular and Square	GL	Experimental and Numerical	Kreutzer et al. (2005a and 2005b)
$\Delta p = 32\frac{Q_l \mu_l L_g}{hf^3}$	A decrease in the channel curve radius enhanced the pressure drop An increase in vorticity enhanced the pressure linearly Pressure drop was decreased with	$0.2\ mm \leq w \leq 0.4$ m h = 0.15 mm $0.0047 \leq Ca \leq 0.0074$ $11.6 \leq Re \leq 22.6$ $20.4 \times 10^3 \leq Pe \leq 39.6 \times 10^3$ $0.01\ ms^{-1} \leq V_l \leq 0.07\ ms^{-1}$ $V_g = 0.08\ ms^{-1}$	Rectangular	GL	Experimental and Numerical	Fries and von Rohr (2009) Han and Chen (2018)
$\Delta p = \varepsilon_l f\left(\frac{4L}{d}\right)\left[\frac{1}{2}\rho_l\left(V_l + V_g\right)^2\right]$	The pressure distribution in liquid slug and gas bubble was significantly different due to the interfacial effects	d = 0.5 mm $V_g = 0.245\ ms^{-1}$ $V_l = 0.255\ ms^{-1}$	2D	GL	Numerical	Xu et al. (2021)

	The interfacial pressure difference at the nose was greater than the tail of the gas bubble	$Re = 280$ $Ca = 0.006$				
Total pressure drop $\Delta p = 16 + \frac{7.16(3Ca)^{\frac{2}{3}}}{2L^{*}Ca}$ Curve fitting after scaled using $\left(\frac{Ca}{Re}\right)^{\frac{1}{3}}$ $\Delta p = 16 + \frac{1.92}{L^{*}}\left(\frac{Re}{Ca}\right)^{\frac{1}{3}}$	The pressure drop behaviour with $L^{*}(Ca/Re)^{\frac{1}{3}}$ was approximated by two asymptotes The total pressure drop was a summation of Poiseuille flow and Taylor components Poiseuille flow was dominant when $L^{*}(Ca/Re)^{\frac{1}{3}}$ was greater than 0.1 and Taylor flow was dominant for $L^{*}(Ca/Re)^{\frac{1}{3}}$ less than 0.1	$d = 1$ mm $1.58 \leq Re \leq 1024$ $0.0023 \leq Ca \leq 0.2$ $0.034 \leq Bo \leq 0.28$	Circular	GL	Experimental	Walsh et al. (2009)
$\Delta p = 56.9\left[1 + 0.07\left(\frac{d_H}{L_s}\right)\left(\frac{\rho_l d\sigma}{\mu_l^2}\right)^{\frac{1}{3}} + 5.5 \times 10^{-5}\left(\frac{L_s}{d_H Re}\right)^{-1.6}\right]$	Shorter liquid slugs and higher inertia force empowered the inner recirculation region At $\frac{L_s}{D_h} \leq 3$, and Re=200, the pressure drop approached to that proposed by Kreutzer et al. (2005a)	$d_H = 0.4$ mm $0.05 \leq We \leq 5.5$	Square	GL	Experimental	Qian et al. (2019)
$\Delta p = 16\left[1 + 0.931\frac{R\,F}{V_l}\frac{1}{Ca^{\frac{1}{3}}+3.34Ca}\right]$	Pressure drop was assumed as a summation of frictional and interfacial components The accuracy of the proposed pressure drop model increased for Re greater than 150	$d = 0.25$ mm $0.0023 \leq Ca \leq 0.008$ $41 \leq Re \leq 159$	Circular	GL	Experimental	Warnier et al. (2010)

$\Delta p_{sf} = \frac{4V_s\alpha L}{\frac{0.5(R\text{-}\delta)^2}{\mu_d}} + \frac{4V_m\mu_c(1\text{-}\alpha)L}{0.5\ R^2} + \frac{L}{L_{uc}}7.446\frac{\sigma}{R}Ca^{\frac{2}{3}}$ $\Delta p_{mf} = \frac{4V_s\alpha L}{\frac{R^2\text{-}(R\text{-}\delta)^2}{\mu_c} + \frac{0.5(R\text{-}\delta)^2}{\mu_d}} + \frac{4V_m\mu_c(1\text{-}\alpha)L}{0.5\ R^2} + \frac{L}{L_{uc}}7.446\frac{\sigma}{R}Ca^{\frac{2}{3}}$	Pressure drop was assumed as a summation of frictional and interfacial components Stagnant film (sf) reduced the channel diameter effectively Moving film (mf) considered the dispersed phase frictional drop	$0.248 \leq d \leq 0.498$ mm $0.03\ ms^{-1} \leq V_s \leq 0.5\ ms^{-1}$ $0.1 \leq \frac{Q_o}{Q_a} \leq 4$	Circular	LL	Experimental	Jovanović et al. (2011)
$\Delta p_{\Delta F} = \frac{2R_b}{R^2}\frac{w}{U_s}\frac{L_c}{L_{uc}}\sigma$ $\Delta p_{trans} = \text{-}aN_{uc}L_s\left\{1+\frac{1}{2bL_s}[1\text{-}\exp(\text{-}bL_s)]\right\}$	The dominant role of the number of bubbles compared the gas holdup on the pressure losses	$3.04\times10^{-4} < Ca < 9.6\times10^{-3}$ $0.053 < \varepsilon_l < 0.917$	Circular	GL and LL	Analytical and Experimental	Han and Chen (2018)
$\Delta p_{uc} = \frac{4\mu_c V_m L_s}{0.5\ R^2}\frac{L}{L_{uc}} + \frac{4V_m\mu_c L_f}{0.5\ R^2\left[\left(1+\left(\frac{R_i}{R}\right)^4\right)\left(\frac{1}{\gamma}\text{-}1\right)\right]}\frac{L}{L_{uc}} + \frac{L}{L_{uc}}9.402\frac{\sigma}{R}Ca^{\frac{2}{3}}$	The pressure drop prediction was only valid for long droplets The interfacial pressure drop increased as the diameter decreases The interfacial pressure drop was negligible for very long slugs and droplets	$d = 1.06$ mm $0.0045 \leq Ca \leq 0.008$ $21 \leq Re \leq 41$	Circular	LL	Experimental and Numerical	Gupta et al. (2013)
$\Delta p = 16\left[1 + 1.061\frac{R\,F}{V_l}\frac{1}{Ca^{\frac{1}{3}} + 3.34Ca}\left(1\text{-}\frac{Q_d}{Q_t}\right)^{\frac{1}{3}}\right]$	Total pressure drop was increased as the total volumetric flow rate enhances The total pressure drop approaches to an asymptotic value of 16 for single-phase flow for $\frac{L_c}{d}(Ca/Re)^{\frac{1}{3}}$ greater than 0.12	$d = 1.59$ mm $1.45 \leq Re \leq 567.59$ $4.49\times10^{-5} \leq Ca \leq 0.06$ $1.5 \leq \frac{\mu_c}{\mu_d} \leq 953$	Circular	GL LL	Experimental	Eain et al. (2015)

images can be produced via CFD. Meanwhile, there is still room to pay more attention to this region because of the important effect of film thickness on the frictional pressure drop, bubble or droplet profile, and heat and mass transfer.

- Contact angle play a major role in the flow pattern as long as two phases are in contact with the inner surface of the tube, except for Taylor flow is, i.e., gas bubbles or dispersed liquid droplets surrounded by a liquid film.
- The transition criterion from one flow regime into another one has been investigated by many researchers, resulting in numerous criteria based on the nature of the flow, experimental approach, and key parameters.
- The quantitative attempts to correlate slug length, liquid film thickness (recently summarized by Etminan et al. (2022a) in a comprehensive review paper), and pressure drop have been compared. These correlations include non-dimensional numbers, superficial velocity ratios, volumetric flow rate ratios, void fraction, and other thermophysical characteristics of phases.

Chapter 3

Prediction of Liquid Film Thickness in Taylor Flows[1]

3.1 Overview

Two-phase Taylor flow has received considerable attention from researchers in recent decades due to its potential use in a wide variety of industrial and medical applications. A large number of experimental, analytical, and numerical efforts have been taken by researchers to understand the fundamental characteristics of two-phase flows and the relevant transport phenomena. This chapter presents a comprehensive review of the hydrodynamics, flow pattern, and liquid film thickness in two-phase flows through mini- and microchannels with different cross-sectional geometries. This chapter also reviews correlations that predict liquid film thickness in microchannels for gas-liquid and liquid-liquid flows. The variations of liquid film thickness are plotted over a wide range of capillary numbers for both experimental and computational studies. This study shows that the effects of cross-sectional area on the flow patterns and flow characteristics have not been sufficiently investigated by researchers, particularly for rectangular cross-sectional area with different aspect ratios.

[1] This chapter is written based on:
Etminan, A., Muzychka, Y.S., Pope, K. (2022a) Liquid film thickness of two-phase slug flows in capillary microchannels: a review paper. The Canadian Journal of Chemical Engineering. 100(2), 325–348.
DOI: 10.1002/cjce.24068

3.2 Introduction

The investigation of two-phase flows is rapidly increasing and significant advances have been made since the 1980s. Two-phase flow refers to a combination of liquid, gas, and solid phases moving through a channel. The interaction between phases determines the flow pattern and the amount of heat and mass transfer in each phase, where the distinct phases are recognizable. Most energy-related engineering applications involve two-phase flows whilst three-phase flows can be also observed in some special industrial applications, such as a typical oil and gas reservoir, which includes oil, gas, and water simultaneously. Two-phase flows can be classified as gas-liquid (GL), liquid-liquid (LL), liquid-solid particles (LS), and gas-solid particles (GS). These flows can also involve phase changes, such as evaporation, boiling, condensation, melting, and freezing, causing the matter to change from one state to another. Therefore, it is necessary to understand the characteristics of multiphase flows, flow patterns, the interaction between different phases, and the interaction between phases and the solid walls of the channel to have an optimized microchannel system, where the pressure drop is the lowest and the heat and mass transfer rates are well controlled.

To the best of my knowledge, the earliest attempt to address a visible liquid film thickness in a GL flow dates back to Vaillant (1913). It first used the phrase pre-wet to refer to the inner surface of microchannels and possibly even macrochannels, but never answered the question about the existence of microscopic or macroscopic film left behind the contact line at the trailing edge of the bubble. One of the oldest articles on the subject, by Fairbrother and Stubbs (1935) discussed the measurement method in a bubble-tube and the apparent velocity of flow as a linear function of the bubble velocity. Since the bubble was expanded over the entire cross-sectional area of the channel, the velocity of the bubble was nearly equal to the velocity of the liquid phase flow. Their experiments also revealed that the difference between the true and apparent velocities was proportional to the square root of the bubble velocity but had specific amounts for each liquid considered, such as water, benzene, ethyl alcohol, and aniline. Taylor (1961) confirmed and extended the results of Fairbrother and Stubbs (1935) by designing an experiment to measure the amount of liquid that is left behind by a gas bubble inside a tube. Taylor (1961) found an asymptotic value of 0.55 for these very viscous fluids to reach a capillary number (Ca) of 1.9 (i.e., 135 times the greatest value proposed by Fairbrother and Stubbs (1935) beforehand). One of the most cited references in the literature discussing the motion of long bubbles in circular tubes is Bretherton (1961). It indicated that inertial forces were negligible, and described the film left on the inner walls of the channel when the film thickness was sufficiently thin. It also found the effects of viscous forces on the profile of the interface can be explained by the lubrication equations in fluid dynamics.

Bretherton solved two problems for investigating the film thickness and pressure drop for a single gas-bubble. First, the tube diameter was so small that the gravitational effect was negligible. Second, when the tube was larger, placed in a vertical position, and sealed at one end, gravity had to be considered. Based on the physics of the flows, Bretherton found that the viscous stresses and pressure drop were proportional to the Ca. Bretherton's analysis was limited to infinitely long bubbles and very low Ca. Teletzke (1983) and Park and Homsy (1984) continued Bretherton's theory and formalized it to match an asymptotic expansion. Teletzke (1983) theoretically studied the finite length of bubbles, the effect of intermolecular forces in the film region, and the liquid viscosity. The hydrodynamics and stability of submicroscopic film thickness (i.e., less than a few microns thick) were developed by other researchers (Mohanty, 1981; Mohanty et al., 1981; Teletzke et al., 1988). The displacement of the contact line in LL flow, which can be named spontaneous or forced movement, was studied in the literature (de Gennes, 1985; Hirasaki and Lawson, 1985; Joanny, 1986; Teletzke et al., 1987). The results showed that the lubrication equation predicted the velocity distribution when the thickness of a thick layer of liquid surrounding the gas bubble was varied slowly. The effect of the inner surface of the capillary tube on the motion of a gas bubble was investigated by Bretherton (1961), Teletzke (1983), and Schwartz et al. (1986). The surface modification in two-phase flow in microchannels was experimentally studied by Cubaud et al. (2006). The water / air flow moved through a microchannel with a square cross-sectional area and the bubble profiles were identified in the stationary and the moving bubble cases. The results revealed the importance of the surface influence on the behaviour of two-phase flows, where the interfacial properties between the multiphase flow and the inner surface of the tube were dramatically enhanced.

Two models, the separated flow model (SFM) and the homogeneous flow model (HFM), have been used by many investigators to classify two-phase flows in numerical analysis (Richter, 1983; Agrawal and Bhattacharyya, 2008; Chingulpitak and Wongwises, 2010; Furlong and Schmidt, 2012; Kim and Mudawar, 2015). Based on the SFM, each phase can be considered as a region with its velocity and temperature fields; however, having the temperature and velocity distributions of both phases is necessary to solve the problem and some corrections must be also applied to the solution due to the interface between phases. Meanwhile, the same flow and temperature fields are assumed for two phases. Richter (1983) used the SFM to study hydrodynamics and thermal non-equilibrium effects on the depressurization. In contrast, Chingulpitak and Wongwises (2010) indicated that the HFM was more effective for designing and optimizing the helical capillary tubes working with different refrigerants. Agrawal and Bhattacharyya (2008) compared both models in an adiabatic capillary circular tube and proved that the SFM predicted pressure distribution along the tube better than the HFM. Another comprehensive comparison between both models was performed by Furlong and Schmidt (2012) who found that the SFM shows a smaller error when determining the mass flow rate and has higher accuracy for simulations. However, there was a serious limitation with the SFM when the working fluid properties were near the critical point.

This chapter is organized in the following way. Section 3.3 shows the importance of two-phase flows in different areas of applications. Section 3.4 defines the fundamentals of macro- and microchannels, proposes criteria for classification, and investigates common junctions. Section 3.5 presents flow maps and patterns by summarizing occurrence conditions for each flow regime. A detailed study of existing correlations to predict liquid film thickness in Taylor flow through microchannels is conducted in Section 3.6.

3.3 Areas of Two-Phase Flow Applications

The early stages of microfluidics advancement occurred in the late 1980s, when microflow measurement instruments (sensors, micropumps, and microvalves) were developed in the fields of life sciences and chemistry (Manz et al., 1990; Gravesen et al., 1993). The most common applications of multiphase flows involve pipelines, power systems, oil and gas, heat exchangers, reactors, medical devices, meteorology and climate systems, sewage treatment plants, groundwater flows, air-conditioning equipment, condensers, submerged combustion systems, refrigeration plants, evaporators, distillation plants, marine propellers, cryogenic plants, DNA biochips, and cellular analysis. For instance, the operating fluid in a steam power cycle is converted from a liquid state into steam when it passes the boiler. Another example is the cavitation phenomenon in a pump when fluid flow is suddenly changed into vapour due to the huge pressure drop when its amount is very close to the vapour pressure of the operating fluid. Petersen (1982) extended the miniaturization of electronic devices to machining mechanical microdevices, known as microelectromechanical systems (MEMS).

From the research point of view, knowledge of the flow pattern and the thermal parameters of two-phase flow in micro- or minichannel reactors (MCRs) is necessary to design and optimize the reactors. Each phase inside a reactor has a specific behaviour, which not only affects the fluid flow and the heat transfer characteristics but may interact with other phases involved in the flow. Therefore, it is essential to understand the details and all aspects of MCRs properly. An MCR includes parallel channels to enhance the rate of heat and mass transfer under specific operational circumstances, which have been studied by many researchers during past decades (Edvinsson and Cybulski, 1995; Machado et al., 1999; Cybulski et al., 1999; Broekhuis et al., 2001; Nijhuis et al., 2001; Kreutzer et al., 2001; Boger et al., 2003, 2004a, 2004b; Kiwi-Minsker and Renken, 2005; Pangarkar et al., 2008; Gascon et al., 2015; Macchi et al., 2019). Due to the high potential of MCRs to quickly complete processes, they work with a precise mass transfer rate in the Taylor flow regimes. The MCRs are not just used as chemical and biocatalytic reactors by investigators (Burns and Ramshaw, 1999; Schubert et al., 2001; Kreutzer et al., 2005a; Watts and Haswell, 2005; Miyazaki and Maeda, 2006; Moulijn et al., 2011; Karande, 2012; Bolivar and Nidetzky, 2013; Haase et al., 2015; Meller et al., 2017), but MCRs are also used as extractors and absorbers in industries (Kashid and Agar, 2007; Ganapathy et al., 2014; Tsaoulidis and Angeli, 2015). Xu and Xie (2017) recently classified different LL microfluidic extractors (ME): stop-flow MEs, concurrent MEs, and countercurrent MEs regarding the flow configurations. They summarized the performance, operational factors, advantages, and disadvantages of each ME group presented by authors during the past seven decades. In another paper, Yao et al. (2015) investigated a comprehensive study on the applications of MCRs. Their review was concerned with the structure of MCRs and their application on the synthesis of nanoparticles, organics, polymers, and bio-substances. They showed that the nanostructure of glass, metal oxide, plastic, ceramic, silicone, and prepolymer causes the high efficiency of MCRs, which can be used in vehicles and aircrafts.

Finally, the electronic industries have been benefited from the simplicity, low cost, and suitability of manufacturing processes using the vigorous development of microelectronic packaging (Wu et al., 2012; Liqun et al., 2013) and capillary effects, such as wire-bonding machines (Chen and Lin, 2000; Tan et al., 2004; Xu et al., 2011; Tanna et al., 2012; Tseng et al., 2015a, 2015b; Cao et al., 2020), extrusion process, and solder balls-producing machines (Yu, 2010). Figure 3.1 indicates the size characteristics of different microfluidic systems.

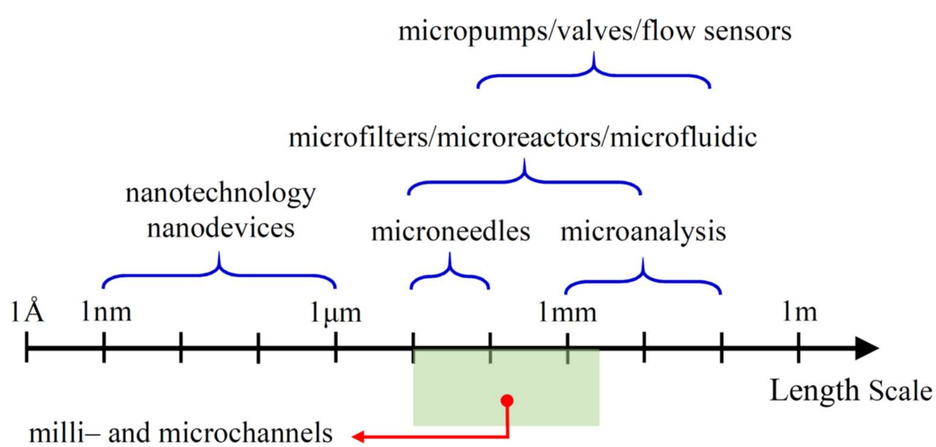

FIGURE 3.1: Size of the particles involved in microfluidic devices, reproduced from Nguyen and Wereley (2019)

3.4 Definition and Classification of Macro / Microchannel

Due to the very small diameter of the capillary microchannel involved in two-phase flow, the inertial ($\sim\rho U^2$) and gravitational ($\sim\rho gZ$) forces are not as important as the viscous ($\sim\mu Ud^{-1}$) and interfacial ($\sim\sigma d^{-1}$) forces. As mentioned before, both effective viscous and interfacial stresses are a function of the inversed diameter of the channel. Bretherton (1961) showed that the gravitational effect was negligible when the non-dimensional parameter of $\rho gd^2\sigma^{-1}$ was less than 3.368, where the density was replaced by the difference in densities of fluids inside and outside the gas bubble. The proposed limitation was satisfied with the bubble profile obtained by static equilibrium analysis between surface tensions and gravitational stresses.

Dimensional analysis is a powerful method in engineering to analyze the relations between different physical quantities in governing equations using basic units, such as length (L), mass (M), time (T), and temperature (K). In fluid mechanics, non-dimensional parameters involve a group of physical properties, in which each one is valid only under specific operational conditions. Regarding the nature of the non-dimensional groups, they can be divided into two categories: empirical and fundamental considerations (refer to Awad, 2012 for further details). These groups of physical parameters are important for deriving correlations for measuring some important variables in two-phase flows. Some of the most common dimensionless groups in multiphase flows are listed in Table 3.1.

Going through the literature in the field of transport phenomena, there is no clear agreement on classifying the channels based on the size of the cross-sectional area. It is important to establish some criteria to understand how a channel can be called a mini-, macro-, or microchannel. Table 3.2 presents some of the proposed criteria to classify the very small-diameter channels. The hydraulic diameter has been suggested by many authors while some other dimensionless numbers have also been proposed. These different criteria (compiled in Table 3.2) make it challenging to have a comprehensive criterion. But regardless of the physics of the flow and its pattern, a majority of studies on transport phenomena use the criterion suggested by Kandlikar and Grande (2003).

TABLE 3.1: Common non-dimensional numbers in multiphase flows

Name	Symbol	Definition	Concept
Archimedes	Ar	$Ar^{\frac{1}{2}} = \frac{\sqrt{\rho_l(\rho_l - \rho_g)gD^3}}{\mu_l}$	The ratio of gravitational force to viscous force
Bond	Bo	$Bo = \frac{gD^2(\rho_l - \rho_g)}{4\sigma}$	The ratio of gravitational (buoyancy) to capillary force scales
Capillary	Ca	$Ca = \frac{\mu_l U}{\sigma}$	The ratio of viscous forces to capillary forces
Cahn	Cn	$Cn = \frac{\delta}{D}$	The ratio of the interface thickness to the tube diameter
Ca/Re	Ca/Re	$\frac{Ca}{Re} = \frac{\mu^2}{\rho D\sigma}$	(N/A)
Nusselt	Nu	$Nu = \frac{\left(\frac{Q}{A}\right)D}{k(T_w - T_m)} = \frac{hD}{k}$	The ratio of convective to conductive heat transfer across (normal to) the boundary
Ohnesorge	Oh	$Oh = \frac{\mu}{\sqrt{D_h\sigma\rho}}$	The ratio of viscous to surface tension forces
Peclet	Pe	$Pe = RePr = \frac{UD}{\alpha}$	The ratio of heat transfer by the motion of fluid to heat transfer by thermal conduction
Prandtl	Pr	$Pr = \frac{\upsilon}{\alpha} = \frac{\mu C_p}{k}$	The ratio of the rate of momentum diffusion versus the rate of thermal diffusion
Reynolds	Re	$Re = \frac{\rho UD}{\mu}$	The ratio of inertial to viscous forces
Suratman	Su	$Su = \frac{Re}{Ca}$	The ratio of Reynolds number to the Capillary number
Weber	We	$We = Ca\ Re = \frac{\rho U^2 D}{\sigma}$	The ratio of inertial to interfacial forces

Based on the shape of the cross-sectional area, the microchannels can be classified into two large groups: circular and noncircular tubes. The latter category includes square, rectangle, triangle, trapezoid, and more. The interfacial effects appear at the entrance of a two-phase flow, where the injected flow is combined by the carrier flow. On the other hand, at the junction of the two flows, two-phase flow is created with specific configurations. The dispersed phase is introduced into the carrier fluid at the entrance region of the channel as a spherical or elongated bubble shape. The type of intersection is significant in forming a slug flow pattern. The most common type of junctions used in two-phase flows are illustrated in Figure 3.2. Table 3.3 provides a summary of different types of junctions used by researchers to create two-phase flows within microchannels. The T- and Y-junctions are the most popular types of intersections used to generate a slug pattern of two-phase flows with specific effects

TABLE 3.2: Proposed criteria to classify very small-diameter channels

Ref.	Criteria		Remark(s)
Shah (1979)	Hydraulic diameter	$D_h = 4A/P$	Micro: $D_h < 6\ \mu m$ Macro: $D_h > 6\ \mu m$
Brauner and Maron (1992)	Bond or Eötvös number	$Bo\ or\ Eo = \frac{(\rho_l - \rho_g) D_h^2 g}{(2\pi)^2 \sigma}$	Micro: $Eo > 1$
Kew and Cornwell (1997)	Confinement number	$Co = \frac{1}{D_h}\sqrt{\sigma / g(\rho_l - \rho_g)}$	Micro: $Co < 0.5$
Mehendale et al. (1999)	Hydraulic diameter	D_h	Micro: $D_h = 0.001 - 0.1$ mm Meso: $D_h = 0.1 - 1$ mm Macro (compact): $D_h = 1 - 6$ mm Conventional: $D_h > 6$ mm
Triplett et al. (1999)	Hydraulic diameter and Laplace constant	D_h and $La = \sqrt{\sigma / g(\rho_l - \rho_g)}$	Micro: $D_h \leq La$
Kandlikar and Grande (2003)	Hydraulic diameter	D_h	Molecular nanochannels: $D_h < 0.1\ \mu m$ Transitional channels: $D_h = 0.1 - 10\ \mu m$ Transitional nanochannels: $D_h = 0.1 - 1\ \mu m$ Transitional microchannels: $D_h = 1 - 10\ \mu m$ Microchannels: $D_h = 0.01 - 0.2$ mm Minichannels: $D_h = 0.2 - 3$ mm Conventional channels: $D_h > 3$ mm
Harirchian (2010)	Convective confinement number	$Bo^{0.5} \times Re = \frac{1}{\mu_l}\left(\frac{g(\rho_l - \rho_g)}{\sigma}\right)^{0.5} GD^2 = 160$	The transition from micro to macrochannel
Li and Wu (2010a, 2010b, and 2010c), Wu et al. (2011)	Confinement number	$Bo \times Re^{0.5} = \frac{g(\rho_l - \rho_g) D_{th}^2}{\sigma}\left(\frac{G(1-x) D_{th}}{\mu_l}\right)^{0.5} = 200$	The transition from micro to macrochannel
Ong and Thome (2011)	Confinement number	Co	Micro: $Co < 0.3$ Meso: $Co < (0.3 - 0.4) - 1$

on the slug formation process. A T-junction can be installed at the horizontal and vertical directions, where each junction follows different slug / bubble formation steps. The angle of the Y-junction is a dominant factor in producing slug and bubbly two-phase flows.

Han and Chen (2018) conducted a careful three-dimensional numerical study of the droplet formation in a T-junction microchannel. They showed the effects of the flow rate ratio and thermophysical properties on the droplet formation process and its diameter. Figure 3.3 presents the variation of droplet formation and its diameter at different flow rate ratios in the T-junction of the microchannel. Their results revealed that the effective diameter of the droplet was decreased when the continuous phase flow rate increased, and the dispersed phase flow rate remained constant. The droplet generation frequency was decreased as the flow rate ratio increased and breakup happened when the shear force was greater than the interfacial tension.

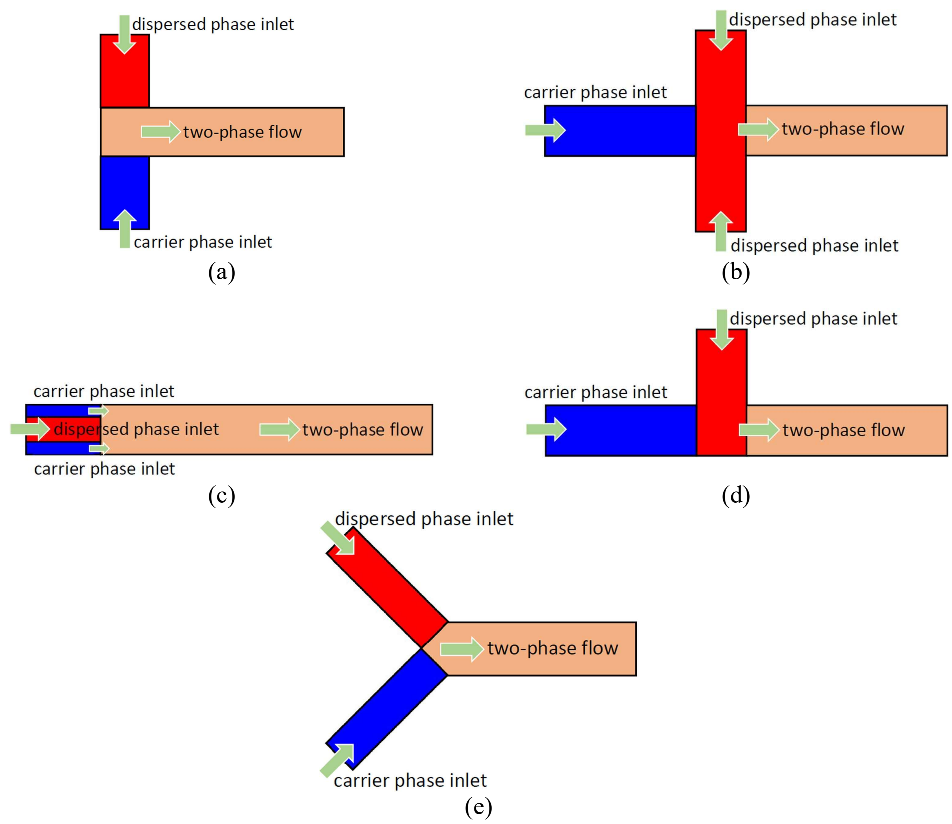

FIGURE 3.2: Schematic views of the most common junction configurations in two-phase flows; (a) T-junction, (b) cross-junction, (c) concentric-junction, (d) cross T-junction, and (e) Y-junction

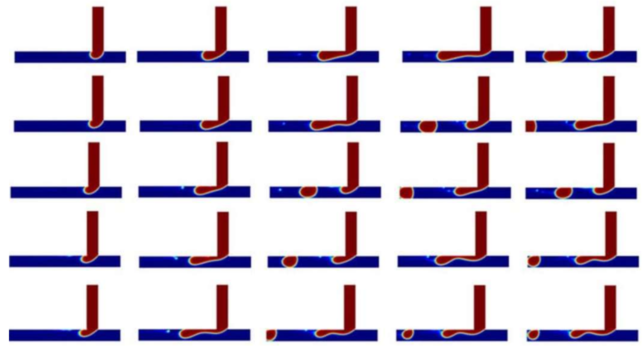

FIGURE 3.3: Volume fraction plots of droplet formation and breakup at 0.015 s to 0.035 s by a step of 0.005 s from left to right versus an increase in flow rate ratio from top to down, Han and Chen (2018)

3.5 Flow Patterns in Multiphase Flows

In very small-diameter channels, the surface tension and viscous forces are more important than the gravitational and inertial forces. In macro- and mini-channels, the flow patterns are highly dependent on the transport phenomena, the type of channels, the superficial velocities, and fluid properties, such as density, viscosity, and surface tension. As mentioned earlier, the channels are classified into three categories: mini-, macro-, and microchannels based on their dimensions. Kawaji and Chung (2003) presented different types of two-phase flow patterns in mini- and microchannels and they suggested that two-phase flows in these channels have similarities (illustrated by Figure 3.4). According to the literature, the use of the word mini-channel refers to the transition between macrochannel and microchannel, however this term is commonly known as mesochannel, which is more popular. Regarding the patterns of two-phase flows, they are categorized into two large groups: segmented and continuous flows. The first group involves slug, bubbly, annular, wavy, churn, and droplet flow regimes.

Significant research and studies have previously been conducted to determine the characteristics of flow patterns in microchannels. Flow maps were sketched by multiple scholars (e.g., Rodman, 1947; Gazley, 1949; Baker, 1953; Hughes et al., 1953; Alves, 1954) to recognize the formation of gas bubbles added into the carrier liquid phase. To observe the flow patterns, they used glass or transparent plastic sections in their piping systems and plotted different flow pattern regimes, including wave, slug, plug, stratified, annular, and bubble, using the surface tension, the viscosity

TABLE 3.3: Experimental and numerical studies on two-phase flow in microchannels using different types of junctions

Ref.	Junction	Cross-Section	Phase System	Remark(s)
Taylor (1961)	T	Circular	Air / Glycerin and strong sucrose solution (golden syrup) diluted with water	The amount of liquid left behind the bubble was increased versus the capillary number
Schwartz et al. (1986)	Concentric	Circular	Air / Water	The long gas bubbles moved faster than short ones
Irandoust et al. (1992)	T	Circular	Air / Water, Ethanol, Ethylene Glycol	The length of slugs and the velocity had an insignificant impact on the mass transfer rate
Berčič and Pintar (1997)	T	Circular	Methane / Water	The mass transferred in the thin liquid film surrounding the gas bubble was not dominant The length and velocity of slugs had an insignificant impact on mass transfer rate
Triplett et al. (1999)	Cross	Circular	Air / Water	Higher mixture volumetric flux led to longer bubbles and shorter liquid slugs
Tokeshi et al. (2000)	Y	Rectangular	Fe Complex / Chloroform	The extraction efficiency in the microchannel was less than that in the separatory funnel
Cramer et al. (2004)	Concentric	Rectangular	Water / Oil	Small droplets of oil were achieved at high velocities of the carrier phase and low interfacial force
Cubaud and Ho (2004)	Cross	Square	Air / Water	Because of the small channel size, wettability played an important role in the system
Günther et al. (2004)	T	Rectangular	Air / Ethyl Alcohol	3D recirculation in liquid slugs enhancing mixing
Maruyama et al. (2004)	Y	Rectangular	*n*-Heptane / Water	The partition walls induced slight turbulence in the two-phase flow in the microchannel
Kreutzer et al. (2005)	Concentric	Circular	Air / Water, Decane, Tetradecane	More bubbles per unit channel length caused a higher pressure loss
Bowden et al. (2006)	Y	Rectangular	Hexane / Oil	The addition of hexane to the oil before its injection into the device increased the efficiencies of separation and extraction

Cubaud et al. (2006)	Cross	Square	Air / Water	The reduction in the size of the channels dramatically enhanced the effects of the walls on two-phase flow
Xu et al. (2006)	Cross-T	Rectangular	Water / Anhydrous Hexadecane	The size of oil droplet was reduced with an increase in the carrier phase rate but slightly increased as the oil flow rate increased
Zhao et al. (2006)	T	Rectangular	Water / Kerosene	Six distinct flow configurations were recognized at the junction: 1- oil slugs at the junction 2- monodispersed droplets at the junction 3- droplet population in the centre of the microchannel 4- parallel flows that had a smooth interface at the junction 5- parallel flows that had a wavy interface at the junction 6- chaotic thin striations flow at the junction
Kashid and Agar (2007)	Y	Circular	Water / Cyclohexane	The power required for producing interfacial area was ascertained from the pressure drop over the Y-junction
Kashid et al. (2007)	Y	Circular	*n*-Butyl / Water	The internal circulations in the slugs improved the mass transfer rate by surface renewal at the phase interface
Steijn et al. (2007)	T	Square	Air / Ethanol	The rapid constriction of the bubble neck started when the neck radius equaled one-fourth of the channel width
Steinbrenner et al. (2007)	Cross	Rectangular	Air / Water	The water film thickness in a stratified flow regime varied significantly with the gas superficial velocity
Yue et al. (2007)	Y	Rectangular	CO_2 / Water	The transition from slug to churn flow regimes occurred at the highest superficial liquid velocity
Zhao et al. (2007)	T Cross	Rectangular Square	*n*-Butanol / Water	The overall mean volumetric mass transfer coefficient was increased by decreasing the volumetric flux ratio
Cubaud and Mason (2008)	Cross	Square	Water / Silicone, Glycerol, Isopropanol, Ethanol, Aqueos and Ethylic mixtures of Glycerol	The capillary number of each phase highly affected the shape of oil droplet and thread formation
Dessimoz et al. (2008)	T Y	Rectangular	Water / Dyed Toluene, Hexane	An increase and decrease of the interfacial tension force were favorable for slug flow and parallel flow, respectively

Kirpalani et al. (2008)	T	Circular	Ethanol / Nitrogen	The channel bends caused the flow pattern transitions
Yue et al. (2008)	Y	Rectangular Square	CO_2 / Water	Taylor bubble formation process in the microchannels was found to be in the squeezing regime at lower superficial liquid velocities while the transition to the dripping regime was observed at the highest superficial liquid velocity of 1 m/s
Warnier et al. (2008)	Cross mixer Smooth mixer	Rectangular	Nitrogen / Water	The gas bubble velocity did not affect the liquid film thickness A constant fraction of the cross-section area of the channel was occupied by film thickness for different channel diameters
Fries and von Rohr (2009)	T	Rectangular	Ethanol / Nitrogen	Small bend radius enhanced mass transfer efficiently over the channel centre line
Niu et al. (2009)	T	Circular	CO_2, N_2 / Polyethylene Glycol Dimethyl	The increase of superficial gas and liquid velocities caused an increase in volumetric mass transfer coefficient
Walsh et al. (2009)	T	Circular	Air / Water, FC40, Dodecane, AR20 *n*-Hexane / Silicone Oil	The scaling group in a model for the prediction of pressure drop in slug/bubble segmented flows as a function of L^* and Ca/Re, and demonstrated the theory of Bretherton was found lacking
Yue et al. (2009)	Y	Rectangular	Air / Water	A quiet stationary liquid film around the bubbles caused the bubbles to move faster than liquid slugs
Dessimoz et al. (2010)	T Y	Circular	CO_2 / Water	Interfacial tension and inertia mainly determined the flow
Fouilland et al. (2010)	T	Circular	Water / Nitrogen	The pressure gradient ratio between the film and the gas core determined the film thickness and the velocity ratio between the film and the gas
Su et al. (2010)	T	Circular	H_2S / Methyldiethanolamine	For a constant superficial liquid velocity, removal efficiency was decreased with an increase in the gas to liquid ratio
Yun et al. (2010)	T	Rectangular	Nitrogen / Aqueous Surfactant Solution, Acetone, Ethanol	The film thickness around a Taylor bubble was varied along the direction from the bubble nose to its tail and the dimensionless maximum or minimum film thickness were correlated in terms of the Weber number
Asthana et al. (2011)	Cross	Square	Water / Oil	The oil slug movement in the carrier flow increased mixing and disrupted the boundary layer
Jovanović et al. (2011)	Y	Circular	Water / Toluene, Ethylene Glycol	It was found that the film velocity was of negligible influence on the pressure drop

Kashid et al. (2011)	T Y Concentric Caterpillar	Square Trapezoidal Rectangular Circular	Water / Acetone, Toluene	The rate of mass transfer was highly dependent on the flow regimes and the geometry of two-phase contacting
Roudet et al. (2011)	T	Circular	Air / Water	Dominant inertia effects on bubble shape; a larger slug-annular regime
Asadolahi et al. (2012)	T	Circular	Water / Nitrogen Ethylene Glycol / Nitrogen	A decrease in Nusselt number with an increase in homogeneous void fraction
Sarkar et al. (2012)	Cross	Rectangular	Acid-*n*-Butanol / Water Succinic	Continuous phase and organic phase alternated depending on inlet junction and flowing conditions
Eain et al. (2013)	T Segmenters	Circular	Water / Pd5 Baysilone, Dodecane, AR20 Silicone, FC40 Fluorinert	Once the flow transitioned into the visco-inertial regime, film thickness was no longer solely dependent on capillary number and an expression was presented that accounts for the increased inertial effects by incorporating the Weber number
Gupta et al. (2013)	T	Circular	Water / Hexadecane	For a droplet of sufficiently large volume, the shapes of the front and the rear menisci of the droplet were observed to be independent of the droplet volume, with only the length of the uniform thickness film region growing with an increase in the droplet volume
Ganapathy et al. (2014)	T	Circular	CO_2 mixed with N_2 / Aqueous DEA	Pressure drop increased by up to 17% due to the increase in the viscosity of the solution
Dai et al. (2015)	T	Circular	Water / Hexadecane	Without internal recirculation: 1- long slugs could be expected to approach the single-phase limit, $Nu^* \rightarrow 1$ 2- long droplets approach core-annular flow, $Nu^* \rightarrow 4.2$

Eain et al. (2015)	T Segmenters	Circular	Air / Water, Pd5, Ethylene Glycerol Water / Pd5 Baysilone, Dodecane, AR20 Silicone, FC40 Fluorinert	The existence of a threshold viscosity ratio of 4.5
Li et al. (2015)	T	Rectangular	Silicon Oil / Aqueous Solution	Slug dynamics of viscoelastic liquid in oil
Tsaoulidis and Angeli (2015)	T	Circular	Aqueous (HNO_3 solution) / TBP, IL	The extraction efficiency, which indicated how close to equilibrium values the final concentrations were, and the mass transfer coefficient decrease as the channel size increased
Yagodnitsyna et al. (2016)	T	Rectangular	Water / Kerosene, Paraffin Oil Paraffin Oil / Castor Oil	In most cases, the slug length was shorter than the plug
Huang et al. (2017)	T	Circular	Air / Water	The profile of the bubble nose was determined using a matrix of sensors
Han and Chen (2018)	T	Rectangular	Oil / Water	Discussed in the text
Rajesh and Buwa (2018)	T	Square	Air / Water Oil / Water, SDS	The dynamics of bubble / slug formation at the T-junction was governed by the relative magnitudes of viscous force, the gas phase inertial force and surface tension force acting on the air-oil interface
Wu and Sundén (2019)	Y to Cross	Quasi-Trapezoidal	Water / Butanol Water / Hexane	Compared to a junction angle of 90°, a junction angle of 45° tends to provide a larger tubing / threading regime at the inlet junction and a wider annular flow regime

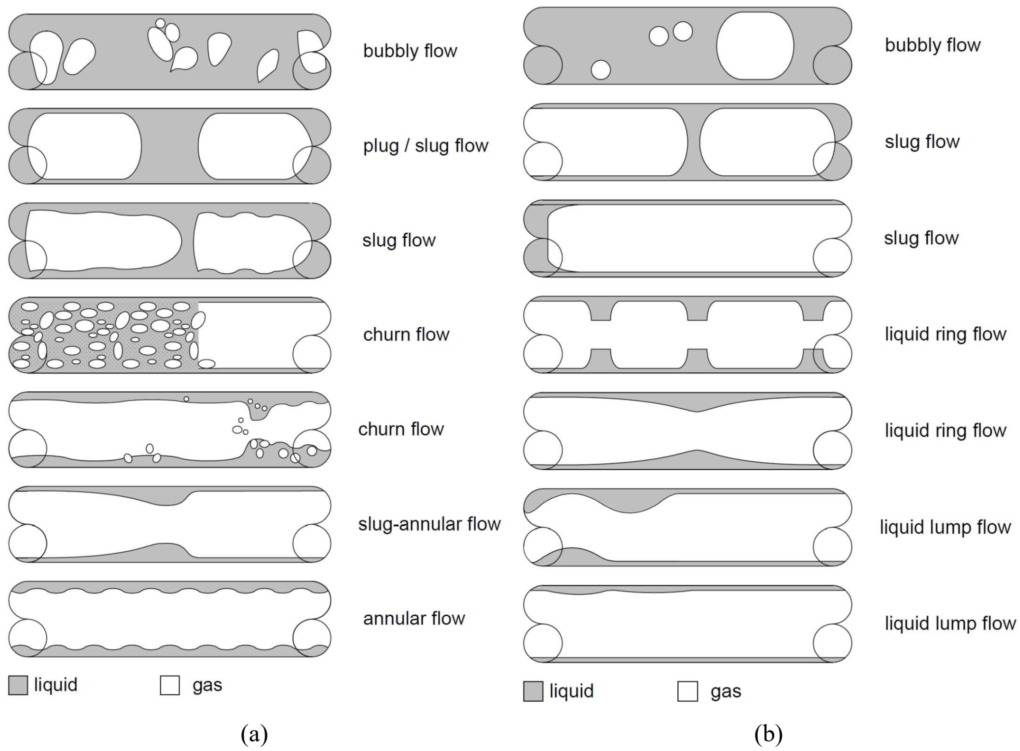

FIGURE 3.4: Different types of two-phase flow regimes in (a) mini-channels, and (b) microchannels, Kawaji and Chung (2003)

of the liquid phase, and superficial velocity and density of both phases. Hewitt and Roberts (1969) classified different regions in two-phase flows utilizing X-ray and high-speed photography instruments. Their experimental data was plotted in terms of superficial momentum fluxes of gas ($\rho_G V_G^2$) and liquid ($\rho_L V_L^2$) phases, which was previously suggested by Wallis (1962) to evaluate the transitions from one flow regime to another. Many other investigators, e.g., Govier and Aziz (1972), Mandhane et al. (1974), Taitel et al. (1980), Weisman and Kang (1981), Brauner et al. (1998), Triplett et al. (1999), Brauner (2003), Akbar et al. (2003), Cubaud and Ho (2004), Kreutzer et al. (2005b), Steijn et al. (2007), Yue et al. (2008), Fouilland et al. (2010), Kashid et al. (2011), Ong and Thome (2011), Bolivar and Nidetzky (2013), and Yagodnitsyna et al. (2016) conducted experimental and numerical research to observe the flow patterns of two-phase flows in channels, where the plots of each flow pattern were provided for greater clarification. A classification has been summarized in Table 3.4 according to the significant differences in two-phase flow maps. A brief description of each type of flow regime has been listed in Table 3.4 for GL and LL situations, along with the occurrence conditions.

Relevant non-dimensional groups have been used to show the regime of each two-phase flow, which is highly dependent on the data obtained by the experiment method. These groups include Re, Ca, We, Su, We Oh, flow rate ratios, and superficial velocities selected by investigators to plot flow pattern maps and identify the distinct transition. Experimental data collected by many researchers using a variety of working fluids and tubes sizes are shown in Figure 3.5.

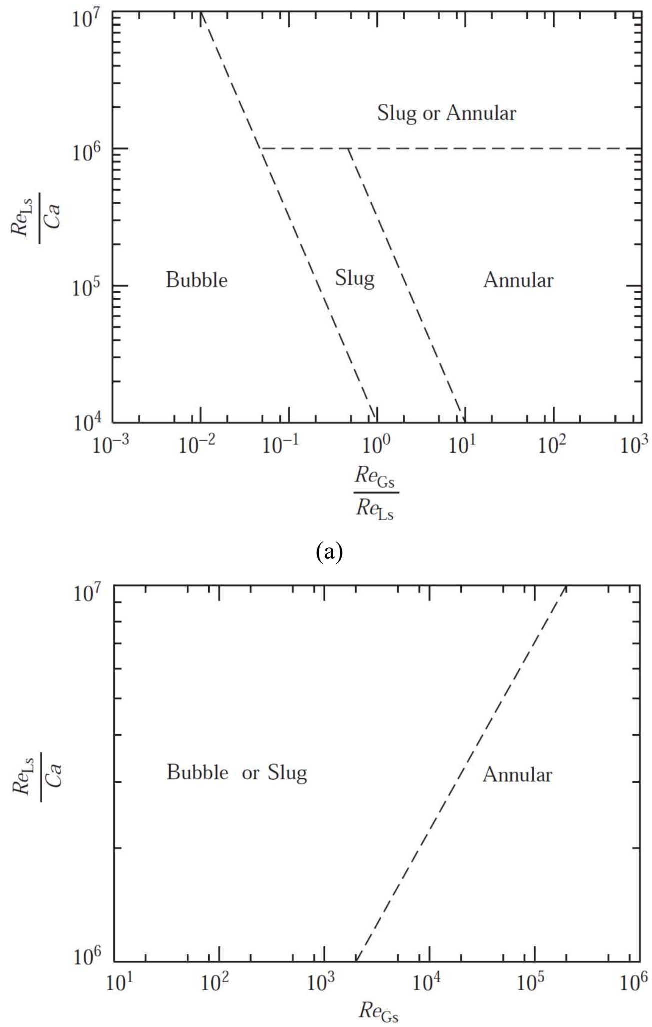

(b)

FIGURE 3.5: Flow pattern maps in microgravity two-phase and annular flows when (a) $10^4 < \mathrm{Re/Ca} < 10^7$ (b) $10^6 < \mathrm{Re/Ca} < 10^7$, Jayawardena et al. (1997)

TABLE 3.4: Definitions of different gas-liquid (GL) and liquid-liquid (LL) two-phase flow regimes and occurrence conditions

Flow Pattern	**GL**	**LL**	**Occurrence Conditions**
Bubbly Flow	small non-wetting gas-bubbles are dispersed in the liquid carrier phase and tend to disperse uniformly in the liquid	(N/A)	when the shear forces are dominant or at very high liquid velocities and low gas to liquid ratios
Slug / Plug / Bubble Train / Segmented / Intermittent Flow (Taylor Flow)	the gas-bubbles merge together to form elongated bubbles and slugs. A thin film of liquid surrounds the slugs and some small bubbles may appear in liquid slugs too	the droplets of the dispersed phase merge together to form slugs with a diameter and a length similar to and larger than the channel diameter, respectively, and are surrounded by a thin-film of the carrier phase	at intermediate liquid velocities, rolling waves of liquids are formed and increased to the point of forming a slug flow
Annular Flow (T- or Y-junction)	a thin film of liquid surrounds the continuous gas flow phase in the annular core of the channel	a thin liquid-film surrounds the other continuous liquid phase in the annular core of the channel	at very high gas velocity and low liquid velocity
Mist Flow	the continuous gas phase involves the fine droplets of liquid phase	refer to Slug Flow	when the shear forces are so high
Dispersed Flow	refer to Bubbly Flow	the continuous carrier phase is filled by the fine droplets of another liquid phase with diameters less than the hydraulic diameter of the channel	when the flow rate is increased
Parallel Flow (Concentric junction)	same as LL situation	two continuous liquid flows wet the channel walls and move in parallel forming a straight interface	at very high gas velocity and low liquid velocity and the shear force of the continuous phase is dominant over the surface tension force

Deformed Interface Flow	(N/A)	the irregular droplets are generated by the dispersed liquid phase in both annular and parallel regimes	at relatively high flow velocity. This flow regime is less stable and behaves as a transition between the slug and the parallel regimes
Churn / Chaotic Flow	this flow regime is similar to slug flow but highly disordered, in which the vertical motion of the liquid is oscillatory. And, the concentration of gas bubbles destroy the continuity of liquid phase flow	same as GL situation	the flow rates of liquid and gas are intermediate between the annular and slug flows and an increase in the velocity of flow induces instability in that
Stratified Flow	same as LL situation	two different liquid flows travel through the channel, where the difference in their densities separates them into two layers	at low flow rates of liquid and gas

3.6 Correlation of Liquid Film Thickness in Two-Phase Flows in Microchannels

The measurement of liquid film thickness is significantly important to understand the hydrodynamics of two-phase flows through microchannels. The film thickness is important in the analysis of heat and mass transfers in microchannels. The study of the literature on the measurement of the liquid film thickness in two-phase flows in microchannels is presented in this section. Regarding the cross-sectional geometry of the channel, the study is divided into two subsections: circular and noncircular cross-sections. Some key features of each study include analysis method, phases, materials, flow conditions, and available correlations, which have been tabulated in Tables 3.5 and 3.6.

3.6.1 Microchannels with Circular Cross-Sectional Area

The earliest correlation used to predict the thickness of liquid film dates back to the mid-1930s when Fairbrother and Stubbs (1935) followed an experimental method allowing water to flow at a constant volumetric rate through a long capillary tube contained an air bubble. Their study was focused on a single air-bubble placed in a horizontal configuration. The measurement of effective liquid film thickness around a stationary / moving air-bubble in an inclined glass capillary tube was investigated by Marchessault and Mason (1960). The influence of the bubble velocity on the flow resistance factor and film thickness was observed. For the first time, the proposed correlation by Marchessault and Mason (1960) to determine the film thickness involved the bubble velocity, along with the Ca. Ratulowski and Chang (1989) carried out a mathematical method to introduce a correlation in order to measure the film thickness for both the axisymmetric and planar geometries, which approaches the correlation of Bretherton (1961). The results of Ratulowski and Chang (1989) matched the asymptotic analysis for a horizontal configuration and for single infinite- and finite-length bubbles. To measure the liquid film thickness in a vertical capillary tube involving air / water, ethanol, and glycerol, Irandoust and Andersson (1989) proposed an empirical equation that was substantially different from previous correlations. The new correlation estimated the amount of thickness to be much more than those

TABLE 3.5: Literature on the correlation of liquid film thickness around the bubble / slug in two-phase flows in circular cross-section area microchannels

Ref.	**Analysis Method**	**Phases**	**Materials**	**Flow Conditions** (Re, Ca, We, Bo, etc.)	**Research Aspects**	**Correlation**
Fairbrother and Stubbs (1935)	Experimental	GL	Air / Water	$D = 2.26$ mm $0 \leq Ca \leq 0.015$	Horizontal flow Single slug	$\frac{\delta}{R} = 0.5\ Ca^{0.5}$
Marchessault and Mason (1960)	Experimental	GL	Air / Water	$D = 1.484$ mm $7 \times 10^{-6} \leq Ca \leq 2 \times 10^{-4}$	Film thickness Bubble resistance factor Stationary and moving bubble	$\frac{\delta}{R} = -0.05\left(\frac{\mu_l}{\sigma}\right)^{0.5} + 0.89Ca^{0.5}$
Taylor (1961)	Experimental	GL	Refer to Table 3.3	$D = 2$ and 3 mm $0 \leq Ca \leq 1.9$	Film thickness	Just data points
Bretherton (1961)	Experimental Analytical	GL	Air / Water	$D = 1$ mm $1 \times 10^{-3} \leq Ca \leq 0.01$	Film thickness Pressure drops Single slug Horizontal flow	for $Ca < 0.005$ $\frac{\delta}{R} = 1.338Ca^{\frac{2}{3}}$
Suo and Griffith (1963)	Experimental	GL	Nitrogen / Water Air / Water Nitrogen / *n*-Heptane Helium / *n*-Heptane	$0.5\ \text{mm} \leq D \leq 0.8$ mm $0.5 \leq \frac{U_s}{U_b} \leq 1$ $23 \leq \frac{\mu_l}{\mu_b} \leq 58$	Stationary film thickness	$\frac{\delta}{R} = 1 - \sqrt{\frac{U_s}{U_g}}$
Chen (1986)	Experimental	GL LL	Air / Oil, Water	$2 \times 10^{-4} \leq Ca \leq 2 \times 10^{-3}$	Horizontal capillary tube Film thickness Stationary and moving bubble	$\frac{\delta}{R} = 1.337\ Ca^{\frac{2}{3}}$

Schwartz et al. (1986)	Experimental	GL	Air / Water	$D = 1$ and 2 mm $6 \times 10^{-6} \leq Ca \leq 1 \times 10^{-3}$	Film thickness Slug Length	$\frac{\delta}{R} = 1.338\ Ca^{\frac{2}{3}}$
Irandoust and Andersson (1989)	Experimental	GL	Air / Water, Ethanol, Glycerol	$1\ mm \leq D \leq 2\ mm$ $9.5 \times 10^{-4} \leq Ca \leq 1.9$	Upward flow Film thickness	$\frac{\delta}{R} = 0.36\left(1.0 - e^{-3.08\ Ca^{0.54}}\right)$
Ratulowski and Chang (1989)	Numerical Analytical	GL	Air / (N/A)	$3 \times 10^{-3} \leq Ca \leq 0.01$ $Bo = 4 \times 10^{-4}$	Matched Asymptotic Analysis Infinite bubbles, L>d Finite bubbles, L<d	$\frac{\delta}{R} = 1.338\ Ca^{\frac{2}{3}}$
Aussillous and Quéré (2000)	Experimental Analytical (Scaling Approach)	GL	Air / Silicone Oils, Ethanol , Heptane, Decane	$D = 0.84, 1.24, 1.56,$ and 2.92 mm $0.01 \leq Ca \leq 1$	Scaling law Film thickness Upward flow Single Slug Threshold in capillary number, Ca^{*}	$\frac{\delta}{R} = \frac{1.34\ Ca^{\frac{2}{3}}}{1 + 3.35\ Ca^{\frac{2}{3}}}$
Bico and Quéré (2000)	Experimental	LL	Ethylene Glycol / Silicone Oil	$D = 0.68$ and 1.02 mm $1 \times 10^{-3} \leq Ca \leq 0.01$	Film thickness Velocity of slug Trains of slugs	$\frac{\delta}{R} = 2.14\ Ca^{\frac{2}{3}}$
Kreutzer et al. (2001)	Experimental	GL	Hydrogenation of Methylstyrene/ Toluene	$D = 2$ mm $2.7 \times 10^{-4} \leq Ca \leq 1.11 \times 10^{-2}$ $437.27 \leq Re \leq 1457.56$	Film thickness Mass transfer rate	$\frac{\delta}{R} = 0.36\left(1.0 - e^{-2.13\ Ca^{0.52}}\right)$
Grimes et al. (2006)	Experimental	LL	Water / FC40, Tetradecane, Dodecane	$D = 0.762$ mm $1.3 \times 10^{-5} \leq Ca \leq 7.2 \times 10^{-2}$	Film thickness Droplet shape	$\frac{\delta}{R} = 5.0\ Ca^{\frac{2}{3}}$

Han and Shikazono (2009)	Experimental Analytical (Scaling Approach)	GL	Air / FC40, Ethanol, Water	$D = 0.3, 0.5, 0.7, 1,$ and 1.3 mm $0 \leq Ca \leq 1$ $0 \leq Re \leq 2000$	Film thickness Horizontal flow Multiple slugs	for $Re < 2000$: $\frac{\delta}{R} = \frac{1.34\ Ca^{\frac{2}{3}}}{1 + 3.13Ca^{\frac{2}{3}} + 0.504Ca^{0.672}Re^{0.589} - 0.352We^{0.629}}$ for $Re > 2000$: $\frac{\delta}{R} = \frac{212\left(\frac{\mu^2}{\rho\sigma}\frac{1}{D}\right)^{\frac{2}{3}}}{1 + 497\left(\frac{\mu^2}{\rho\sigma}\frac{1}{D}\right)^{\frac{2}{3}} + 7330\left(\frac{\mu^2}{\rho\sigma}\frac{1}{D}\right)^{0.672} - 5000\left(\frac{\mu^2}{\rho\sigma}\frac{1}{D}\right.}$
Eain et al. (2013)	Experimental	LL	Water / Pd5, Dodecane, FC40, AR20	$D = 1.59$ mm $0.002 \leq Ca \leq 0.119$ $0.047 \leq We \leq 0.697$ $14.46 \leq Re \leq 100.96$	Film thickness	$\frac{\delta}{R} = 0.35Ca^{0.354}We^{0.097}$
Klaseboer et al. (2014)	Numerical Analytical	GL	(N/A)	$0 \leq Ca \leq 1.9$	Pressure drop Film thickness	$\frac{\delta}{R} = \frac{1.338\ Ca^{\frac{2}{3}}}{1 + 3.732\ Ca^{\frac{2}{3}}}$
Ni et al. (2017)	Numerical	GL LL	Air / Water, Ethanol, FC40	$D = 1.06$ mm $0.006 \leq Ca \leq 0.35$ $10 \leq Re \leq 950$	Film thickness Flow pattern Pressure distribution	$\frac{\delta}{R} = \frac{1.34\ Ca^{\frac{2}{3}}}{1 + 3.13Ca^{\frac{2}{3}} + 0.504Ca^{0.672}Re^{0.589} - 0.305We^{0.664}}$

TABLE 3.6: The literature on the correlation of liquid film thickness around the bubble / slug in two-phase flows in noncircular cross-section area microchannels

Ref.	Cross-Section	Analysis Method	Phases	Materials	Flow Conditions (Re, Ca, We, Bo, etc.)	Research Aspects	Correlation
Ratulowski and Chang (1989)	Square	Numerical Analytical	GL	Air / (N/A)	$Ca > 0.003$ $Bo = 4 \times 10^{-4}$	Asymptotic Analysis Infinite bubbles, $L > D$ Finite bubbles, $L < D$	for $Ca > 0.04$: $\delta = 0.6933 - 0.0977 \ln Ca$
Heiszwolf et al. (2001)	Square	Experimental	GL	Hydrogenation of Methyl styrene / Toluene	$2.1 \times 10^{-3} \leq Ca \leq 6.9 \times 10^{-3}$	Film thickness	$\frac{\delta}{R} = 0.72\left(1.0 - 0.7\, e^{-2.25\, Ca^{0.445}}\right)$
Kreutzer et al. (2001)	Square	Experimental	GL	Hydrogenation of Methyl styrene / Toluene	$D_h = 2$ mm $2.1 \times 10^{-3} \leq Ca \leq 6.9 \times 10^{-3}$ $437.27 \leq Re \leq 1457.56$	Film thickness	The correlation has been derived from data provided by Thulasidas et al. (1995) $\frac{\delta}{R} = 0.5\left(0.6 - e^{-2.25\, Ca^{0.445}}\right)$
Cubaud and Ho (2004)	Square	Experimental	GL	Air / Water	$D_h = 0.2$ and 0.525 m $0.001 \leq Ca \leq 0.2$	Pressure drop Film thickness Flow pattern	Critical film thickness in wedging flow: $\delta_C = 2\left[\frac{\sigma}{g(\rho_l - \rho_g)}\right]^{\frac{1}{2}} \sin\left(\frac{\theta_{rec}}{2}\right)$

Yun et al. (2010)	Rectangular	Experimental	GL	Acetone / Poloxamer 188 with Water	$0.05 \leq \mathrm{We} \leq 5.5$	T and cross junctions Film thickness Liquid slug length Pressure drop	$\frac{\delta_{fmax}}{D_h} = 0.39\mathrm{We}^{0.09}$ $\frac{\delta_{fmin}}{D_h} = 0.02\mathrm{We}^{0.62}$
Patel et al. (2017)	Square	Experimental	GL	Air / Water	$D_h = 0.51$ and 1.02 m $\mathrm{Ca} = 6.75 \times 10^{-3}, 1.37 \times 10^{-2}, 1.15 \times 10^{-2}$	Corner film thickness Different operational conditions Different channel diameter	$\frac{\delta}{D_h} = 0.085\ \mathrm{Ca}^{-0.137}$

suggested by previous scholars who derived for very low capillary numbers. The tube orientation, measurement methods, and the method and equipment's accuracy might be considered sources of errors.

Bico and Quéré (2000) experimentally investigated a train of slugs in a capillary tube involving ethylene glycol / silicone oil. The length of droplets was kept at a constant value, while the viscosity ratio of the liquids involved ranged from 4–4000. An experimental method, along with the scaling law, was used by Aussillous and Quéré (2000) to measure the liquid film thickness in air / silicone oil, ethanol, heptane, and decane two-phase flows. Their study was carried out on a vertical flow of single slug to find the film thickness correlation and the threshold capillary number, Ca^*, which is always smaller than Ca. Aussillous and Quéré (2000) precisely proposed an empirical correlation to measure liquid film thickness, which was in agreement with previous significant correlations. The major effort was conducted to compute the mass transfer rate in a three-phase monolith reactor by Kreutzer et al. (2001) using data of Thulasidas et al. (1995) to derive a correlation determining the thickness of the liquid film of methyl styrene / toluene multiphase flow in a round tube. Another experimental study on water / FC40, tetradecane, and dodecane two-phase flow was carried out by Grimes et al. (2006) to find a correlation for measuring film thickness around the water droplets. Figure 3.6 shows the experimental data provided by Grimes et al. (2006). The results indicated that Bretherton's theoretical correlation underestimated the liquid film thickness using the carrier liquid viscosity to define Ca. The solution suggested by Grimes et al. (2006) uses the liquid plug viscosity for defining Ca.

The development of water droplets in all considered carrier fluids was captured over a range of Ca and mean velocities (Figure 3.7). The shape of the water droplet changed from a cylindrical geometry with two hemispheres at both ends to an elongated bullet-like shape at higher Ca, which was previously reported by Olbricht and Kung (1992). Han and Shikazono (2009) experimentally investigated the air / FC40, ethanol, and water two-phase flows over a wide range of Reynolds numbers to derive two correlations for measuring the thickness of liquid film. Their study focused on a horizontal tube involving multiple slugs.

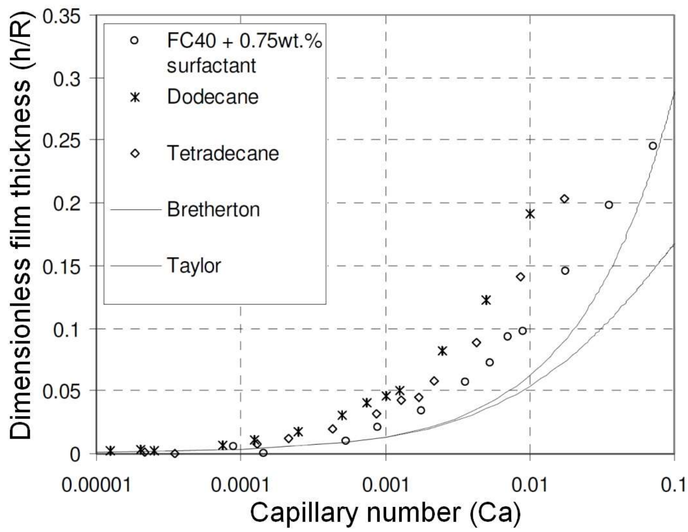

FIGURE 3.6: Film thickness measuring for different carrier fluids comparing with other correlations, Grimes et al. (2006)

Their findings showed that the film thickness was a function of three non-dimensional groups, Re, Ca, and We numbers, and remained at a constant value for the Reynolds numbers greater than 2000. The LL two-phase flow involving water, Pd5, dodecane, FC40, and AR20 was experimentally analyzed by Eain et al. (2013) to measure liquid film thickness by using a correlation. The proposed formula highlights the dependency of liquid film thickness on two non-dimensional groups, Ca, and We. Klaseboer et al. (2014) numerically followed an extended version of Bretherton's model for long Taylor bubbles to find a correlation for measuring the liquid film thickness. Their proposed formula showed a slight difference compared to correlations obtained by Aussillous and Quéré (2000) and Taylor (1961). Numerical simulation of LL and GL flows involving air / water, ethanol, and FC40 was performed by Ni et al. (2017) using commercial software package COMSOL Multiphysics. Ni et al. (2017) derived a correlation in the same form as Han and Shikazono (2009), using a modification of the coefficients and the presence of the Weber number. Invalidity of Bretherton's theory for $Ca > 0.003$ and high inertia flow (i.e., $Re \gg 1$) was addressed by Habibi Matin and Moghaddam (2021). Two modified versions of Bretherton's theory conducted by Aussillous and Quéré (2000) and Klaseboer et al. (2014) independently. They showed that the modified Bretherton's correlation can predict the liquid film thickness over a wide range of Ca up to 2, which satisfies an essential assumption (i.e., the thickness of liquid film must be thin enough compared to the tube diameter) considered by Bretherton. The experimental results obtained by Habibi Matin and Moghaddam (2021) indicated that the modified Bretherton's theory can still be employed when the inertia of flow is insignificant for Reynolds numbers less than 280. Their results showed larger deviations as capillary and Reynolds numbers increased shown in Figure 3.8.

3.6.2 Microchannels with Noncircular Cross-Sectional Area

Few studies have been conducted to determine the film thickness of liquid in microchannels with noncircular cross-section areas. Noncircular cross-section areas include many shapes, such as squares, triangles, and rectangles with different aspect ratios. Each shape has specific properties that affect the flow pattern, the development of droplets / bubbles, the liquid boundary layer, and the thickness of liquid-film. In comparison to the amount of research on film thickness in circular channels, noncircular channels have not received as much attention from researchers, even though there is a wide range of industrial applications for noncircular channels. Ratulowski and Chang (1989) numerically analyzed the air-liquid two-phase flow in a channel with a square cross-section area to present a correlation for measuring the liquid film thickness. Their asymptotic analysis was carried out for both an infinite and a finite length of bubbles. Kreutzer et al. (2001) experimentally studied the two-phase flow of hydrogenation of methyl styrenetoluene in a microchannel with a square cross-section area to measure the liquid film thickness in the uniform region. Their proposed correlation was valid over a vast range of Reynolds numbers using the data provided by Thulasidas et al. (1995) for round and square cross-sectional ducts. Critical film thickness in wedging flow consisting of elongated bubbles was determined by Cubaud and Ho (2004). According to their findings, the interactions between the bubble and the glass surface of the channel made three types of wedging bubbles in terms of the bubble velocity: completely dried-out, partially dried-out, and the wetted surface controlled by a thin layer of liquid (Figure 3.9). This liquid film can be considered as a nonmoving flow, while the liquid flows in the corner of the square cross-section.

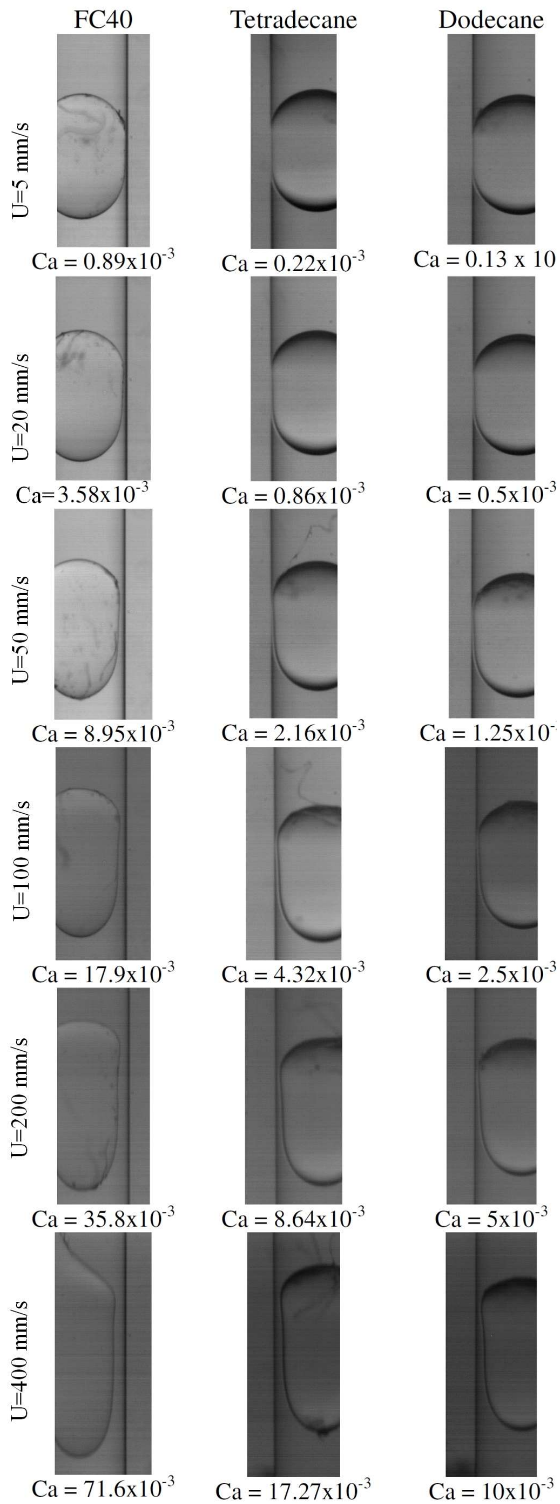

FIGURE 3.7: Visualization of water droplets for all carrier fluids at different mean velocities and capillary numbers, Grimes et al. (2006)

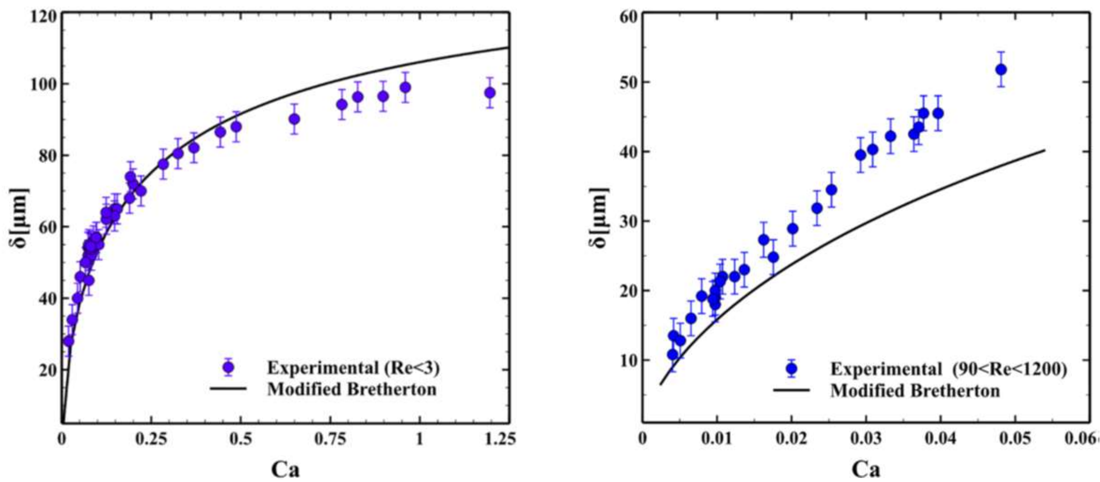

(a) (b)

FIGURE 3.8: Measured effect of capillary number on film thickness in a circular microchannel with an inner diameter of 0.6 mm for (a) silicone oil and (b) FC-72, Habibi Matin and Moghaddam (2021)

Yun et al. (2010) experimentally studied the GL flow of acetone / poloxamer 188 with water in a microchannel with a rectangular cross-section area, where the thickness of the liquid-film around a Taylor gas bubble was not uniform but was varied in both lateral and axial directions from the nose of the bubble to the tail. They proposed two correlations to find the highest and the lowest values of liquid film thickness based on the hydraulic diameters and Weber numbers. Generation of uniform water slugs through a T-junction superhydrophobic microchannel was experimentally carried out by Song et al. (2019). They showed the effects of different coating using modified silica nanoparticles at the inner side of rectangular microchannel on the contact angle and flow characteristics, such as slug length and pressure drop. They also established an empirical scaling law for a static slug length in a nearly square cross-sectional microchannel with a contact angle of 160°. Based on their results, the breakup mechanism followed four steps: intrusion, blocking, squeezing, and pinch-off. At the moment of pinch-off, the pressure drop was significantly dependent on the slug length and flow rate ratio. Recently, Chao et al. (2020) experimentally demonstrated the influence of thin liquid film surrounding bubbles in a microchannel with a square cross-sectional area on the pressure drop. Their high-speed visualization showed the evolution of the liquid film involves three steps: the lodged, dry bubble, and channel wall, as illustrated in Figure 3.10. Not enough driving pressure force in case 1 caused the bubble to remained dry (the lodged). Even by such a slow increase in the driving pressure, the bubble was deformed and started to move. Eventually, the liquid in the corner of the cross-section was pushed into the central region and a thin layer of liquid appeared (case 5). In the enlarged view of case 3, some liquid droplets were formed due to the metastable liquid film rapture mechanism.

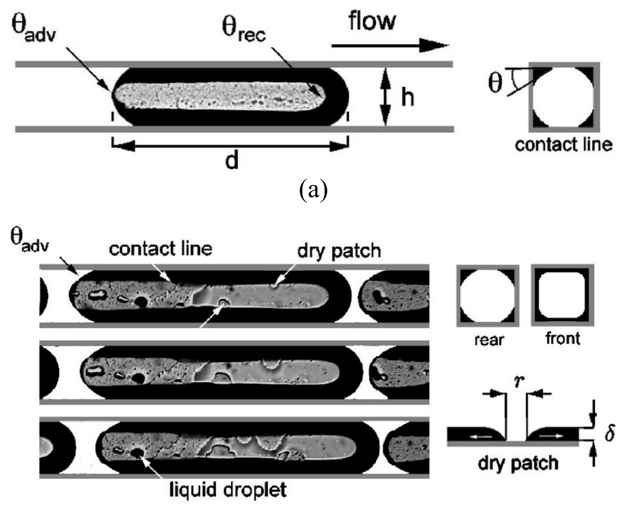

(b)

FIGURE 3.9: Two types of wedging flow regime: (a) drying bubble, and (b) sequential photos of a hybrid bubble, Cubaud and Ho (2004)

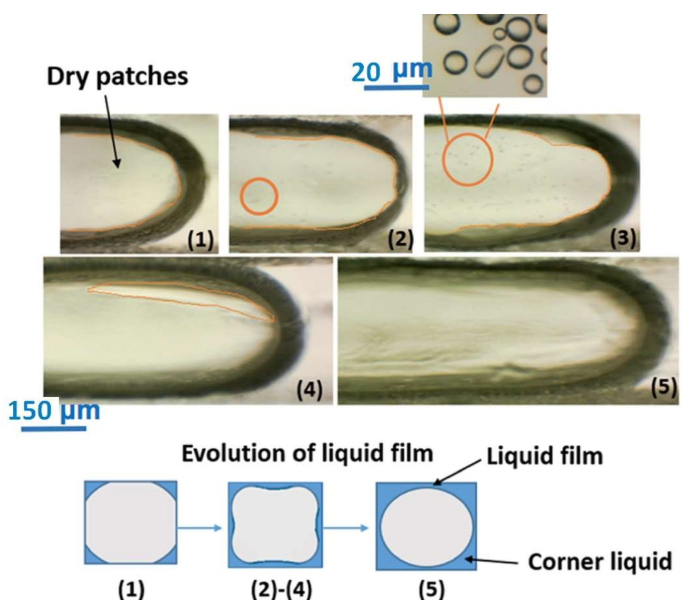

FIGURE 3.10: Snapshots of high-speed visualization for dry-bubble removal process, Chao et al. (2020)

The aspect ratio of rectangular cross-sectional area capillaries also known as the confinement effect can change the force balance within the film region. The thinnest film occurs along the longer side of cross section as Habibi Matin and Moghaddam (2021) and Magnini et al. (2022) addressed it experimentally and numerically, respectively. The first authors found that by increasing aspect ratio from 1.5 to 5.5, the dimensionless liquid film thickness along the longer side, for example, was increased up to 50% due to a decrease in the local pressure within the film region. Bretherton's theory and even modified versions of that underestimated the film thickness for all the operational liquids (i.e., silicone oil, IPA, and FC-72), and the deviation became more noticeable as the aspect ratio increased. The results obtained by the latter authors over a wide range of aspect ratios, 1–8, capillary number, 0.005–0.5, and Reynolds number, 1–1000, showed a flatter phase interface along the longer side. The strong effects of aspect ratio accompanied by the increase in capillary and Reynolds numbers caused the film region along the bubble to be not uniform.

The correlations of the liquid film thickness and the Ca, which were tabulated earlier, have been illustrated in Figure 3.11. The symbols used in this figure are to make the variations more observable and are not data points. According to the nature of microfluidics applications, the approximate values of superficial velocity, viscosity, and surface tension can be reasonably considered as ~10 μm s^{-1} to 10 cm s^{-1}, ~10^{-3} kg $m^{-1}s^{-1}$, and ~0.05 N m^{-1}, respectively. Therefore, the capillary number varies in a range of 2×10^{-7} to 2×10^{-3}, which highlights the importance of the starting zone of Figure 3.11a to be zoomed-in. The Irandoust correlation predicts the film thickness better than others for the entire considered Ca, particularly about 30% overestimation compared with other equations at a domain of the Ca between 0.2–0.6. Even though the correlations of Aussillous and Quéré (2000) and Klaseboer et al. (2014) have different formulas, approximately the same trend is recognizable. All of the correlations approach an asymptotic value at large Ca, which is not practical because of the very low value of the Ca in real micro-sized channel applications. In the zoomed-in view, Figure 3.11b, the differences between thickness predictions are depicted, where the correlation of Bico and Quéré (2000) calculates the value of thickness greater than others due to a coefficient of 2.14. He et al. (2010) correlated their experimental

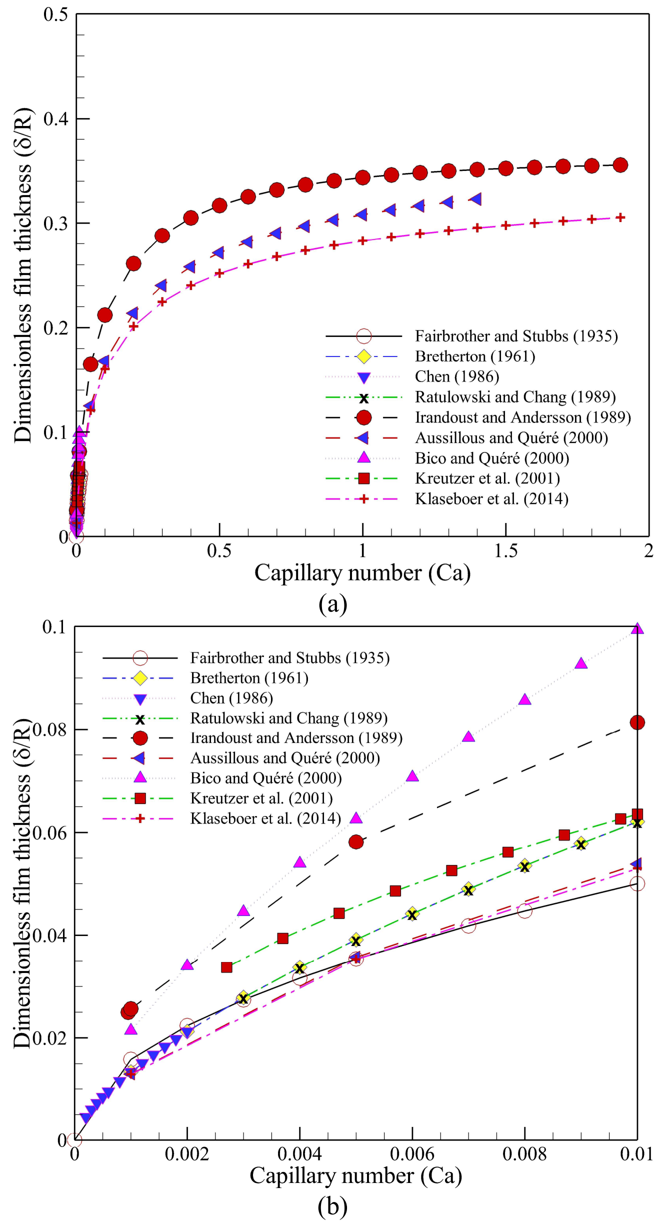

FIGURE 3.11: Variation of dimensionless liquid film thickness with the capillary number by correlations in the literature, (a) whole domain of Ca, (b) zoomed-in view over a very small domain of Ca

data for measuring dimensionless film thickness in a range of Ca between 0.002–0.01 by a constant value of 0.087, which cannot explain how the Ca affects the liquid film thickness.

Figure 3.12 shows the available data points of liquid film thickness in capillaries obtained experimentally and numerically over the past decade. Since a majority of the data points is concentrated over a very small domain of the Ca, an enlarged view is illustrated for the Ca varying from 0–0.01. In the legend of this graph, some key details of each research is summarized. As was numerically found by Ni et al. (2017), an increase of tube diameter makes the liquid film thicker. Also, for the same diameter tube, the film thickness of air / ethanol two-phase flow is greater than that of air / water due to the higher viscosity of ethanol than water. This trend was also observed at other diameters. The experimental and numerical results obtained by Asadolahi et al. (2012) are close to each other. It should be noticed that Sun et al. (2018) measured the liquid film thickness of transient boiling water flow in microchannels. Figure 3.12 also shows the experimental data provided by Eain et al. (2013) for dodecane/water two-phase flow (displayed by symbol 0). Because of the significant difference between the properties of dodecane and other liquids, the values of the film thickness are further apart from other data. The rest of the experimental and the numerical data displayed in this figure indicates that an equation could be obtained to predict the film thickness versus the Ca. From a statistical perspective, the sum of squared errors (SSE) and root mean square errors (RMSE) are two important measures showing the discrepancy between the data and estimated values of the considered mathematical model. Here, the correlation of Aussillous and Quéré (2000), displayed by a solid line in Figure 3.12, also predicts the liquid film thickness over the domain of the Ca in the experimental data very well, with a SSE and a RSME in the orders of 10^{-5} and 10^{-3}, respectively.

3.7 Conclusions

This chapter has presented a comprehensive literature review on two-phase flows focusing on liquid film thickness around the gas bubble / liquid slug. Possible applications of two-phase flows, classification of two-phase flows on the geometrical features, the different junctions for creating a two-phase flow, and the proposed correlations for measuring the liquid film thickness have been thoroughly covered by this study. This chapter divides the related articles into two large groups: circular and noncircular microchannels. The following conclusions can be obtained from the reviewed papers:

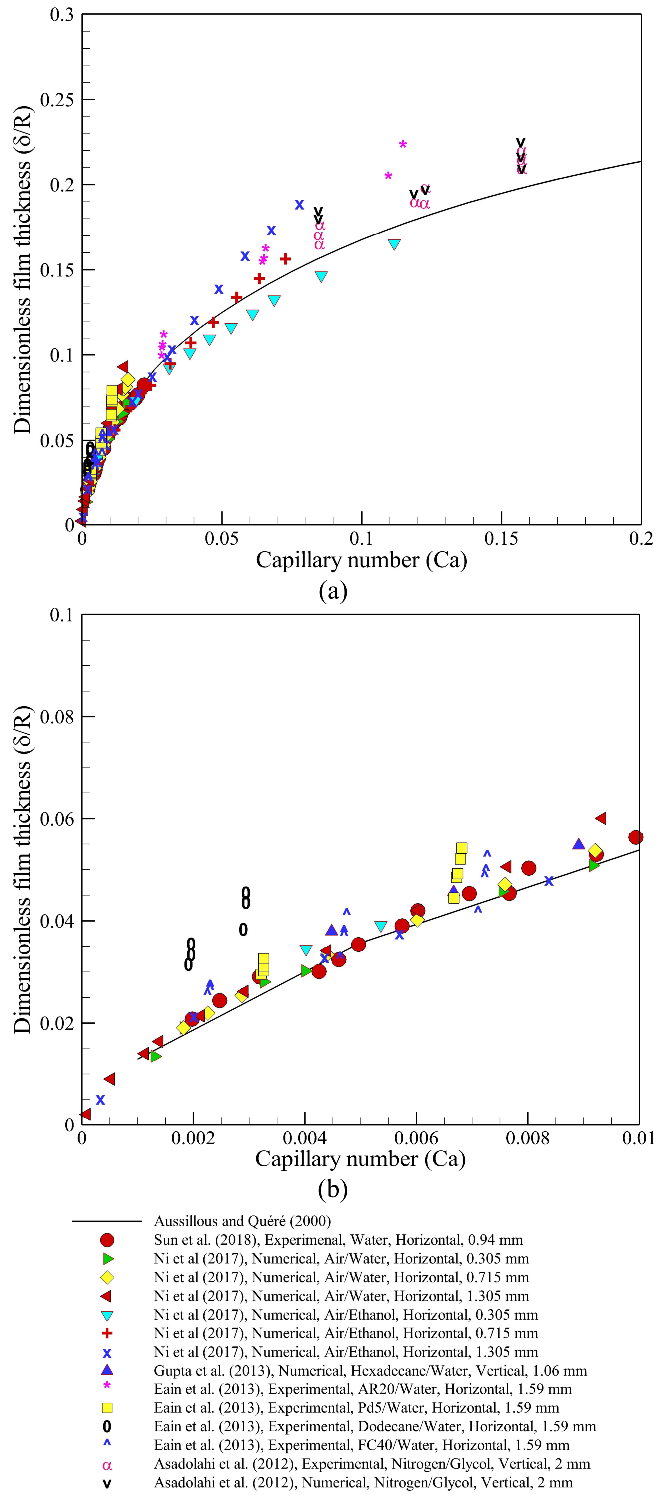

FIGURE 3.12: Experimental and numerical data of dimensionless liquid film thickness in circular microchannels versus Ca for (a) whole domain of Ca, and (b) zoomed-in view over a very small domain of Ca (the model of Aussillous and Quéré (2000) is also shown by a solid line)

- Multiphase flows are not limited to the aforementioned applications, and the multiphase flows can be seen in a majority of industrial and medical applications.
- There is no global consensus to classify circular and noncircular channels based on the diameter of their cross-sectional areas. While experimental methods, instruments, and other factors can affect the physics of flow in the channel, it is a factual challenge to predict a firm rule as a definition of microchannels. Different types of junctions have been used to produce two-phase flows. Each junction has specific characteristics affecting the development of a gas bubble or liquid slug, as well as a flow pattern.
- Flow regimes in channels are highly dependent on the size of cross-sectional areas of the channels and there are some obvious differences between the flow patterns in micro- and minichannels.
- The types of flow regimes in microchannels are also dependent on the situation of two-phase flows, GL and LL, and require specific occurrence conditions.
- The liquid film thickness correlations often include non-dimensional groups and are significantly important to understand the pressure drops, heat transfer rate, and Nusselt number.
- Thanks to the series of experimental data found in the literature, a correlation attained by Aussillous and Quéré (2000) predicts the thickness of liquid film around the gas bubble over the constant film thickness region perfectly. This model makes a quantitative description on the Bretherton model for long Taylor bubbles movement in a capillary and the thickness of liquid film.

There are still vague aspects of the details of liquid film thickness in microchannels with square cross-sectional areas, particularly rectangular cross-sectional areas with different aspect ratios. Future investigations can aim to fill this gap for a better understanding of the effect of geometrical features on the flow pattern in LL two-phase flows.

Chapter 4

Film Thickness and Pressure Drop for Gas-Liquid Taylor Flow in Microchannels[1]

4.1 Overview

Computational fluid dynamics (CFD) has been widely employed by investigators to simulate Taylor flow in microchannels. High-resolution images captured by numerical techniques reveal significant details of an ultra-thin liquid film around the gas bubble. The interface between the liquid and the gas phases is a decisive factor in order to determine the flow pattern, the gas bubble profile, the bubble length-separation distance, the slug length, and so forth. Since the thickness of the liquid film is on the order of 10–15 μm for low capillary number flows, the mesh generation requires careful modeling to capture it and transport phenomena, such as momentum and heat. The present study is to develop a model of a transient Taylor flow in a two-dimensional microchannel using commercial ANSYS Fluent software. The volume of fluid (VoF) method was employed to simulate the interface between two phases, i.e., air and water. A comprehensive grid study was carried out to identify a sufficiently

[1] This chapter is written based on:
Etminan, A., Muzychka, Y.S., Pope, K. (2020) Numerical simulation of Taylor flow in the entrance region of microchannels. The 5th World Congress on Momentum, Heat and Mass Transfer (MHMT'20), Lisbon, Portugal.
DOI: 10.11159/icmfht.189

Etminan, A., Muzychka, Y.S., Pope, K. (2021b) Film thickness and pressure drop for gas-liquid Taylor flow in microchannels. Journal of Fluid Flow, Heat and Mass Transfer. 8(1), 59–70.
DOI: 10.11159/jffhmt.2021.008

fine mesh to capture the film layer around the gas bubble in the uniform film thickness region. Film thickness, bubble curvature, pressure drop, bubble / slug lengths are determined to investigate gas-liquid Taylor flow in micro capillaries. The results show that the liquid film thickness remains almost constant, but the length of the flat film region increases as the air bubble proceeds downstream. The curvatures of the nose and the tail of the gas bubbles were studied during traveling through the channel. Variations of the lengths of slugs and plugs were also measured as the functions of time. The numerical results were validated by available correlations of liquid film thickness, and slug length in previous studies, which show a good agreement.

4.2 Introduction

Micro-structured mechanical systems are increasingly emerging in compact industrial applications. A microchannel has been designed to minimize pressure drop and maximize transport phenomena in numerous energy-related microfluidic purposes, such as heat exchangers, fuel cells, and microreactors. A typical gas-liquid two-phase flow refers to a mixture of two distinct phases and the phases are separated by interfacial lines. Such flows remain in the laminar flow regime due to predominant viscous and surface tension forces in them, which simplifies the numerical simulations by omitting the need for turbulence modelling.

The patterns of gas-liquid two-phase flows in microchannels are highly dependent on the transport phenomena, the type of channels, the phase's superficial velocities, and the fluid properties, such as density, viscosity, and surface tension. Considering the remarkably low-velocity flow and very small-diameter channels, the gravitational and inertia forces are insignificant compared to surface tension and viscous forces. Various flow patterns, such as bubbly, Taylor (also known as slug or segmented), churn, annular, stratified, and wavy have been reported by investigators (e.g., Kawahara et al., 2009; Cubaud and Ho, 2004; Kreutzer et al., 2005b; Yue et al., 2008; Fouilland et al., 2010; Kashid et al., 2011; Sur and Liu, 2012; Bolivar and Nidetzky, 2013; Yagodnitsyna et al., 2016; Kong et al., 2018; Deendarlianto et al., 2019). An informative way to describe the patterns of multiphase flows is to map the flow pattern on an x-y graph, where the axes could be volumetric flow rate ratios, phase superficial velocities, and non-dimensional numbers such as Reynolds (Re), capillary (Ca), and Weber (We) (e.g., Jayawardena et al., 1997; Triplett et al., 1999; Chung and Kawaji, 2004; Ghiaasiaan, 2014). Slug pattern occupies a large region in these maps. Consequently, accurate predictions of the gas bubble formation, growth, and propagation in microchannels are required, and calculations of some predominant flow parameters including void fraction, pressure drop, and liquid film thickness are taken into account.

The interaction structures of different phases and between phases and the solid walls not only establish the patterns of multiphase flows but also predict the amount of pressure drop through the microchannel. Having an optimized microchannel with the lowest pressure drop is required to predict the value of the frictional pressure drop at first. Walsh et al. (2009) considered the total pressure drop as a summation of two components: single-phase flow and interaction. Some scholars decomposed the pressure drop in a unit cell into three components, namely, pressure drop in a liquid slug, pressure drop in the flat film region, and pressure drop at the nose and tail transitional regions of the gas bubble (e.g., Kreutzer et al., 2005b; Fouilland et al., 2010; Song et al., 2019).

In Taylor flow, the void fraction is defined as the fraction of the channel volume that is occupied by the gas phase. The value varies from 0 to 1 at different locations in the channel. The void fraction experiences fluctuations depending on the flow pattern, which is influenced by the volumetric flow rates and superficial velocities of phases. Therefore, the time-averaged void fraction is most often computed in two-phase flows. The most broadly used model to predict the void fraction in a wide variety of multiphase flows is the drift-flux model proposed by Zuber and Findlay (1968). In the model, the void fraction can be obtained as a function of the distribution parameter and gas volumetric flow rate, for a horizontal configuration, where the drift velocity is zero. Based on the type of multiphase flow, the configuration, and the flow pattern, different distribution parameters have been proposed (e.g., Kawahara et al., 2009; Kariyasaki et al., 1992; Mishima and Hibiki, 1996; Saisorn and Wongwises, 2008; Ishii and Hibiki, 2011; Minagawa et al., 2013). Howard and Walsh (2013) theoretically derived a distribution parameter in the drift-flux void fraction model by assuming a long cylindrical gas bubble in a tube. Kurimoto et al. (2017) measured the void fraction and the pressure drop of gas-liquid flow in microchannels. Their data were compared to those provided by Hayashi et al. (2010 and 2011) and Kurimoto et al. (2013), resulting in a more reliable distribution parameter for predicting void fraction.

In Taylor flows, a thin layer of continuous flow always surrounds gas bubbles. Even though the thickness of the liquid is thin, it significantly affects the pressure drop, the transport phenomena, and the curvatures of the bubble. As illustrated in Figure 4.1, the bubble's curvatures follow a semi-hemispherical profile, at both ends (the nose and tail caps). The bubble, with curvatures at both ends follows the semi hemispherical profiles. This type of curvature is well demonstrated in both experimental and analytical data as well (e.g., Bretherton, 1961; Taylor, 1961; Schwartz et al., 1986; Irandoust and Andersson, 1989; Aussillous and Quéré, 2000; Fujioka and Grotberg, 2005; Han and Shikazono, 2009).

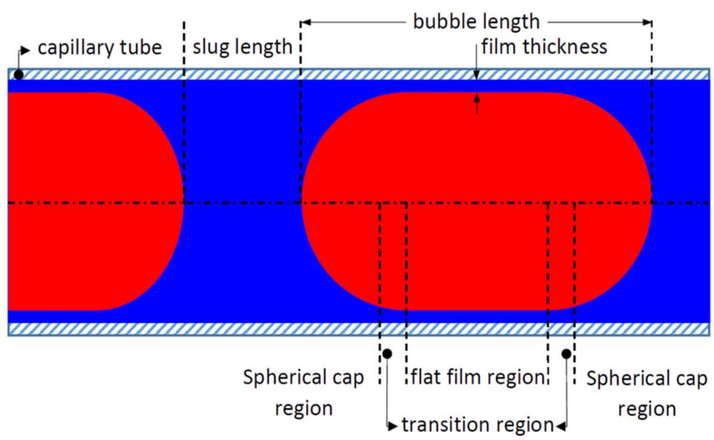

FIGURE 4.1: Schematic representation of different regions in a typical gas-liquid Taylor flow

A transition region that does not obey a semi hemispherical meniscus links the nose or tail cap with a flat / steady length of liquid film thickness. The measurement of liquid thickness in the flat region has recently appeared in major studies concerning gas-liquid flows in microchannels, which has been correlated as a function of non-dimensional numbers Ca, Re, and We. Some correlations for film thickness are compiled in Table 4.1, which will be addressed later to validate the results of the present study.

TABLE 4.1: Available correlations for the liquid film thickness in Taylor flow

Ref.	Correlation for (δ/R)	Film Thickness (μm)
Fairbrother and Stubbs (1935)	$0.5\ Ca^{1/2}$	9.82
Bretherton (1961) Schwartz et al. (1986)	$1.338\ Ca^{2/3}$	11.26
Aussillous and Quéré (2000)	$1.34\ Ca^{2/3}/(1+3.35\ Ca^{2/3})$	10.14
Kreutzer et al. (2001)	$0.36\left(1\text{-}e^{-2.13\ Ca^{0.52}}\right)$	12.63
Han and Shikazono (2009)	$1.34\ Ca^{2/3}$ $/(1+3.13\ Ca^{2/3}+0.504\ Ca^{0.672}Re^{0.589}\text{-}0.352\ We^{0.629})$	10.60
Klaseboer et al. (2014)	$1.338\ Ca^{2/3}/(1+3.732\ Ca^{2/3})$	10.00
Ni et al. (2017)	$1.34\ Ca^{2/3}$ $/(1+3.13\ Ca^{2/3}+0.504\ Ca^{0.672}Re^{0.589}\text{-}0.305\ We^{0.664})$	10.05

Two other crucial parameters to characterize two-phase flows in the capillaries are the lengths of liquid slugs and gas bubbles. The lengths remained constant through the channels in a fully developed gas-liquid flow, which have been taken into account by investigators (e.g., Laborie et al., 1999; Broekhuis et al., 2001; Garstecki et al., 2006; Qian and Lawal, 2006; Song et al., 2019). Table 4.2 presents the non-dimensional lengths of a stable liquid slug and gas bubble in terms of a constant tube diameter. The deviation in the slug lengths gathered in Table 4.2 is due to flow conditions and tube configurations.

TABLE 4.2: The lengths of liquid plug (carrying phase) and bubble / slug (dispersed phase)

Ref.	Approach	Plug Length $(L_p.D^{-1})$ (carrying phase)	Bubble / Slug Length $(L_b.D^{-1})$ (dispersed phase)
Gupta et al. (2009)	numerical	1.3	2
Qian et al. (2019)	numerical	2.07–3.02	1.56–2.06
	experimental	2.16–3.25	1.54–1.97

This chapter presents a numerical study of air / water flow in a two-dimensional microchannel. The gas bubble formation at a concentric junction is investigated to show how a gas bubble generates, propagates, and moves through the microchannel. The gas bubble profile, nose and tail curvatures, liquid film thickness, liquid slug lengths, gas bubble lengths, and steady or flat film thickness are predicted throughout the computational domain to capture the interface and transport phenomena.

A schematic of a two-dimensional microchannel is illustrated in Figure 4.2. Airflow enters at the core of the inlet cross-section and the water flow enters at an annular cross-section around the core. Airflow is in over 70% of the inlet diameter, which leads to the same volumetric flow rates for both flows in an axisymmetric microchannel. A mixture of phases exits the channel at the outlet.

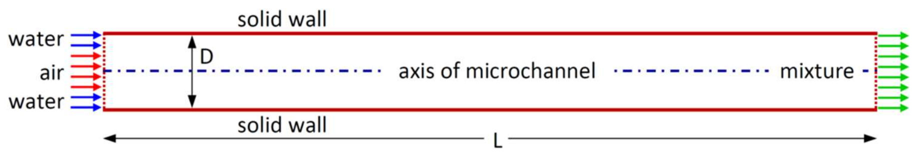

FIGURE 4.2: Schematic of two-dimensional microchannel used in the simulations

4.3 Governing Equations and Mathematical Model

An incompressible gas-liquid two-phase flow is assumed in a two-dimensional microchannel where each phase is a Newtonian fluid with constant thermophysical properties. The gas and liquid phases are immiscible and phase change does not occur within the microchannel. Therefore, the continuity and the momentum equations take on the following forms

$$\nabla \cdot \vec{u} = 0 \tag{4.1}$$

$$\frac{\partial(\rho\vec{u})}{\partial t} + \nabla \cdot (\rho\vec{u}\vec{u}) = -\nabla p + \nabla \cdot [\mu(\nabla\vec{u} + (\nabla\vec{u})^T)] + \rho\vec{g} + \overrightarrow{F_{su}} \tag{4.2}$$

where μ and ρ denote the dynamic viscosity and density, respectively. The last term in the momentum equation represents the surface tension force per unit area, which is approximately considered as a body force surrounding the interface line between phases (Brackbill et al., 1992),

$$\overrightarrow{F_{su}} = \sigma\kappa\delta\vec{n} \tag{4.3}$$

where σ, κ, δ, and $\vec{n}$ represent the surface tension force, radius of curvature or surface normal (viewed from the gas bubble), Dirac delta function, and unit normal vector on the interfacial line (from the gas to liquid phases), respectively.

The curvature of the interface line and normal vector are defined as functions of the volume fraction (α):

$$\kappa = \nabla \cdot \vec{n} \tag{4.4}$$

$$\vec{n} = \frac{\nabla\alpha}{|\nabla\alpha|} \tag{4.5}$$

The gravitational force ($\rho\vec{g}$) becomes negligible when there are both a small-diameter microchannel and dominant surface tension effects, which appear in Bond number (Bo), also known as Eötvös number (Eo),

$$\mathrm{Bo} = \frac{gD^2\Delta\rho}{\sigma} \tag{4.6}$$

where D, g, and $\Delta\rho$ represent the microchannel diameter, gravitational acceleration, and difference between phase densities, respectively. Bo is estimated to be on the order of 10^{-2}, therefore, the gravitational term is neglected in the momentum equation (Triplett et al., 1999). Different criteria has been developed to justify the dominant surface tension compared to the gravitational force, such as $\mathrm{Eo} \ll 2\pi^2$ proposed by Brauner and Maron (1992).

The momentum equation solution predicts a shared velocity field for both phases, throughout the computational domain. The accuracy of the predicted velocities, in the vicinity of the interface, can be adversely affected when the difference between superficial velocities is significant. Due to the presence of two phases in the computational domain, a volume fraction equation can be assumed,

$$\frac{\partial \alpha}{\partial t} + \vec{u} \cdot \nabla \alpha = 0 \tag{4.7}$$

The value of the volume fraction varies from 0 to 1. In Taylor flow, where a train of the gas bubbles moves in a continuous liquid flow, the importance of the volume fraction becomes insignificant inside the gas bubbles and within the liquid slugs. This parameter must be taken into account in the vicinity of the gas-liquid interface region to accurately predict the interfacial effects and momentum transport between phases.

To capture the gas-liquid interface in multiphase flows, ANSYS Fluent offers the level set and the VoF methods. The level set method assumes a value of zero as the level set of a smooth function at the interface of the two phases. The amount of the level set function is negative in the gas phase and positive in the liquid phase. The VoF method solves a single set of momentum equations and calculates the volume fraction equation of each phase within the computational domain. This approach can be used for steady and transient two-phase flows to identify the gas-liquid interface. A user-defined source term can be specified on the right side of the volume fraction equation, which ANSYS Fluent assumes to be zero by default. The volume-fraction weighted average is employed to compute the thermophysical properties of the two phases, such as density and viscosity in the governing equations. If the volume fraction of the second phase (α_2) is tracked, then the amount of property (φ) in each control volume in the two-phase flow is represented by

$$\varphi = \alpha_2 \varphi_2 + (1 - \alpha_2) \varphi_1 \tag{4.8}$$

where the subscripts 1 and 2 denote each phase. One limitation is that the solution may not converge for viscosity ratios greater than 10^3. In an arbitrary fluid volume, three cases are possible: $\alpha_i = 0$ when the volume is empty of fluid i^{th}, $\alpha_i = 1$ when the volume is full of fluid i^{th}, and $0 < \alpha_i < 1$ when the volume contains the interface between phases 1 and 2.

An explicit approach is selected to discretize time steps by a standard finite-difference interpolation scheme applied to the volume fractions at the previous time step. In particular, ANSYS Fluent can compute the values of the face fluxes near the interface line by interpolation using either an interface reconstruction or a finite volume (FV) discretization scheme. The reconstruction scheme obtains the amount of flux on the faces whenever a cell is filled with a phase. The finite volume discretization approach can only be employed with an explicit VoF method using first-order upwind or second-order upwind, and quadratic upstream interpolation for convective kinematics (QUICK) algorithms. The VoF method calculates a time step based on the transient time characteristic over a control volume, which is not necessarily equal in other governing equations. In the vicinity of the interface region, the ratio of the volume of each cell and the sum of the outgoing flux from the faces of the finite volume leads to the time taken to empty a cell. The Courant number (Co) includes the smallest such time-step,

$$\mathrm{Co}=\frac{\Delta \mathrm{t}}{\Delta \mathrm{x}/\mathrm{U}_{\mathrm{fluid}}} \tag{4.9}$$

where the $\Delta \mathrm{x}$ and $\mathrm{U}_{\mathrm{fluid}}$ represent the grid size and fluid velocity, respectively. In the following simulations, the maximum value of the Co is 0.25, and a fixed time step of 10^{-6} is employed to reduce total computational time unless it causes an unexpected increase in the Courant number. To prevent divergence of the solution in such cases, a variable time step between 10^{-6} and 10^{-7} is selected, particularly at the moments of gas bubble breakup.

Conversely, the implicit approach does not have limitations on the Courant number enabling larger grid sizes and time-steps compared to the explicit approach. However, its higher numerical diffusion in the interface region reduces the accuracy of predictions for interface curvature between phases, which are illustrated in Figure 4.3. The explicit approach allows employing a geo-reconstruct as the volume fraction discretization scheme resulting in a clear and crisp prediction of interface curvature with no numerical diffusion. The modified HRIC creates a thicker interface, a longer air bubble, and considerable numerical diffusion on the axis inside the bubble. This

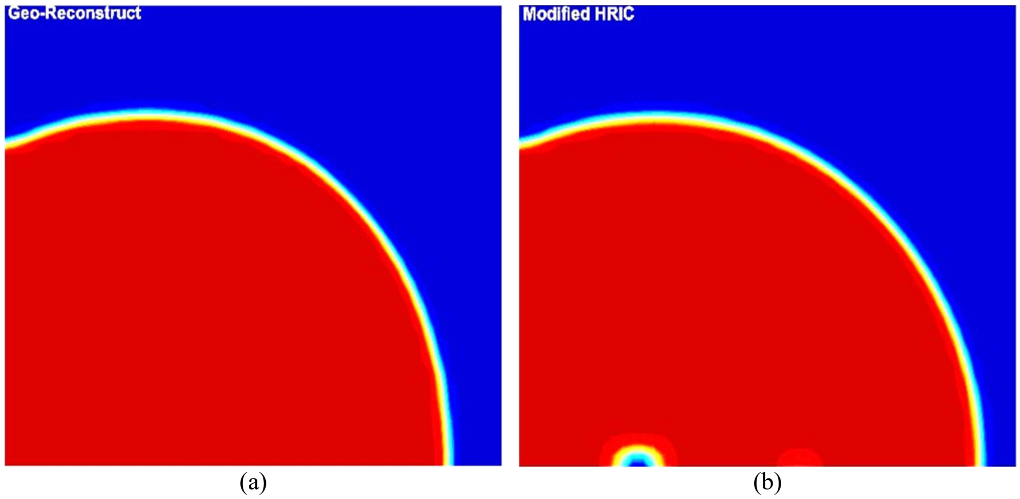

FIGURE 4.3: Prediction of the interfacial line in the introducing region by (a) explicit, and (b) implicit approaches (air is coloured red and water is coloured blue)

weakness causes divergence during air bubble breakup. Consequently, the explicit approach along with the geo-reconstruct discretization scheme are maintained for the simulations in this chapter.

Surface tension effects appear due to the interaction and attractive forces between molecules in the flow. Surface tension acts inward at the surface and is required to stay in equilibrium. The pressure gradient creates an outward force to balance surface tension force at the surface. In ANSYS Fluent, the surface tension force is modeled as a continuum surface force (Brackbill et al., 1992). In that model, a wall-adhesion angle (θ_w) or a contact angle in conjunction with the surface tension force needs to be specified. Therefore, the surface normal vector is represented by

$$\vec{n} = \hat{n}_w \cos\theta_w + \hat{t}_w \sin\theta_w \tag{4.10}$$

where $\hat{n}_w$ and $\hat{t}_w$ are the unit vectors normal and tangential to the wall. The contact angle must be specified. Some other researchers assumed dry-out on walls showing no liquid film thickness and the gas bubbles were in direct contact with the walls (e.g., He et al., 2007; Kumar et al., 2007). Conversely, significant mesh refinement near the walls is required to predict boundary layer behaviour and liquid film thickness, which was employed by Qian and Lawal (2006).

4.4 Problem Description

This study is carried out to perform a systematic numerical simulation of two-phase flow in a two-dimensional microchannel. The geometric parameters of the microchannel are depicted in Figure 4.2 where the channel diameter (D) is 0.5 mm and the channel length (L) is 5 mm. The entrance length of channels is 10 times the diameter (White, 2011), therefore, the flow is developing. The velocity inlet boundary condition is assumed for both phases. Outlet flow boundary condition is applied at the exit plane of the channel. The axisymmetric geometry of the microchannel allows the simulations to be conducted for only half of the actual computational domain resulting in lower computational time. Therefore, the axis boundary condition is set on the axis of the channel, where the radial gradients for all variables are zero. Finally, the typical no-slip boundary condition is presumed at the solid wall of the microchannel. The properties of operating fluid flows are at room temperature of 25°C (Table 4.3). The superficial velocities of the air and water are 0.245 $m.s^{-1}$ and 0.255 $m.s^{-1}$, respectively, and the average velocities of phases is 0.5 $m.s^{-1}$. These flow conditions result in Ca, Re, and We values of 0.00618, 279.93, and 1.73, respectively. Air and water flows enter the channel uniformly when the channel is filled with water at an average velocity as the initial condition for the simulations.

TABLE 4.3: Thermophysical properties of air and water used in the simulations

Fluid	Density ($kg.m^{-3}$)	Dynamic Viscosity ($kg.m^{-1}.s^{-1}$)	Surface Tension ($N.m^{-1}$)
Air	1.1845	1.849×10^{-5}	0.072
Water	997.1	8.905×10^{-4}	

4.5 Numerical Formulation

To avoid a de-coupling of velocity and pressure variables for scale-resolving simulations (SRS), a proper algorithm must be chosen considering a few key factors: geometry of the problem, properties of fluids involved, flow regime, and activated additional models (if any). The uncomplicated geometry and non-activated additional models for the laminar flow regime limit the convergence criterion by the pressure-velocity coupling. Semi-implicit method for pressure linked equations-consistent

(SIMPLEC) algorithm can be used to couple pressure and velocity fields in the Navier-Stokes equations. The SIMPLEC is designed to manipulate the proper corrections in the velocity equation by removing less significant terms (e.g., Patankar, 1980; van Doormaal and Raithby, 1984; Versteeg and Malalasekera, 2007). The rectangular computational domain, constructed from square cells, and the absence of distorted meshes allows the skewness correction to be set to 0, which significantly reduces the convergence difficulties in the simulations (ANSYS Users' Guide, 2017). The SIMPLEC algorithm computes the gradients of scalar flow parameters, such as pressure, density, volume fraction, and velocity components at the centre of cells using the values of the parameters at the cell faces. The pressure-based algorithm employs under-relaxation factors to control the values of variables at every iteration. Thus, the pressure and momentum under-relaxation factors are set to 0.3 and 0.7, respectively, to improve convergence speed and solution stability. The scaled residuals show a slightly decreasing trend as the time is marching forward and remain on the order of 10^{-6} to 10^{-7}. For time-dependent flows, ANSYS can discretize the generic transport equations by iterative and non-iterative time advancement (NITA) schemes. In the present study, a first order non-iterative time marching scheme is employed to reduce the computational time for each time-step. The NITA scheme does not require the outer iterations resulting in a significant reduction of computational expense (e.g., ANSYS Users' Guide, 2017; Armfield and Street, 1999; Perot, 1993). This scheme is also beneficial for the user-defined quantity of sub-iterations for each individual governing equation, as well as the correction tolerance, which are set to 10^{-7}.

Least squares cell-based, green-gauss cell-based, and green-gauss node-based approaches are available to calculate not only the gradient interpolation of the flow parameters, but also secondary diffusion terms and the derivatives of velocity at the centre of cell faces. An accurate method, which provides the highest accuracy, and least computational expense is highly problem-dependent (Gupta et al., 2009; ANSYS Users' Guide, 2017). The incompressibility of the flow in the present study allows the least square to be selected. For pressure interpolation, the PRESTO! scheme is not appropriate because of its high dissipation rate resulting in a delay (e.g., Patankar, 1980; Versteeg and Malalasekera, 2007). The body force weighted, second-order upwind, and geo-reconstruct schemes are assumed for pressure, momentum, and volume fraction interpolations, respectively, to achieve high accuracy predictions with minimal computational expense. The second-order upwind scheme discretizes the convective terms using two upstream nodes to calculate variables at the cell faces. Its accuracy is second-order regarding Taylor series analysis (ANSYS Users' Guide, 2017). Another scheme for momentum interpolation is QUICK. The QUICK discretizes the momentum equation and computes a higher-order value of convective variables at the cell faces. This is using a second-order central difference for diffusion terms and a third-order central difference for convection terms. This scheme is of benefit to a weighted average of second-order upwind to interpolate scalar variables at the cell faces. The QUICK scheme provides more accuracy compared to second-order upwind for computing variables on structured meshes (e.g., Patankar, 1980; Versteeg and Malalasekera, 2007). Hence, the QUICK discretization scheme has been employed in the following simulations. In addition to an appropriate time step and the number of iterations for each time step, under relaxation factor adjustment is required to make a robust solver and prevent divergence. A poor-quality mesh can make numerical instabilities during solutions. Therefore, a comprehensive mesh study has been carried out to find an independent grid size.

4.6 Grid Independence Study

Proper grid resolution is important in numerical studies to capture transport phenomena, particularly Taylor flow in microchannels. The film thickness is computed by different empirical correlations (e.g., Bretherton, 1961; Schwartz et al., 1986; Aussillous and Quéré, 2000; Han and Shikazono, 2009; Kreutzer et al., 2001; Ni et al., 2017). The film thickness ranges from 9 to 13 microns, which will be used to establish the grid size. Most of the correlations are based on experimental data of air / water two-phase flows except (Kreutzer et al., 2001). The liquid film thickness is typically measured in a fully developed Taylor flow where the measuring location is far from the junction and the film thickness remains constant. Whereas, this study is investigating developing Taylor flow in the entrance region of a microchannel.

Three discretization approaches can be considered; coarse, fine-coarse, and fine. The coarse approach divides the whole domain into square-shaped cells starting with

25 × 25 μm cells as the first trial. Figure 4.4 represents the liquid volume fraction for a coarse-size mesh of 25 microns (case I) at every 1 ms to show the air-bubbles emerging and moving downstream. Since the size of cells is greater than the approximate film thickness, the boundary layer, liquid film, and interfacial near the wall cannot be properly predicted. The boundary layer is not realized by the simulations and dry-out is observed at the wall. Furthermore, the air / water interface becomes thick, sharp, and without a semi hemispherical curvature at the rear end.

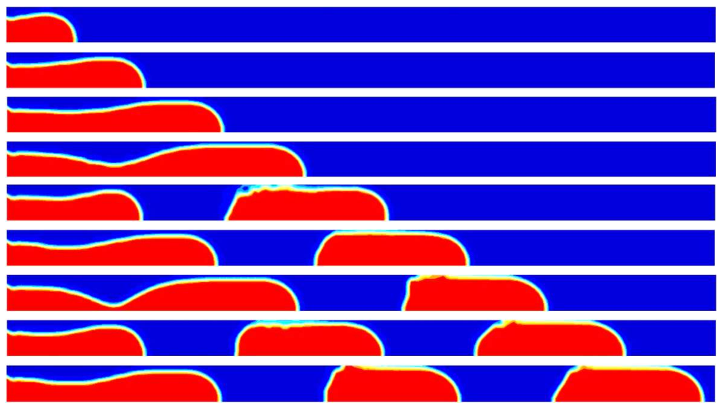

FIGURE 4.4: Liquid volume fraction plots for a uniform coarse-sized mesh of 25 μm (air is coloured red and water is coloured blue)

Four other refinements are investigated to determine an independent mesh which are presented in Table 4.4, at 9 ms. Case I is not able to capture film thickness and only two bubbles are generated over 9 ms. By halving the grid size, case II, three shorter air bubbles are observed, but the liquid film thickness is not properly predicted. Case III captures liquid film thickness successfully and three bullet-shaped air bubbles are generated over 9 ms, when the lengths of bubbles are decreased as time progresses. As illustrated in Figure 4.5, for a coarse-sized mesh of 6.25 μm, at every 1 ms, further decreasing the grid size, predicts an approximately identical flow pattern. The grid refinement from case III to IV makes a 3.7% variation, while from case IV to V leads to a 1.4% variation. The flow patterns, lengths and quantity of slugs and plugs are not dependent on the mesh refinement further than case IV. Therefore, the following numerical predictions are conducted with the mesh refinement of case IV.

A time history of air bubble formation, growing, necking, breaking off, and moving through the channel is illustrated in Figure 4.5 for mesh case IV. The semi

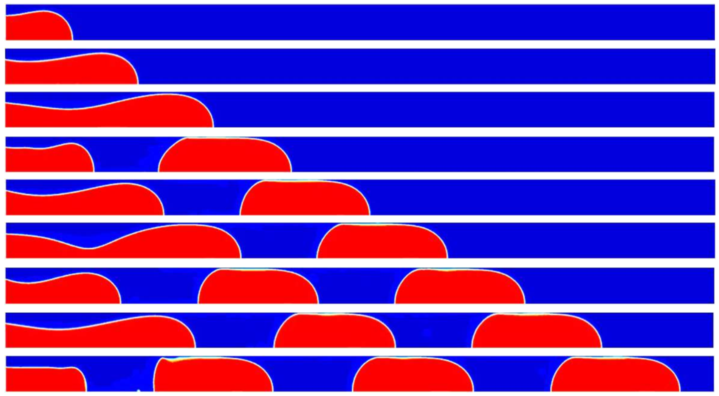

FIGURE 4.5: Liquid volume fraction plots for a uniform coarse-sized mesh of 6.25 μm (air is coloured red and water is coloured blue)

hemispherical nose meniscus remains constant, but the tail meniscus is deforming from an approximate flat cap to semi hemispherical as the bubble moves downstream. The liquid film thickness is captured throughout the channel. The liquid film thickness involves only two grids and it is not sufficient to capture the boundary layer and transport phenomena properly. Consequently, mesh refinement over a thickness of 15 μm along the channel's wall is required to find an adequate size of grids, which estimates the thickness accurately and prevents non-physical pressure jumps across the interface (Gupta et al., 2009).

TABLE 4.4: Mesh independence for core region

Case	**Mesh Size** (μm)	**Bubble Breakup** (ms)			**Film Thickness** (μm)	**Slug Length** ($L_s.D^{-1}$)		**Bubble Length** ($L_b.D^{-1}$)		
		3rd	**2nd**	**1st**		**2nd**	**1st**	**3rd**	**2nd**	**1st**
I	25	–	7.04	4.23	fully dry-out	–	1.32	–	2.11	1.89
II	12.5	8.84	6.08	3.74	partially dry-out	1.22	1.16	1.72	1.74	1.91
III	8.33	8.78	6.29	3.62	10.41	1.14	1.12	1.70	1.72	1.84
IV	6.25	8.45	6.10	3.57	10.24	1.12	1.09	1.68	1.71	1.82
V	5	8.43	6.08	3.52	10.23	1.12	1.10	1.67	1.71	1.81

In the fine-coarse approach, the presence of the solid walls encourages the mesh generation process to employ a non-uniform distribution perpendicular to the flow direction. Over a thickness of 15 μm along with the channel's wall, 5, 6, and 7 cells are considered to enable the simulations of capturing boundary layer and film thickness successfully. The length of cells is set to a constant value of 6.25 μm. The fine grid near the wall and the coarse grid in the core region of the microchannel allow accurate predictions of film thickness and also reduce the computational time. The corresponding total numbers of cells are 34,400, 35,200, and 36,000. With these meshes, a linear slope of the interface line between two phases at the inlet can be assumed to calculate the advection of each phase at the cell faces. The refinements have resulted in the average film thicknesses of 11.67, 10.94, and 10.85 μm for mesh sizes of 3, 2.5, and 2.43 μm, respectively (see Table 4.5). Since an insignificant change of 0.8% is predicted by mesh refining from 2.5 to 2.43 μm, the grid size of 2.5 μm is selected. This mesh refinement prevents non-physical pressure jump in uniform liquid film region as observed by Gupta et al. (2009) and results in minimum false diffusion and truncation error (e.g., Patankar, 1980; Versteeg and Malalasekera, 2007).

TABLE 4.5: Mesh independence for near the wall region

Case	**Mesh Size** (μm)	**Film Thickness** (μm)			**Slug Length** ($L_s.D^{-1}$)		**Bubble Length** ($L_b.D^{-1}$)		
		3rd	**2nd**	**1st**	**2nd**	**1st**	**3rd**	**2nd**	**1st**
I	3	12.50	11.50	11.00	1.15	1.14	1.79	1.76	1.85
II	2.5	10.75	11.14	10.94	1.16	1.14	1.78	1.75	1.85
III	2.43	10.62	11.10	10.83	1.16	1.13	1.78	1.75	1.86

As illustrated in Figure 4.6, the interface line between phases occupies the entire computational domain as the air bubbles move downstream. It means that mesh refinement should be applied over the domain entirely with equal-sized cells in both directions. A square-shape mesh of 2.5 μm is utilized to determine possible changes in the flow pattern and the quantitative aspects of problem. The results show non-remarkable deviations and therefore, the third approach is not a proper mesh generation approach. Therefore, a square coarse grid can be adopted throughout the core region and a refined grid near the wall of the channel for the modelling of gas-liquid two-phase flow.

The computational domain is discretized into 35,200 cells and the simulations run on a DELL workstation with Intel® Xeon® E5-1650 v3 @3.5 GHz processor. CPU cash and memory (RAM) are 15 MB and 32 GB, respectively. The average time-marching for a time-step calculation is 2.87 seconds and each simulation takes approximately seven hours to complete.

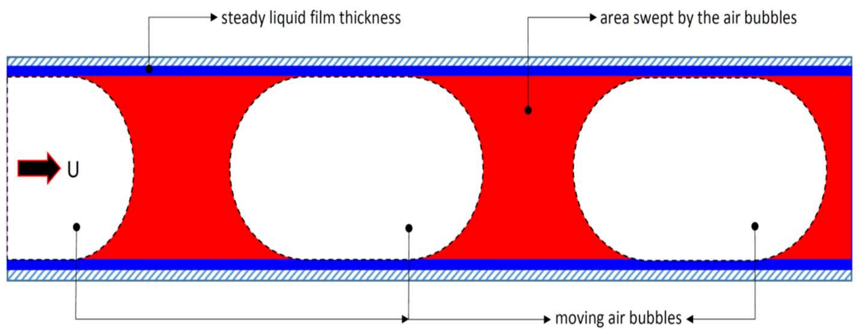

FIGURE 4.6: Schematic representation of the area swept by the moving air bubbles through the microchannel

Figure 4.7 shows a time history of volume fraction for a non-uniform fine-sized mesh, case II, at every 1 ms. A train of air bubbles (coloured red) follows a hydrodynamics evolution process involving emersion, elongation, filling, necking, breaking off, and moving. The bullet-like bubbles travel downstream with an insignificant change in the nose curvature, while the rear curvature experiences an undulation over one millisecond after breakup moment. According to Table 4.5, maximum variations of 5%, 1.7%, and 3.6% are observed for bubble length, slug length, and film thickness, respectively.

4.7 Results and Discussion

A developing Taylor flow causes some ripples at the liquid film, which are shown by the enlarged views of the film regions of three air bubbles in Figure 4.8. The ripples disappear as the bubble moves downstream, due to time marching.

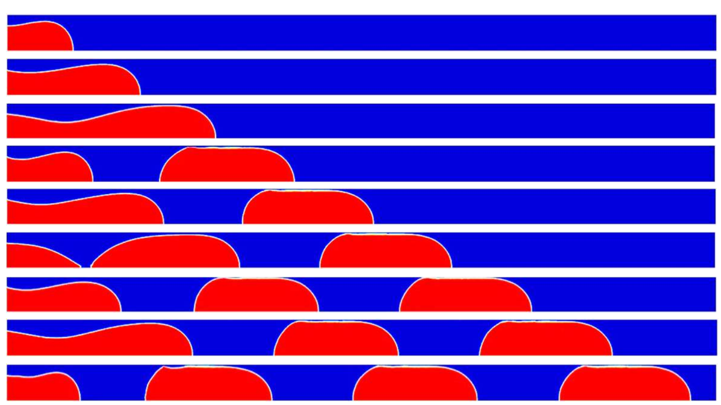

FIGURE 4.7: Liquid volume fraction plots for a non-uniform fine-sized mesh, case II (air is coloured red and water is coloured blue)

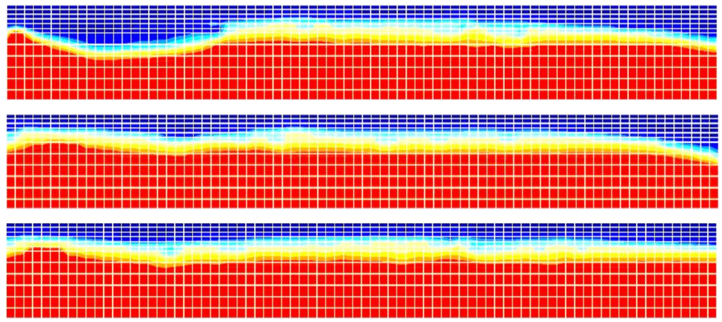

FIGURE 4.8: Zoomed-in views of liquid film thickness regions of the 3rd, 2nd, and 1st air bubbles from top to down, respectively, at 9 ms

The length of the flat film region becomes longer (the nose and tail transition lengths become shorter) as the bubble travels to the outlet, as presented in Table 4.6. The variations of the lengths of transition and flat regions become smaller as the bubble moves. Two spheres at the nose and tail with a radius of R_1 and R_2, respectively can approximately fit the semi hemispherical meniscus at the nose and rear parts of the bubbles. As is also presented in Table 4.6, the radius of the nose curvature is less than that of the tail but the bullet-like profile of the second bubble remains almost constant.

TABLE 4.6: Predicted air bubble shapes and geometric details

Bubble	**Meniscus Radius** (μm)		**Transition Length** (μm)		**Flat Region Length** (μm)
	R_1	**R_2**	**nose**	**tail**	
1st	210	240	120	109	502
2nd	210	240	166	158	399
3rd	200	240	227	275	265

As illustrated in Figure 4.9, the highest axial velocity is at the centre of the bubbles along the axis of the microchannel. At the caps of the bubbles, the axial velocity component is lower and the radial velocity component is higher at the bubble's centre increased. This behaviour was previously found by Gupta et al. (2009) using vectors and discussed by Fukagata et al. (2007) using streamlines. For developing flow, only a minimal change in axial velocity is predicted. A localized backflow is also observed at the tail transition region due to an adverse pressure gradient at that region which was also predicted by Gupta et al. (2009).

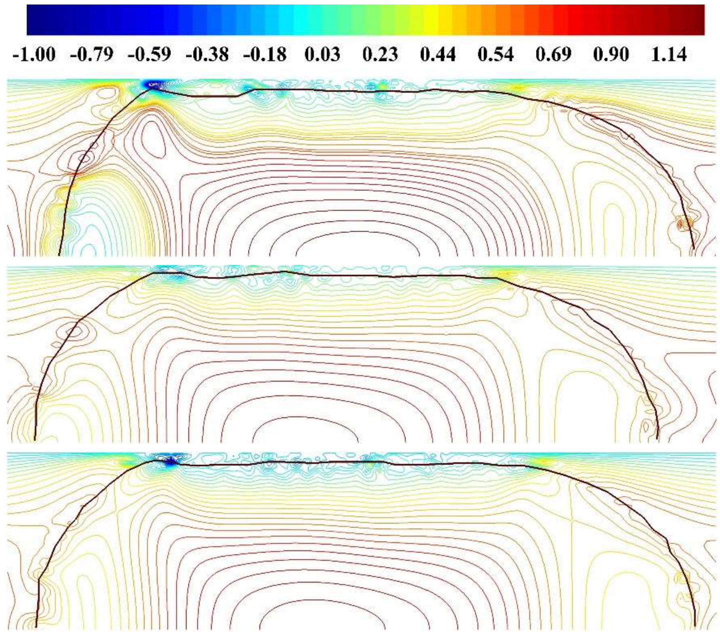

FIGURE 4.9: Axial velocity component contour inside and outside of the 3rd, 2nd, and 1st air bubbles from top to down, respectively, at 9 ms (thick solid line indicates the curvature of the bubbles)

Two homogenous and separated flow models have been employed by researchers to predict the frictional pressure drop. The first model postulates the same velocity for both gas and liquid phases, which implies that the slip ratio at the interactive boundaries is equal to one. This model considers two or more different phases as a single phase. The values of the flow properties are dependent on the quality, while the frictional pressure drop can be computed by single-phase flow theory derived by White (2011) as follows:

$$f = \left(\frac{1}{2}\frac{D}{\rho U^2}\right)\left(\frac{dp}{dx}\right)_L \tag{4.11}$$

where D, L, U, and x indicates the diameter of the tube, the length, the mean velocity $(U_{GS} + U_{LS})$, and the axial direction of the channel. The Hagen-Poiseuille equation is a physical law to compute the pressure drop of a Newtonian and incompressible flow through a long and circular tube with a constant cross-section area. The flow regime remained laminar due to the Reynolds number of the microflows, where the friction factor becomes $f = 16/Re$ for round tubes and the Eq. (4.11) can be rearranged in the following way.

$$\Delta p = \frac{16}{Re}\left(\frac{1}{2}\rho U^2\right)\frac{4L}{D} \tag{4.12}$$

In Taylor flow, the pressure drop is affected by the curvatures of the slugs, the slug and plug lengths, and steady film thickness. Figure 4.10, shows the pressure distribution on the axis of the microchannel for gas-liquid Taylor flow and at 9 ms. A volume fraction plot has been affixed to this figure where the dispersed phase is coloured red and the continuous phase is coloured blue.

The pressure drop over a unit cell can also be described by three components, which has been proposed by Kreutzer et al. (2005b), Fouilland et al. (2010), and Ni et al. (2017):

$$\Delta p_{uc} = \Delta p_p + \Delta p_f + \Delta p_{cap} \tag{4.13}$$

where the last two terms in Eq. (4.13) represent the total pressure drop over the gas bubble. Hagen-Poiseuille Eq. (4.12) can calculate the pressure drop over the liquid plug in fully developed flow without internal circulation as below:

$$\frac{\Delta p_p}{L_p} = \frac{32\mu U}{D^2} = 32\ Ca\ \frac{\sigma}{D^2} \tag{4.14}$$

According to Eq. (4.14), the pressure drop over the liquid plug is 56,955 Pa/m where the corresponding value from the present numerical simulation over two halves of adjacent liquid plugs to the first bubble is 60,345 Pa/m indicating an acceptable agreement with 5% deviation. The difference becomes much more for the second unit cell where the flow regime is slightly further away from fully developed conditions. As illustrated in Figure 4.10, the pressure distributions over the steady film region are almost constant and Δp_f is negligible, which agrees with Fouilland et al. (2010).

Conversely, the normal stress at the interface within the steady film region is no longer present and the Laplace pressure at the interface can predict the pressure difference. The pressure difference between inside the gas bubble and the liquid at the wall is $\sigma/R_b = 301$ Pa, which the corresponding value from the simulation for the first unit cell is so close with less than 2% deviation. As the pressure distribution at the wall, within the flat film region, shows fluctuations due to the interactions between the wall and interface (not displayed here), its mean value is computed by integrating over the flat region. However, the interfacial pressure difference in the hemispherical nose region of the first air bubble is of the order of $2\sigma/R_b = 602$ Pa, whereas the simulations predict 513 Pa. The difference is due to the developing conditions and the assumption of non-exact hemispherical shape of the gas bubble. The last term in Eq. (4.13) can be calculated by lubrication theory discussed by Bretherton (1961) assuming insignificant inertia forces and exact semi-hemispherical profile at both caps of the bubble.

$$\Delta p_{cap} = 7.16 \frac{(3\ \mathrm{Ca})^{2/3} \sigma}{D} \tag{4.15}$$

The numerically predicted bubble cap pressure difference is approximately 61 Pa compared to 72 Pa predicted by Eq. (4.15). This deviation can also be attributed to the significant difference between the nose and the rear meniscus, non-exact semi hemispherical cap curvatures, and the inertia effects. Consequently, the pressure drop per a unit length is 60,700 Pa.

4.8 Conclusions

In this chapter, numerical predictions of air / water Taylor flow, for developing flow, in a microchannel with a circular cross-sectional area were investigated. A mesh independence study showed that the mesh size caused different interactions between two phases and the channel wall, i.e., dry-out, partially dry-out, and fully wetted to explain whether the wall was kept dry or wet. The new numerical predictions showed that the liquid film thickness of the bubbles remained almost constant, but the length of the flat film region increased as the air bubble moved downstream. The results of this study provide useful new insights into gas-liquid Taylor flow.

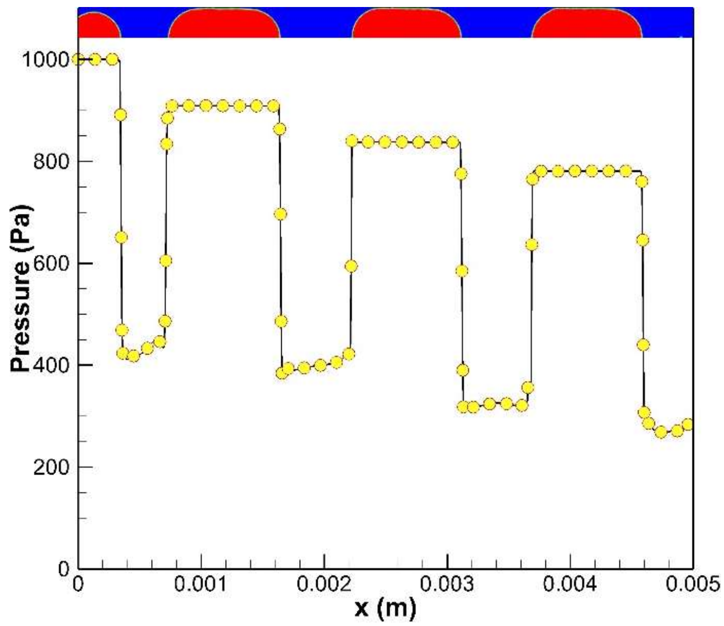

FIGURE 4.10: Pressure distribution on the axis of the microchannel at 9 ms

Chapter 5

Characterization of Gas-Liquid and Liquid-Liquid Microflows[1]

5.1 Overview

This chapter presents a CFD-based simulation method for air / water and water / dodecane Taylor flows through an axisymmetric microchannel with a circular cross-sectional area. A systematic analysis is conducted by exploring the effects of different superficial velocities and apparent viscosities on the hydrodynamics of a slug flow regime. A concentric junction is employed to make bubbles of air in a continuous flow of water and slugs of water in a continuous flow of dodecane oil. A time-history study is conducted to predict the air-bubble and water-slug evolution processes, in particular at the moment of slug breakup. The results show that the larger apparent viscosity ratio of phases involved in the liquid-liquid flow generates a more stable interface. However, the liquid slug length is less and film thickness is slightly larger in liquid-liquid compared to gas-liquid flow. Furthermore, variations in gas and liquid holdups are correlated by the superficial velocity ratio. The numerical analysis developed in this chapter is in good agreement with the correlations and data in the literature.

[1] This chapter is written based on:
Etminan, A., Muzychka, Y.S., Pope, K. (2021c) CFD modelling for gas-liquid and liquid-liquid Taylor flows in the entrance region of microchannels. In the ASME Fluids Engineering Division Summer Meeting. 85307, V003T08A009.
DOI: 10.1115/FEDSM2021-64172

5.2 Introduction

Micro-sized energy-related applications, such as lab-on-a-chip devices, heat exchangers, fuel cells, and microreactors can be improved with the enhanced heat transfer characteristics of multiphase flow or microflow. The patterns of gas-liquid (GL) and liquid-liquid (LL) two-phase flows in microchannels are highly problem-dependent. The type of channels, phase superficial velocities, phase densities, apparent viscosities, surface tensions, and transport phenomena, such as momentum, heat, and mass dictate the pattern of multiphase flow. Various flow patterns, such as bubbly, Taylor, churn, annular, stratified, and wavy have been reported by investigators (e.g., Kreutzer et al., 2005c; Fouilland et al., 2010; Deendarlianto et al., 2019). A segmented flow, also known as Taylor flow, is a GL or LL two-phase flow in microchannels and microcapillaries as long as the phases are separated by an interface. In this type of microflow, due to insignificant inertia forces compared to viscous and surface tension forces, the flow regime remains laminar, which simplifies the numerical simulations by omitting turbulence modelling. Many scholars have also considered GL and LL Taylor flows to investigate the process of slug formation and transport phenomena in different flow circumstances (e.g., Gupta et al., 2009; Qian et al., 2019).

Two different methods may be considered in numerical analysis when describing the motions of fluids in two-phase flows: continuous fluid (Eulerian) and discrete particle (Lagrangian). The first method solves the governing partial differential equations to predict the motion of the continuum-based fluid flow, while the second method follows the movement of fluid particles or molecules to predict fluid flow and heat transfer. The physics of flow including momentum, heat, and mass transfers can be described by the conversation equations as the governing equations. An additional advection equation is required to predict the interface between different phases involved. Over the past few decades, several methods have been developed to determine the interaction between phases, such as volume of fluid (VoF), level set, phase field, and lattice Boltzmann method (LBM). The VoF method predicts the interfacial curvatures using the Euler method (Sontti and Atta, 2017).

5.3 Problem Description

This chapter presents a CFD-based analysis to study gas-liquid and liquid-liquid two-phase flows in an axisymmetric microchannel with a circular cross-sectional area. Figure 5.1a illustrates a typical segmented flow with a concentric junction to introduce dispersed flow. The axisymmetric geometry of the microchannel allows the simulations to proceed for only half of the actual computational domain resulting in lower computational time. The simulations are conducted on a two-dimensional section A-A, as illustrated in Figure 5.1b. The channel radius (D/2) is 0.25 mm and the channel length (L) is 5 mm. The two-phase flow never approaches a fully developed flow and is expected to find changes in slug shapes and other parameters along the channel axis as the flow proceeds. The velocity inlet boundary condition is assumed for both phases and an outlet flow boundary condition is applied at the exit plane of the channel. Axis boundary condition is applied on the axis of the channel, where the radial gradients for all variables are set to zero. The no-slip boundary condition is presumed at the solid wall of the microchannel. The simulations are conducted on a horizontal plane, where the gravity acceleration is negligible due to an insignificant impact on the Taylor flow in microchannels (Gupta et al., 2009; Sontti and Atta, 2017).

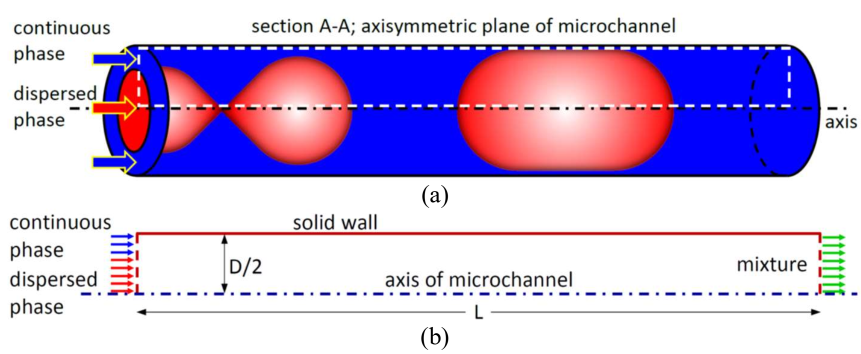

FIGURE 5.1: Schematic representations of (a) Taylor bubble or slug formation by a concentric circular junction in microchannel, (b) computational domain and flow configuration at section A-A

The properties of operating fluids at room temperature of 25 °C are presented in Table 5.1. The superficial velocities of the phases range from 0.1 m.s^{-1} to 0.4 m.s^{-1} by a step of 0.05 m.s^{-1}. These flow conditions result in a capillary number (Ca), Reynolds number (Re), and Weber number (We) values of 0.00618, 279.93, and 1.73, respectively, for the GL case and 0.01336, 135.67, and 1.81, respectively, for the LL case. The phases enter the channel uniformly when the channel is filled with water for the GL case and dodecane for the LL case at an average velocity of 0.5 m.s^{-1} as the initial condition prior to running the simulations.

TABLE 5.1: Properties of the dispersed and continuous phases used in the simulations

Fluid	Density (kg.m^{-3})	Dynamic Viscosity (kg.m^{-1}.s^{-1})	Surface Tension (N.m^{-1})
Air	1.1845	1.849×10^{-5}	
Water	997.1	8.905×10^{-4}	0.072
Dodecane	754.3	0.00139	0.052

In Taylor flows, gas bubbles or liquid slugs always are surrounded by a thin layer of carrier fluid. Although the thickness of the liquid film is very thin, it significantly affects the pressure drop, transport phenomena, and bubble / slug profiles. As displayed in Figure 5.2, the bubble or slug curvatures follow an approximately semi-hemispherical profile, at two ends (the tail and nose caps). Transitional regions link the spherical cap regions with a flat / uniform film region. These types of curvatures are well demonstrated in experimental and analytical studies. A unit cell can consist of two halves of subsequent slugs and a full plug or two halves of subsequent plugs and a full slug, the latter of which is illustrated in Figure 5.2 by a dashed outline and employed by many researchers to show the variations of flow parameters (Gupta et al., 2009; Sontti and Atta, 2017). The measurement of liquid film thickness in the flat region has been appearing in the majority of studies concerning gas-liquid and liquid-liquid segmented flows in microchannels, which can be a function of non-dimensional numbers Ca, Re, and We.

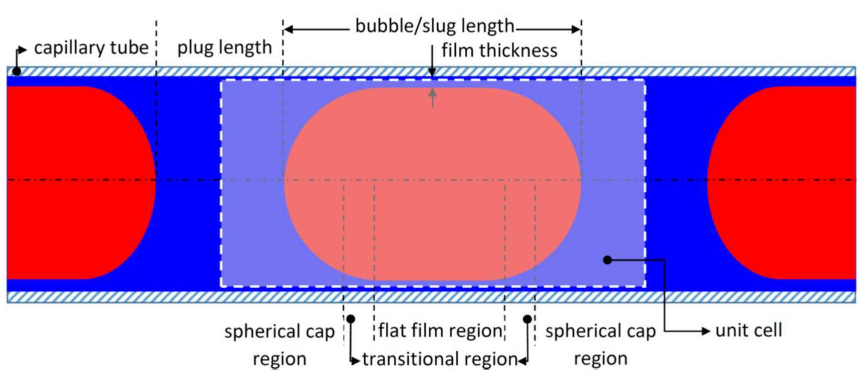

FIGURE 5.2: Different regions of a typical Taylor flow (dispersed slugs are coloured red and carrying flow is coloured blue)

5.4 Numerical Model and Volume of Fluid (VoF) Method

In this chapter, two incompressible GL and LL two-phase flows are assumed in an axisymmetric circular microchannel where each phase is a Newtonian fluid with constant thermophysical properties. The gas and liquid phases are immiscible and phase change does not occur within the microchannel. Therefore, the continuity and momentum equations take on the following forms

$$\frac{\partial \rho}{\partial t} + \nabla.(\rho\vec{u}) = 0 \tag{5.1}$$

$$\frac{\partial(\rho\vec{u})}{\partial t} + \nabla.(\rho\vec{u}\vec{u}) = -\nabla p + \nabla.[\mu(\nabla\vec{u} + (\nabla\vec{u})^{T})] + \rho\vec{g} + \vec{F}_{su} \tag{5.2}$$

where μ and ρ denote the dynamic viscosity and density, respectively. The last term in the momentum equation represents the surface tension force per unit area, which is approximately considered as a body force surrounding the interfacial line between phases (Brackbill et al., 1992):

$$\vec{F}_{su} = \sigma\kappa\delta\vec{n} \tag{5.3}$$

where σ, κ, δ, and $\vec{n}$ represent the surface tension force, radius of curvature or surface normal (viewed from the gas bubble or liquid slug), the Dirac delta function, and unit normal vector on the interfacial line (from the gas to liquid phases), respectively. The normal vector and the curvature of the interfacial line are defined as functions of the volume fraction (α):

$$\vec{n} = \frac{\nabla\alpha}{|\nabla\alpha|} \tag{5.4}$$

$$\kappa = \nabla.\vec{n} \tag{5.5}$$

The gravitational force ($\rho\vec{g}$) becomes negligible when there are both a small-diameter microchannel and dominant surface tension effects, which appear in Bond number (Bo), also known as Eötvös (Eo) number,

$$\mathrm{Bo} = \frac{gD^2\Delta\rho}{\sigma} \tag{5.6}$$

where D, g, and $\Delta\rho$ represent the microchannel diameter, gravitational acceleration, and difference between phase densities, respectively. Under circumstances of the present study, Bo is estimated to be on the order of 10^{-2} that is significantly less than the Bond number limit of 0.842 reported by Bretherton (1961). Therefore, the gravitational term is negligible.

The momentum equation solution predicts a shared velocity field for both phases, throughout the computational domain. The accuracy of the predicted velocities, in the vicinity of the interface, can be adversely affected when the difference between superficial velocities is significant. Due to the presence of two phases in the computational domain, and the absence of any mass transfer between phases, a volume fraction or void fraction continuity equation can be assumed,

$$\frac{\partial\alpha}{\partial t} + \vec{u}.\nabla\alpha = 0 \tag{5.7}$$

The value of the volume fraction varies from 0 to 1. In Taylor flow, where a train of the gas bubbles moves in a continuous liquid flow, the importance of the volume fraction becomes insignificant inside the gas bubbles and within the liquid plugs. This parameter must be taken into account in the vicinity of interface to accurately predicts the interfacial effects and momentum transport between phases.

To capture the GL and LL interfaces in multiphase flows, ANSYS Fluent offers the level set and the VoF methods. The level set method can be used for steady and transient two-phase flows assuming a value of zero as the level set of a smooth function at the interface of the two phases. The amount of the level set function is negative in the gas phase and positive in the liquid phase. The VoF method solves a single set of momentum equations and calculates the volume fraction equation of each phase within the computational domain. A user-defined source term can be specified on the right side of the volume fraction equation, which ANSYS Fluent assumes to be zero by default. The volume-fraction weighted average is employed to compute the thermophysical properties of the two phases, such as density and viscosity in the governing equations. If the volume fraction of the second phase (α_2) is tracked, then the amount of property (φ) in each control volume in the two-phase flow is presented by

$$\varphi = \alpha_2\varphi_2 + (1 - \alpha_2)\varphi_1 \tag{5.8}$$

where the subscripts 1 and 2 denote either gas or liquid phase. One limitation is that the solution may not converge for viscosity ratios greater than 10^3. In an arbitrary fluid volume, three cases are possible: $\alpha_i = 0$ when the volume is empty of fluid i^{th}, $\alpha_i = 1$ when the volume is full of fluid i^{th}, and $0 < \alpha_i < 1$ when the volume contains the interface between phases 1 and 2.

An explicit approach is selected to discretize time steps by a standard finite-difference interpolation scheme applied to the volume fractions at the previous time step. In particular, ANSYS Fluent can compute the values of the face fluxes near the interfacial line by interpolation either using an interface reconstruction or a finite volume (FV) discretization scheme. The reconstruction scheme obtains the amount of flux on the faces whenever a cell is filled with a phase. The finite volume discretization approach can only be employed with an explicit VoF method using first-order upwind or second-order upwind, and quadratic upstream interpolation for convective kinematics (QUICK) algorithms. The VoF method calculates a time step based on the transient time characteristic over a control volume, which is not necessarily equal in other governing equations. In the vicinity of the interface region, the ratio of the volume of each cell and the sum of the outgoing flux from the faces of the finite volume leads to the time taken to empty a cell. The Courant number (Co) includes the smallest such time-step defined by

$$\mathrm{Co} = \frac{\Delta t}{\Delta x / U_{\mathrm{fluid}}} \tag{5.9}$$

where the Δx and U_{fluid} represent the grid size and fluid velocity, respectively. In the following simulations, the maximum value of the Co is 0.25, and a fixed time step of 10^{-6} is employed to reduce total computational time unless it causes an unexpected increase in the Courant number and problem divergence. To prevent divergence of the solution in such cases, a variable time step between 10^{-6} and 10^{-7} is selected, particularly at the moments of breakups.

Surface tension effects appear due to attractive and repulsive forces between molecules in the flow. Surface tension acts inward at the surface and is required to stay in equilibrium. The pressure gradient creates an outward force to balance surface tension force at the surface. In ANSYS Fluent, the surface tension force is modelled as a continuum surface force. In that model, a wall-adhesion angle (θ_w) or a contact angle in conjunction with the surface tension force needs to be specified. Therefore, the surface normal vector is represented by

$$\vec{n} = \hat{n}_w \cos\theta_w + \hat{t}_w \sin\theta_w \tag{5.10}$$

where $\hat{n}_w$ and $\hat{t}_w$ are the unit vectors normal and tangential to the wall. The contact angle must be specified. Some other researchers assumed dry-out on walls showing no liquid film thickness and the gas bubbles were in direct contact with the walls. Conversely, significant mesh refinement near the walls is required to predict boundary layer behaviour and liquid film thickness, which was employed by Gupta et al. (2009).

5.5 Solution Methodology

The uncomplicated geometry and non-activated additional models for the laminar flow regime limit the convergence criterion by the pressure-velocity coupling. Semi-implicit method for pressure linked equations-consistent (SIMPLEC) algorithm is used to couple pressure and velocity fields in Navier-Stokes equations. The

SIMPLEC is designed to manipulate the proper corrections in the velocity equation by removing less significant terms. The rectangular computational domain, constructed from square cells, and the absence of distorted meshes allows the skewness correction to be set to 0, which significantly reduces the convergence difficulties in the simulations. The SIMPLEC algorithm computes the gradients of scalar flow parameters, such as pressure, density, volume fraction, and velocity components at the center of cells using the values of the parameters at the cell faces. The pressure and momentum non-iterative under relaxation factors are set to 1 and the correction tolerances are set to 10^{-7}, to improve convergence speed and solution stability. The scaled residuals show a slightly decreasing trend as time is marching forward and remain on the order of 10^{-6} to 10^{-7}. For time-dependent flows, ANSYS can discretize the generic transport equations by iterative and non-iterative time advancement (NITA) schemes. In the present study, a first order non-iterative time marching scheme is employed to reduce the computational time for each time-step. The NITA scheme does not require the outer iterations resulting in a significant reduction of computational expense. This scheme is also beneficial for the user-defined quantity of sub-iterations for each individual governing equation.

The incompressibility of the flow in the present study allows the least square to be selected. The body force weighted, second-order upwind, and geo-reconstruct schemes are assumed for pressure, momentum, and volume fraction interpolations, respectively, to achieve high accuracy predictions with minimal computational expense. The second-order upwind scheme discretizes the convective terms using two upstream nodes to calculate variables at the cell faces. Its accuracy is second-order regarding Taylor series analysis. The QUICK scheme is selected for momentum interpolation. The QUICK scheme discretizes the momentum equation and computes a higher-order value of convective variables at the cell faces. This is using a second-order central difference for diffusion terms and a third-order central difference for convective terms. This scheme is of benefit to a weighted average of second-order upwind to interpolate scalar variables at the cell faces. The QUICK scheme provides more accuracy compared to second-order upwind for computing variables on structured meshes.

A mesh independence study is conducted resulting in a fine rectangular mesh size of 2.5 × 6 μm for near the wall of the channel region of 15 μm thickness and a square mesh size of 6 × 6 μm for the core region of the channel was previously suggested by Gupta et al. (2009) and Etminan et al. (2021b). The fine grid sizes near the wall and the coarse grid in the core region of the microchannel allow accurate predictions of film thickness and also reduces the computational time (further details of mesh generation and grid independence are in Etminan et al., 2021b).

5.6 Results and Discussion

The present study aims to investigate the effects of different superficial velocity ratios on the hydrodynamics of GL and LL Taylor flows. Experimental and numerical data from the literature are used to validate the present numerical analysis. Due to the flow conditions, the capillary numbers are so low that a very thin layer of liquid would be expected between the dispersed slugs and the microchannel's wall. The interfacial effects in this thin liquid region significantly affect the flow pattern and pressure drop, which are discussed in the following.

5.6.1 Slug Formation Process

Evolutions of air-bubble and water-slug formations and reshaping with time are illustrated in Figure 5.3 for a superficial velocity of 0.25 m.s^{-1}. A five-stage slug formation process involves introducing, expanding, contracting, necking, and breakup. As shown in Figure 5.3, the length of the water-slug is less than that of the air-bubble and the water-plug is more elongated than the dodecane-plug. The radii of the dispersed air-bubble and water-slug are controlled by the channel's radius, surface tension, shear stress, and volumetric flow rate ratio of phases. Since density difference in the GL case is much more than the LL case; $\Delta\rho_{GL} = 4.1\Delta\rho_{LL}$, the volume of the bubbles becomes greater than the slugs. The small capillary diameter enforces the air-bubbles to be more elongated compared to water-slugs (Figure 5.3). The apparent viscosity ratio of the LL flow is significantly greater than that of the GL; $\mu_w/\mu_d = 30.87\,\mu_a/\mu_w$. It causes a more stable interfacial boundary, particularly near the microchannel wall. In addition, in the near wall region, the contribution of cohesion

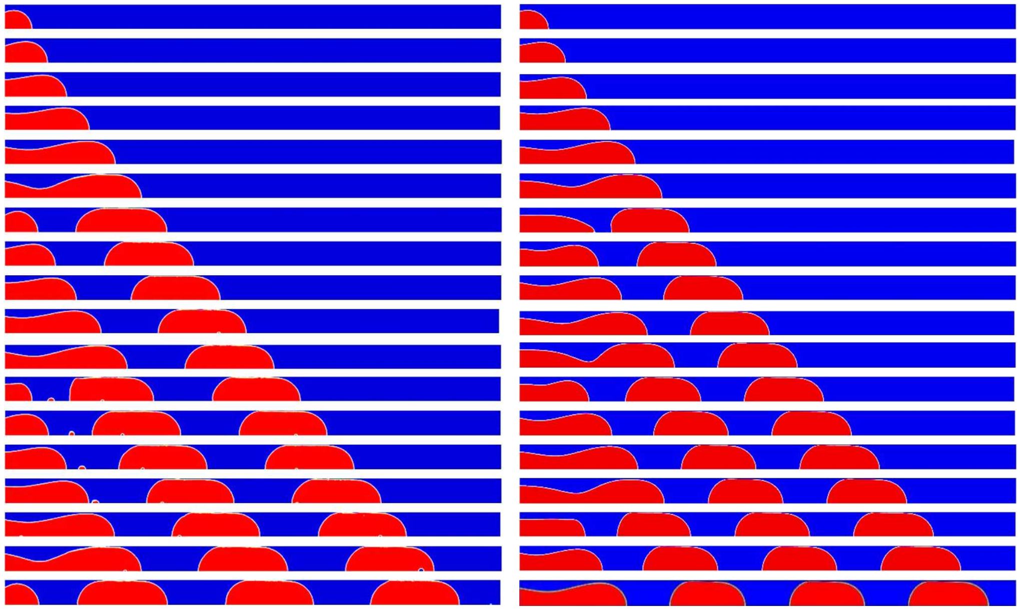

FIGURE 5.3: Time-history of (a) air-bubble and (b) water-slug evolutions at every 0.5 ms for superficial velocity ratio of unity (air is coloured red and water is coloured blue for the GL and water is coloured red and dodecane is coloured blue for the LL)

and adhesion forces cause appreciable diffusion around the air-bubble and a non-physical pressure drop. In GL flow, more numerical diffusion is observed, resulting in very small bubbles on the axis of the channel, after necking and breakup.

5.6.2 Breakup of Slugs

The apparent viscosity ratio of the LL flow is considerably more than for GL flow. A high apparent viscosity moves the breakup point further downstream and also causes a semi-hemispherical rear meniscus in LL flow faster than GL flow (Figure 5.4). Due to the very low capillary number, the ratios of the surface tension and viscous forces (1/Ca) are on the order of 161.81 and 74.85 for GL and LL flows, respectively, which verifies a significant role of surface tension in breakup. Since the cross-sectional area of the microchannel is occupied by an air-bubble or water-slug, a sudden pressure loss occurs at the moments of necking and breakup. The boundary layer effects and flow resistance within the film region cause the pressure drop.

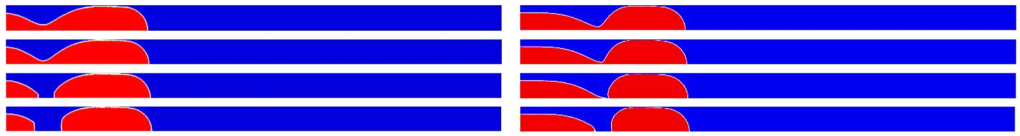
(a) (b)

FIGURE 5.4: Necking and breakup processes of (a) air-bubble and (b) water-slug at every 0.05 ms for superficial velocity ratio of unity (air is coloured red and water is coloured blue for the GL and water is coloured red and dodecane is coloured blue for the LL)

5.6.3 Hydrodynamics of Gas-Liquid and Liquid-Liquid Taylor Flows

Two other crucial parameters to characterize two-phase flows in capillaries are the lengths of slugs and plugs. The lengths remained constant through the channels in a fully developed Taylor flow. Figure 5.5 depicts the volume fraction contours for GL and LL flows at superficial velocities varying from 0.1 m.s^{-1} to 0.4 m.s^{-1}, with a step of 0.05. The slugs are generated at an approximately constant frequency for each superficial velocity. As the velocity of the dispersed phase is enhanced, the slug lengths in both cases are increased. An increase in dispersed phase velocity also increases the inertial forces, which elongates the slugs before the breakup, particularly for LL flow. As the dispersed water velocity is increased to 0.4 m.s^{-1} in the LL flow, the high inertial forces accompanied by an apparent viscosity ratio (μ_w/μ_d) of 0.64 causes a significant change in the flow pattern from a segmented regime to a slug / annular regime. At the highest superficial velocity ratio of 4 for LL flow (the last plot in Figure 5.5b), breakup is not observed due to low inertia of the carrying phase flow around the perimeter of the microchannel. The interfacial shear stress of relatively high-velocity water on the liquid film thickness becomes predominant and the dispersed phase flows continuously.

The characteristics of bubble and liquid slug formation for different superficial velocity ratios (dispersed phase velocity to the carrying phase velocity) are is presented in Tables 5.2 and 5.3. At the lowest velocity ratio (0.25), the high inertia of the carrying flow causes the slug formation to lag and only two slugs are generated. As the dispersed phase velocity is increased three breakups occur and the same size air-bubbles and water-slugs are generated. It causes more elongated slugs and more-shortened liquid plugs accordingly. Gupta et al. (2009) showed the non-dimensional

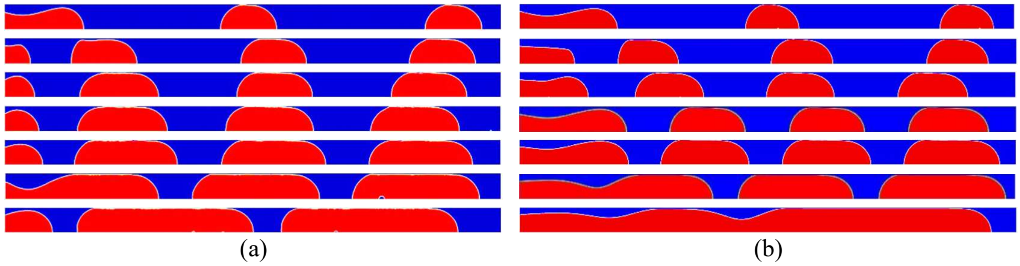

FIGURE 5.5: Phase volume fraction plots of (a) air-bubble and (b) water-slug for superficial velocities of 0.1-0.4, 0.15-0.35, 0.2-0.3, 0.25-0.25, 0.3-0.2, 0.35-0.15, and 0.4-0.1 m.s^{-1} from top to down, respectively (air is coloured red and water is coloured blue for the GL and water is coloured red and dodecane is coloured blue for the LL)

lengths of air-bubble and water-plug are 2 and 1.3, respectively. More recently, Qian et al. (2019), employed numerical and experimental techniques to find a domain of 1.56 to 2.07 for slug length and 2.07 to 3.02 for plug length. The difference between the lengths identified by Gupta et al. (2009) and Qian et al. (2019) compared to the results in this chapter are due to different channel diameters, phase properties, and flow conditions. The results show that the length of an air-bubble is longer than that of a water-slug, with the highest difference of 13.9% at velocity ratio of unity.

Furthermore, the length of the first slug slightly differs from the second slug for the GL and LL cases. The mean slug length differences are 1.04% and 4.52% for GL and LL, respectively, indicating GL's tendency for more rapidly reaching a fully developed Taylor flow condition compared to LL. The mean values of the liquid film thickness with a confidence level of 95% are 10.69 ± 4.71% and 12.16 ± 3.69% for the GL and LL cases, respectively. Therefore, the averaged film thickness for LL is 12.1% greater than for GL, which can be attributed to the different thermophysical properties and larger capillary number. The measurement of the liquid thickness in the flat film region has appeared in studies concerning two-phase flows in microchannels, which has been often correlated as a function of non-dimensional numbers Ca, Re, and We. For verification, an insignificant deviation of 0.8% is obtained from comparing the mean film thickness between the new results and the correlations for the GL flow in the literature (e.g., Bretherton, 1961; Aussillous and Quéré, 2000; Kreutzer et al., 2005c; Han and Shikazono, 2009).

TABLE 5.2: Characteristics of the air bubble formation process at different superficial velocities

Velocity ($m.s^{-1}$)		**Slug Breakup** (ms)			**Slug Length** ($L_s.D^{-1}$)			**Plug Length** ($L_p.D^{-1}$)		**Film Thickness**‡
air	**water**	**3rd**	**2nd**	**1st**	**3rd**	**2nd**	**1st**	**2nd**	**1st**	(μm)
0.10	0.40	–	7.81	4.31	–	1.13	1.15	2.78†	2.98	11.25
0.15	0.35	9.57	6.57	3.60	1.33	1.33	1.34	2.10	2.07	11.44
0.20	0.30	9.11	6.24	3.37	1.59	1.52	1.53	1.58	1.59	10.88
0.25	0.25	8.76	5.97	3.19	1.81	1.77	1.80	1.17	1.15	10.63
0.30	0.20	8.43	5.87	2.94	2.08	2.10	2.09	0.89	0.88	10.62
0.35	0.15	–	6.41	3.31	–	2.56	2.57	0.68†	0.66	10.00
0.40	0.10	–	8.04	4.08	–	3.55	3.56	0.50†	0.56	10.00

‡The film thickness is averaged by the liquid film thickness in the flat region(s) of the fully detached slugs, not using a slug immediately after breakup.
†This length is measured between a fully detached and emerging slug.

TABLE 5.3 Characteristics of the water slug formation process at different superficial velocities

Velocity ($m.s^{-1}$)		**Slug Breakup** (ms)			**Slug Length** ($L_s.D^{-1}$)			**Plug Length** ($L_p.D^{-1}$)		**Film Thickness**‡
water	**dodecane**	**3rd**	**2nd**	**1st**	**3rd**	**2nd**	**1st**	**2nd**	**1st**	(μm)
0.10	0.40	–	5.67	4.58	–	1.08	1.09	2.59†	2.85	11.25
0.15	0.35	9.48	6.74	3.99	1.22	1.24	1.24	1.86	1.89	11.88
0.20	0.30	8.19	5.92	3.53	1.39	1.37	1.41	1.26	1.28	11.94
0.25	0.25	7.53	5.45	3.33	1.51	1.51	1.61	0.89	0.88	12.98
0.30	0.20	7.86	5.66	3.48	1.78	1.78	1.93	0.67	0.66	12.66
0.35	0.15	–	6.94	4.18	–	2.32	2.56	0.51†	0.52	12.25
0.40	0.10	N/A (refer to the discussion on Figure 5.5)								

‡The film thickness is averaged by the liquid film thickness in the flat region(s) of the fully detached slugs, not using a slug immediately after breakup.
†This length is measured between a fully detached and emerging slug.

The data of the air / water and water / dodecane interface locations for the second slugs have been extracted by the WebPlotDigitizer software illustrated in Figure 5.6. The slug shapes are obtained for a superficial velocity ratio of one to compare with the data of Gupta et al. (2009). In Figure 5.6, the different profiles have been aligned at the tail where the non-dimensional horizontal axis is zero. The non-dimensional vertical axis, representing the radii of the slugs, is equal to the radius of the microchannel. The lengths of slugs differ from Gupta et al. (2009) because of the considerable differences between the phase velocities and phase properties. However, comparing slug profiles by aligning the tails verifies that the tail menisci are very close to each other and the same confirmation is achieved for the nose menisci by matching noses together (not displayed here). Some ripples are observed near the tail meniscus due to the pressure fluctuations and interaction between surface tensions and viscous forces in the film region (Gupta et al., 2009). Higher $\mathrm{Re/Ca}$ ratios, which are caused by lower viscosity fluids in GL flow compared to LL flow, increases the length of the nose and the radius of the slug.

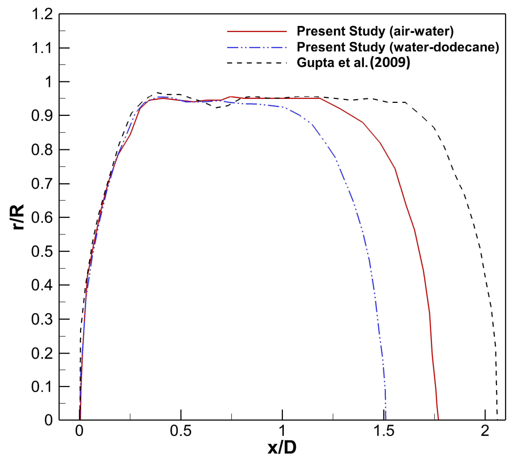

FIGURE 5.6: Comparison of the slug profiles obtained from the simulations and the data from Gupta et al. (2009) for the GL and LL cases at the superficial velocity ratio of unity (The slug profiles are aligned at the tails; $x/D = 0$)

5.6.4 Gas and Liquid Holdups

Gas / liquid holdup (void fraction or volume fraction), ε_G, is defined as the ratio of volume occupied by the dispersed phase to the total volume for an entire channel or unit cell. The quantity of gas holdup varies from zero for single-phase liquid flow to one for single-phase gas flow, including for Taylor flows with a thin liquid thickness. Two empirical correlations were suggested by Ali et al. (1993) for narrow channels ($D_H \sim 1$ mm) and Armand and Treschev (1946) to estimate gas holdup, respectively, as:

$$\varepsilon_G = 0.8\beta \tag{5.11}$$

$$\varepsilon_G = 0.833\beta \tag{5.12}$$

where β is the homogeneous void fraction or volumetric quality and defined as a function of phase superficial velocities,

$$\beta = \frac{U_{GS}}{U_{GS} + U_{LS}} \tag{5.13}$$

The square of the gas bubble radius to the channel radius ratio was verified as the gas holdup showing a huge deviation from that computed by the correlations of Ali and Armand. More recently, Gupta et al. (2009) also found a 10% difference between measured gas holdup and the predictions of the Armand correlation. The steady bubble velocity, U_b, in a horizontal microchannel configuration can be determined by a ratio of gas-phase superficial velocity to gas holdup,

$$U_b = \frac{U_{GS}}{\varepsilon_G} \tag{5.14}$$

For constant superficial velocities, the bubble velocity is a constant value of 0.6002 and 0.625 $m.s^{-1}$ based on the Armand and Ali correlations, respectively. Varying the gas superficial velocities changes the flow pattern, as illustrated in Figure 5.7a. In this chapter, gas holdup in a unit cell is computed as the ratio of air bubble volume to unit cell volume. The predicted bubble velocity for the highest and lowest superficial velocity ratios differ from the Armand correlation by 18.6% and 29.7%, respectively. Additionally, the steady air bubble velocity is slightly more than the water slug. It is caused by a greater pressure gradient between the nose and tail of the air bubbles compared to the water slugs. The slug velocity from the simulations can be obtained as the magnitude of velocity at the nose of the slugs. For example, at a superficial velocity ratio of unity, it differs by 7.6% and 9% from the exact values of 0.5068 and 0.48 for the GL and LL cases, respectively for the second slug, and these differences have been decreased by 2.5% and 3% for the first slug. Therefore, the flow is very close to reaching a fully developed condition near the exit plane and GL reaches that faster than the LL. Besides, the air bubbles move faster than the average velocity, the sum of two superficial velocities, due to the lubricating effects as is frequently declared in the literature. The mean water plug velocity can be calculated by integrating the axial velocity component, on the axis of the channel, between two sequential bubbles, resulting in a value of 0.4620 $m.s^{-1}$. From mass conservation,

$$Q_p = Q_f + Q_b \tag{5.15}$$

where the subscripts b, f, and p indicate the bubble, film, and plug, respectively. For circular microchannels at very low capillary numbers, the liquid film thickness is less than 15 μm and the liquid velocity in the film region is approaching zero. Therefore, from a scaling analysis it can be approximated that $(D - D_b) \sim 2\delta$ and $(D + D_b) \sim 2D$, which simplify Eq. (5.15) to

$$\frac{U_b}{U_p} = 1 + \frac{4\delta}{D} \tag{5.16}$$

where the bubble velocity in Eq. (5.16) is 0.5018 $m.s^{-1}$ indicating a 1% difference from the exact value obtained by gas holdup for the superficial velocity of one, for example.

The ratio of volume of the dispersed phase by the microchannel volume is beneficial on a more in-detail hydrodynamic analysis. The volume of an arbitrary phase in a cell zone can be obtained by the summation of the phase volume fraction multiplied by the cell volume,

$$\int \alpha_p d\forall = \sum_{i=1}^{n} \alpha_{p_i} |\forall_i| \tag{5.17}$$

where p, α, and ∀ indicate selected phase, selected phase volume fraction, and the volume, respectively.

Figure 5.7b shows the variations of total gas and liquid holdups in the entire microchannel versus the superficial velocity ratio for air / water and water / dodecane cases at 9 ms. The total volume of the axisymmetric microchannel is 9.818×10^{-10} m^3. An increase in the velocity ratio enhances the holdups for both the GL and LL cases in the same way. By a regression analysis on the data shown in Figure 5.7b, the following linear logarithmic correlation can be proposed to compute the holdup, ε, in terms of the superficial phase velocity ratio in Taylor flow:

$$\varepsilon = 0.2008 \, \mathrm{Ln}\left(\frac{U_d}{U_c}\right) + 0.4433 \tag{5.18}$$

where U_d and U_c represent superficial velocities of the dispersed and continuous phases, respectively. This correlation is obtained by the minimization of the sum of squared errors (SSE) and root mean square errors (RMSE) on the data resulting in ~1% discrepancies between the actual data of the GL and LL cases, and the values predicted by Eq. (5.18).

To predict the liquid film thickness in terms of dependent and independent flow variables, the multivariable power least squares method (MPLSM) can be employed. The results indicated that the data of liquid film thickness in the GL flow could be explained by gas holdup (ε) and superficial Weber numbers,

$$\frac{\delta}{R} = 0.0013 \, \mathrm{Ln}\left[\frac{We_{LS}\,(1-\varepsilon)}{(We_{GS}\,\varepsilon)^{0.15}}\right] + 0.0432 \tag{5.19}$$

where,

$$We_{LS} = \frac{D U_{LS}^2 \rho_w}{\sigma} \tag{5.20}$$

$$We_{GS} = \frac{D U_{GS}^2 \rho_a}{\sigma} \tag{5.21}$$

Based on Eq. (5.19), the liquid film thickness is more dependent on the continuous (water) phase than the dispersed (air) phase. The mean absolute deviation (MAD) of non-dimensional film thickness (δ/R) is defined as:

$$\mathrm{MAD} = \frac{\left|\left(\frac{\delta}{R}\right)_{\mathrm{correlation}} - \left(\frac{\delta}{R}\right)_{\mathrm{simulation}}\right|}{\left(\frac{\delta}{R}\right)_{\mathrm{simulation}}} \times 100\% \tag{5.22}$$

where the values of the simulation and correlation come from Table 5.2 and Eq. (5.19), respectively. The MAD is resulted in only 1.42% indicating satisfactory accuracy of Eq. (5.19), for liquid film thickness prediction. A summary of liquid film thickness correlations and experimental data is recently presented by Etminan et al. (2022a).

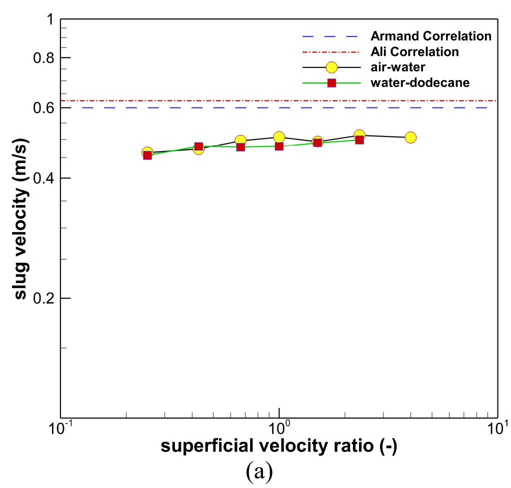

FIGURE 5.7: Variations of (a) slug velocity and (b) slug holdup in the whole microchannel in terms of the superficial velocity ratio

5.6.5 Pressure Distribution

The interactive structure of different phases and between phases and solid walls represent the predominant parameters to describe the flow pattern of multiphase flow and pressure drop through the channel. Two homogenous and separated flow models have been employed by researchers to predict the frictional pressure drop. The first model postulates the same velocity for both gas and liquid phases, which implies that the slip ratio at the interactive boundaries is equal to one. This model considers two or more different phases as a single phase. The values of the flow properties are dependent on the quality, while the frictional pressure drop can be computed by single-phase flow theory:

$$f = \left(\frac{1}{2}\frac{D}{\rho U^2}\right)\left(\frac{dp}{dx}\right)_L \tag{5.23}$$

where D, L, U, and x indicate the tube diameter, length, mean velocity $(U_{GS} + U_{LS})$, and axial direction of the channel. The Hagen-Poiseuille equation can be used to compute the pressure drop of a Newtonian, incompressible flow through a long and circular tube, with constant cross-sectional area. The flow regime remains laminar due to the low Reynolds number of the microflows, where the friction factor becomes $f = 16/Re$ for round tubes and Eq. (5.23) can be rearranged in the following way.

$$\Delta p = \frac{16}{Re}\left(\frac{1}{2}\rho U^2\right)\frac{4L}{D} \tag{5.24}$$

In Taylor flow, the pressure drop is affected by slug curvature, slug and plug length, and steady film thickness. Figure 5.8, shows the pressure distribution on the axis of the microchannel for two GL and LL cases with a superficial velocity ratio of one, and at 9 ms. A volume fraction plot has been affixed to this figure where the dispersed phase is colored red and the continuous phase is colored blue.

The pressure drop over a unit cell can also be described by three components (Kreutzer et al., 2005c; Fouilland et al., 2010; Ni et al., 2017):

$$\Delta p_{uc} = \Delta p_p + \Delta p_f + \Delta p_{cap} \tag{5.25}$$

where the last two terms in Eq. (5.25) represent the total pressure drop over the gas bubble. The pressure drop over the liquid plug can be calculated by Hagen-Poiseuille Eq. (5.24) in fully developed flow without internal circulation:

$$\frac{\Delta p_p}{L_p} = \frac{32\mu U}{D^2} = 32\ Ca\ \frac{\sigma}{D^2} \tag{5.26}$$

According to Eq. (5.26), the pressure drop over the liquid plug is 56,955 Pa/m where the corresponding value from the present numerical simulation over two halves of subsequent liquid plugs to the first bubble is 60,345 Pa/m, indicating an acceptable agreement with 5% deviation. This difference becomes much more for the second unit cell where the flow regime is slightly further away from a fully developed condition. As illustrated in Figure 5.8a, the pressure drop distributions over the steady liquid film region are almost constant and Δp_f is negligible, which agrees with Fouilland et al. (2010). Conversely, the normal stress at the interface, within the steady film region is no longer present and the Laplace pressure at the interface can predict the pressure difference. The pressure difference between inside the gas bubble and the liquid at the wall is 295 Pa, which agrees well with the exact value of $\sigma/R_b = 301$ Pa. However, the interfacial pressure difference in the hemispherical nose region of the first air bubble is of the order of $2\sigma/R_b = 602$ Pa, whereas the simulations predict 513 Pa. The difference is due to the developing conditions and assumption of non-exact hemispherical shape of the gas bubble. The last term in Eq. (5.25) can be calculated by lubrication theory discussed by Bretherton (1961) assuming insignificant inertia forces and exact semi-hemispherical profile at both caps of the bubble.

$$\Delta p_{cap} = 7.16 \frac{(3\ \mathrm{Ca})^{2/3} \sigma}{D} \tag{5.27}$$

The numerically predicted bubble cap pressure difference is ~61 Pa compared to 72 Pa predicted by Eq. (5.27). This deviation can also be attributed to the significant difference between the nose and the rear meniscus, non-exact semi-hemispherical cap curvatures, and the inertia effects. Consequently, the pressure drop per unit length by Eq. (5.25) is 60,700 Pa.

The apparent friction factor and the pressure drop per unit length for Taylor flow in microchannels are obtained by Kreutzer et al. (2005c), as follow:

$$f = \frac{16}{\mathrm{Re}} \left[1 + 0.07 \frac{D}{L_p} \left(\frac{\mathrm{Re}}{\mathrm{Ca}} \right)^{1/3} \right] \tag{5.28}$$

$$\frac{\Delta p}{L} = \varepsilon_L f\left[\frac{4}{D}\left(\frac{1}{2}\rho U^2\right)\right] \tag{5.29}$$

where liquid holdup, ε_L, is $1 - \varepsilon_G$, gravitational effects are negligible, and the flow is fully developed. Under present circumstances, Eqs. (5.28) and (5.29) lead to the values of 0.18 and 88,518 Pa/m, respectively. The pressure distribution is no longer constant in the liquid slugs as illustrated in Figure 5.8b, due to the strong internal liquid circulation inside the slugs. The maximum pressure location is in the rear half of the slugs which can be attributed to the slug movement and a significant change in the velocity field inside the liquid slugs. The large pressure drop over the contracting region of the emerging liquid slug is due to expansion of the slug.

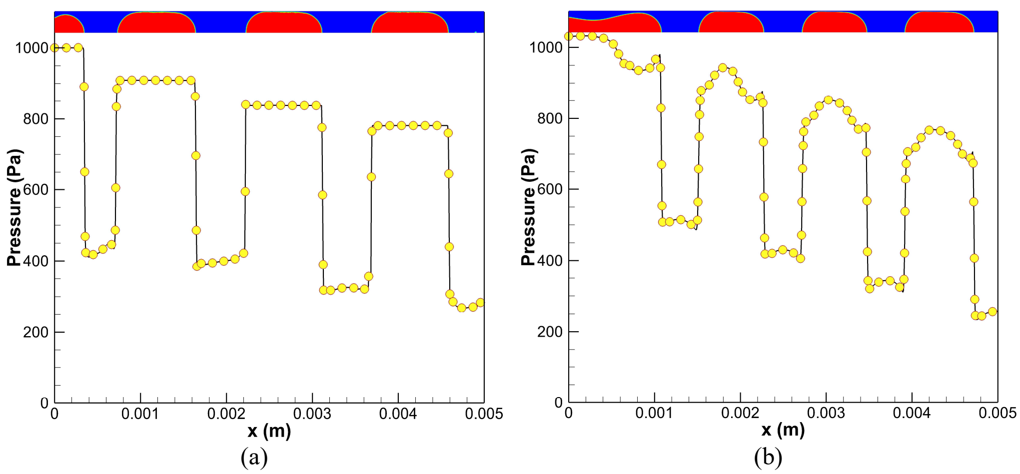

FIGURE 5.8: Pressure distributions on the axis of the microchannel, in unity superficial velocity ratio, and at 9 ms for (a) GL and (b) LL flows

5.7 Conclusions

A computational analysis of the GL and LL Taylor flows in an axisymmetric microchannel with a circular cross-sectional area was conducted. Air and water were introduced by a concentric junction into the carrying flow; water and dodecane, respectively. The influence of varying superficial velocities and thermophysical properties were discussed to reveal more in-depth detail of the hydrodynamics of the segmented flow in microchannels. A precise time-history of slug formation was presented to understand its different evolution steps; introducing, expanding, contracting, necking, and breakup. The results showed that the higher dynamic viscosity ratio of the LL flow compared to GL flow takes the main responsibility of establishing a more stable interface, moving the breakup point to the downstream, and making the semi-hemispherical curvatures at the two ends of the slugs faster. The length of air bubble was greater than water slug which the highest difference happened at the velocity ratio of unity. Besides, the air bubbles moved faster than the average velocity because of the lubricating effects as was often affirmed in the literature. To the best of our knowledge, the variation of holdup with the superficial velocity ratio was numerically correlated, for the first time. For the LL case, the highest pressure was located in the rear half of the slugs which can be attributed to the slug movement and a significant change in the velocity field inside the liquid slugs, while the pressure remained constant inside the slugs of the GL. The pressure difference between the gas bubble and the liquid phase at the wall is 295 Pa, which agrees well with the exact value of $\sigma/R_b = 301$ Pa. However, the interfacial pressure difference in the hemispherical nose region of the first air bubble is of the order of $2\sigma/R_b = 602$ Pa, whereas the simulations predict 513 Pa. The results of the present numerical study provided useful new insights into gas-liquid and liquid-liquid capillary channels. The methodology can be also easily extended to heat transfer in such Taylor flow.

Chapter 6

Hydrodynamic Characteristics of Two-Phase Flows through Microchannels with a Sudden Diameter Expansion[1]

6.1 Overview

This chapter investigates a CFD-based analysis for gas-liquid and liquid-liquid Taylor flows through a circular axisymmetric microchannel with a sudden enlargement. A series of simulations are conducted by exploring the influence of different superficial velocity ratios, apparent viscosities, and channel expansion on the hydrodynamics of slug flow. A concentric junction introduces dispersed airflow into a continuous flow of water for gas-liquid flow, and the junction introduces dispersed water into a continuous flow of dodecane for liquid-liquid flow. The air-bubble and water-slug evolution processes, slug breakup, and slug expansion are investigated. In all cases, the lengths of air bubbles and water slugs increase with increasing superficial velocity ratio, particularly before the expansion. For gas-liquid flow, the apparent viscosity ratio causes a fluctuating interface over the uniform film region. However, the water slug length is shorter and the film region is slightly thicker in liquid-liquid compared to gas-liquid flow. The numerical analysis developed in this chapter is in good agreement with the existing correlations and experimental data in the literature.

[1] This chapter is written based on:
Etminan, A., Muzychka, Y.S., Pope, K. (2022b) Numerical investigation of gas-liquid and liquid-liquid Taylor flow through a circular microchannel with a sudden expansion. The Canadian Journal of Chemical Engineering. 100(7), 1596–1612.
DOI: 10.1002/cjce.24229

6.2 Introduction

Whether in single-phase or multiphase flow, the interactions between existing forces, such as surface tension, viscous, inertial, gravitational, pressure gradient, and interfacial effects are important in microstructured devices. The simultaneous presence of gas and liquid phases in many industrial sectors, such as pharmacological, biological, chemical, and petroleum, create a serious challenge for researchers to figure out hydrodynamic characteristics and transport phenomena in such flows. The hydrodynamics of single-phase flow in microchannels shows similarities to a conventional channel with a larger diameter (e.g., Herwig and Hausner, 2003; Sharp and Adrian, 2004; Hetsroni et al., 2005; Kohl et al., 2005; Morini et al., 2007; Park and Punch, 2008). However, due to the increased effects of surface tension compared to inertial forces in milli- and microchannels, the flow regimes and transport phenomena in such flows are different from those investigated by scholars over the last few decades.

The lattice Boltzmann method (LBM) has frequently been employed to study flow characteristics through a microchannel with a sudden expansion for a wide range of Knudsen number to show the compressibility effects and pressure drop at the intersection of a channel (e.g., Nie et al., 2002; Lee and Lin, 2005; Li et al., 2011; Liou and Lin, 2014). Khodaparast et al. (2014) experimentally studied the flow visualization in a circular microchannel with a sudden expansion using particle image velocimetry (PIV). They found the same trends of flow characteristics and vortex length for a larger scale. Their measurements were devoted to single-phase flow and the pressure drop was estimated using two approaches: introducing velocimetry results into the Navier–Stokes equation (Bauer and Koengeter, 1999; Fujisawa et al., 2005; Fujisawa et al., 2006; van Oudheusden et al., 2007) and finding pressure gradients on the walls in the region of interest (Oliveira et al., 1998).

The interaction between phases in a two-phase flow introduces more complexities in the analysis of flow patterns and transport phenomena. Chai et al. (2015) studied gas-liquid (GL) intermittent flow patterns and frictional pressure drop in a set of rectangular microchannels with an array of periodic cavities. They compared the collected data with the existing correlations proposed by other researchers based on two models: homogenous (McAdams et al., 1942; Cicchitti et al., 1960; Dukler et al., 1964; Collier and Thome, 1994) and separated mixture (Lockhart and Martinelli, 1949; Chisholm, 1967). Their results revealed a weak prediction of frictional pressure drop by the homogenous model. Wang et al. (2010) showed a poor predictive ability of the model. Wang et al. (2010) also proposed a modified version of the homogenous model considering the effects of some key parameters, such as Bond number, Weber number, Froude number, Reynolds number, and gas quality. This modified model showed more accurate predictive ability compared to existing correlations for a broader range of operational conditions. The effects of a sudden diameter expansion on an air / water two-phase flow in millichannels were also experimentally conducted (Zhang and Goharzadeh, 2019; Zitouni et al., 2021), indicating a significant impact of the presence of dispersed phase on the behaviour of flow, film thickness, and pressure drop.

The surface tension and viscous effects are more dominant forces than the gravitational and inertial forces in channels with very small diameter. The flow patterns in macro- and microchannels are significantly affected by several parameters, such as transport phenomena (e.g., momentum, heat, and mass), diameter of channels, orientation of channel, superficial velocities, and thermophysical properties (e.g., viscosity, surface tension, and density). Two-phase flow in mini- and microchannels have been experimentally and numerically conducted by multiple scholars to determine flow patterns and the process of gas bubbles formation. Typically, flow pattern maps have been displayed using non-dimensional numbers (e.g., Re, Ca, and We), surface tension, viscosity, velocity, and density of both phases, and classify flow patterns as bubbly, slug (segmented or Taylor), churn, stratified, slug-annular, or annular (e.g., Govier and Aziz, 1972; Mandhane et al., 1974; Taitel et al., 1980; Weisman and Kang, 1981; Brauner et al., 1998; Brauner, 2003; Triplett et al., 1999; Akbar et al., 2003; Cubaud and Ho, 2004; Kreutzer et al., 2005c; Steijn et al., 2007; Yue et al., 2008; Fouilland et al., 2010; Kashid et al., 2011; Ong and Thome, 2011; Bolivar and Nidetzky, 2013; Ghiaasiaan, 2014; Yagodnitsyna et al., 2016). Except for stratified flow patterns, all other flow regimes have been observed for both macro- and microchannels. Kawaji and Chung (2003) conducted a careful study on two-phase flow patterns in mini- and microchannels by showing the similarities and differences between these two common channels. To maintain Taylor flow in mini- and microchannels, Svetlov and Abiev (2018) introduced a special coaxial-spherical junction for having a slug flow regime over a wide range of phase volumetric flow rates to improve the efficiency of such channels. They also correlated the length of the bubbles to geometric dimensions, features of the mixer shape, and phase superficial velocity ratio. Svetlov and Abiev (2021) mathematically analyzed a significant role of the continuous phase flow rate on the hydrodynamic characteristics and droplet formation. The frequently observed flow regime maps in macro- and microchannels are illustrated in Figure 6.1 using gas and liquid superficial velocities by reproducing the data of Triplett et al. (1999). They considered air-water Taylor flow in a horizontal straight channel with a diameter of 1.45 mm. Based on the current flow conditions, the flow map (shown by the red circles in Figure 6.1) is located in the slug zone.

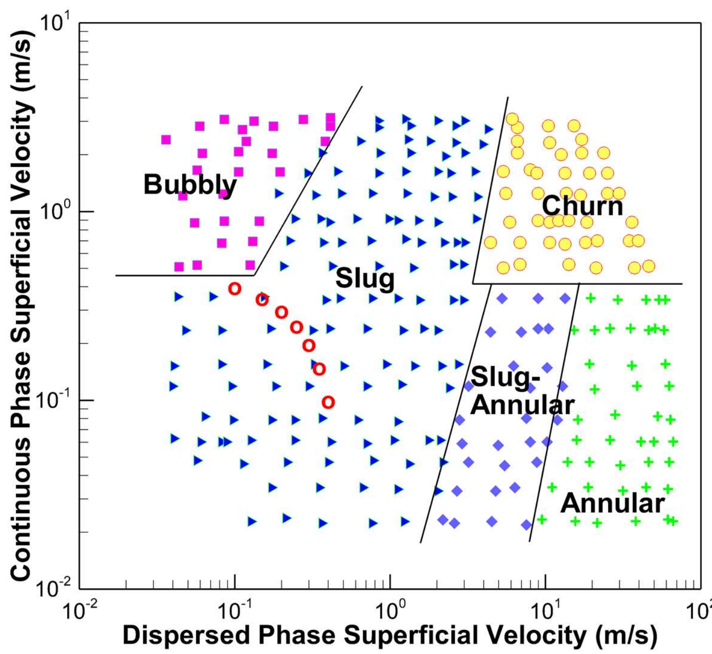

FIGURE 6.1: Reproducing the data of different flow patterns and transition lines for a horizontal circular channel with a diameter of 1.45 mm observed by Triplett et al. (1999) and the present study pattern shown by red circles (o) (the transition solid lines are only indicative and were not introduced by Triplett et al. (1999))

In this chapter, a comprehensive study is conducted to evaluate several interface capturing schemes and pressure gradient models. Subsequently, a series of numerical simulations are carried out to investigate slug flow parameters including bubble / slug formation, breakup, slug / plug length, liquid film thickness, bubble / slug curvature, and pressure drop. The singularity of a sudden expansion's influence on two-phase flow behaviour is also studied. The results are validated by available experimental and numerical data in the literature.

6.3 Solution Methodology

6.3.1 Problem Description and Governing Equations

Figure 6.2 shows the configuration of a microchannel with a concentric junction to introduce dispersed flow. The flow field analysis can be conducted for half of the actual two-dimensional domain due to the cylindrical geometry of the channel in order to save computational expense. The channel's radius (D/2) and length (2L) are 250 and 10,000 µm, respectively. In the middle, a series of channel diameter expansions of 5%, 10%, 15%, and 20% equal to 12.5, 25, 37.5, and 50 µm, respectively, are considered to find the effects of geometry on the flow parameters and transport phenomena. At the inlet, the dispersed phase enters at the core and the carrier phase enters the annulus around the core entry uniformly. At the exit, an outlet condition is employed where a fully developed state is attained. The no-slip boundary condition is assumed at the wall and the radial gradients for all flow variables on the microchannel's axis are set to zero. The simulations are conducted on a horizontal plane, where the gravity acceleration is negligible due to an insignificant impact on the Taylor flow in microchannels (Triplett et al., 1999; Gupta et al., 2009; Sontti and Atta, 2017).

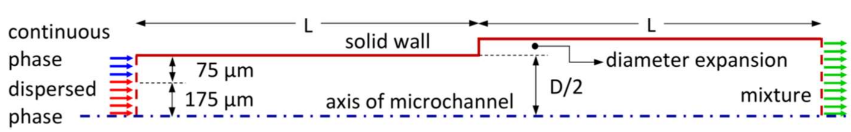

FIGURE 6.2: Schematic of the problem under consideration

The properties of operating fluids at room temperature (25 °C) and atmospheric pressure (1 atm) are presented in Table 6.1. The superficial velocities of the phases vary from 0.1–0.4 ms^{-1} by a step of 0.05 ms^{-1}. Under these flow conditions, the capillary number (Ca), Reynolds number (Re), and Weber number (We) are 0.00618, 279.93, and 1.73, respectively, for the GL flow, and 0.01336, 135.67, and 1.81, respectively, for the liquid-liquid (LL) flow. Uniform dispersed and continuous flows enter the microchannel when it is filled with water for the GL flow, and dodecane for the LL flow at an average velocity of 0.5 ms^{-1} as the initial condition prior to running the simulations. It is noteworthy that dodecane (also known as dihexyl or bihexyl) is a straight-chain liquid alkane of the paraffin series emerging in reprocessing plants and aviation fuels (Rydberg, 2004).

TABLE 6.1: Properties of the dispersed and continuous phases in following simulations

Flow	**Phase**	**Fluid**	**Density** ($kg \cdot m^{-3}$)	**Dynamic viscosity** ($kg \cdot m^{-1} \cdot s^{-1}$)	**Surface tension** ($N \cdot m^{-1}$)
GL	Dispersed	Air	1.1845	1.849×10^{-5}	0.072
	Continuous	Water	997.1	8.905×10^{-4}	
LL	Dispersed	Water	997.1	8.905×10^{-4}	0.052
	Continuous	Dodecane	754.3	1.39×10^{-3}	

This chapter presents two incompressible GL and LL Taylor flows in an axisymmetric cylindrical microchannel. Each phase is treated as a Newtonian and incompressible fluid with constant thermophysical properties during simulations. The dispersed phase is immiscible with the continuous phase, phase change is not taken into account through the channel, and viscous dissipation is negligible. Under these circumstances, conservation equations of mass and momentum in both gas and liquid phases are as follows:

$$\frac{\partial \rho}{\partial t} + \nabla.(\rho \vec{u}) = 0 \tag{6.1}$$

$$\frac{\partial (\rho \vec{u})}{\partial t} + \vec{u}.\nabla(\rho \vec{u}) = -\nabla p + \nabla.[\mu(\nabla \vec{u} + (\nabla \vec{u})^T)] + \rho \vec{g} - \sigma \kappa \delta \vec{n} \tag{6.2}$$

where μ denotes the dynamic viscosity and ρ represents the density. The ratio of gravitational to surface tension effects can be showed in a non-dimensional number called Bond number (Bo), which is known as Eötvös (Eo):

$$\mathrm{Bo} = \frac{\mathrm{g}\mathrm{D}^2\Delta\rho}{\sigma} \tag{6.3}$$

where D is the microchannel diameter, g is the gravitational acceleration, and $\Delta\rho$ is the difference between phase densities. The Bo is less than 10^{-2} under the conditions assumed in this study, which is significantly less than the Bo limit of 3.368 reported by Bretherton (1961). In the presence of the dominant surface tension effects in macro- and microchannels, the gravitational force ($\rho\vec{g}$) turn into a negligible term in the momentum equation (Triplett et al., 1999). The surface tension effect is described by the last term in Eq. (6.2) where σ is surface tension, κ is the radius of curvature viewed from the dispersed phase slug, δ is the Dirac delta function, and $\vec{n}$ is an outward normal vector at the interface from the gas to liquid phase. The intermolecular attractive forces in a liquid create the surface tension force acting inward and must be balanced with an outward pressure gradient force through the surface.

The last term in the momentum equation can be also approximately modelled as a body force surrounding the interface (Brackbill et al., 1992; Li et al., 2000; Yokoi, 2013). The first model, the continuum surface force (CSF), approximates the surface tension generated by changing in stress as a body force over a finite region of fluid surrounding the interface in a non-conservative way. Conversely, the continuum surface stress (CSS) model is utilized in most variable surface tension applications in a more conservative way (Brackbill et al., 1992; Adaze et al., 2019). The normal vector and the curvature of the radius of interfacial curvature are expressed in terms of the volume fraction (α):

$$\vec{n} = \frac{\nabla\alpha}{|\nabla\alpha|} \tag{6.4}$$

$$\kappa = \nabla.\vec{n} \tag{6.5}$$

Implementation of these models must be carefully taken into account to consider the importance of a balance between the pressure and viscous forces. Otherwise, inaccurate velocities called spurious or parasitic currents are predicted near the interface that cannot be improved with mesh refinement or shorter time-steps (Harvie et al., 2006).

The solution to the momentum equation within the computational domain predicts a shared velocity field for dispersed and continuous phases, and the accuracy of the solution is adversely impacted by superficial velocity difference around the interface. There is no mass transfer between two phases in the computational domain, and a volume fraction or void fraction (or any other scalar variable) continuity equation can be assumed as a simple advection equation:

$$\frac{\partial \alpha}{\partial t} + \nabla(\alpha \vec{u}) = 0 \tag{6.6}$$

where the volume fraction changes between 0 and 1. The significance of the volume fraction must be considered in the vicinity of the interface (inside the gas bubbles and liquid plugs is not significant) to have a precise prediction of the interfacial effects and momentum transport. The mass conservation equation for one or more of the phases must be solved to track the interface between phases. Hence, special interpolation treatment is required to compute the flux of diffusion and convection on the control volume faces entirely or partially located in the interface region. A proper discretization scheme enables numerical simulation of multiphase flow to model the convective terms in the transport equations with the lowest numerical diffusion value or dispersion phenomena. The excessive diffusion of a numerical discretization scheme defects the actual interface with non-physical wrinkles resulting in a diffused (thick) and poor interfacial region between the phases (e.g., Ubbink and Issa, 1999; Dendy et al., 2002; Panahi et al., 2006; Queutey and Visonneau, 2007; Heyns et al., 2013; Zhang et al., 2014). Two groups of interpolating schemes have been introduced: geometrical reconstructing and algebraically formulated differencing. Therefore, a proper and accurate volume fraction discretization scheme can be chosen from a wide range of methods, such as the compressive interface capturing scheme for arbitrary meshes (CICSAM), geo-reconstruct, compressive, and a modified high-resolution interface capturing (HRIC). Advantages and limitations of the volume fraction discretization schemes are presented in Table 6.2 (Lopes and Quinta-Ferreira, 2009; Barral et al., 2019).

The volume of fluid (VoF) method computes a specific time step using the transient time characteristic over a control volume, which can be different compared to that in other governing equations (ANSYS Fluent Users' Guide). The volume of each cell over the sum of the outgoing flux from the faces in the interface leads to a time-step taken to empty a cell. The Courant number (Co), which contains the smallest time-step (Δt), is defined as follows:

$$\mathrm{Co} = \frac{\Delta t}{\Delta x / U_{\mathrm{fluid}}} \tag{6.7}$$

where the Δx denotes the grid size and U_{fluid} is the fluid velocity. In contrast to the explicit approach, the implicit approach has no limitation on the Co, allowing for larger grid sizes and time-steps. Nevertheless, the higher numerical diffusion of implicit approach in the interface shows poor prediction of interface curvature (ANSYS Fluent Users' Guide; Etminan et al., 2021b). A constant time-step of 10^{-6} is assumed to decrease computational efforts as long as Co is not increased unexpectedly and the VoF simulation remains converged. Otherwise, a variable time-step ranging from 10^{-6} to 10^{-7} is chosen, specifically at the moments of slug breakups.

Figure 6.3 illustrates the contour of volume fraction using different interpolation schemes. Both the compressive and the modified HRIC schemes predict a thicker interface, more elongated gas bubble, and much more numerical diffusion on the channel's axis, and around the slug nose, as previously mentioned by Etminan et al. (2021b). This weakness causes solution divergence at the moments of bubble / slug breakup and expansion near the channel wall. Conversely, the geo-reconstruct and CICSAM result in a sharp and more accurate interfacial curvature without numerical diffusion. According to the quadrilateral meshes and ANSYS Fluent User's Guide, the geo-reconstruct discretization scheme is kept for the following numerical simulations.

TABLE 6.2: A short summary of interpolation schemes to compute the volume fraction

Scheme	Interpolation function	Remarks	Ref.
CICSAM	$\tilde{\phi}_f = \begin{cases} \min\left(1, \frac{\tilde{\phi}_D}{C_f}\right) & 0 \le \tilde{\phi}_D \le 1 \\ \tilde{\phi}_D & \tilde{\phi}_D < 0 \text{ or } \tilde{\phi}_D > 1 \end{cases}$	• The interface sharpness is the same level as Geo-Reconstruction • High-viscosity ratio • Available only with Eulerian multiphase flow • Inexpensive computationally • Considers the angle between the interfacial curvature and the direction of flow • Suitable for any arbitrary mesh • Satisfies the convective boundedness criterion (CBC)	Ubbink (1997) Ubbink and Issa (1999) Wacławczyk and Koronowicz (2008)
Geo-Reconstruct	Standard piecewise linear	• Available only with Eulerian multiphase flow • Expensive computationally • Time-accurate transient behaviour of the VoF • Improper for highly twisted hexahedral meshes • Not applicable for zero-thickness walls[b]	Youngs (1982) Gupta et al. (2009) Jabbari et al. (2014)
Modified-HRIC	$\tilde{\phi}_f = \begin{cases} \tilde{\phi}_c & \tilde{\phi}_c < 0 \text{ or } \tilde{\phi}_c > 1 \\ 2\tilde{\phi}_c & 0 \le \tilde{\phi}_c \le 0.5 \\ 1 & 0.5 < \tilde{\phi}_c \le 1 \end{cases}$	• Inexpensive computationally • An improvement in robustness and stability of calculations • A non-linear difference between downwind and upwind • Avoid the explicit dependence on the Courant-Friedrichs-Lewy[a] (CFL) conditions	Muzaferija (1997) Muzaferija et al. (1998) Park et al. (2009)
Smoothed Heaviside	$H_\varepsilon(\alpha) = \begin{cases} -\frac{1}{2} & \alpha \le -\varepsilon \\ \frac{1}{2}\left[\left(\frac{\alpha}{\varepsilon}\right) + \frac{1}{\pi}\sin\left(\frac{\pi\alpha}{\varepsilon}\right)\right] & -\varepsilon < \alpha < \varepsilon \\ \frac{1}{2} & \alpha \ge \varepsilon \end{cases}$	• The general form of step functions • Ability for sharp interface curvature modeling	Brackbill et al. (1992) Sussman et al. (1994) Fukagata et al. (2007) Yokoi (2013)
Donor-Acceptor	Standard interpolation	• Available for quadrilateral and twisted hexahedral meshes • Not applicable for zero-thickness walls[b] • Depending on the interface orientation and local flow direction, this scheme predicts the volume fraction by pure downwinding, pure upwinding, or a blend of the two	Hirt and Nichols (1981)

[a] Making the stability of unstable numerical analysis for convective terms modelling
[b] Where two subdomains meet each other making a two-sided wall within the computational domain

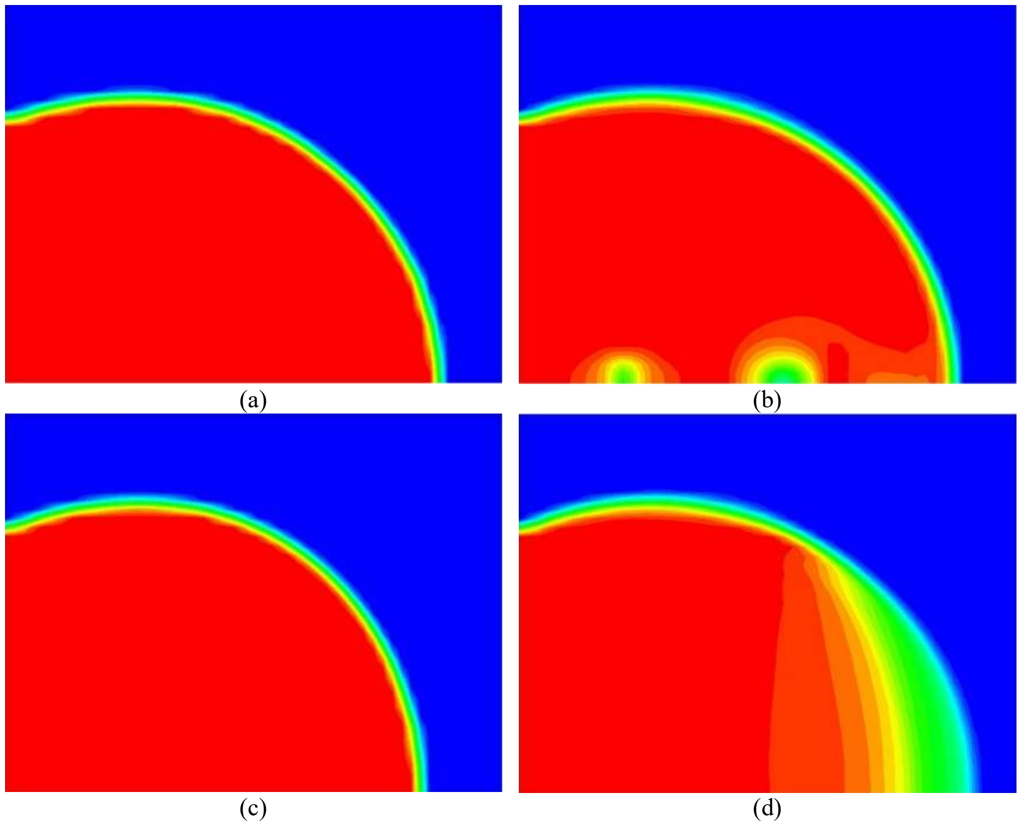

FIGURE 6.3: Contour of the volume fraction using (a) compressive interface capturing scheme for arbitrary meshes (CICSAM), (b) compressive, (c) Geo-Reconstruct, and (d) modified high-resolution interface capturing (HRIC) (the air is coloured red and the water is coloured blue)

6.3.2 Numerical Discretization Procedure and Boundary Conditions

To solve governing Eqs. (6.1) and (6.2), a consistent version of the semi-implicit method for pressure linked equations (SIMPLEC) algorithm is employed to couple pressure and velocity fields. By eliminating less important terms from the velocity equation, the SIMPLEC is able to manipulate the proper corrections (Patankar, 1980; van Doormaal and Raithby, 1984; Versteeg and Malalasekera, 2007). In the presence of straight geometry of channel, a constructed-quadratic mesh with skewness correction of 0 is allowed to be used, alleviating the convergence difficulties in the numerical simulations (Hinze, 1975; Lilly, 1992; Armsfield and Street, 1999). Non-iterative under-relaxation factors and correction tolerances for pressure and momentum are set to 1 and 10^{-7}, respectively, to accelerate the convergence and stabilize the solution (Etminan et al., 2021b). A first order noniterative time advancement (NITA) scheme is selected to decrease the computational effort over each time-step, showing a slightly downward trend as time is marching forward and scaled residuals remain in the order of 10^{-6}–10^{-7}. In this numerical analysis, pressure, momentum, and volume fraction are interpolated by the body force weighted, second-order upwind, and geo-reconstruct schemes, respectively, to obtain accurate predictions in an optimal computational expense. The quadratic upstream interpolation for convective kinematics (QUICK) scheme is selected to discretize the momentum equation and predict a higher-order difference by considering a three-point upstream weighted quadratic interpolation at the cell faces (Patankar, 1980; Versteeg and Malalasekera, 2007).

For the finite volume (FV) discretization method, variables and fluxes are kept at the centre of a control volume, but the convection terms in the governing equations need the value at the centre of a face. Hence, the gradient terms in the flow conservation equations must be modelled using a green-gauss cell-based (GGCB), green-gauss node-based (GGNB), or least squares cell-based (LSCB) method. These spatial discretization schemes are required to find the values of scalar variables, such as pressure, temperature, and the derivatives of velocity components at the faces of cells. The gradient of a scalar variable at the cell centre via the green-gauss and least-squares discretization schemes, respectively, are as follows:

$$\nabla\phi_{co} = \frac{1}{\forall}\sum_{f}\overline{\phi}_f\vec{A}_f \tag{6.8}$$

$$\nabla\phi_{co} = [J]^{-1}\Delta\phi \tag{6.9}$$

where the subscripts co and f represent the cell centre and face centre, respectively. The cell volume and the product of the face area and unit vector are shown by $\forall$ and $\vec{A}_f$, respectively, while [J] is a coefficient matrix made by the centre-to-centre distances between a cell and the neighbour cells.

The arithmetic average of the facial and nodal values of a property (ϕ) in the GGCB and GGNB, respectively, can be calculated by the following:

$$\overline{\phi}_f = \frac{\phi_{co} + \phi_{cn}}{2} \tag{6.10}$$

$$\overline{\phi}_f = \frac{1}{N_f}\sum_{n}^{N_f}\overline{\phi}_n \tag{6.11}$$

where N_f and subscript cn represent the number of nodes on the face and a property at the surrounding cell centre. The nodal value of $\overline{\phi}_n$ is calculated by a weighted average of the cell values surrounding the nodes (Holmes and Connell, 1989; Rauch et al., 1991).

The weakness and strength of each scheme are highly problem dependent, and a proper scheme varies from one problem to another. The comparable properties of the discretization schemes mentioned earlier are presented in Table 6.3. Generally, the GGNB shows the highest accuracy, computational expense, and the best compatibility with a highly skewed and distorted mesh followed by non-availability for a polyhedral mesh.

TABLE 6.3: The weaknesses and strengths of different spatial discretization schemes

Remarks	**GGCB**	**GGNB**	**LSCB**
Accuracy	●	●●●	●●
Computational cost	●	●●●	●●
Irregular (skewed and distorted) mesh	●	●●●	●●
Polyhedral mesh	●	○	●
Skewness error	●	○	○
Linear assumption of variables	●	●	●
Using node value	○	●	○
Using face value	●	○	○
Using cell value of surrounding cells	○	○	●

The number of solid circles indicates the most appropriate scheme and a hollow circle means non-availability

The pressure contours in the second unit cell are plotted in Figure 6.4 using different spatial discretization schemes for air/water with a superficial velocity ratio (dispersed phase velocity to the carrying phase velocity) of unity. All the simulations were started under the same initial conditions and the same discretization and numerical methods. In the GGCB and LSCB cases, a significant non-physical pressure jump is observed inside the bubble and exactly on the axis of the microchannel. Conversely, the pressure oscillations are seen in the liquid film region using these schemes. GGNB shows the lowest pressure oscillations in the film region and inside the bubble, although some insignificant non-physical pressure jumps remain in the film and at the rear cap regions of the air bubble.

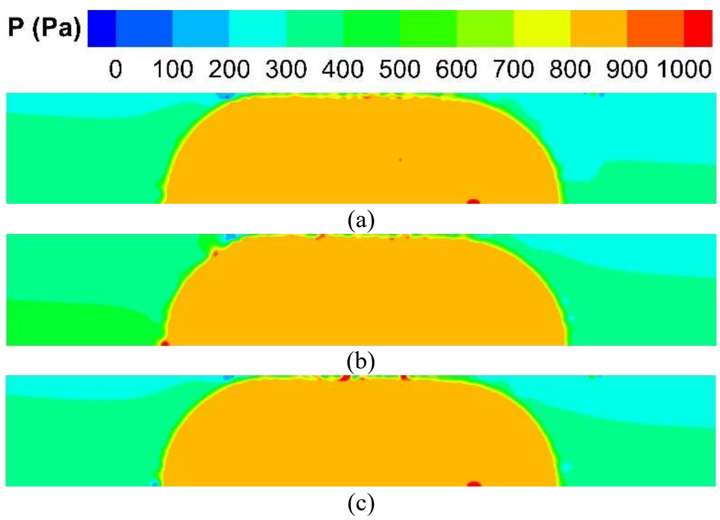

FIGURE 6.4: Pressure contour plots using (a) green-gauss cell based (GGCB), (b) green-gauss node-based (GGNB), and (c) least squares cell-based (LSCB) schemes in the second unit cell for air / water with a superficial velocity ratio of unity

Figure 6.5 displays the pressure distributions and the axial velocity component, on the axis of the microchannel and inside the second unit cell, using different spatial discretization schemes. In the presence of a rectangular, structured mesh (i.e., a skewness ratio of zero), these schemes predict very similar pressures. At the gas / liquid interface on the microchannel's axis (X/D~– 0.95 and 0.9), the GGNB scheme predicts the pressure with the lowest ripples and a value between the other schemes. Also, the GGCB and LSCB schemes predict the axial velocity with fluctuations at the gas / liquid interfacial region. Conversely, the GGCB scheme overestimates the axial velocity inside and outside the nose cap with an unexpected peak. Therefore, it can be reasonably concluded that GGNB shows more accuracy compared to other schemes in two-phase straight microchannel flows. Figure 6.5 also shows the field velocity vectors coloured by the pressure and axial velocity component on 14 vertical iso-surfaces using the GGNB scheme. The rapid change of the slug curvatures in the nose and rear transition regions causes a significant change in the velocity distributions which is consistent with the data in the literature (Gupta et al., 2009; Fukagata et al., 2007). The velocity profile starts to be developed as a parabolic distribution soon after the slug.

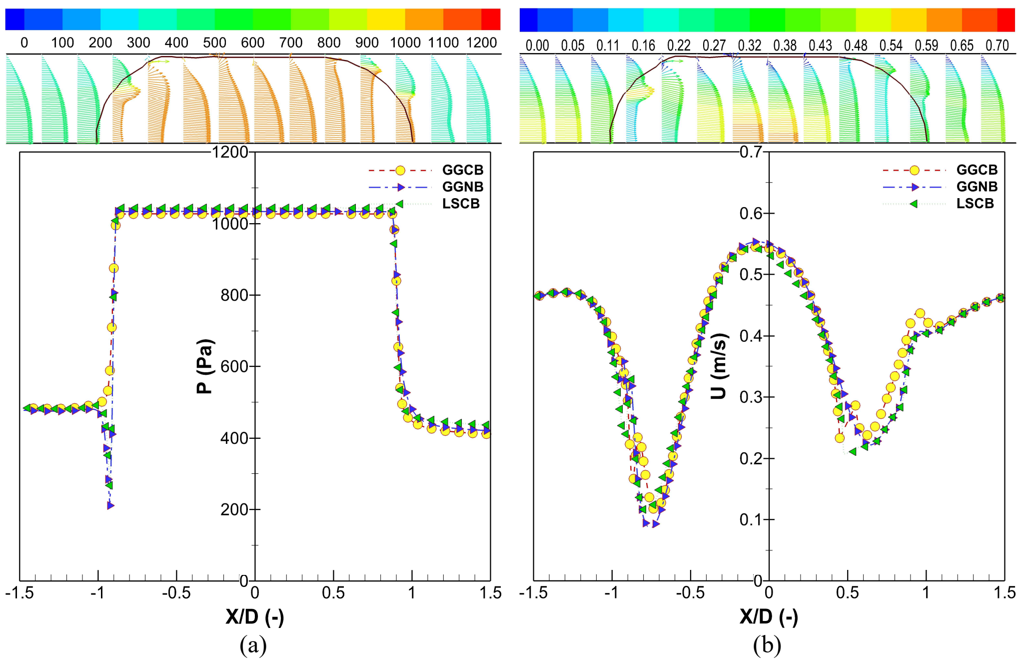

FIGURE 6.5: Distributions of (a) pressure and (b) axial velocity on the microchannel's axis in the second unit cell using different spatial discretization schemes for air/water with a superficial velocity ratio of unity. The field velocity vectors coloured by the pressure and axial velocity component are also shown on the top (the unit cells are aligned at the middle, X/D=0)

6.4 Results

6.4.1 Grid Independence Study and Numerical Method Validation

The computational domain is divided into two regions: core and near wall. A refined mesh is used near the channel's wall for capturing the accurate interface and liquid film and a coarse mesh is used in the rest of the channel for limited computational cost (e.g., Gupta et al., 2009; Asadolahi et al., 2012; Sontti and Atta, 2017; Fletcher and Haynes, 2017). This work follows the same mesh independence as in the study conducted by Etminan et al. (2021b) over a thickness of 15 and 20 µm for the GL and LL flows, respectively. In both flow cases, five grid sizes of 3, 2.5, 2.14, 1.88, and 1.67 µm are used, and the last three sizes show mesh-independent results. Consequently, the grid size of 2.14 µm is assumed over the film region. It is also found that further mesh refinement not only enhances the computational expense but also induces a nonphysical pressure jump within the film region (Gupta et al., 2009; Etminan et al., 2021b). To ensure that the predicted results are not dependent on the size of the mesh in the core region, liquid film thickness and slug length are evaluated for five different equal-length mesh numbers of 1000, 1400, 1600, 2000, and 2500 in the axial direction. Table 6.4 presents the corresponding numerical results for both GL and LL flows for a superficial velocity ratio of unity and without channel expansion. As can be seen, no significant changes are observed in the film thickness and slug length after three grid miniaturizations with less than 1% deviation between the last two grid cases. Therefore, an independent mesh size of 5 × 5 µm is adopted for the core region of the microchannel, providing accurate solutions and resulting in total numbers of 108000 and 112000 for the GL and LL flows, respectively.

TABLE 6.4: Liquid film thickness and slug length for different number of grids in gas-liquid (GL) and liquid-liquid (LL) cases for a superficial velocity ratio of unity and without expansion

Flow	**Number of Grids**	**Liquid Film Thickness, δ** (µm)	**Error (%)**	**Slug Length** (µm)	**Error (%)**
GL	31 000	12.52	—	972.3	—
	56 000	11.86	5.565	931.6	4.369
	72 000	11.31	4.863	909.7	2.407
	108 000	10.94	3.382	900	1.078
	165 000	10.87	0.644	896.1	0.435
LL	33 000	17.25	—	831.7	—
	58 800	16.27	6.023	790.5	5.212
	75 200	15.38	5.787	770.3	2.622
	112 000	14.73	4.413	760	1.355
	170 000	14.61	0.821	754.4	0.742

Table 6.5 presents a list of references and respective correlations to validate the results of this study for air / water two-phase flow in a straight microchannel without an expansion. Mean film thickness is averaged over the steady film region where the curvature of the interface likely becomes uniform. The exact location of the interface to measure film thickness is assumed where the volume fraction is 0.5 (Etminan et al., 2021b). Computations fluid dynamics (CFD) results agree very well with the calculations by lubrication theory (Bretherton, 1961; Aussillous and Quéré, 2000) over a moderate range of the capillary number. Furthermore, decreasing Ca causes the deviation from lubrication theory to reduce to 1.9%. Increasing Ca (or the ratio of viscous to capillary effects), the thickness of the liquid film is also increased, resulting in a lower resistance between the air bubble and the solid wall of the channel. The results of the LL flow are also summarized in Table 6.6, which show a reasonable agreement to the other calculations using correlations from lubrication theory (e.g., Bretherton, 1961; Aussillous and Quéré, 2000; Kreutzer et al., 2001). The present results show more deviation from the analytical data (e.g., Irandoust and Andersson, 1989) and experimental data (e.g., Eain et al., 2013) because of significant different in experiments setup, tube diameter, and physical properties of operational phases. For the experimental conditions of Eain et al. (2013) the correlation is valid for Ca between 0.002–0.003 for water/dodecane flow. The correlation proposed by Aussillous and Quéré (2000) over a wide range of Ca values is used to validate our results, indicating a mean absolute deviation of ~7.7%.

The profiles of an air bubble and a water slug in a fully developed region of a straight channel are illustrated by Figure 6.6 for a superficial velocity ratio of unity. The profiles of interface of the present study and those extracted from Gupta et al. (2009) are compared by aligning the slugs' tails and noses together. The exact locations of the interfaces are extracted by WebPlotDigitizer software and the coordinate axes are nondimensionalized by the channel diameter and radius. The air bubble length predicted by Gupta et al. (2009) is longer due to the considerable difference between thermophysical properties and phase superficial velocities. However, the rear cap curvatures agree very well, which is also achieved for the nose curvatures when the noses are matched together. Some ripples are near the tail meniscus due to pressure fluctuations, interaction between surface tensions, and

TABLE 6.5: Comparison of liquid film thickness values in gas-liquid (GL) flow with correlations in the literature for a superficial velocity ratio of unity and without expansion

Ref.	Correlation	Liquid Film Thickness, δ (μm)			
		Capillary Number, Ca			
		0.01237	0.00742	0.00618	0.0052
Fairbrother and Stubbs (1935)	$0.5\mathrm{Ca}^{1/2}$	13.90	10.77	9.83	9.01
Bretherton (1961)	$1.338\mathrm{Ca}^{2/3}$	17.82	12.68	11.22	10.00
Irandoust and Andersson (1989)	$0.36\left(1\text{-}e^{-3.08\mathrm{Ca}^{0.54}}\right)$	22.48	17.63	16.13	14.82
Aussillous and Quéré (2000)	$1.34\mathrm{Ca}^{2/3}/\left(1+3.35\mathrm{Ca}^{2/3}\right)$	15.20	11.30	10.14	9.14
Kreutzer et al. (2001)	$0.36\left(1\text{-}e^{-2.13\mathrm{Ca}^{0.52}}\right)$	17.56	13.79	12.63	11.62
Han and Shikazono (2009)	$\dfrac{1.34\mathrm{Ca}^{2/3}}{(1+3.13\mathrm{Ca}^{2/3}+0.504\mathrm{Ca}^{0.672}\mathrm{Re}^{0.589}\text{-}0.352\mathrm{We}^{0.629})}$	16.70	11.93	10.60	9.48
Present Study	(N/A)	16.27	12.22	10.94	9.81

TABLE 6.6: Comparison of liquid film thickness values in liquid-liquid (LL) flow with correlations in the literature for a superficial velocity ratio of unity and without expansion

Ref.	Correlation	Liquid Film Thickness, δ (μm)			
		Capillary Number, Ca			
		0.02673	0.01604	0.01336	0.01123
Bretherton (1961)	$1.338\mathrm{Ca}^{2/3}$	29.79	21.20	18.76	16.71
Irandoust and Andersson (1989)	$0.36\left(1\text{-}e^{-3.08\mathrm{Ca}^{0.54}}\right)$	31.78	25.34	23.30	21.48
Aussillous and Quéré (2000)	$1.34\mathrm{Ca}^{2/3}/\left(1+3.35\mathrm{Ca}^{2/3}\right)$	23.05	17.56	15.87	14.38
Kreutzer et al. (2001)	$0.36\left(1\text{-}e^{-2.13\mathrm{Ca}^{0.52}}\right)$	24.90	19.79	18.19	16.78
Han and Shikazono (2009)	$\dfrac{1.34\mathrm{Ca}^{2/3}}{(1+3.13\mathrm{Ca}^{2/3}+0.504\mathrm{Ca}^{0.672}\mathrm{Re}^{0.589}\text{-}0.352\mathrm{We}^{0.629})}$	23.87	17.98	16.19	14.64
Eain et al. (2013)	$0.35\mathrm{Ca}^{0.354}\mathrm{We}^{0.097}$	29.42	22.24	20.12	18.29
Present Study	(N/A)	21.15	16.34	14.73	13.37

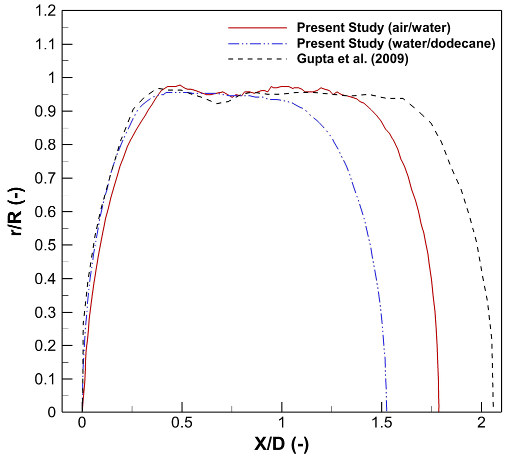

(a)

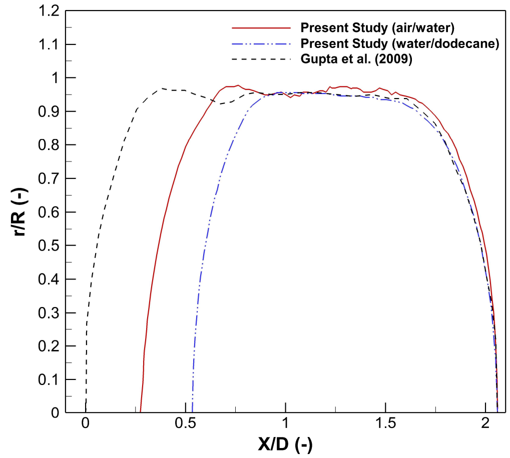

(b)

FIGURE 6.6: Comparison of Taylor slug profiles aligned at (a) tails and (b) noses in a microchannel without diameter expansion and for a superficial velocity ratio of unity

viscous forces in the film region, as also addressed by Gupta et al. (2009). Higher Re/Ca ratios, which are caused by lower viscosity fluids in the GL flow compared to the LL flow, increases the radii of the air bubble and the nose hemisphere.

6.4.2 Discussion

In this section, results of the diameter sudden expansion on the GL and LL two-phase Taylor flow are investigated and discussed. In the following simulations, the time is sufficiently long to achieve fully developed flow, then the numerical analyses are conducted and the data is collected. In the present study, the slug flow regime is the primary flow pattern in all microchannels. Figure 6.7 illustrates the evolution of air-bubble formations and reshaping with time, for a superficial velocity ratio of unity. A five-stage slug formation process involves introducing, expanding, contracting, necking, and breakup. The radii of the air-bubble in the GL flow and water-slug in the LL flow are dominantly affected by the channel's radius and the interaction between the wall and the phases. Greater density difference in GL flow compared to LL flow ($\Delta\rho_{GL} = 4.1\Delta\rho_{LL}$) delays the breakup and makes the air bubbles longer. The small capillary diameter also causes the air-bubbles to be more elongated compared to water slugs. The apparent viscosity ratio of the LL flow is significantly greater than that of the GL ($\mu_w/\mu_d = 30.87\ \mu_a/\mu_w$). This viscosity ratio creates a more stable interface, particularly near the microchannel wall. Also, in the near-wall region, the contribution of cohesion and adhesion forces cause appreciable diffusion around the air-bubble and a nonphysical pressure jump. More numerical diffusion in GL flow creates very small bubbles on the axis of the channel, after necking and breakup, which dissipates as the bubble travels downstream.

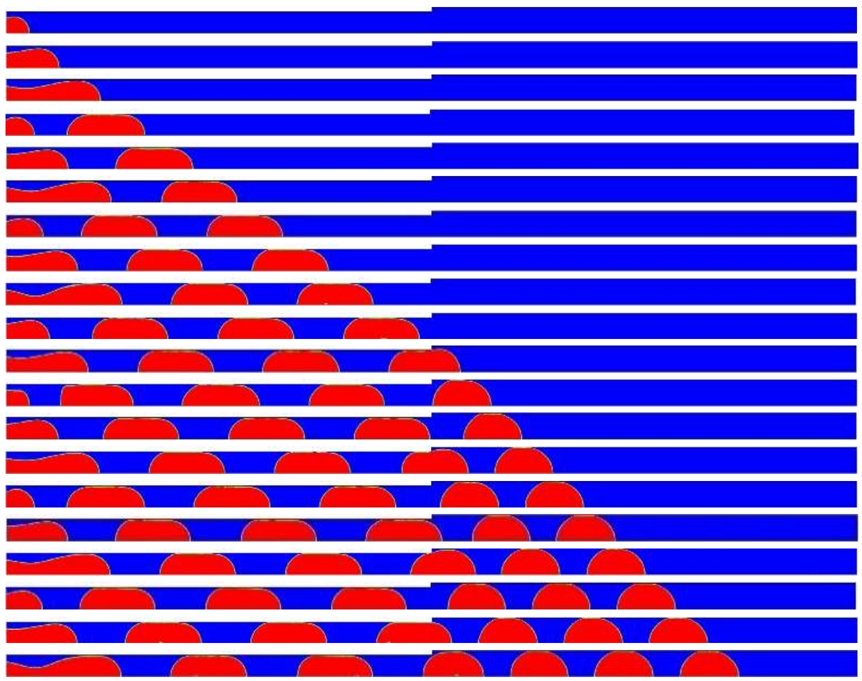

FIGURE 6.7: Time-history of air volume fraction plots for a superficial velocity ratio of unity, diameter expansion of 25%, and at every 1 ms (The air is coloured red and the water is coloured blue)

Air volume fraction plots around the sudden diameter expansion region at every 0.1 ms are illustrated in Figure 6.8. As the air-bubble is approaching the expansion region, the pressure gradient between the bubble and plug decreases up to ~18%, resulting in more diffusion and a thicker interface. The sudden cross-section expansion impacts the downstream flow characteristics, as well as upstream flow by introducing oscillations in the interface. Although the oscillation is concentrated on the interface, the pressure distribution on the microchannel's axis, within the air bubble, shows fluctuations due to a constant pressure inside the bubble.

Figure 6.9 shows the influence of the channel diameter expansion on the shape of air-bubbles and water-slugs for GL and LL Taylor flows at 40 ms. As the channel diameter is increased the slugs and plugs are shortened in the channel's axial direction. The bullet-like slugs are deformed to a spherical shape with no uniform film region, particularly for LL flow. This is a consequence of decreased shear force on the bullet shaped slugs due to the lower dispersed phase velocity. The results also revealed that the lower pressure gradient per unit length after the diameter expansion enhances flow circulation inside the slugs, in particular within the front half, which agrees well with Fukagata et al. (2007). This is due to the lesser influence of the shear wall on the velocity of slugs.

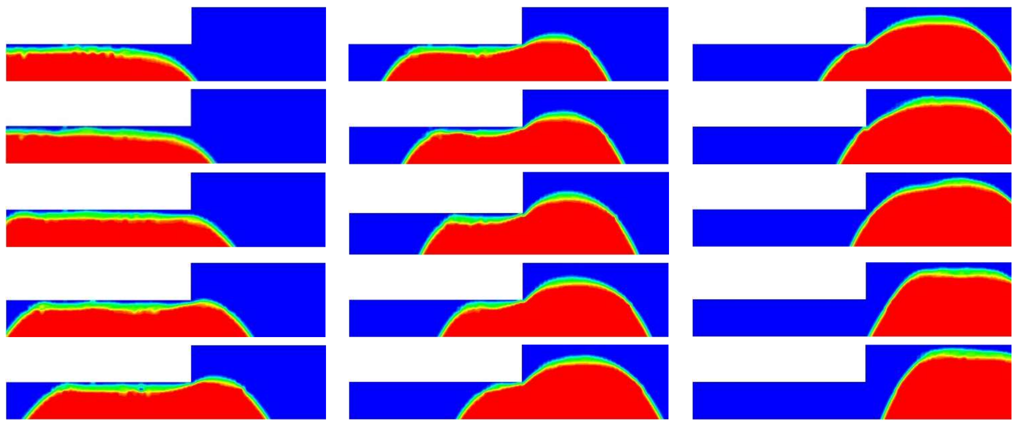

FIGURE 6.8: Enlarged snapshots of an air bubble passing the sudden expansion cross-section, in a sequence of 0.1 ms, for a superficial velocity ratio of unity and a 25% diameter expansion (enlargement in the radial direction is intentionally displayed twice the axial direction; the air is coloured red and the water is coloured blue)

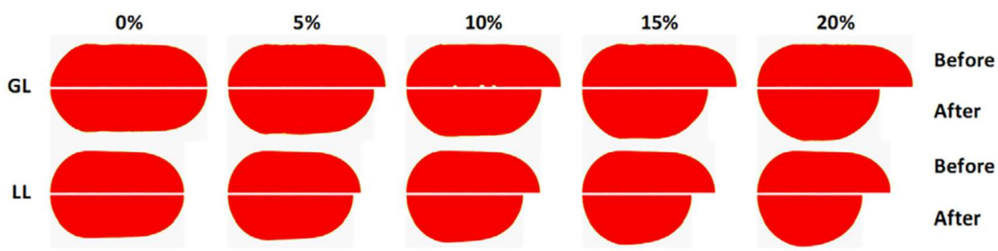

FIGURE 6.9: Effects of various diameter expansions on the shape of slugs in the gas-liquid (GL) and liquid-liquid (LL) flows for superficial velocity ratio of unity

Figure 6.10 shows the variations of air-bubble and water-slug lengths within the microchannel for different diameter expansions. Regarding the lengths of slugs and plugs and breakup frequency, there are seven fully detached air bubbles and eight shorter fully detached water slugs throughout the channel in GL and LL flows, respectively. The influence of diameter expansion on the characteristics of upstream flow is insignificant compared to the region after diameter enlargement. Each 5% diameter expansion increases the cross-sectional area by ~110%, decreases the mean slug length by 8.9%, 6.2%, 7.6%, and 3.3% for air-bubble, and by 5.9%, 5.2%, 5.9%, and 5.4% for water-slug, indicating a smoother decline in the LL flow. Due to the greater density difference between the phases for GL compared to LL, the effects of diameter expansion on slug length are also significantly greater. Furthermore, each 5% sudden diameter expansion affects the fully developed condition by a slight change of air-bubble and water-slug lengths in the order of ~1.6% throughout the channel for GL and only after the expansion section for the LL.

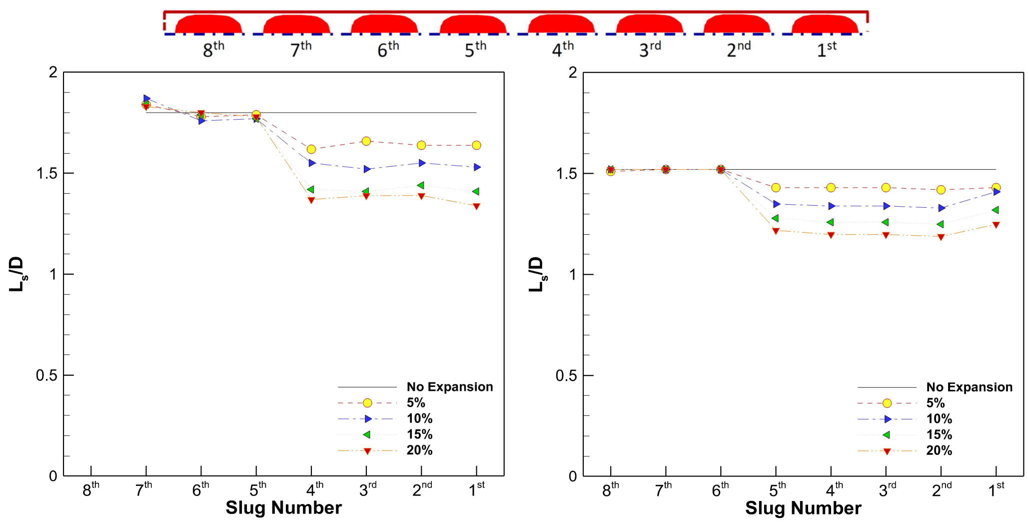

(a) (b)

FIGURE 6.10: Distributions of dimensionless slug lengths within the microchannel for superficial velocity ratio of unity at 20 ms in terms of the diameter expansion for (a) air/water (b) water / dodecane flows

The characteristics of the air bubble and water slug formation for different superficial velocity ratios are presented in Tables 6.7 and 6.8. At the lowest velocity ratio (0.25), the high inertia of the carrying flow causes the slug formation to lag and only two slugs are generated. As the dispersed phase velocity is increased, three breakups occur and the same size air-bubbles and water slugs are generated. It causes more elongated slugs and more-shortened liquid plugs. Gupta et al. (2009) showed that the non-dimensional lengths (L/D) of air-bubble and water-plug are 2 and 1.3, respectively. More recently, Qian et al. (2019) employed numerical and experimental techniques to find a range of 1.56–2.07 for slug length and 2.07–3.02 for plug length. The difference between the lengths identified compared to the results in this paper is likely due to different channel diameters, phase properties, and flow conditions. The results show that the length of an air-bubble is longer than that of a water-slug, with the highest differences of 18.4% and 13.2% at a velocity ratio of unity before and after the expansion, respectively. Furthermore, the lengths of the two subsequent slugs slightly differ from each other while travelling through the channel to reach a fully developed condition, indicating GL's higher tendency for Taylor flow condition compared to LL. Recently, a comprehensive review on the hydrodynamics of Taylor flow through mini- and microchannels was published (Etminan et al., 2021a). It shows the dependency of slug length on the properties of phases, volumetric flow rate ratio, gas holdup, and nondimensional numbers.

The measurement of film thickness is another major area of study in Taylor flow in microchannels. Etminan et al. (2022a) summarized a list of correlations for liquid film thickness in microchannels and some have been used for validation in this study. The measured film thicknesses presented in Tables 6.7 and 6.8 show that the mean values of the liquid film thickness for GL, with a confidence level of 95%, are 11.38 ± 2.15% μm and 9.22 ± 4.62% μm before and after the expansion, respectively. The mean values of the liquid film thickness for LL with a confidence level of 95% are 14.43 ± 3.1% μm and 14.25 ± 6.85% μm before and after the expansion, respectively. Therefore, the averaged film thickness for LL is 26.8% and 54.5% greater than those for GL before and after the expansion, respectively, which can be attributed to the greater viscosity effects of LL flow. As the dispersed water velocity is increased to 0.4 ms^{-1} in LL flow, the high inertial forces accompanied by an apparent viscosity ratio (μ_w/μ_d) of 0.64 causes a significant change in the flow pattern, from a segmented regime to a slug / annular regime. The flow breakup is not observed at the highest superficial velocity ratio of 4 for LL due to the low inertia of the carrying phase flow around the perimeter of the microchannel.

Different steps of a slug evolution are periodic with a constant frequency and the length and shape of the generated slugs are kept constant. Consequently, the flow characteristics can be studied in only a unit cell consisting of a single air or water slug and two halves of the adjacent liquid plugs before and after the expansion, as illustrated in Figure 6.11. The figure shows the pressure distribution on the channel's axis, inside a unit cell, before / after the diameter expansion. A diameter expansion affects the pressure distribution slightly more in upstream compared to downstream, particularly for LL flow. Pressure distribution inside the slugs increases as the diameter increases,

TABLE 6.7: Characteristics of the air / water Taylor flow for diameter expansion of 25% at different superficial velocities

Velocity (ms^{-1})		**Dimensionless Air Slug Length** (L_sD^{-1})						**Dimensionless Water Plug Length** (L_pD^{-1})						**Mean Liquid Film Thickness, δ^a** (μm)	
Air	**Water**	4th / 8th	3rd / 7th	2nd / 6th	1st / 5th	**Mean Length** Before	After	4th / 8th	3rd / 7th	2nd / 6th	1st / 5th	**Mean Length** Before	After	Before	After
0.10	0.40	1.15	1.09[b]	0.98	1.00	1.15	0.99	2.96[c]	3.02	2.32	2.38	3.02	2.35	11.54	—
		—	—	—	—			—	—	—	—				
0.15	0.35	1.33	1.05	1.05	1.05	1.33	1.05	2.09	1.49[b]	1.27	1.30	2.10	1.28	11.74	9.00
		—	—	1.36	1.31			—	—	0.98[c]	2.10				
0.20	0.30	1.25[b]	1.23	1.21	1.22	1.55	1.22	1.60	0.88	0.92	0.87	1.58	0.89	11.17	9.03
		—	—	1.55	1.55			—	—	1.53[c]	1.57				
0.25	0.25	1.37	1.39	1.39	1.34	1.80	1.37	1.05[b]	0.63	0.60	0.63	1.16	0.62	10.91	9.40
		—	1.83	1.80	1.78			—	0.76[c]	1.15	1.18				
0.30	0.20	1.57	1.57	1.56	1.57	2.09	1.57	0.83[b]	0.43	0.45	0.45	0.90	0.44	11.90	10.25
		—	2.14	2.08	2.05			—	0.54[c]	0.89	0.92				
0.35	0.15	2.21[b]	1.89	1.91	1.90	2.60	1.90	0.68	0.30	0.30	0.29	0.67	0.30	11.20	9.14
		—	—	2.61	2.58			—	—	0.69[c]	0.66				
0.40	0.10	3.67	2.93[b]	2.65	2.65	3.67	2.65	0.52[c]	0.53	0.20	0.20	0.53	0.20	11.18	8.50
		—	—	—	—			—	—	—	—				

[a] This thickness is averaged by the film thickness in the flat region(s) of the fully detached bubbles, not using a bubble immediately after breakup or passing expansion.

[b] This length is located at the expansion of the microchannel and is not considered to compute the mean value.

[c] This length is measured between a fully detached bubble and a non-fully detached bubble and is not considered to compute the mean value.

TABLE 6.8: Characteristics of the water / dodecane Taylor flow for diameter expansion of 25% at different superficial velocities

Velocity (ms^{-1})		**Dimensionless Water Slug Length (L_sD^{-1})**						**Dimensionless Dodecane Plug Length (L_pD^{-1})**						**Mean Liquid Film Thickness, δ^a** (μm)	
Water	**Dodecane**	4th / 8th	3rd / 7th	2nd / 6th	1st / 5th	**Mean Length** Before	After	4th / 8th	3rd / 7th	2nd / 6th	1st / 5th	**Mean Length** Before	After	Before	After
0.10	0.40	1.08	1.06	1.01	1.01	1.08	1.03	2.83	2.70[b]	2.31	2.35	2.83	2.33	13.45	—
		—	—	—	1.09			—	—	—	1.55[c]				
0.15	0.35	1.03[b]	1.08	1.08	1.08	1.24	1.08	1.94	1.36	1.39	1.40	1.91	1.38	13.93	—
		—	—	1.24	1.24			—	—	1.68[c]	1.88				
0.20	0.30	1.13	1.13	1.13	1.14	1.37	1.13	0.79	0.83	0.78	0.70	1.28	0.78	14.60	—
		—	1.36	1.37	1.34[b]			—	1.24[c]	1.28	1.28				
0.25	0.25	1.20	1.20	1.19	1.25	1.52	1.21	0.47	0.46	0.47	0.36	0.90	0.44	14.71	13.53
		1.52	1.52	1.52	1.22			0.87[c]	0.90	0.90	0.79[b]				
0.30	0.20	1.38	1.38	1.38	1.48	1.78	1.40	0.27	0.28	0.28	0.30	0.67	0.28	15.07	13.75
		1.78	1.78	1.79	1.38			0.63[c]	0.67	0.67	0.68				
0.35	0.15	1.72	1.73	1.75	1.90	2.23	1.78	0.25[b]	0.18	0.18	0.18	0.51	0.18	14.81	15.46
		—	2.21	2.25	2.24			—	0.48[c]	0.51	0.51				
0.40	0.10	—	—	2.55[b]	6.09	—	6.09	—	—	0.62[c]	0.25	—	0.25	—	—
		Refer to discussion in text						Refer to discussion in text							

[a] This thickness is averaged by the film thickness in the flat region(s) of the fully detached bubbles, not using a bubble immediately after breakup or passing expansion.

[b] This length is located at the expansion of the microchannel and is not considered to compute the mean value.

[c] This length is measured between a fully detached bubble and a non-fully detached bubble and is not considered to compute the mean value.

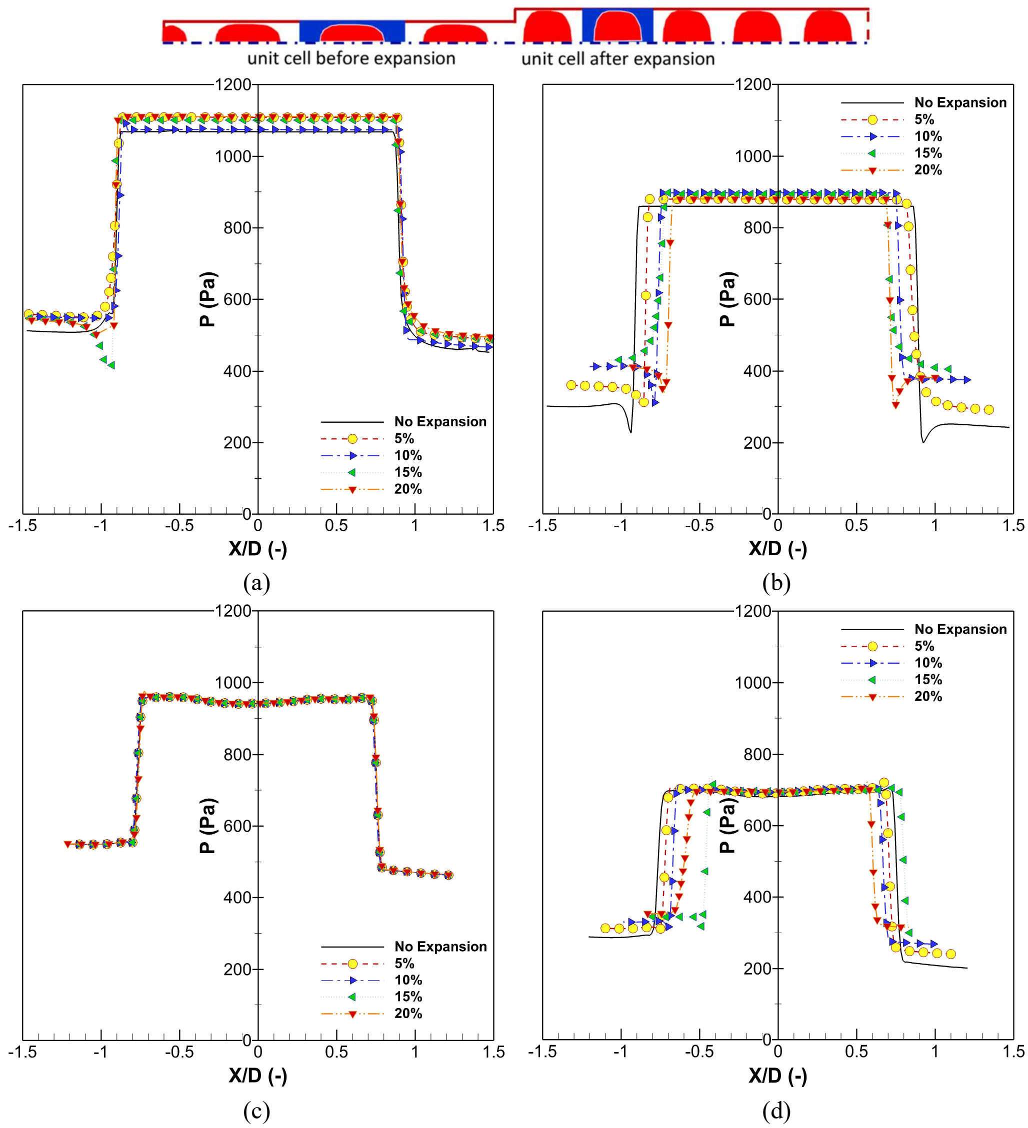

FIGURE 6.11: The effects of diameter expansion on pressure distribution on the microchannel's axis within a unit cell before (a, c) and after (b, d) expansion in air / water (a, b) and water / dodecane (c, d) flows with a superficial velocity ratio of unity (the unit cells before and after diameter expansion are aligned at the middle, X/D=0, shown on the top)

and the length of the slugs is decreased, which causes the most significant change in pressure distribution around the slug caps. There is a low-pressure region next to the rear cap of the slugs as observed by Gupta et al. (2009) and Kreutzer et al. (2005c) due to the interface undulation.

In Taylor flow, slug curvature, slug and plug length, and liquid film thickness are three key parameters affecting the pressure drop within a unit cell that can also be divided into three main parts: plug, film, and cap (e.g., Kreutzer et al., 2005c; Fouilland et al., 2010; Ni et al., 2017):

$$\Delta P_{uc} = \Delta P_p + \Delta P_f + \Delta P_{cap} \tag{6.12}$$

The pressure drop distributions in the uniform liquid film region remained constant and ΔP_f became insignificant, as displayed in Figure 6.11, which agrees with Fouilland et al. (2010). Within the uniform film region, however, the normal stress at the interface is no longer present, and the pressure difference can be predicted using the Laplace pressure. In addition to the pressure loss components in Eq. (6.12), an energy expenditure in liquid phase caused by the frequency of renewal of the interfacial surface must be taken into account (Abiev, 2011). The theoretical interfacial pressure gradient in the hemispherical nose region of the first air bubble is on the order of $2\sigma/R_b$, whereas the numerical simulations predict accurately for different superficial velocity ratios as illustrated in Figure 6.12. The CFD calculations are in excellent agreement with the theoretical results by showing the mean absolute deviations of 1.39% and 0.59% before and after diameter expansion, respectively. These differences are attributed to the developing flow conditions and a non-exact hemispherical profile assumption of the air-bubbles cap.

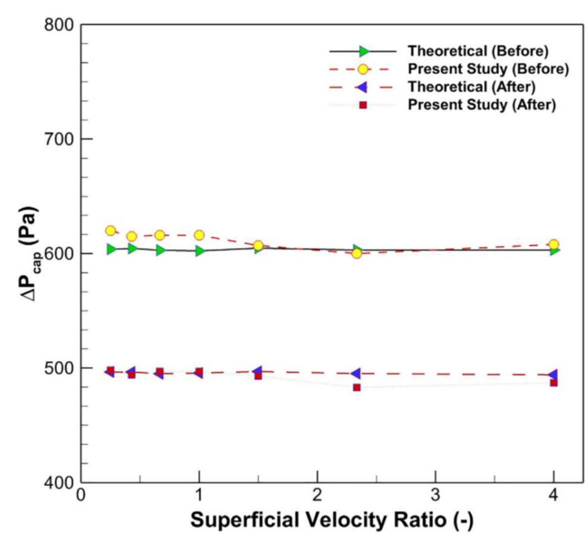

FIGURE 6.12: Interfacial pressure difference in the nose hemispherical cap of air bubble before and after a 25% diameter expansion versus different superficial velocity ratios

6.5 Conclusions

The present study reported a series of numerical analyses of air / water and water / dodecane two-phase flows in a microchannel with a sudden diameter expansion. The flow physics associated with the different physical properties, superficial velocities, and diameter expansions provide insight into Taylor flow and were evolved within the entrance, transition (i.e., over the diameter expansion section), and fully developed regions. It was shown that an increase in superficial velocity ratio elongated air bubbles and water slugs. Another interesting finding was that the higher apparent viscosity ratio for LL flow lessened the fluctuation of the interface within the uniform film region and enhanced the thickness of the liquid film. The results also revealed that the diameter expansion increased the pressure distribution inside the slugs, shortened the slugs, and changed the pressure around the slug caps. In conclusion, the numerical results of this study offered a greater understanding of two-phase Taylor flow in capillary microchannels, and the methodology reported herein can be also extended to either heat or mass transfer applications in these types of segmented flow.

Chapter 7

Experimental and Numerical Analysis of Heat Transfer and Flow Phenomena in Taylor Flow through a Straight Mini-channel[1]

7.1 Overview

This chapter experimentally and numerically investigates the hydrodynamic characteristics, and heat transfer of developing and fully developed laminar liquid-liquid Taylor flows. The problem is conducted in circular mini-channels with different diameters subjected to a constant wall temperature boundary condition. An experimental setup is designed employing an open-loop water / oil two-phase non-boiling flow at mini scale tubing sizes of 1.42, 1.52, and 1.65 mm. Two silicone oils with the dynamic viscosities of 1 and 5 cSt at several volumetric flow rates are used to establish segmented flow. The impacts of the channel diameter, viscosity, and flow rate ratio on the flow pattern, pressure drop, film thickness, and heat transfer rate are discussed. It is found, in good agreement with the literature, that the pressure drop generated by the interface increases the total pressure loss up to 200% compared to the single-phase flow. Furthermore, introducing segmented water slugs enhances the rate of heat transfer significantly as the dimensionless thermal length decreases. The results also explain how recirculating regions within the slugs influence the film region and the physics of backflow. Furthermore, introducing segmented water slugs enhances

[1] This chapter is written based on the materials, which are intended to be submitted to the Journal of Heat Transfer.

the heat transfer rate significantly as the dimensionless thermal length decreases. A significant relation between the recirculating regions and heat transfer has been demonstrated for the first time.

7.2 Introduction

Two-phase flow refers to the interactive flow of two components, called dispersed and continuous, commonly occurring in channels. Superficial phase velocity ratio, phase viscosity, and channel diameter characterize the pattern of two-phase flow by the terminology of bubbly, Taylor (a.k.a. bubble train, segmented, and slug), churn, and annular (Kreutzer et al., 2005c). Mainly, gas-liquid and liquid-liquid Taylor flows consist of a train of equal-length bubbles / slugs with the same diameter as that of the tube, which is surrounded by a thin layer of carrying phase and is separated by carrying phase plugs. Through millimetric and microfluidic devices, two-phase Taylor flows have been a significant drive in almost all industrial applications to reduce the size and enhance heat and mass transport phenomena. Due to the length and frequency of the dispersed phase slugs efficiently control the hydrodynamic characteristics and improve the rates of heat and mass transfer, the Taylor flow regime is pertinent to many energy-related engineering applications, such as cooling devices (Kercher et al., 2003; Che et al., 2012; Dai et al., 2015) and compact heat exchangers (e.g., Ghani et al., 2017; Abdollahi et al., 2020). Apart from microfluidic heat exchange applications, many reacting systems and chemical engineering applications involve gas-liquid and liquid-liquid Taylor flows, including fuel cells (e.g., Jhong et al., 2013; Cao et al., 2021), micromixers (e.g., Su et al., 2012; Wu et al., 2016), microreactors (e.g., Sotowa et al., 2009; Fu et al., 2015; Cao et al., 2022), absorption reaction (e.g., Shao et al., 2010; Wangfeng et al., 2013; Pang et al., 2020), rectification (e.g., Osorio-Nesme et al., 2012), nitrification (e.g., Yao et al., 2019), extraction (e.g., Baier, 1999; Takeshita, 2010), polymerization (e.g., Kataoka et al., 1995; Mohmmed et al., 2021), and material synthesis (e.g., Elvira et al., 2013) to name but a few.

Energy dissipation, heat and mass transfers, and material consumption are critical factors in energy-related and process applications. Utilizing Taylor flow in such applications can aim for more compact heat exchangers and optimal operational conditions, which is in line with sustainable development. Understanding Taylor flow's hydrodynamic characteristics and thermal behaviours are of interest to meet this achievement. Several microchannel heat exchangers have been designed to enhance heat transfer rate, such as diverging, converging, and wall-mounted vortex generators. All the designs can increase convective surface area and flow circulation (Zhang et al., 2020a). Due to dominant surface tension and viscous effects in such channels, any change in flow structure may lead to significant variations in pressure drop, wall-to-bulk flow temperature difference, and phase concentration throughout the channels. Therefore, dispersed bubble or slug formation (e.g., Zhao et al., 2006; Dore et al., 2012b; Deendarlianto, 2019; Lim et al., 2019; Li et al., 2020), slug breakup (e.g., Hibiki and Ishii, 2000; Kreutzer et al., 2005b; Komrakova et al., 2014), liquid film thickness (Patel et al., 2017), slug length (e.g., Kreutzer et al., 2005c and 2005d; Song et al., 2019; Zhang et al., 2020b), slug velocity (e.g., Qian et al., 2019), pressure drop (e.g., Kreutzer et al., 2005d; Walsh et al., 2009; Warnier et al., 2010; Jovanović et al., 2011), and heat and mass transfer coefficients (e.g., Yao et al., 2020; Vasilev et al., 2022) are of interest. The interactions of convection and advection either inside or outside of bubble / droplet Taylor flow throughout the capillaries are responsible for providing sustainable optimal flow conditions where the pressure drop is low and heat and mass transfer are high. To sum up, a superior comprehension of Taylor flow hydrodynamics and heat / mass transfer mechanisms enables us to attain these targets.

Taylor flow increases the mass transfer rate in the radial direction, which is desired, while decreasing the axial transport. There are two different two-phase slug flows called: a traditional plug or slug flow and a segmented or Taylor flow. Traditional two-phase slug flow includes a range of lengths, shapes, and distributions of dispersed phase slugs in the carrier phase, making the analysis much more complicated. Conversely, Taylor flow that shows a uniform distribution of same-sized dispersed slugs, called a train, which is more applicable to theoretical analysis. In addition to the geometrical features and thermophysical properties, flow circulation within the Taylor slugs, the hydrodynamic and thermal boundary conditions introduce more complexities for analyzing such flows.

This chapter presents a combination of experimental and numerical methods to investigate hydrodynamic characteristics and the heat transfer rates of water / oil Taylor flow through mini-scale channels. There is a paucity of research exploring the effects of the channel's diameter, superficial velocities ratio, and viscosity on slug curvature and film thickness in gas-liquid and liquid-liquid Taylor flows. Therefore, our experiments and numerical simulations are aimed at addressing this deficit in the literature by analyzing velocity field, flow pattern, pressure drop, and heat transfer rate qualitatively and quantitatively.

7.3 Experimental Procedures

7.3.1 Experiment Setup

The schematic of our experimental facility at the Microfluidics Laboratory is shown in Figure 7.1. This experimental setup aims to: (1) produce a steady train of slugs, where the length and frequency of slugs can be precisely controlled by phase volumetric flow rate and the phase flow rate fraction, (2) capture high-resolution snapshots of flow patterns to be analyzed for determining hydrodynamic characteristics, (3) measure pressure drop over a constant length of tubing, and (4) provide a thermal test section under a constant wall temperature boundary condition. Each of these aspects will be explained in the following before discussing the results.

A pair of high-precision Harvard PHD 2000 programmable syringe pumps are used as a fluid supplying unit to establish a continuous pulsation-free distilled water / silicone oil Taylor flow using two or four Hamilton glass gastight syringes. The tubing system consists of a tee junction and a set of straight transparent mini-channels with inner diameters of 1.42, 1.52, and 1.65 mm to provide two-phase laminar flow. An Omega pressure transmitter, model PX409-001DWU5V, with a pressure range of 0–1 psi measures the pressure drop over a length of 200 mm. The flow pattern is visualized to measure slug length, liquid film thickness, and slug curvature prior to entering the thermal section. The use of transparent tubing assures us of having a continuous segmented flow without any slug coalescence. A high-speed Phantom camera v611 controlled by a computer captures the images of the two-phase slug flow. The camera has a resolution of 1280 × 800, a pixel size of 20 μm, and a 12-bit depth, providing high-quality images of flow patterns to predict slug shape, curvature, and liquid film thickness. A unique manual-focus Canon MP-E 65 mm f/2.8 1-5x lens captures micro shots and close-ups of slugs. Two T-type Omega thermocouples are also employed to measure the inlet and outlet bulk temperatures of the flow at the test section located inside an isothermal bath manufactured by Fisher Scientific Co. Due to the high thermal conductivity of copper metal, a copper tube with an inner diameter, wall thickness, and length of 1.65, 0.7, and 100 mm, respectively, is used to establish a

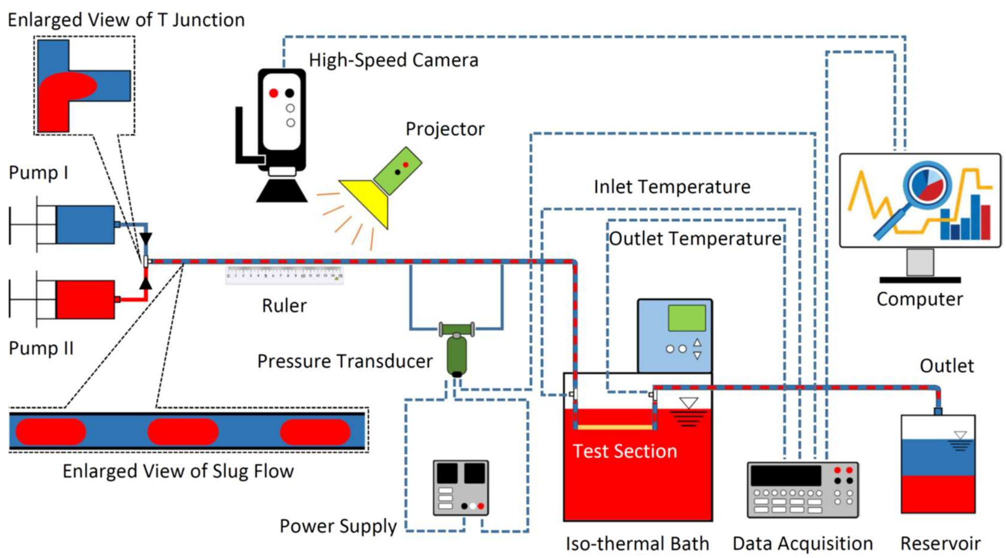

FIGURE 7.1: Schematic of the experimental setup for measuring slug length, film thickness, pressure drop, and heat transfer rate

thermal section that provides accurate uniform temperature distribution within the tube's wall.

Table 7.1 displays the thermophysical properties of the fluids involved in the experiments and simulations at standard pressure and temperature. Two pure silicone fluids with super-low and low dynamic viscosities of 1 cSt and 5 cSt, respectively, are examined. The properties of silicone oils are obtained from the manufacturer, i.e., Clear Co. They are mainly composed of Octamethyltrisiloxane. These silicone oils are clear, colourless, and essentially odorless. The low surface tension (i.e., high spreadability) of these silicone oils introduces them as carrying flow in two-phase water / oil systems. In addition, the low viscosity-temperature coefficient (VTC) of these oils assures insignificant change in their viscosities over the range of operational temperatures. Experiments are conducted within a wide range of volumetric flow rates, three fluids, and three tube diameters resulting in the experimental parameters presented in Table 7.2.

TABLE 7.1: Thermophysical properties of operational fluids

Fluid	**Density** ($kg \cdot m^{-3}$)	**Dynamic viscosity** ($kg \cdot m^{-1} \cdot s^{-1}$)	**Specific heat capacity** ($J.kg^{-1}.K^{-1}$)	**Thermal conductivity coefficient** ($W.m^{-1}.K^{-1}$)	**Surface tension** ($N \cdot m^{-1}$)
Distilled Water	1000	8.905×10^{-4}	4221	0.599	0.0720
Silicone Oil (1 cSt)	818	8.18×10^{-4}	2000	0.100	0.0427
Silicone Oil (5 cSt)	918	0.00459	1632	0.117	0.0428

TABLE 7.2: Experimental parameters

Parameter (unit)	**Distilled Water**	**Silicone Oil** (1 cSt)	**Silicone Oil** (5 cSt)
Volumetric Flow Rate ($ml.min^{-1}$)	1 – 20	1 – 20	1 – 20
Reynolds Number (–)	14 – 336	12 – 298	2 – 60
Capillary Number (–)	$9.6 \times 10^{-5} – 2.6 \times 10^{-3}$	$3.7 \times 10^{-4} – 9.9 \times 10^{-3}$	$1.8 \times 10^{-3} – 4.9 \times 10^{-2}$
Weber Number (–)	1.3×10^{-3} – 0.875	4.4×10^{-3} – 2.95	3.6×10^{-3} – 2.94
Prandtl Number (–)	6.28	16.36	64.02
Peclet Number (–)	87 – 2110	196 – 4875	128 – 3841

7.3.2 Uncertainty and Error Analysis

Uncertainty and error analysis are crucial for quantifying experimental data with the lowest discrepancy. Uncertainty refers to a lack of experimental measurement sureness ranging from a shortage of certainty to a complete lack of information. The uncertainties of measuring equipment in our experiments, such as syringe pumps, thermocouples, pressure transmitters, and tubing, are specified by the manufacturers, which are presented in Table 7.3. The uncertainties associated with most of the measured flow parameters are highly dependent on the magnitudes of parameters.

Before going through the methodology and results, an error analysis associated with our experimental measurements is carried out to quantify potential error (W) associated with any calculated flow parameter (E) using the method of Kline and McClintock (1953),

$$W_E = \sqrt{\left(\frac{dE}{dy_1}w_1\right)^2 + \left(\frac{dE}{dy_2}w_2\right)^2 + \cdots + \left(\frac{dE}{dy_n}w_n\right)^2} \tag{7.1}$$

where w indicates the uncertainty associated with any measured variable (y) presented in Table 7.3. The uncertainties of thermophysical properties are ±2–5 % resulting in errors associated with dimensional and non-dimensional groups, such as superficial velocity, Reynolds number (Re), friction factor (f), Prandtl number (Pr), and heat transfer. Error calculations are based on treating experimental measurements as probability distributions. The error analysis allows the calculations to be quantified regarding a probability distribution for each parameter and the range of possible obtained values. Table 7.4 presents the uncertainty analysis determining a range of overall uncertainty for each dimensional and non-dimensional group.

TABLE 7.3: The uncertainties of measuring equipment used in our experiments

Equipment	Measurement	Uncertainty
Syringe Pump	Volumetric Flow Rate [$ml.min^{-1}$]	± 0.25% of reading
Thermocouple	Temperature [°C]	± 0.1 °C
Isothermal Bath	Temperature [°C]	± 0.1 °C
Pressure Transmitter	Pressure Difference [psi]	± 1% of reading
Tubing	Inner Diameter [mm]	± 0.02 mm
Test Sections	Length [mm]	± 0.02 mm

TABLE 7.4: The uncertainties of dimensional and non-dimensional flow parameters

Parameters	A	$U = \frac{Q}{A}$	$\dot{m} = \rho Q$	$f = \frac{\Delta P}{2\rho U^2}\frac{D}{L}$	$Re = \frac{\rho U D}{\mu}$	$Ca = \frac{\mu U}{\sigma}$
Uncertainty	2.4%–2.8%	2.4%–2.8%	2%–5%	3.3%–5.6%	3.1%–5.6%	3.7%–7.6%
Parameters	ΔT	$Pr = \frac{C_P \mu}{k}$	$L^* = \frac{L/D}{Re\,Pr}$	$q = \dot{m} C_p \Delta T$	$\bar{q} = \frac{q}{A_s}$	$q^* = \frac{\bar{q} D}{k\,\Delta T}$
Uncertainty	± 0.2 °C	3.5%–8.7%	3.5%–8.7%	3.3%–7.3%	4.1%–7.8%	5.5%–10%

A frequently used measure to provide the differences between the values of predicted and measured flow parameters is root mean squared error (RMSE). A lower RMSE shows a higher accuracy for comparing predicted and measured data as it is scale-dependent (Hyndman and Koehler, 2006),

$$\mathrm{RMSE} = \sqrt{\frac{\sum_{i=1}^{N}(\hat{y}_i - y_i)^2}{N}} \tag{7.2}$$

where $\hat{y}$ and y indicate the predicted and measured experimental values of flow parameters, while N represents the number of data points.

7.3.3 Pressure Drop and Heat Transfer Benchmarking Tests

This section presents pressure drop and heat transfer benchmarking as methods to validate measurement results. Benchmarking is a practical way to measure the performance of experimental methods by using theoretical data. The best-known theoretical Fanning friction factor (f) and mean wall heat flux ($q^{\star}$) are employed to evaluate the uncertainty of the experimental equipment and the quality of the measurement setup.

Pressure drop benchmarking tests are designed under the same flow conditions for single-phase distilled water and silicone oil flows, using three straight transparent plastic tubing sizes of 1.42, 1.52, and 1.65 mm. The flow regime remained laminar and fully developed, considering the operational conditions. Comparing experimental results and well-established theories guarantees an accurate experimental procedure. The Hagen-Poiseuille, Eq. (7.3), is a physical law to compute the pressure drop of a Newtonian and an incompressible flow through a long and circular tube with a constant cross-sectional area. Pressure drop is a function of friction factor (f), fluid density (ρ), channel geometries (D and L), and averaged velocity (U) as:

$$\Delta P = f\left(\frac{1}{2}\rho U^2\right)\frac{4L}{D} \tag{7.3}$$

Static head and wall friction significantly impact pressure drop, which the measurements revealed the apparent friction factor, f, in Eq. (7.3) was close to the Fanning friction factor (Kreutzer et al., 2005c). According to the Fanning's theory, the friction factor for smooth round tubes is often taken to be $f=16/Re$, as shown by a solid line in Figure 7.2a. This figure also presents the variation of friction factor versus

Reynolds number for distilled water and silicone oil flows over a test section of 200 mm in length at the room temperature of 21°C. The volumetric flow rate changes from 1 up to 10 ml/min resulting in a range of Reynolds numbers varying from 2 to 168. The results reveal that the collected experimental data are within the ±10% range of the theoretical Fanning model. This precise measurement also shows insignificant effects of surface roughness on the results. The numerical analysis also predicts the pressure drop even closer to the Hagen-Poiseuille law compared to the experimental results. For instance, the deviation varies from 8 to 2.4% when the volumetric flow rate of single-phase distilled water changes from 1 to 10 ml/min through the tube with a diameter of 1.65 mm.

Heat transfer benchmarking is performed by a 100 mm straight copper tube with an inner diameter of 1.65 mm placed in an isothermal bath horizontally under constant wall temperature. The wall of the copper tube is thin enough for the temperature to be distributed uniformly within the wall. The copper tube is precisely cut, and its two ends are carefully smoothed. Two thermocouples are placed at the minimum distance (i.e., 3 mm) from two ends of the copper tubing using two plastic T-junctions. The high thermal conductivity ratio of copper to plastic tubing secures equivalent temperatures measured by thermocouples to those of the flow at the entrance and exit of the copper test section. The volumetric flow rates of distilled water and 5 cSt silicone oil are ranged from 1 to 20 ml/min, where the flow regime remained laminar due to the low inertia forces (i.e., Reynolds numbers of water and oil flows vary from 14 to 289 and from 2 to 51, respectively). A dimensionless mean heat transfer coefficient or Nusselt number based on the averaged heat flux is defined as follows:

$$\overline{\mathrm{Nu}}_{\mathrm{D}} = \frac{\overline{\mathrm{q}}\mathrm{D}}{\mathrm{k}\Delta \mathrm{T}_{\mathrm{lm}}} \tag{7.4}$$

where

$$\overline{\mathrm{q}} = \frac{\mathrm{Q}}{\mathrm{A_s}} = \frac{\dot{\mathrm{m}}\mathrm{C_p}\Delta \mathrm{T}}{\pi \mathrm{DL}} = \frac{\rho \mathrm{UDC_p}(\mathrm{T_o} - \mathrm{T_i})}{4\mathrm{L}} \tag{7.5}$$

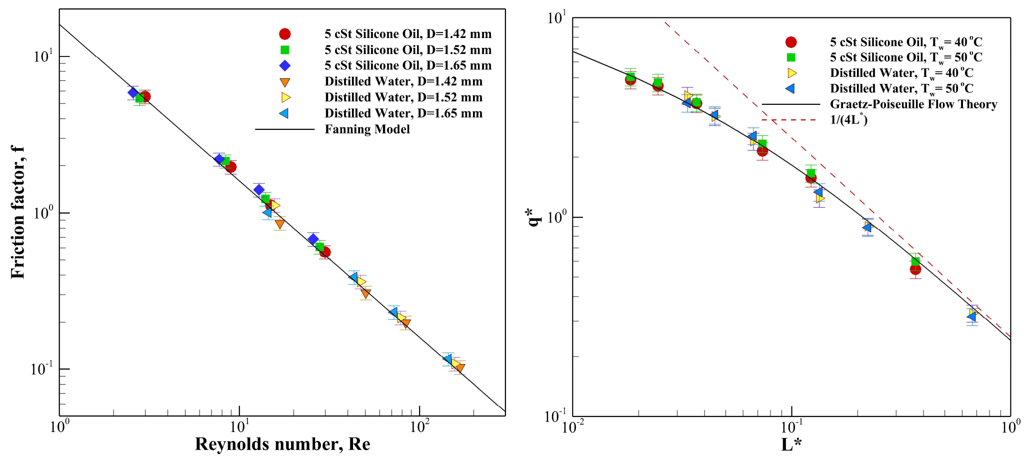

(a) (b)

FIGURE 7.2: Distributions of (a) Fanning friction factor versus Reynolds number for three tubing sizes and two fluids (b) mean wall heat flux versus dimensionless thermal channel length for two wall temperatures and two fluids, with ±10% error

$$\Delta T_{lm} = \frac{(T_w - T_i) - (T_w - T_o)}{\ln \dfrac{(T_w - T_i)}{(T_w - T_o)}} \tag{7.6}$$

where k, ρ, C_p, and $\dot{m}$ are thermal conductivity coefficient, density, specific heat capacity, and mass flow rate, respectively. T_i and T_o are the measured inlet and outlet temperatures, while T_w is the setpoint temperature of the isothermal bath. The heat transfer area of the copper tube is its inner surface area (A_s), which is equal to πDL. The dimensionless mean wall heat flux is defined as:

$$q^{\star} = \frac{\overline{q}D}{k(T_w - T_i)} \tag{7.7}$$

Muzychka et al. (2010) proposed a general model to predict heat transfer in Graetz flow that considers the boundary layer and fully developed regions. Their model followed an asymptotic approach proposed earlier by Churchill and Usagi (1972). Therefore, the mean Nusselt number and dimensionless heat flux can be presented by Greatz-Poiseuille flow theory in a circular tube as follows (Muzychka et al., 2011; Muzychka, 2014):

$$\overline{\mathrm{Nu}}_{\mathrm{D}} = \left[\left(\frac{1.614}{\mathrm{L}^{\star 1/3}}\right)^{5} + 3.65^{5}\right]^{1/5} \tag{7.8}$$

$$\mathrm{q}^{\star} = \left[\left(\frac{1.614}{\mathrm{L}^{\star 1/3}}\right)^{-3/2} + \left(\frac{1}{4\mathrm{L}^{\star}}\right)^{-3/2}\right]^{-2/3} \tag{7.9}$$

where the dimensionless thermal channel length or inverse Graetz number is defined as

$$\mathrm{L}^{\star} = \frac{\mathrm{L/D}}{\mathrm{Pe}} = \frac{\mathrm{L/D}}{\mathrm{Re\ Pr}} = \frac{\mathrm{Lk}}{\rho \mathrm{C_P U D^2}} \tag{7.10}$$

The value of $\mathrm{q}^{\star} = 1/(4\mathrm{L}^{\star})$ is the up limit of heat transfer rate, which can be obtained by flowing a fluid through a long channel under constant wall temperature, therefore, $\mathrm{q}^{\star}$ behaves asymptotically to this limit as thermal tube length approaches infinity. Eqs. (7.7)–(7.9) can be used to validate the experimental results with theories presented in Figure 7.2b. The results show a good agreement with less than 10% error compared with Graetz-Poiseuille flow theory. Considering isothermal boundary conditions of 40 and 50 °C, the measured data disclose the slight influence of these two different wall temperatures on the mean wall heat flux as was shown by Alrbee et al. (2021).

7.4 Numerical Solution Methodology

A computational fluid dynamics (CFD) method for two-phase distilled water / silicone oil flow through a straight mini-channel with concentric inlets has been set up such that the details, boundary conditions, and thermophysical properties are compatible with the experimental setup employed for the experiments. Distilled water is dispersed through the core region, and the carrying silicone oil flows through the annular region to establish a uniformly segmented Taylor flow. Two-phase CFD simulations are conducted based on the following assumptions: steady-state flow, incompressible flow, Newtonian fluids, constant thermophysical properties, and negligible gravity effects.

7.4.1 Governing Equations and Discretization Methods

The liquid-liquid two-phase Taylor flow is assumed to be in an axisymmetric plane, where both phases are immiscible, and the phase change from one state to another does not occur throughout the computational domain. All calculations within the three sections (i.e., flow pattern, pressure drop, and isothermal bath) are performed for fully developed Taylor flow conditions. Therefore, the main governing equations in the framework of the Eulerian one-fluid approach are taken on the following forms:

Continuity equations:

$$\frac{\partial(\alpha_d)}{\partial t} + \nabla \cdot (\alpha_d \mathbf{u}_d) = 0 \tag{7.11}$$

$$\frac{\partial(\alpha_c)}{\partial t} + \nabla \cdot (\alpha_c \mathbf{u}_c) = 0 \tag{7.12}$$

Momentum equation:

$$\frac{\partial(\rho \mathbf{u})}{\partial t} + \nabla \cdot (\boldsymbol{\rho} \mathbf{u} \mathbf{u}) = -\nabla p + \nabla \cdot [\mu(\nabla \mathbf{u} + \nabla \mathbf{u}^T)] + \rho \mathbf{g} + \mathbf{F}_{su} \tag{7.13}$$

Energy equation:

$$\frac{\partial(\rho E)}{\partial t} + \nabla \cdot [\mathbf{u}(\boldsymbol{\rho} \mathbf{E} + p)] = \nabla \cdot (k_{eff} \nabla T) + S_h \tag{7.14}$$

where α_c and α_d represent the volume fractions of continuous and dispersed phases respectively. The governing equations (7.11)–(7.14) employ the volume-fraction weighted average to compute the thermophysical properties of the two phases, such as density, viscosity, and thermal conductivity coefficient. If the volume fraction of the second phase (α_2) is tracked, then the amount of property (φ) in each control volume in the two-phase flow is represented by $\varphi = \alpha_1\varphi_1 + \alpha_2\varphi_2$ where subscripts 1 and 2 denote each phase. One limitation of this approach is that the solution may not converge at viscosity ratios greater than 10^3. The relation between two volume fractions is $\alpha_1 + \alpha_2 = 1$. For an arbitrary fluid volume, three cases are possible: $\alpha_i = 0$ when the volume is empty of the i^{th} fluid, $\alpha_i = 1$ when the volume is full of the i^{th} fluid, and $0 < \alpha_i < 1$ when the volume contains the interface between phases 1 and 2. For the last case, the Geo-reconstruct method is responsible for reconstructing the two-phase interface. Therefore, the properties ρ, μ, and k_{eff} are the local values of the mixed phase density, $kg.m^{-3}$, dynamic viscosity, Pa.s, and effective thermal conductivity, $W.m^{-1}.K^{-1}$, respectively, which are shared by the phases. The last two terms in the momentum equation denote the gravitational acceleration and surface tension force per unit area, which can be approximated by a body force surrounding the interface between the phases (Brackbill et al., 1992). The gravitational term $\rho\mathbf{g}$, is insignificant when the channel diameter is sufficiently small and the surface tension effects are dominant, resulting in a Bond number ($Bo = gD^2\Delta\rho/\sigma$) of the order of 10^{-2} (Triplett et al. 1999). Based on the operational flow conditions in our simulations, the highest value of the Bond number is less than 10^{-2}, which is considerably smaller than the criterion, $4\pi^2$, proposed by Brauner and Maron (1992). Furthermore, the source term in the momentum equation is defined as $\mathbf{F}_{su} = \sigma\kappa\delta\mathbf{n}$, $N.m^{-3}$, including the surface tension force σ, radius of curvature or surface normal κ, Dirac delta function δ, and normal unit vector at the interface $\mathbf{n}$. The radius of interface curvature is specified as $\kappa = \nabla \cdot \mathbf{n}$ where $\mathbf{n} = \nabla\alpha/|\nabla\alpha|$. The last term in the energy equation is a source term representing the contributions of radiation and other volumetric heat sources, which are not considered in present simulations (Brackbill et al., 1992).

The commercial software ANSYS Fluent 19.0 is employed to carry out CFD simulations and solve the aforementioned governing equations and several other equations that predict the multiphase flow properties around the interface and phase volume fractions. ANSYS Fluent offers the level-set and volume-of-fluid (VoF) methods to capture the interface in two-phase flows. The level set method assumes a zero value for the level-set of a smooth function at the interface between two phases. The amount of the level-set function is negative in the gas phase and positive in the liquid phase. The VoF method solves a single set of momentum equations and calculates the volume fraction equation of each phase within the computational domain. VoF is a robust approach for identifying the liquid-liquid interface, particularly for steady and transient two-phase flows, which are selected in the simulations that follow.

A consistent version of the semi-implicit method for pressure linked equations (SIMPLEC) algorithm is employed to couple pressure and velocity fields. By eliminating less important terms from the velocity equation, SIMPLEC can manipulate the proper corrections. In the presence of a straight channel, a constructed-quadratic mesh with a skewness correction of zero may be used, which alleviates convergence difficulties in the numerical simulations (Versteeg and Malalasekera, 2007). An explicit approach is selected to discretize the time steps using a standard finite-difference interpolation scheme applied to the volume fractions at the previous time step. In particular, ANSYS Fluent can compute the values of face fluxes near the interface line by interpolation using either an interface reconstruction or a finite volume (FV) discretization scheme. The reconstruction scheme obtains the amount of flux on the faces whenever a cell is filled with fluid. The finite volume discretization approach can only be employed with an explicit VoF method using first-order upwind or second-order upwind and QUICK algorithms.

Two key factors limit the accuracy of the velocity and temperature fields near the phase interface: significant gradients of velocity or temperature and large discrepancies in the phase densities. Owing to the trivial differences between the mean velocities/temperatures of the phases in two subsequent slug and plug and the densities of the phases (e.g., the densities differences are 22% for water / 1 cSt silicone oil and 9% for water / 5 cSt silicone oil), the simulations would lead to convergence and acceptable precision.

7.4.2 Solver Settings and Boundary Conditions

The VoF method calculates a time-step based on the transient time characteristic over a control volume, which is not necessarily identical to other governing equations. In the vicinity of the interface, the ratio of the volume of each cell to the sum of the outgoing flux from the faces of the finite volume gives the time required to empty a cell. The Courant number ($\mathrm{Co} = \Delta t U_{\mathrm{fluid}} / \Delta x$) includes the smallest time-step where U_{fluid} and Δx are the fluid velocity and the grid size, respectively. In the following simulations, the maximum value of Co is 0.25, and a constant time step of 10^{-6} is utilized to reduce the total computational expenses unless it causes an unexpected increase in the Courant number. A variable time step between 10^{-6} and 10^{-7} is selected, particularly at the moments of water slug breakup, to converge the solution in such cases. The non-iterative under-relaxation factors and correction tolerances for the pressure and momentum are set to 1 and 10^{-7}, respectively, to accelerate the convergence and stabilize the solution. A first-order non-iterative time advancement (NITA) scheme is used to decrease the computational effort over each time-step, showing a slight downward trend as time progresses and the scaled residuals remain in the order of 10^{-6}–10^{-7}. The boundary conditions considered in the simulations are as follows:

- Uniform velocity and temperature distributions at the inlet of the channel
- Outlet flow at the exit of the channel
- No-slip boundary condition at the wall
- Constant wall temperature distribution at the wall

7.4.3 Grid Independence Study and Validation of Numerical Method

A grid independence test finds the optimal grids, i.e., the smallest number of grids and lowest computational expenses. An insignificant difference in the numerical results between two grid generation scenarios can be considered a criterion to determine the independency of results on the various grid conditions. Therefore, the optimal grid design is crucial to improving the accuracy of the numerical simulations.

Most CFD solvers employ traditional, also known as handcrafted, and adaptive meshing methods to discretize the computational domains, which is divided into core and near-wall regions. Figure 7.3 displays schematic representations of generated meshes in the two regions. As seen, mesh refining in handcrafted meshing generates rectangular grids in the near-wall region that can potentially develop discretization errors. This defect is no longer observed in the boundary adaptive meshing where the quad grids keep the square shape unchanged, as a refinement happens over a known number of original grids next to the wall, e.g., three grids in Figure 7.3(b). We examined both to find an independent mesh, which provides accurate results and speeds up the simulations.

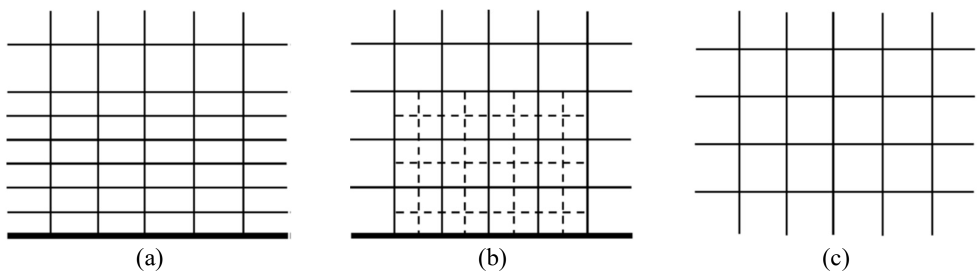

FIGURE 7.3: Distributions of two non-uniform grids within the near-wall region using (a) handcrafted, (b) boundary adaptive meshing, and (c) uniform coarse grids within the core region

Based on the handcrafted meshing, a refined mesh is considered near the channel's wall for predicting the boundary layer, accurate interface, and liquid film and a coarse mesh is used in the rest of the channel to reduce computational cost (Gupta et al., 2009; Asadolahi et al., 2012; Fletcher and Haynes, 2017; Sontti and Atta, 2017). This work follows the same mesh independence as in the study conducted by Etminan et al. (2021b) over a thickness of 45 μm. Four grid sizes of 15, 7.5, 3.75, and 3 μm are used, and the last two sizes show mesh-independent results. Consequently, the grid size of 3.75 μm is assumed over the film region. It is also found that further mesh refinement not only enhances the computational expense but also induces a non-physical pressure jump, i.e., an unphysical situation within the film region (Gupta et al., 2009; Etminan et al., 2021b and 2022b). To ensure that the predicted results are not dependent on the size of mesh in the core region, liquid film thickness, slug length, and mean Nusselt number are calculated for four different equal-length quad mesh sizes of 25.16, 20, 15, and 10 μm in the axial direction. Table 7.5 presents the corresponding numerical results for distilled water / 1 cSt silicone oil at a superficial velocity ratio of unity. As can be seen, no significant changes are observed in the film thickness, slug length, and Nusselt number after three grid miniaturizations with less than 3.8, 2.6, and 2% deviations, respectively, between the last two grid cases. Therefore, an independent mesh size of 15 × 15 μm is adopted for the core region of the microchannel, providing accurate solutions and resulting in a total number of 220,000 cells. These mesh refining and coarsening, accompanied by fine enough resolution within high-gradient regions, guarantee accurate results and keep the total number of grids manageable. In some areas, too much of mesh refining is never what is required; however, it is another disadvantage of the traditional meshing method, resulting in less accuracy in representing the interface somehow and longer computational times. Therefore, the boundary adaptive meshing procedure with two refinements is employed to refine the near-wall region, and the results are also presented in Table 7.5. A grid size of 15 μm and two quad grid sizes of 3.75 and 7.5 μm discretize the core region and two equal-thickness regions along the wall, respectively. It lessens the grid numbers up to 22%, which reduces the computational expense accordingly. As a consequence, adaptive meshing has been selected for the rest of the simulations in this study, considering the lower grid numbers and faster convergence.

TABLE 7.5: Results of liquid film thickness, slug length, and Nusselt number using two meshing approaches in distilled water / 1 cSt silicone oil two-phase Taylor flow at a superficial velocity ratio of unity

Meshing	**Number of Grids**	**Liquid Film Thickness** [μm]	**Error** [%]	**Slug Length** [μm]	**Error** [%]	**Nusselt Number**	**Error** [%]
Traditional (Handcrafted)	138 000	29.37	—	2513.1	—	34.41	—
	169 950	27.76	5.8	2435.2	3.2	32.53	5.8
	220 000	26.07	6.5	2362.0	3.1	31.09	4.6
	363 000	25.12	3.8	2302.1	2.6	30.48	2.0
Adaptive	121 000	27.86	—	2397.0	—	32.14	—
	140 800	26.13	6.6	2329.4	2.9	31.03	3.6
	180 400	25.10	4.1	2301.8	1.2	30.49	1.8

Table 7.6 presents the verification of our obtained results from numerical simulation by comparing them with various empirical correlations. The data are for the distilled water / silicone oil (1 cSt) system in a tube with an inner diameter of 1.65

mm at a superficial velocity of 0.156 m/s resulting in the same volumetric flow rate of 10 ml/min for each phase. Mean film thickness is averaged over the steady film region where the curvature of the interface likely becomes uniform, i.e., far enough downstream of the phase inlets that the liquid film thickness remains unchanged. The exact location of the interface to measure film thickness is assumed where the volume fraction is 0.5 (Etminan et al., 2021b). According to the table, the CFD results agree very well with the calculations by lubrication theory for a capillary number of 3.12×10^{-3}. For example, an established relationship for film thickness obtained from the present numerical simulation is 0.03R, close to those calculated by the correlations (i.e., 0.029R, 0.032R, and 0.036R).

TABLE 7.6: Comparison of liquid film thickness values with available correlations for Taylor flow in a horizontal microchannel

Reference	**Correlation**	**Liquid Film Thickness** [μm]	**Relationship δ/R**
Bretherton (1961)	$1.338\ \mathrm{Ca}^{2/3}$	23.56	0.029
Aussillous and Quéré (2000)	$\frac{1.34\ \mathrm{Ca}^{2/3}}{1 + 3.35\ \mathrm{Ca}^{2/3}}$	26.70	0.032
Kreutzer et al. (2001)	$0.36\ (1 - \mathrm{e}^{-2.13\ \mathrm{Ca}^{0.52}})$	29.87	0.036
Present computations	—	25.10	0.030

The developed numerical model is also verified by the profile of a steady Taylor slug in a unit cell within the fully developed region of a straight channel at a superficial velocity ratio of unity. Figure 7.4 shows the slug interface of our CFD simulations and those obtained from Gupta et al. (2009) and Sontti and Atta (2017) by aligning the slugs' tails together. The exact locations of the interface and the coordinate axes are non-dimensionalized by the channel diameter and radius. A slight deviation is observed over the film region where the differences between numerical discretization methods, thermophysical properties, and phase superficial velocities become more important. However, the rear and nose curvatures agree very well. Some ripples are seen near the tail meniscus due to pressure fluctuations, the interaction between surface tensions, and viscous forces in the film region, as also addressed by Gupta et al. (2009) and Sontti and Atta (2017).

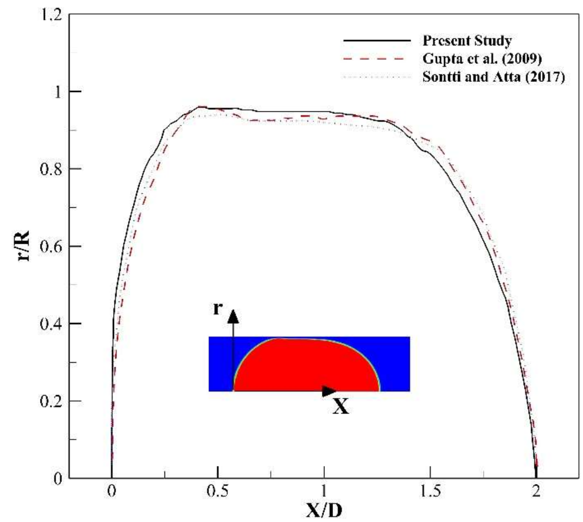

FIGURE 7.4: Verification of a Taylor slug profile in a unit cell by comparing with profiles in the literature for air / water system with a superficial velocity of 0.256 m/s through a channel with a radius of 250 μm (flow direction is from left to right)

7.5 Results

Fluid flow characteristics and convective heat transfer of distilled water / silicone oil Taylor flow through mini-scale tubing are studied for the flow parameters given in Table 7.2. The slug length and film thickness are critical parameters in both experimental and CFD calculations that measured flow downstream of tee/concentric junctions where a consistent train of Taylor slugs is observed without any slug coalescence and merging. An image processing in IrfanView (version 64 4.60) is developed to extract the average slug length and film thickness from a series of snapshots for each test. Steady-state conditions are seen in numerical simulations, while slug length varies up to 13% for the measurements herein. Many researchers have also reported the same uncertainty in experimental measurements, e.g., Eain et al. (2015) found up to 10% in slug length. After validating the numerical model for CFD simulations and experimental setup through benchmarking the results of single-phase flow, in the following sections, we will discuss the results of such flow in a horizontal configuration.

7.5.1 Flow Patterns

Taylor flow, which potentially enhances heat and mass transfer rates in industrial applications, is predominantly affected by the geometrical details of the channel / junctions, the configuration of the channel, thermophysical properties of phases, and superficial velocities of phases. Each phase's wetting or drainage effects are also responsible for the flow regimes in multiphase flows. This chapter is focused upon the Taylor flow in capillaries through experiments and computational fluid dynamics (CFD) simulations. Figure 7.5 shows a series of Taylor flows with different slug lengths through a mini-channel with an inner diameter of 1.65 mm over water volumetric flow rates ranging from 2.5 to 10 ml/min. In a high enough oil-to-water volumetric flow rate, the individual short slugs move through the carrying phase at very low liquid superficial velocities, and the interaction between the slugs is negligible. A decrease in the oil-to-water volumetric flow rate causes long slugs with rounded noses that span the cross-sectional area of the channel. Non-dimensionalized slug length, i.e., L_S/R decreases as the oil-to-water flow rate ratio increases (e.g., the corresponding values of 4.19 and 2.39 for the lowest and highest flow rate ratios, respectively). A slight difference between the patterns obtained by experiments and CFD simulations is observed due to uncertainties in experimental equipment and the operational conditions, which will be explained in the following sections. The slug length is especially important in miniaturized devices dealing with heat and mass transport phenomena, where capillary forces dominate.

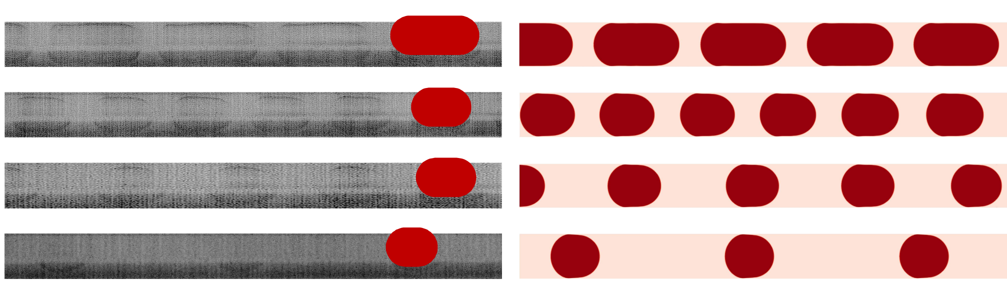

FIGURE 7.5: The flow patterns of the two-phase distilled water / silicone oil (1 cSt) Taylor flow by experiments (left column) and numerical simulations (right column) using four oil-to-water volumetric flow rates of 5:10, 10:10, 10:5, and 10:2.5 from top to down, respectively (flow direction is from left to right)

7.5.2 Slug Shape and Liquid Film Thickness

Reynolds (1886) first proposed the theory of lubrication to explain the behaviour of thin liquid films between solid surfaces, which was significantly practical in lubricating systems. Fairbrother and Stubbs (1935) pioneered the studies on a liquid film and its contribution to differentiating actual and apparent velocities of air bubbles within capillaries through experiments. They showed that, for small enough film thickness, the speed difference is proportional to fourfold the bubble and tube diameters ratio, which can also be presented as the square root of the linear velocity of the bubble. A comprehensive understanding of the interaction between two immiscible fluids and a microchannel wall can lead to solving such complex interfacial flow resulting in the exact relocating of the interface (e.g., Cueto-Felgueroso and Juanes, 2008; Huerre et al., 2015). The motion of long air bubbles and the predicting bubble profiles in capillary tubes were carefully studied by Bretherton (1961) through the balance between viscous and surface tension forces. The theory was restricted by some assumptions: steady motion interface, incompressible flow, negligible viscosity of gas phase, constant interfacial tension, fully wetted wall, negligible viscous stress tangential to the interface, and insignificant gravitational effects. Based on the Bretherton's analysis, the dimensionless forms of inertial, gravitational, and viscous forces in terms of surface tension are $\rho R U_s^2/\sigma$, $\rho g R^2/\sigma$, and $\mu U_s/\sigma$, respectively. Bretherton then obtained the Landau-Levich equation (Landau and Levich, 1942) after substituting the pressure term in the Young-Laplace equation, which governs the curvature of the bubble as shown in the universal form below,

$$\frac{d^3\eta}{d\xi^3} = \frac{\eta - 1}{\eta^3} \tag{7.15}$$

where the non-dimensional radial and axial coordinates from the scaling analysis are $\eta = r/\delta$ and $\xi = x(3\ \mathrm{Ca})^{1/3}/\delta$, respectively.

Figure 7.6 (at the top) depicts a schematic of the meniscus of a Taylor slug at rest, which was considered by Bretherton using an asymptotic solution to close the Landau-Levich equation. As shown, the interface's curvature is divided into three regions. The frontal and rear cap menisci (i.e., Region I) must have constant mean curvatures due to no viscous stresses for a stationary bubble, resulting in a spherical shape on the tube axis without any singularity (Bretherton, 1961). The exponential (i.e., $\eta \approx 1$) and parabolic (i.e., $\eta \gg 1$) solutions describe two portions of the transient region followed by a film region with a constant thickness of $\delta = 0.643\ (3\mathrm{Ca})^{2/3}\mathrm{R}$. Bretherton's theory is only valid when the Reynolds number is low enough, i.e., Re $\ll 1$, to ignore the inertia of flow and the capillary number is less than 0.003. Several numerical analyses (e.g., Ratulowski and Chang, 1990; Giavedoni et al., 1997; Fujioka and Grotberg, 2004) and recent experiments conducted by Habibi Matin and Moghaddam (2021) have challenged the performance of the theory as the capillary number goes beyond 0.003. An extended transition region usually accompanied by a sharp nose cannot be verified by the theory (Habibi Matin and Moghaddam, 2021). The capability of liquid film thickness prediction by the Bretherton’s theory was also shown to be not agree well with the experimental results at low and high capillary numbers (e.g., Aussillous and Quéré, 2000; Grimes et al., 2006). As shown in Figure 7.6, the results also break down the theory, even for a valid range of Ca, when the volumetric flow rate ratio increases and the capsular shape of the slugs changes to a more-spherical profile. It happens due to the remarkable change in the surface tension to viscous force ratio, which eventually reforms the slugs from the typical bullet shape to a more-spherical shape. The curvature at the transition regions establishes the thickness of the liquid film and, consequently, its length. Referring to the last slug profile in Figure 7.6, one can confirm that there is no uniform film region, so we observe two spherical menisci at two ends connected to each other by transition interfaces. The motion of slugs enlarges the radius of meniscus, at the tail compared to that at the nose, which was well confirmed by Etminan et al. (2021b). A slight difference between the profiles is due to different junctions, i.e., T-junction for experiments and concentric junction for the CFD simulations. Furthermore, the Marangoni effect caused by fluid impurities is potentially another source of errors affecting the phase interface during experiments, further detailed by Kreutzer et al. (2005b).

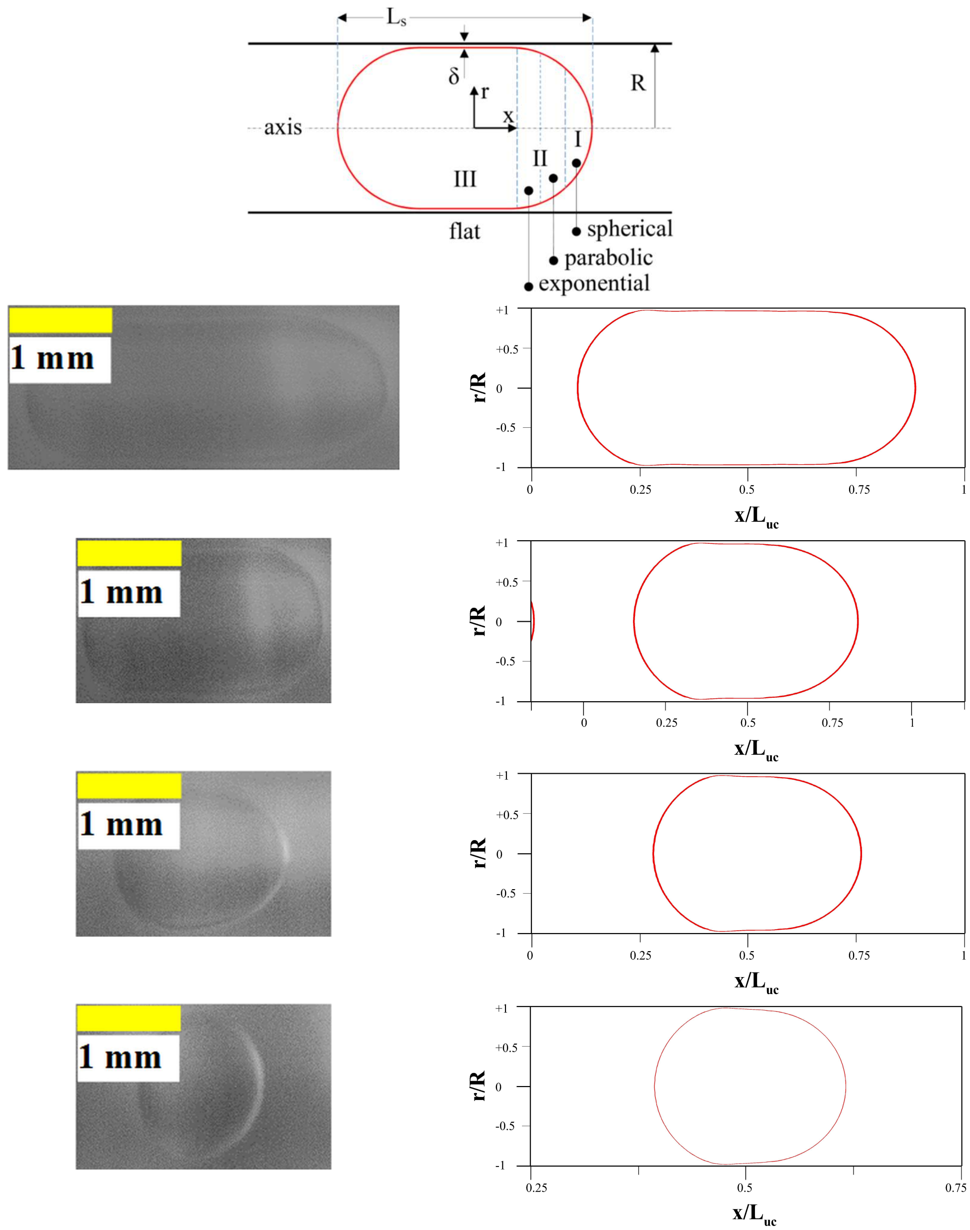

FIGURE 7.6: Schematic of different regions of the curvature of a typical Taylor slug (at the top) and Taylor slug profiles for distilled water / silicone oil (1 cSt) system flowing in a tube with an inner diameter of 1.65 mm, and oil-to-water volumetric flow rates of 0.5, 1, 2, and 4, respectively, from top to bottom obtained through experiments (left column) and CFD simulations (right column)
(flow direction is from left to right)

Figure 7.7 displays the cross comparisons of experimental data and CFD results for the two-phase flow of distilled water / silicone oil. As shown, the numerical simulations are liable to predict the normalized unit cell length and film thickness with good agreement with those obtained through experiments, where the majority of errors for the length and film thickness are less than ±10% and ±20%, respectively. These discrepancies can be attributed to image visualization, especially in the length calculations and film thickness predictions. The liquid scatter effects, such as light refraction, cause the phase interface to be much brighter (as also shown in Figure 7.6) and destroy the certain location of the interface. Therefore, due to the experimental uncertainties presented in Tables 7.3 and 7.4, and limitations on flow pattern visualizations, the CFD results will mostly be shown in the upcoming subsections to indicate the influence of phase flow rate ratio and superficial velocities on the hydrodynamic of such flows.

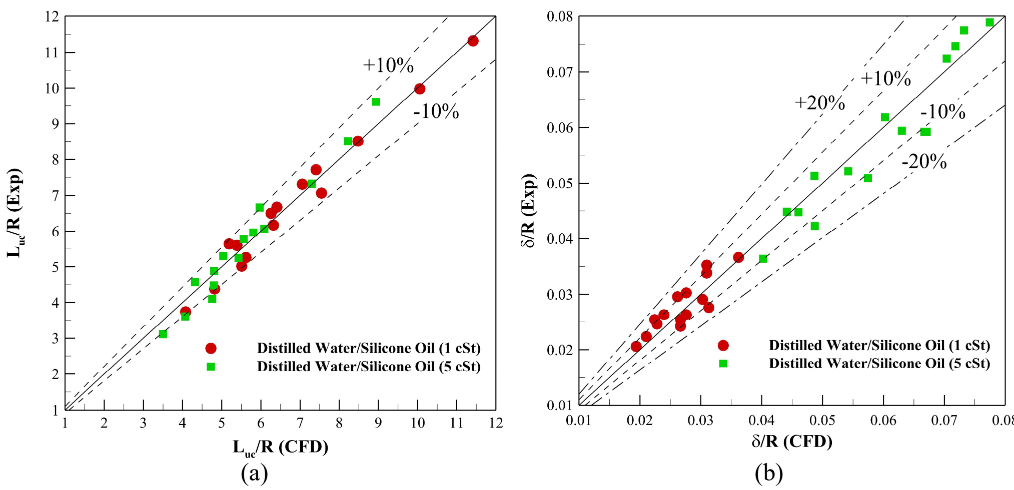

FIGURE 7.7: CFD simulations versus experiments for normalized (a) unit cell length and (b) liquid film thickness

7.5.3 Velocity Fields in the Slug, Plug, and Film Region

Slug speed and length are dominantly influenced by the phase volumetric flow rate and film thickness. Three pairs of recirculation regions are observed in each slug, including the main circulation in the middle, which is normally the largest, and two recirculation regions at the leading and trailing caps. Specifically, we consider three points on the axis of the tube called central part of slug (CS), tip of slug (TS), and central part of plug (CP) to describe how the magnitude of velocity changes as phase volumetric flow rate ratio varies. The mean velocity of two-phase flow can be calculated by $\mathrm{U_m} = (\mathrm{Q_c} + \mathrm{Q_d})/\mathrm{A}$, which varies from 0.156 m/s to 0.078 m/s as the volumetric flow rate ratio changes from 0.5 to 4 for a capillary with an inner diameter of 1.65 mm, for example, and used to normalize all the velocities. The results show that the velocities at CS and CP are the same for the unity volumetric flow rate ratio. The same trend is also observed at TS, where the local speed equals the mean velocity with an insignificant difference, i.e., less than 3%. With an increase in oil-to-water volumetric flow rate from 0.5 to 4, the superficial velocity of continuous flow becomes dominant to dictate its inertia in the plug region and increase the normalized local velocity at CP up to 206%. The slug tip speed slightly increases to reach 20% beyond the mean velocity as the recirculating region in the nose region becomes more robust. Conversely, any increase in continuous-to-dispersed phase flow rate makes the central recirculation region smaller, and the normalized local velocity at CS drops from 160% to 124%. Similar behavior is also observed using two smaller tube sizes of 1.52 and 1.42 mm. The cap recirculation regions occupy more and squeeze the central part much more as the slug profile forms a semi-spherical shape with a short uniform film region.

Figure 7.8 shows the radial and axial velocity component contours. It can be seen that the highest and lowest axial velocities occur in the middle of the core recirculation region and in the leading and trailing vortices, respectively. Dominant shear stresses within the boundary layer reduce the axial velocity significantly to generate even backflow over the rear transient region, which will be detailed in section 7.5.4. By increasing the oil-to-water volumetric flow rate, the magnitude of axial velocity in cap vortices decreased as the slug length is shortened to form a more spherical profile. The magnitude of radial velocity over the film region remains constant near zero to be consistent with the uniform film thickness. The high radial velocity value between the recirculation regions is responsible for carrying the heat from the hot wall into the slugs/plugs, and moving fresh fluid from the central part of slugs/plugs to the heated wall. The same scenario can also be seen for the flow pattern within the continuous phase plugs.

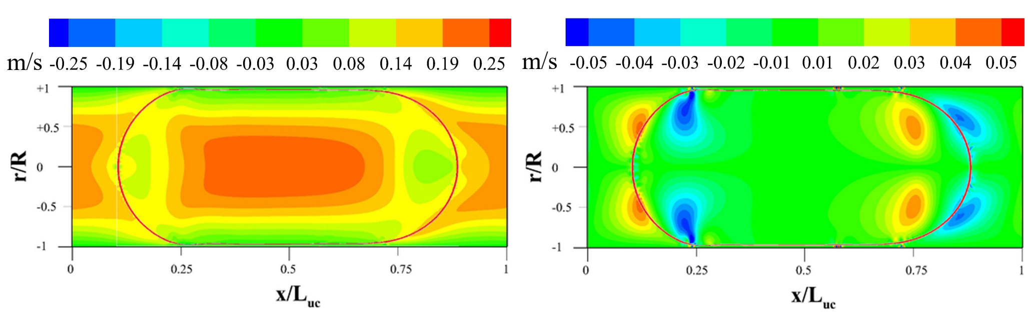

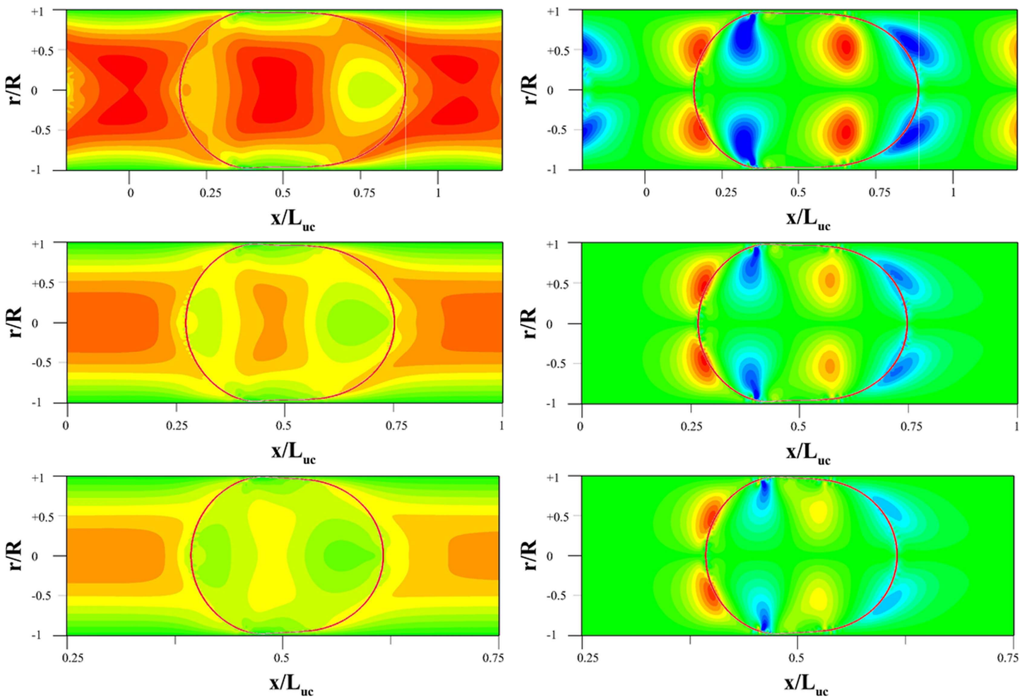

FIGURE 7.8: Contours of axial velocity (left column) and radial velocity (right column) components within a unit cell in the fully developed region of a distilled water / silicone oil (1 cSt) system through a tube with an inner diameter of 1.65 mm, and oil-to-water volumetric flow rates of 0.5, 1, 2, and 4 from top to bottom, respectively (flow direction is from left to right)

7.5.4 Recirculation Patterns and Isotherms

Radial and axial velocity components are important to generate recirculation in flow, which is critical to determining the hydrodynamic interaction between phases in the Taylor flow. Figure 7.9 (left column) illustrates three pairs of recirculation regions in the slugs: a large recirculation in the middle and two at the caps. The recirculation region in the middle is normally the largest, and the frontal recirculation is larger than that at the rear. An increase in the oil-to-water flow rate ratio speeds up the superficial velocity and the inertia of the continuous phase, leading to much more interaction with the nose and tail menisci. This enlarges and empowers the cap vortices and squeezes the core vortex. This also enhances the momentum and the heat transfer rates since the continuous phase flow transports much more momentum transfer and heat from the heated wall and diffuses to the interface displayed in Figure 7.9 (right column). Following Taylor's rough sketch of possible streamlines, the same pattern is also found in the carrying phase plug with only a pair of vortices (Taylor, 1961).

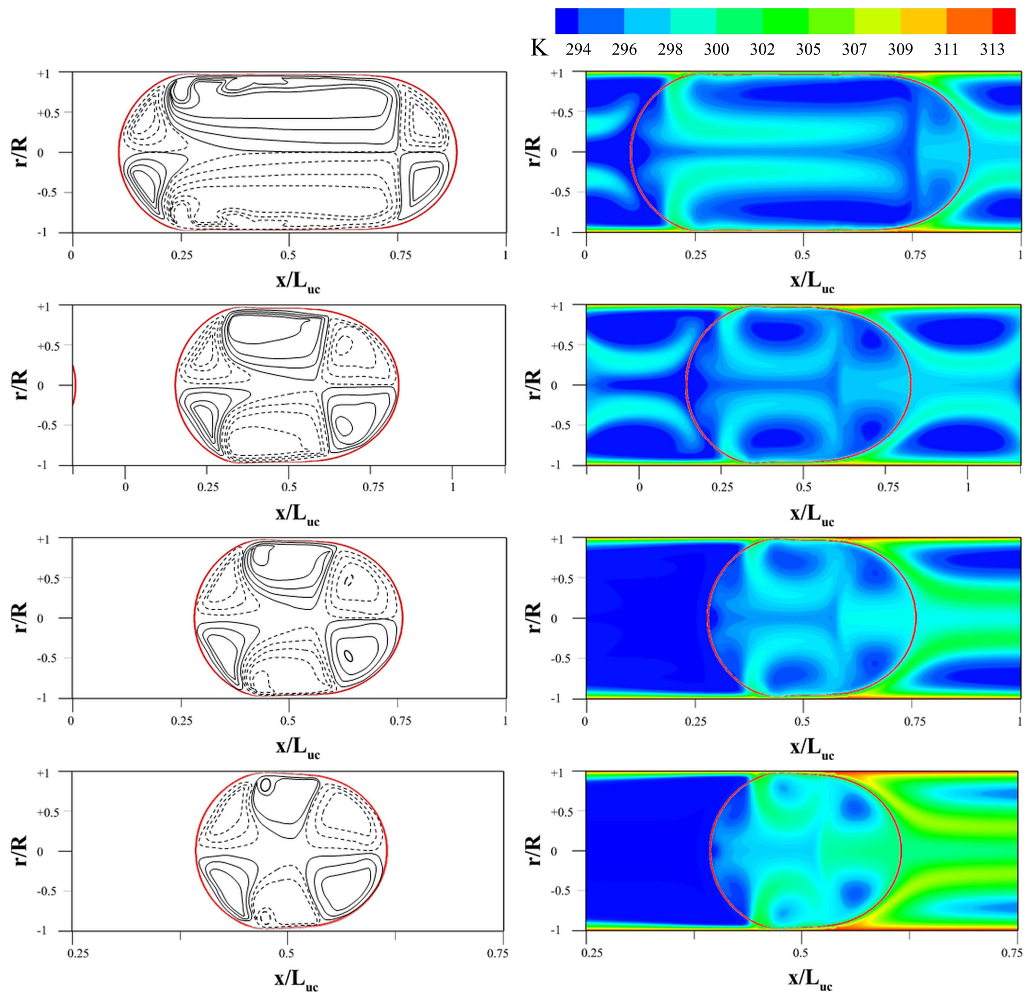

FIGURE 7.9: Recirculation regions (left column) and temperature contours (right column) within a slug in the fully developed region of a distilled water / silicone oil (1 cSt) system through a tube with an inner diameter of 1.65 mm, and oil-to-water volumetric flow rates of 0.5, 1, 2, and 4, respectively, from top to bottom (solid and dashed lines indicate counter clockwise and clockwise recirculation, respectively)
(flow direction is from left to right)

7.5.5 Physical Explanation for Local Backflow in the Film Region

The cross-sectional areas of the slugs remain a circular shape surrounded by a thin layer ($\delta \ll R$) of the carrying phase over a uniform film region. By considering the laminar flow regime, insignificant inertia, and end effects (also known as entry and exit effects) within the film region, the velocity varies linearly from zero, at the wall, to U_S, at the interface. Backfill of the carrying phase left behind a moving slug can be calculated by considering a backward motion of the tube at a velocity of U_S. This imaginary situation keeps the slug at rest and a mean backflow in the film region at a velocity of $U_s/2$ (Marchessault and Mason, 1960), which halved the slug velocity obtained by Fairbrother and Stubbs (1935), who assumed the film at rest for the long enough slugs (i.e., $L_s > 3R$). The slug can also be considered long enough when its length becomes 10 times the dimensional length of $\delta(3\,Ca)^{-1/3}$ (Klaseboer et al., 2014). From the sequential snapshots of flow in the film region, it is observed that the carrying phase shows the backflow, particularly near the rear transient region. In contrast, the flow in the middle of the slug moves downstream even faster than the mean velocity of flow due to the lubricating action caused by the film region. For example, Figure 7.10 displays zoomed-in views of axial velocity distribution within the rear transient, film, and nose transient regions for the same volumetric flow rate of 5 ml/min. A local backflow is found due to an adverse pressure gradient and change in the interface, which was also reported by Gupta et al. (2009) and Meyer et al. (2014). The core anti-clockwise recirculation in the slug changes the direction of local flow in the film region. In contrast, two clockwise vortices in the cap regions and their effects on the transient interface break down the local backflow. The convection terms in all directions and the diffusion term in the radial direction in momentum equation in the axial direction are negligible. Therefore, considering the scaling analysis and substituting the Laplace pressure loss $2\sigma/R$ in the simplified momentum equation leads the velocity becomes of the order of $U \sim 2\sigma\delta^2/(\mu LR)$, which also verifies our CFD results.

7.5.6 Pressure Drop

As discussed, operational conditions and the superficial velocities of the phases affect flow pattern, slug length, slug meniscus, and film thickness. This section presents pressure drops as measured and predicted through experiments and CFD simulations over a slug unit cell. As displayed in Figure 7.11, in the absence of the film region (i.e., dry-out condition) and the advancing (θ_a) and receding (θ_r) contact angles between the interface and the wall, the pressure drop over a unit cell in such Taylor flow can be modeled in terms of the frictional and interfacial contributions as below,

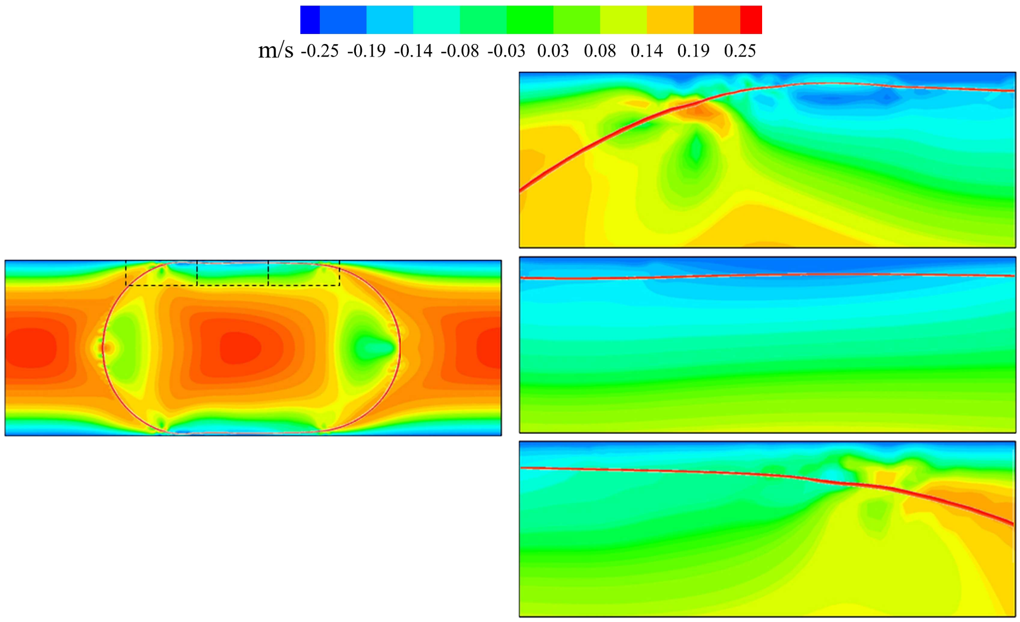

FIGURE 7.10: Plot of the axial velocity within a unit cell (left column) and the zoomed-in views (right column) over the rear transient, uniform film thickness, and nose transient regions, respectively, from top to down for a distilled water / silicone oil (1 cSt) system through a tube with an inner diameter of 1.65 mm, and the same volumetric flow rate of 5 ml/min (flow direction is from left to right)

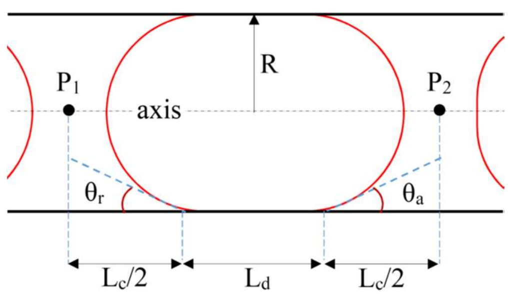

FIGURE 7.11: Schematic representation of two entry and exit points for pressure drop calculations across a slug unit cell without considering the film region

$$\Delta P_T = \Delta P_{Frictional} + \Delta P_{Interfacial} = \Delta P_{Fr,c} + \Delta P_{Fr,d} + \Delta P_{Int} \tag{7.16}$$

where the frictional pressure drops components and the interfacial contribution can be calculated from Hagen-Poiseuille and the Young-Laplace equations for a capillary tube:

$$\Delta P_{Fr,c} = \frac{8\mu_c U_m (1-\alpha) L_{uc}}{R^2} \tag{7.17}$$

$$\Delta P_{Fr,d} = \frac{8\mu_d U_m \alpha L_{uc}}{R^2} \tag{7.18}$$

$$\Delta P_{Int} = \frac{2\sigma}{R}\cos\theta \tag{7.19}$$

where α is the dispersed phase length fraction (L_d/L_{uc}). A theoretical solution was also developed by Bretherton (1961) to predict interfacial pressure drop as a function of a capillary number, i.e., $7.16\ (3\ \mathrm{Ca})^{2/3}\sigma/d$. The change in nose and rear menisci and are comparable to the amount of film thickness to the radius of tube for flows with the Reynolds numbers greater than 100 were not considered by Bretherton theory and we do not follow that theory (Walsh et al., 2009). The presence of two different contact angles between the frontal and rear menisci and the channel wall causes an interfacial pressure drop across a moving slug through a tube (Aota et al., 2009; Adrugi et al., 2016). The values of the advancing and receding contact angles restrict the Laplace pressure loss. The model of pressure drop across the length (L) of the capillary tube can be obtained by combining equations (7.16)–(7.19):

$$\Delta P_T = \frac{L}{L_{uc}}(\Delta P_{Fr,c} + \Delta P_{\mathbf{Fr},d}) + \frac{2L - L_{uc}}{L_{uc}}\Delta P_{Int} \tag{7.20}$$

The model considers a summation of pressure loss in the carrying and dispersed phases separately and pressure loss caused by the interfacial tension at the interface of the phases. It can also be obtained through the force balance in the axis direction of a slug unit cell as,

$$\Delta P_T A = \tau_w P L_{uc} + \Delta P_{Int} A \tag{7.21}$$

where P indicates the perimeter of the cross-section of the tube. Substituting the proper expression for τ_w and simplification yield the total pressure drop over a slug unit cell:

$$\frac{\Delta P_T}{L_{uc}}\frac{D^2}{2\mu_e U} = f\,\mathrm{Re} + \frac{2D}{L_{uc}}\frac{(\cos\theta_r - \cos\theta_a)}{\mathrm{Ca}} \tag{7.22}$$

The presence of Taylor slugs in carrying flow may change the effective viscosity (μ_e) due to the phase interactions and the momentum transfer characteristics. Consequently, the capillary number has been calculated using effective dynamic viscosity through the McAdams model (McAdams, 1942), which considers the structure of each phase, the interaction between the phases, and the volumetric fraction of each,

$$\mu_e = \left(\frac{x}{\mu_d} + \frac{1-x}{\mu_c}\right)^{-1} \tag{7.23}$$

The mass quality (x) satisfies the following limitations: $x = 0$ when $\mu_e = \mu_c$ and $x = 1$ when $\mu_e = \mu_d$. The dimensionless form of the total pressure drop for fully developed Taylor flow in mini-scale capillaries is

$$\Delta P_T^\star = 16 + \frac{1}{L_{uc}^\star} \tag{7.24}$$

where,

$$L_{uc}^\star = \frac{L_{uc}}{2D}\frac{Ca}{(\cos\theta_r - \cos\theta_a)} \tag{7.25}$$

Therefore, the pressure drop of a two-phase Taylor flow through a mini-scale tube is a function of capillary number, length of the unit cell, and the contact angles (Adrugi et al., 2016). The contact angle values are calculated using CFD results and experimental data in our upcoming analysis. Since a Taylor flow is a train of slug unit cells, the total pressure drop between two points per a known length is equal to the total pressure drop across a unit cell, i.e., $\Delta P/L = \Delta P_T/L_{uc}$.

Figure 7.12 shows the total pressure drop across a unit cell for two water / silicone oil systems and three tubing sizes obtained by CFD simulations and experiments. The total pressure drop is dominantly characterized by the interfacial pressure loss in such segmented flow for $L_{uc}^\star \ll 0.1$, is verified well by the CFD and experimental results and was also shown by Walsh et al. (2009) experimentally and analytically. In contrast, the contribution of the interfacial pressure loss decreases as the non-dimensionalized length of the unit cell increases beyond 0.1, which also leads to a more single-phase flow situation (i.e., Poiseuille flow or infinitely long carrying plugs) rather than the Taylor flow. The results also show the validity of the model for both phase systems that feature the robustness of the model to predict the pressure drop in such Taylor flows regardless of the viscosity ratio of the phases, as mentioned by Adrugi et al., 2016. They employed three silicone oils of 1, 3, and 5 cSt over a broader range of flow rates up to 20 ml/min. As the phase fraction remained constant at 0.5, their experimental data showed the same trend as the model.

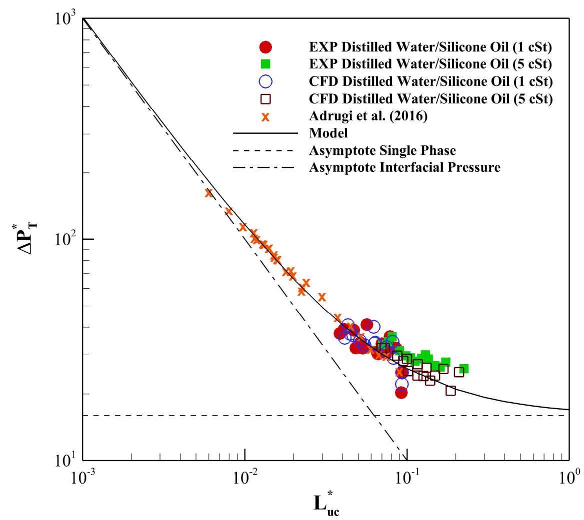

FIGURE 7.12: Distribution of non-dimensionalized total pressure drop across a unit cell through CFD simulations and experiments considering the intersection of asymptotes approach to show the dominancy of each pressure asymptote regions

7.5.7 Heat Transfer Analysis

In this section, the heat transfer analysis is conducted under two constant wall temperatures of 40 and 50 °C passed through a 100 mm length of a copper tube with an inner diameter of 1.65 mm for experiments and across the length of a unit cell in the CFD simulations. The volumetric flow rate ratios vary from 0.5 to 4, and we also considered three new unity volumetric flow rates for 2.5, 5, and 7.5 ml/min. Equations (7.5), (7.7), and (7.10) calculate the mean wall heat flux, dimensionless mean wall heat flux, and dimensionless thermal length, respectively, using effective properties of the phases obtained by the McAdams model. An asymptotic solution of Graetz-slug flow in circular ducts that was developed by Muzychka et al. (2010) also calculates non-dimensionalized mean wall heat flux as,

$$q^{\star} = \left[\left(\frac{1.128}{L^{\star 1/2}}\right)^{-5/2} + \left(\frac{1}{4L^{\star}}\right)^{-5/2}\right]^{-2/5} \tag{7.26}$$

Figure 7.13 shows the distribution of dimensionless mean wall heat flux versus dimensionless thermal length presenting well in agreement with Muzychka's model. As seen, the presence of slugs enhances the heat transfer rate significantly compared to single-phase flow as $L^{\star} \rightarrow 0$. Internal recirculation regions in the slugs and in carrying plugs are responsible for increasing the thermal energy transport rate from the heated walls into the cold main flow (as shown in Figure 7.9 too).

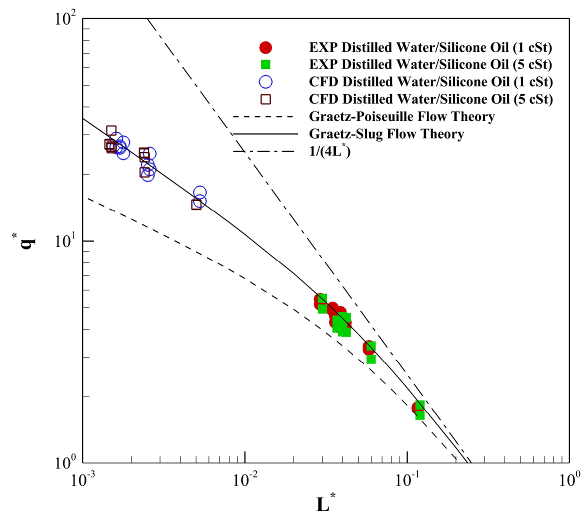

FIGURE 7.13: Distribution of mean wall heat flux versus dimensionless thermal channel length for experimental data and across a unit cell for CFD results

7.6 Conclusions

Experimental and numerical studies have been conducted on the hydrodynamic characteristics and heat transfer of Taylor flow through mini-scale straight tubing with the inner diameters of 1.65, 1.52, and 1.42 mm under a constant wall temperature condition. The theoretical solution of the Poiseuille flow in circular channels verified our experimental setup and the data obtained through the experiments. The results fall within the ±10% range of the Poiseuille model for pressure drop and the Graetz-

Poiseuille model proposed by Muzychka et al. (2010) for heat transfer. Two mesh generation methods called handcrafted and boundary adaptive have been examined to evaluate the effects of grid resolution on the convergence speed and accuracy of the results, e.g., liquid film thickness, slug length, and Nusselt number. The validity of numerical simulations was examined by comparing liquid film thickness and slug profile with the reported data in the literature.

The effects of the dynamic viscosity and volumetric flow rate ratio of the phases on the flow pattern and heat transfer were studied for different tubing sizes. It was found that an increase in the volumetric flow rate from 0.5 to 4, enhanced the inertia of the carrying flow, doubling the normalized local velocity at the centre of the liquid plug. It also enlarged two cap recirculation regions and squeezed the central vortex, followed by the semi-spherical slugs with a short uniform film region. The recirculation regions led to significant change in the flow pattern, shear stresses, and heat transfer, particularly near the film region. A higher volumetric flow rate allowed for more momentum and facilitated a larger thermal energy transfer from the heated wall of the channel to the interface. The influence of interfacial pressure drop decreased as the dimensionless length of the channel approached beyond 0.1, resulting in concise water slugs and long oil plugs.

Further investigations are required to study the mean wall heat flux when the length of the thermal test tube is very long or very short. The numerical and experimental studies on the heat transfer and pressure drop measurements of Taylor flow through the ducts with more complex cross-sections, such as triangle, hexagon, and octagon, would be of interest too. Predicting thermal performance and pressure loss of Taylor flow with various geometries and under a wide range of operating conditions can be carried out by machine learning models.

Chapter 8

Conclusions and Recommendations

This chapter concludes the main findings of the Chapters 4-7 and presents an overview on the achievements of the work shown in this Ph.D. thesis. The content has been ordered with respect to the information provided in the respective chapters. Furthermore, an outlook highlights the possibilities of the future work that might be followed by prospective researchers.

8.1 Summary

In order to establish a CFD-based analysis of gas-liquid and liquid-liquid two-phase flows in the capillaries with circular cross-section, first, two developing and fully developed air / water flows are considered. An in-detailed mesh generation procedure followed by a meaningful grid independence study on several flow parameters are conducted which periodically are used in the rest of this study. It shows the mesh size causes different interactions between two phases and the channel wall, i.e., dry-out, partially dry-out, and fully wetted to explain whether the wall is kept dry or wet. The numerical predictions also show that the liquid film thickness of the air bubbles remained almost constant, but the length of the flat film region increases as the air bubble moves downstream.

The effects of two flow parameters, i.e., superficial velocities and thermophysical properties on the hydrodynamics of the segmented flow in microchannels are discussed to reveal more in-depth detail of such flow. A precise time-history of slug formation is presented to understand its different evolution steps; introducing, expanding, contracting, necking, and breakup. The results show that the higher dynamic viscosity ratio of the LL flow compared to GL flow takes the main responsibility of establishing a more stable interface, moving the breakup point to the downstream, and making the semi-hemispherical curvatures at the two ends of the slugs faster. The length of air bubble is greater than water slug, which the highest difference happens at the velocity ratio of unity. Besides, the air bubbles moves faster than the average velocity because of the lubricating effects as is often affirmed in the literature. To the best of my knowledge, the variation of holdup with the superficial velocity ratio is correlated, for the first time. For the LL case, the highest pressure is located in the rear half of the slugs, which can be attributed to the slug movement and a significant change in the velocity, field inside the liquid slugs, while the pressure remains constant inside the slugs of the GL.

The presence of a sudden diameter expansion at the middle of a microchannel along with the different physical properties and superficial velocities are considered. It is shown that an increase in superficial velocity ratio elongated air bubbles and water slugs. Another interesting finding is that the higher apparent viscosity ratio for LL flow lessens the fluctuation of the interface within the uniform film region and enhances the thickness of the liquid film. The results also reveal that the diameter expansion increases the pressure distribution inside the slugs, shortens the slugs, and changes the pressure around the slug caps.

Experimental and numerical studies on the hydrodynamic characteristics and heat transfer of Taylor flow through mini-scale straight tubing are conducted under a constant wall temperature condition. The theoretical solution of the Poiseuille flow in circular channels verifies our experimental setup and the data obtained through the experiments. The results fall within the ±10% range of the Poiseuille model for pressure drop and the Graetz-Poiseuille model for heat transfer. Two mesh generation methods called handcrafted and boundary adaptive have been examined to evaluate the effects of grid resolution on the convergence speed and accuracy of the results, e.g., liquid film thickness, slug length, and Nusselt number. The validity of numerical simulations is examined by comparing liquid film thickness and slug profile with the reported data in the literature.

The effects of the dynamic viscosity and volumetric flow rate ratio of the phases on the flow pattern and heat transfer are studied for different tubing sizes. It is found that an increase in the volumetric flow rate enhances the inertia of the carrying flow, doubling the normalized local velocity at the centre of the liquid plug. It also enlarges two cap recirculation regions and squeezes the central vortex, followed by the semi-spherical slugs with a short uniform film region. The recirculation regions lead to significant change in the flow pattern, shear stresses, and heat transfer, particularly near the film region. A higher volumetric flow rate allows for more momentum and facilitates a larger thermal energy transfer from the heated wall of the channel to the interface. The influence of interfacial pressure drop decreases as the dimensionless length of the channel approaches beyond 0.1, resulting in concise water slugs and long oil plugs.

8.2 Future Works

The presence of the Taylor slugs in many chemical processes and micro-devices necessitates optimal operational conditions where the interface and Taylor train fluctuations are minimized or at least predictable. The fluctuations can potentially change the hydrodynamics and thermal performance of such flows. The slug deformation dominantly impacts the dynamics of the Taylor slugs as the slugs move downstream. Therefore, much more contribution might be dedicated to understanding the slug breakup mechanism and effective parameters. The effects of the surface roughness on the film region is crucial to understand the physics of transport phenomena in the interface of phases. The numerical and experimental studies on the heat transfer and pressure drop measurements of Taylor flow through the ducts with more complex cross-sections, such as triangle, hexagon, and octagon, would be of interest too. Predicting thermal performance and pressure loss of Taylor flow with various geometries and under a wide range of operating conditions can be carried out by machine learning models. An end-to-end deep machine-learning tool, for example, accurately improves approximations in CFD solvers for solving microchannel flows. Further investigations are required to study the mean wall heat flux when the length of the thermal test tube is very long or very short. Many energy-related applications benefit from micro-sized cooling systems, which specifically introduce two phases through the channels to establish slug flow and enhance cooling performance. The presence of two liquid phases can increase the heat transfer rate, to which further contribution must be dedicated.

References

Abdollahi, A., Norris, S.E., Sharma, R.N. (2020) Fluid flow and heat transfer of liquid-liquid Taylor flow in square microchannels. Applied Thermal Engineering. 172, 115123.

Abiev, R.Sh. (2011) Modeling of pressure losses for the slug flow of a gas-liquid mixture in mini- and microchannels. Theoretical Foundations of Chemical Engineering. 45, 156–163.

Abiev, R.Sh. and Lavretsov, I.V. (2012) Intensification of mass transfer from liquid to capillary wall by Taylor vortices in minichannels, bubble velocity and pressure drop. Chemical Engineering Science. 74, 59–68.

Abiev, R.Sh. (2017) Analysis of local pressure gradient inversion and form of bubbles in Taylor flow in microchannels. Chemical Engineering Science. 174, 403–412.

Adalsteinsson, D. and Sethian, J.A. (1995) A fast level set method for propagating interfaces. Journal of Computational Physics. 118(2), 269–277.

Adalsteinsson, D. and Sethian, J.A. (1999) The fast construction of extension velocities in level set methods. Journal of Computational Physics. 148(1), 2–22.

Adaze, E., Al-Sarkhi, A., Badr, H.M., Elsaadawy, E. (2019) Current status of CFD modeling of liquid loading phenomena in gas wells: a literature review. Journal of Petroleum Exploration and Production Technology. 9, 1397–1411.

Adrugi, W., Muzychka, Y.S., Pope, K. (2016) Pressure drop of liquid-liquid Taylor flow in mini-scale tubing. In ASME International Mechanical Engineering Congress and Exposition, Phoenix, Arizona, USA.

Agrawal, N. and Bhattacharyya, S. (2008) Homogeneous versus separated two phase flow models: adiabatic capillary tube flow in a transcritical CO_2 heat pump. International Journal of Thermal Sciences. 47(11), 1555–1562.

Akagawa, K. and Sakaguchi, T. (1966) Fluctuation of void ratio in two-phase flow: 2nd report, analysis of flow configuration considering the existence of small bubbles in liquid slugs. Bulletin of JSME. 9, 104–110.

Akbar, M.K., Plummer, D.A., Ghiaasiaan, S.M. (2002) Gas-liquid two-phase flow regimes in microchannels. In ASME International Mechanical Engineering Congress and Exposition, New Orleans, LO, USA.

Akbar, M.K., Plummer, D.A., Ghiaasiaan, S.M. (2003) On gas-liquid two-phase flow regimes in microchannels. International Journal of Multiphase Flows. 29(5), 855–865.

Aland, S., Lehrenfeld, C., Marschall, H., Meyer, C., Weller, S. (2013) Accuracy of two phase flow simulations: the Taylor flow benchmark. In 84th Annual Meeting of the International Association of Applied Mathematics and Mechanics (GAMM), Novi Sad, Serbia.

Ali, M.I., Sadatomi, M., Kawaji, M. (1993) Adiabatic two-phase flow in narrow channels between two flat plates. The Canadian Journal of Chemical Engineering. 71(5), 657–666.

Alrbee, K., Muzychka, Y.S., Duan, X. (2019) Laminar heat transfer of gas-liquid segmented flows in circular ducts with constant wall temperature. In 17th International Conference on Nanochannels, Microchannels, and Minichannels (ICNMM), St. John's, NL, Canada.

Alrbee, K., Muzychka, Y.S., Duan, X. (2020) Separated phase analysis of heat transfer in liquid-liquid Taylor flow in a miniscale straight tube. Journal of Heat Transfer. 142(12), 122001.

Alrbee, K., Muzychka, Y.S., Duan, X. (2021) Heat transfer in laminar Graetz and Taylor flows incorporating nanoparticles. Heat Transfer Engineering. 43(12), 975–990.

Alves, G.E. (1954) Co-current liquid-gas flow in a pipe-line contactor. Chemical Engineering Progress. 50, 449–456.

Anderson, D.M. and McFadden, G.B. (1998) Diffuse-interface methods in fluid mechanics. Annual Review of Fluid Mechanics. 30, 139–165.

Andreussi, P., Paglianti, A., Silva, F.S. (1999) Dispersed bubble flow in horizontal pipes. Chemical Engineering Science. 54(8), 1101–1107.

Angeli, P. and Gavriilidis, A. (2008) Hydrodynamics of Taylor flow in small channels: a review. Journal of Mechanical Engineering Science. 222(5), 737–751.

ANSYS Fluent 18.1.0 Users' Guide (2017) SAS Inc.

Aota, A., Mawatari, K., Takahashi, S., Matsumoto, T., Kanda, K., Anraku, R., Hibara, A., Tokeshi, M., Kitamori, T. (2009) Phase separation of gas-liquid and liquid-liquid microflows in microchips. Microchimica Acta. 164(3), 249–255.

Apte, S.V., Mahesh, K., Lundgren, T. (2003) A Eulerian-Lagrangian model to simulate two-phase/particulate flows. Center for Turbulence Research, Center for Turbulence Research, Annual Research Briefs.

Armand, A.A. (1946) The resistance during the movement of a two-phase system in horizontal pipes. Izvestiia Vsesoiuznyi Teplotekhnicheskii Institut. 1, 16–23.

Armfield, S. and Street, R. (1999) The fractional-step method for the Navier-Stokes equations on staggered grids: the accuracy of three variations. Journal of Computational Physics. 153(2), 660–665.

Asadolahi, A.N., Gupta, R., Leung, S.S.Y., Fletcher, D.F., Haynes, B.S. (2012) Validation of a CFD model of Taylor flow hydrodynamics and heat transfer. Chemical Engineering Science. 69(13), 541–552.

Asano, S., Takahashi, Y., Maki, T., Muranaka, Y., Cherkasov, N., Mae, K. (2020) Contactless mass transfer for intra-droplet extraction. Scientific Reports. 10, 7685.

Asthana, A., Zinovik, I., Weinmueller, C., Poulikakos, D. (2011) Significant Nusselt number increase in microchannels with a segmented flow of two immiscible liquids: an experimental study. International Journal of Heat and Mass Transfer. 54(7–8), 1456–1464.

Aussillous, P. and Quéré, D. (2000) Quick deposition of a fluid on the wall of a tube. Physics of Fluids. 12(10), 2367–2371.

Awad, M.M. and Muzychka, Y.S. (2008) Effective property models for homogeneous two-phase flows. Experimental Thermal and Fluid Science. 33(1), 106–113.

Awad, M.M. and Muzychka, Y.S. (2010) Two-phase flow modeling in microchannels and minichannels. Heat Transfer Engineering. 31(13), 1023–1033.

Awad, M.M. (2012) Two-phase flow. In An Overview of Heat Transfer Phenomena. Salim, N.K., Ed., IntechOpen, London, UK.

Baier, G. (1999) Liquid-liquid extraction based on a new flow pattern: two-fluid Taylor-Couette flow. Ph.D. thesis, The University of Wisconsin-Madison, Wisconsin, USA.

Baker, O. (1953) Design of pipelines for the simultaneous flow of oil and gas. In Proceedings of the Fall Meeting of the Petroleum Branch of AIME, Dallas, TX, USA.

Barbosa, M.V., De Lai, F.C., Junqueira, S.L.M. (2019) Numerical evaluation of CFD-DEM coupling applied to lost circulation control: effects of particle and flow inertia. Mathematical Problems in Engineering. 1–13.

Barnea, D., Shoham, O., Taitel, Y. (1982a) Flow pattern transition for downward inclined two-phase flow; horizontal to vertical. Chemical Engineering Science. 37(5), 735–740.

Barnea, D., Shoham, O., Taitel, Y. (1982b) Flow pattern transition for vertical downward two-phase flow. Chemical Engineering Science. 37(5), 741–744.

Barral Jr, A.A., Minussi, R.B., Canhoto Alves, M.V. (2019) Comparison of interface description methods available in commercial CFD software. Journal of Applied Fluid Mechanics. 12(6), 1801–1812.

Bauer, T. and Koengeter, J. (1999) PIV with high temporal resolution for the determination of local pressure reductions from coherent turbulent phenomena. In 3rd International workshop on PIV, Santa Barbara. 671–676.

Berčič, G. and Pintar, A. (1997) The role of gas bubbles and liquid slug lengths on mass transport in the Taylor flow through capillaries. Chemical Engineering Science. 52(21–22), 3709–3719.

Bico, J. and Quéré, D. (2000) Liquid trains in a tube. Europhysics Letters. 51(5), 546–550.

Boger, T., Roy, S., Heibel, A.K., Borchers, O. (2003) A monolith loop reactor as an attractive alternative to slurry reactors. Catalysis Today. 79–80, 441–451.

Boger, T., Zieverink, M.M.P., Kreutzer, M.T., Kapteijn, F., Moulijn, J.A., Addiego, W.P. (2004a) Monolithic catalysts as an alternative to slurry systems: hydrogenation of edible oil. Industrial and Engineering Chemistry Research. 43(10), 2337–2344.

Boger, T., Heibel, A.K., Sorensen, C.M. (2004b) Monolithic catalysts for the chemical industry. Industrial and Engineering Chemistry Research. 43(16), 4602–4611.

Bolivar, J.M. and Nidetzky, B. (2013) Multiphase biotransformations in microstructured reactors: opportunities for biocatalytic process intensification and smart flow processing. Green Processing and Synthesis. 2(6), 541–559.

Bottin, M., Berlandis, J.P., Hervieu, E., Lance, M., Marchand, M., Öztürk, O.C., Serre, G. (2014) Experimental investigation of a developing two-phase bubbly flow in horizontal pipe. International Journal of Multiphase Flow. 60, 161–179.

Bowden, S.A., Monaghan, P.B., Wilson, R., Parnell, J., Cooper, J.M. (2006) The liquid-liquid diffusive extraction of hydrocarbons from a north sea oil using a microfluidic format. Lab on a Chip. 6, 740–743.

Brackbill, J.U., Kothe, D.B., Zemach, C. (1992) A continuum method for modeling surface tension. Journal of Computational Physics. 100(2), 335–354.

Brauner, N. and Maron, D.M. (1992) Identification of the range of 'small diameters' conduits, regarding two-phase flow pattern transitions. International Communications in Heat and Mass Transfer. 19(1), 29–39.

Brauner, N., Maron, D.M., Rovinsky, J. (1998) A two-fluid model for stratified flows with curved interfaces. International Journal of Multiphase Flow. 24(6), 975–1004.

Brauner, N. (2003) Liquid-liquid two-phase flow systems, modelling and experimentation in two-phase flow. Springer, Vienna. 450, 221–279.

Bretherton, F.P. (1961) The motion of long bubbles in tubes. Journal of Fluid Mechanics. 10(2), 166–188.

Broekhuis, R.R., Machado, R.M., Nordquist, A.F. (2001) The ejector-driven monolith loop reactor-experiments and modelling. Catalysis Today. 69(1–4), 87–93.

Burns, J.R. and Ramshaw, C. (1999) Development of a microreactor for chemical production. Chemical Engineering Research and Design. 77(3), 206–211.

Butler, C., Lalanne, B., Sandmann, K., Cid, E., Billet, A.M. (2018) Mass transfer in Taylor flow: transfer rate modelling from measurements at the slug and film scale. International Journal of Multiphase Flow. 105, 185–201.

Cahn, J.W. and Hilliard, J.E. (1958) Free energy of a nonuniform system. I. interfacial free energy. The Journal of Chemical Physics. 28(2), 258–267.

Cahn, J.W. (1959) Free energy of a nonuniform system. II. thermodynamic basis. The Journal of Chemical Physics. 30(5), 1121–1123.

Cahn, J.W. and Hilliard, J.E. (1959) Free energy of a nonuniform system. III. nucleation in a two-component incompressible fluid. The Journal of Chemical Physics. 31(3), 688–699.

Cahn, J.W. (1961) On spinodal decomposition. Acta Metallurgica. 9(9), 795–801.

Cao, J., Zhang, J., Persic, J., Song, K. (2020) Effects of bonding parameters on free air ball properties and bonded strength of Ag-10Au-3.6 Pd alloy bonding wire. Micromachines. 11(8), 777.

Cao, Y., Soares, C., Padoin, N., Noël, T. (2021) Gas bubbles have controversial effects on Taylor flow electrochemistry. Chemical Engineering Journal. 406, 126811.

Cao, Y., Padoin, N., Soares, C., Noël, T. (2022) On the performance of liquid-liquid Taylor flow electrochemistry in a microreactor–a CFD study. Chemical Engineering Journal. 427, 131443.

Chai, L., Wang, L., Zhou, M., Xia, G. (2015) Two-phase flow pattern and pressure drop in silicon multi-microchannel with expansion-constriction cross-section. Experimental Thermal and Fluid Science. 60, 241–251.

Chao, C., Jin, X., Fan, X. (2020) Evolution of thin-liquid films surrounding bubbles in microfluidics and their impact on the pressure drop and fluid movement. Langmuir. 36(49), 15102–15111.

Chaoqun, Y., Yuchao, Z., Chunbo, Y., Minhui, D., Zhengya, D., Guangwen, C. (2013) Characteristics of slug flow with inertial effects in a rectangular microchannel. Chemical Engineering Science. 95, 246–256.

Che, Z., Wong, T.N., Nguyen, N.T. (2012) Heat transfer enhancement by recirculating flow within liquid plugs in microchannels. International Journal of Heat and Mass Transfer. 55(7–8), 1947–1956.

Chen, J.D. (1986) Measuring the film thickness surrounding a bubble inside a capillary. Journal of Colloid and Interface Science. 109(2), 341–349.

Chen, S., Chen, H., Martnez, D., Matthaeus, W. (1991) Lattice Boltzmann model for simulation of magnetohydrodynamics. Physical Review Letters. 67(27), 3776–3779.

Chen, S. and Doolen, G.D. (1998) Lattice Boltzmann method for fluid flows. Annual Review of Fluid Mechanics. 30, 329–364.

Chen, J.L. and Lin, Y.C. (2000). A new approach in free air ball formation process parameters analysis. IEEE Transactions on Electronics Packaging Manufacturing. 23(2), 116–122.

Cheng, H., Hills, J.H., Azzorpardi, B.J. (1998) A study of the bubble-to-slug transition in vertical gas-liquid flow in columns of different diameters. International Journal of Multiphase Flow. 24(3), 431–452.

Chingulpitak, S. and Wongwises, S. (2010) Two-phase flow model of refrigerants flowing through helically coiled capillary tubes. Applied Thermal Engineering. 30(14–15), 1927–1936.

Chisholm, D. (1967) A theoretical basis for the Lockhart-Martinelli correlation for two-phase flow. International Journal of Heat and Mass Transfer. 10(12), 1767–1778.

Choi, Y.J. and Anderson, P.D. (2011) Cahn-Hillard modelling of particles suspended in two-phase flows. International Journal for Numerical Methods in Fluids. 69(5), 995–1015.

Chung, P.M.-Y. and Kawaji, M. (2004) The effect of channel diameter on adiabatic two-phase flow characteristics in microchannels. International Journal of Multiphase Flow. 30(7–8), 735–761.

Churchill, S.W. and Usagi, R. (1972) A general expression for the correlation of rates of transfer and other phenomena. AIChE Journal. 18(6), 1121–1128.

Cicchitti, A., Lombardi, C., Silvestri, M., Soldaini, G., Zavattarelli, R. (1960) Two-phase cooling experiments-pressure drop, heat transfer and burnout measurements. Energia Nuclear. 7, 407–425.

Coleman, J.W. and Garimella, S. (1999) Characterization of two-phase flow patterns in small diameter round and rectangular tubes. International Journal of Heat and Mass Transfer. 42(15), 2869–2881.

Collier, J.G. and Thome, J.R. (1994) Convective boiling and condensation, 3rd edition, Oxford, New York.

Cox, B.G. (1963) On driving a viscous fluid out of a tube. Journal of Fluid Mechanics. 14(1), 81–96.

Cox, B.G. (1964) An experimental investigation of the streamlines in viscous fluid expelled from a tube. Journal of Fluid Mechanics. 20(2), 193–200.

Cramer, C., Fischer, P., Windhab, E.J. (2004) Drop formation in a co-flowing ambient fluid. Chemical Engineering Science. 59(15), 3045–3058.

Cubaud, T. and Ho, C.M. (2004) Transport of bubbles in square microchannels. Physics of Fluids. 16(12), 4575–4585.

Cubaud, T., Ulmanella U., Ho, C.M. (2006) Two-phase flow in microchannels with surface modifications. Fluid Dynamics Research. 38(11), 772–786.

Cubaud, T. and Mason, T.G. (2008) Capillary threads and viscous droplets in square microchannels. Physics of Fluids. 20(5), 053302.

Cueto-Felgueroso, L. and Juanes, R. (2008) Nonlocal interface dynamics and pattern formation in gravity-driven unsaturated flow through porous media. Physical Review Letters. 101(24), 244504.

Cui, Y., Wang, N., Liu, H. (2019) Numerical study of droplet dynamics in a steady electric field using a hybrid lattice Boltzmann and finite volume method. Physics of Fluids. 31(2), 022105.

Cybulski, A., Stankiewicz, A., Edvinsson Albers, R.K., Moulijn, J.A. (1999) Monolithic reactors for fine chemicals industries: a comparative analysis of a monolithic reactor and a mechanically agitated slurry reactor. Chemical Engineering Science. 54(13–14), 2351–2358.

Dai, Z., Guo, Z., Fletcher, D.F., Haynes, B.S. (2015) Taylor flow heat transfer in microchannels-unification of liquid-liquid and gas-liquid results. Chemical Engineering Science. 138, 140–152.

Das, R.K. and Pattanayak, S. (1994) Bubble to slug flow transition in vertical upward two-phase flow through narrow tubes. Chemical Engineering Science. 49(13), 2163–2172.

Das, A.K., Das, P.K., Thome, J.R. (2009a) Transition of bubbly flow in vertical tubes: new criteria through CFD simulation. ASME Journal of Fluids Engineering. 131(9), 091303.

Das, A.K., Das, P.K., Thome, J.R. (2009b) Transition of bubbly flow in vertical tubes: effect of bubble size and tube diameter. ASME Journal of Fluids Engineering. 131(9), 091304.

de Gennes, P.G. (1985) Wetting: statics and dynamics. Reviews of Modern Physics. 57(3), 827–863.

Deendarlianto, Rahmandhika, A., Widyatama, A., Dinaryanto, O., Widyaparaga, A., Indarto, (2019) Experimental study on the hydrodynamic behavior of gas-liquid air-water two-phase flow near the transition to slug flow in horizontal pipes. International Journal of Heat and Mass Transfer. 130, 187–203.

Delnoij, E., Lammers, F.A., Kuipers, J.A.M., van Swaaij, W.P.M. (1997) Dynamic simulation of dispersed gas-liquid two-phase flow using a discrete bubble model. Chemical Engineering Science. 52(9), 1429–1458.

Dendy, E.D., Padial-Collins, N.T., VanderHeyden, W.B. (2002) A general-purpose finite-volume advection scheme for continuous and discontinuous fields on unstructured grids. Journal of Computational Physics. 180(2), 559–583.

Dessimoz, A.L., Cavin, L., Renken, A., Kiwi-Minsker, L. (2008) Liquid-liquid two-phase flow patterns and mass transfer characteristics in rectangular glass microreactors. Chemical Engineering Science. 63(16), 4035–4044.

Dessimoz, A.L., Raspail, P., Berguerand, C., Kiwi-Minsker, L. (2010) Quantitative criteria to define flow patterns in micro-capillaries. Chemical Engineering Journal. 160(3), 882–890.

Dore, V., Tsaoulidis, D., Angeli, P. (2012a) Mixing patterns in water plugs during water/ionic liquid segmented flow in microchannels. Chemical Engineering Science. 80, 334–341.

Dore, V., Tsaoulidis, D., Angeli, P. (2012b) μ-PIV investigation of water/ionic liquid plug flow dynamics in meandering microchannels. In 16th International Symposium on Applications of Laser Techniques to Fluid Mechanics, Lisbon, Portugal, 1–12.

Dukler, A.E., Wicks III, M., Cleveland, R.G. (1964) Frictional pressure drop in two-phase flow: A. A comparison of existing correlations for pressure loss and holdup. AIChE Journal. 10(1), 38–43.

Dukler, A.E. and Taitel, Y. (1986) Flow pattern transitions in gas-liquid systems: measurement and modeling. In Multiphase Science and Technology, Springer: Berlin/Heidelberg, Germany.

Eain, M.M.G., Egan, V., Punch, J. (2013) Film thickness measurements in liquid-liquid slug flow regimes. International Journal of Heat and Fluid Flow. 44, 515–523.

Eain, M.M.G., Egan, V., Howard, J., Walsh, P., Walsh, E., Punch, J. (2015) Review and extension of pressure drop models applied to Taylor flow regimes. International Journal of Multiphase Flow. 68, 1–9.

Edvinsson, R.K. and Cybulski, A. (1995) A comparison between the monolithic reactor and the trickle-bed reactor for liquid phase hydrogenations. Catalysis Today. 24(1–2), 173–179.

Elvira, K.S., i Solvas, X.C., Wootton, R.C.R., deMello, A.J. (2013) The past, present and potential for microfluidic reactor technology in chemical synthesis. Nature Chemistry. 5(11), 905–915.

Etminan, A., Muzychka, Y.S., Pope, K. (2020) Numerical simulation of Taylor flow in the entrance region of microchannels. In 5th World Congress on Momentum, Heat and Mass Transfer (MHMT'20), Lisbon, Portugal.

Etminan, A., Muzychka, Y.S., Pope, K. (2021a) A review on the hydrodynamics of Taylor flow in microchannels: experimental and computational studies. Processes. 9(5), 870.

Etminan, A., Muzychka, Y.S., Pope, K. (2021b) Film thickness and pressure drop for gas-liquid Taylor flow in microchannels. Journal of Fluid Flow, Heat and Mass Transfer. 8(1), 59–70.

Etminan, A., Muzychka, Y.S., Pope, K. (2021c) CFD modelling for gas-liquid and liquid-liquid Taylor flows in the entrance region of microchannels. In the ASME Fluids Engineering Division Summer Meeting. 85307, V003T08A009.

Etminan, A., Muzychka, Y.S., Pope, K. (2022a) Liquid film thickness of two-phase slug flows in capillary microchannels: a review paper. The Canadian Journal of Chemical Engineering. 100(2), 325–348.

Etminan, A., Muzychka, Y.S., Pope, K. (2022b) Numerical investigation of gas-liquid and liquid-liquid Taylor flow through a circular microchannel with a sudden expansion. The Canadian Journal of Chemical Engineering. 100(7), 1596–1612.

Etminan, A., Muzychka, Y.S., Pope, K., Nyantekyi-Kwakye, B. (2022c) Flow visualization: state-of-the-art development of micro-particle image velocimetry. Measurement Science and Technology. 33(9), 092002.

Fairbrother, F. and Stubbs, A.E. (1935) Studies in electro-endosmosis: part VI. the “bubble-tube” method of measurement. Journal of Chemical Society. 1, 527–529.

Falconi, C.J., Lehrenfeld, C., Marschall, H., Meyer, C., Abiev, R., Bothe, D., Reusken, A., Schlüter, M., Wörner, M. (2016) Numerical and experimental analysis of local flow phenomena in laminar Taylor flow in a square mini-channel. Physics of Fluids. 28(1), 012109.

Farokhpoor, R., Liu, L., Langsholt, M., Hald, K., Amundsen, J. (2020) Dimensional analysis and scaling in two-phase gas-liquid stratified pipe flow-methodology evaluation. International Journal of Multiphase Flow. 122, 103139.

Fei, L., Du, J., Luo, K.H., Succi, S., Lauricella, M., Montessori, A., Wang, Q. (2019) Modeling realistic multiphase flows using a non-orthogonal multiple-relaxation-time lattice Boltzmann method. Physics of Fluids. 31(4), 042105.

Fernandes, R.C. (1981) Experimental and theoretical studies of isothermal upward gas-liquid flows in vertical tubes. Ph.D. thesis, University of Houston, Houston, TX, USA.

Fletcher, D.F. and Haynes, B.S. (2017) CFD simulation of Taylor flow: should the liquid film be captured or not? Chemical Engineering Science. 167, 334–335.

Fouilland, T.S., Fletcher, D.F., Haynes, B.S. (2010) Film and slug behaviour in intermittent slug-annular microchannel flows. Chemical Engineering Science. 65(19), 5344–5355.

Fries, D.M. and von Rohr, P.R. (2009) Liquid mixing in gas-liquid two-phase flow by meandering microchannels. Chemical Engineering Science. 64(6), 1326–1335.

Frisch, U., Hasslacher, B., Pomeau, Y. (1986) Lattice-gas automata for the Navier-Stokes equation. Physical Review Letters. 56, 1505–1508.

Fu, T. and Ma, Y. (2015) Bubble formation and breakup dynamics in microfluidic devices: a review. Chemical Engineering Science. 135, 343–372.

Fu, T., Ma, Y., Li, H.Z. (2015) Bubble coalescence in non-Newtonian fluids in a microfluidic expansion device. Chemical Engineering and Processing: Process Intensification. 97, 38–44.

Fuerstman, M.J., Lai, A., Thurlow, M.E., Shevkoplyas, S.S., Stone, H.A., Whitesides, G.M. (2007) The pressure drop along rectangular microchannels containing bubbles. Lab on a Chip. 7(11), 1479–1489.

Fujioka, H. and Grotberg, J.B. (2004) Steady propagation of a liquid plug in a two-dimensional channel. Journal of Biomechanical Engineering. 126(5), 567–577.

Fujioka, H. and Grotberg, J.B. (2005) The steady propagation of a surfactant-laden liquid plug in a two dimensional channel. Physics of Fluids. 17(8), 082102.

Fujisawa, N., Tanahashi, S., Srinivas, K. (2005) Evaluation of pressure field and fluid forces on a circular cylinder with and without rotational oscillation using velocity data from PIV measurement. Measurement Science and Technology. 16(4), 989.

Fujisawa, N., Nakamura, Y., Matsuura, F., Sato, Y. (2006) Pressure field evaluation in microchannel junction flows through µPIV measurement. Microfluidics and Nanofluidics. 2(5), 447–453.

Fukagata, K., Kasagi, N., Ua-arayaporn, P., Himeno, T. (2007) Numerical simulation of gas-liquid two-phase flow and convective heat transfer in a micro tube. International Journal of Heat and Fluid Flow. 28(1), 72–82.

Fukano, T. and Kariyasaki, A. (1993) Characteristics of gas-liquid two-phase flow in a capillary tube. Nuclear Engineering and Design. 141(1–2), 59–68.

Furlong, T.W. and Schmidt, D.P. (2012) A comparison of homogenous and separated flow assumptions for adiabatic capillary flow. Applied Thermal Engineering. 48, 186–193.

Ganapathy, H., Shooshtari, A., Dessiatoun, S., Alshehhi, M., Ohadi, M. (2014) Fluid flow and mass transfer characteristics of enhanced CO_2 capture in a minichannel reactor. Applied Energy. 119, 43–56.

Garimella, S., Killion, J.D., Coleman, J.W. (2003) An experimentally validated model for two-phase pressure drop in the intermittent flow regime for noncircular microchannels. Journal of Fluids Engineering. 125(5), 887–894.

Garstecki, P., Fuerstman, M., Stone, H., Whitesides, G. (2006) Formation of droplets and bubbles in a microfluidic T-junction-scaling and mechanism of break-up. Lab on a Chip. 6(3), 437–446.

Gascon, J., van Ommen, J.R., Moulijn, J.A., Kapteijn, F. (2015) Structuring catalyst and reactor-an inviting avenue to process intensification. Catalyst Science & Technology. 5, 807–817.

Gazley C. (1949) Co-current gas-liquid flow-III. interfacial shear and stability. Heat Transfer and Fluid Mechanics Institute at Berkeley, California, USA.

Ghani, I.A., Sidik, N.A.C., Kamaruzaman, N. (2017) Hydrothermal performance of microchannel heat sink: the effect of channel design. International Journal of Heat and Mass Transfer. 107, 21–44.

Ghiaasiaan, S.M. (2014) Two-phase flow, boiling, and condensation: in conventional and miniature systems. Cambridge University Press, New York, USA.

Giavedoni, M.D. and Saita, F.A. (1997) The axisymmetric and plane cases of a gas phase steadily displacing a Newtonian liquid–a simultaneous solution of the governing equations. Physics of Fluids. 9(8), 2420–2428.

Giavedoni, M.D. and Saita, F.A. (1999) The rear meniscus of a long bubble steadily displacing a Newtonian liquid in a capillary tube. Physics of Fluids. 11(4), 786–794.

Gibbs, J.W. (1878) On the equilibrium of heterogeneous substances. Academy of Arts and Sciences. 16, 441–458.

Goel, D. and Buwa, V.V. (2009) Numerical simulations of bubble formation and rise in microchannels. Industrial & Engineering Chemistry Research. 48(17), 8109–8120.

Govier, G.W. and Aziz, K. (1972) The flow of complex mixtures in pipes. Van Nostrand Reinhold Company, New York, USA.

Gravesen, P., Branebjerg, J., Jensen, O.S. (1993) Microfluidics- a review. Journal of Micromechanics and Microengineering. 3(4), 168–182.

Grimes, R., King, C., Walsh, E. (2006) Film thickness for two phase flow in a microchannel. In the ASME International Mechanical Engineering Congress and Exposition, Chicago, Illinois, USA. 207–211.

Grunau, D., Chen, S., Eggert, K. (1993) A lattice Boltzmann model for multiphase fluid flows. Physics of Fluids A: Fluid Dynamics. 5(10), 2557–2562.

Gubbins, K.E. and Moore, J.D. (2010) Molecular modeling of matter: impact and prospects in engineering. Industrial & Engineering Chemistry Research. 49(7), 3026–3046.

Gunstensen, A.K. and Rothman, D.H. (1991) Lattice Boltzmann model of immiscible fluids. Physical Review A. 43, 4320–4327.

Günther, A., Khan, S.A., Thalmann, M., Trachsel, F., Jensen, K.F. (2004) Transport and reaction in microscale segmented gas liquid flow. Lab on a Chip. 4(4), 278–286.

Gupta, R., Fletcher, D.F., Haynes, B.S. (2009) On the CFD modelling of Taylor flow in microchannels. Chemical Engineering Science. 64(12), 2941–2950.

Gupta, R., Fletcher, D.F., Haynes, B.S. (2010) CFD modelling of flow and heat transfer in the Taylor flow regime. Chemical Engineering Science. 65(6), 2094–2107.

Gupta, R., Leung, S.S.Y., Manica, R., Fletcher, D.F., Haynes, B.S. (2013) Hydrodynamics of liquid-liquid Taylor flow in microchannels. Chemical Engineering Science. 92, 180–89.

Haase, S., Bauer, T., Lange, R. (2015) Numbering-up of a mini- and microchannel contractors and reactors. Chimica Oggi-Chemistry Today. 33, 16–21.

Habibi Matin, M. and Moghaddam, S. (2021) On the extension of Bretherton theory for thin liquid films formed around elongated bubbles. Physics of Fluids. 33(12), 123303.

Han, Y. and Shikazono, N. (2009) Measurement of liquid film thickness in micro square channel. International Journal of Multiphase Flow. 35(10), 896–903.

Han, W. and Chen, X. (2018) Numerical simulation of the droplet formation in a T-junction microchannel by a level-set method. Australian Journal of Chemistry. 71(12), 957–964.

Harirchian, T. and Garimella, S.V. (2009) The critical role of channel cross-sectional area in microchannel flow boiling heat transfer. International Journal of Multiphase Flow. 35(10), 904–913.

Harvie, D.J.E., Davidson, M.R., Rudman, M. (2006) An analysis of parasitic current generation in volume of fluid simulations. Applied Mathematical Modelling. 30(10), 1056–1066.

Hashim, U., Diyana, P.N.A., Adam, T. (2012) Numerical simulation of microfluidic devices. In 10th IEEE International Conference on Semiconductor Electronics (ICSE), Kuala Lumpur, Malaysia.

Hayashi, K., Kurimoto, R., Tomiyama, A. (2010) Dimensional analysis of terminal velocity of a Taylor bubble in a vertical pipe. Multiphase Science and Technology. 22(3), 197–210.

Hayashi, K., Kurimoto, R., Tomiyama, A. (2011) Terminal velocity of a Taylor drop in a vertical pipe. International Journal of Multiphase Flow. 37(3), 241–251.

He, Q., Fukagata, K., Kasagi, N. (2007) Numerical simulation of gas-liquid two-phase flow and heat transfer with dry-out in a micro tube. In 6th International Conference on Multiphase Flow, Leipzig, Germany.

He, Q., Hasegawa, Y., Kasagi, N. (2010) Heat transfer modelling of gas-liquid slug flow without phase change in a micro tube. International Journal of Heat and Fluid Flow. 31(1), 126–136.

Heil, M. (2001) Finite Reynolds number effects in the Bretherton problem. Physics of Fluids. 13(9), 2517–2521.

Heiszwolf, J.J., Engelvaart, L.B., Gvd Eijnden, M., Kreutzer, M.T., Kapteijn, F., Moulijn, J.A. (2001) Hydrodynamic aspects of the monolithic loop reactor. Chemical Engineering Science. 56(3), 805–812.

Helmers, T., Kemper, P., Thöming, J., Mießner, U. (2019) Determining the flow-related cap deformation of Taylor droplets at low Ca numbers using ensemble-averaged high-speed images. Experiments in Fluids. 60(7), 113.

Herwig, H. and Hausner, O. (2003) Critical view on 'New results in micro-fluid mechanics: an example. International Journal of Heat and Mass Transfer. 46(5), 935–937.

Hetsroni, G., Mosyak, A., Pogrebnyak, E., Yarin, L.P. (2005) Fluid flow in micro-channels. International Journal of Heat and Mass Transfer. 48, 1982–1998.

Hewitt, G.F. and Roberts, D.N. (1969) Studies of two-phase flow patterns by simultaneous X-Ray and flash photography. Atomic Energy Research Establishment, Harwell, England, AERE–M 2159.

Heyns, J.A., Malan, A.G., Harms, T.M., Oxtoby, O.F. (2013) Development of a compressive surface capturing formulation for modelling free-surface flow by using the volume-of-fluid approach. International Journal of Numerical Methods in Fluids. 71(6), 788–804.

Hibiki, T. and Ishii, M. (2000) Two-group interfacial area transport equations at bubbly-to-slug flow transition. Nuclear Engineering and Design. 202(1), 39–76.

Hibiki, T. and Mishima, K. (2001) Flow regime transition criteria for upward two-phase flow in vertical narrow rectangular channels. Nuclear Engineering and Design. 203(2–3), 117–131.

Hinze, J.O. (1975) Turbulence. McGraw-Hill Publishing Co., New York.

Hirasaki, G.J. and Lawson, J.B. (1985) Mechanisms of foam flow in porous media: apparent viscosity in smooth capillaries. Society of Petroleum Engineers Journal. 25(2), 176–190.

Hirt, C.W. and Nichols, B.D. (1981) Volume of fluid (VOF) method for the dynamics of free boundaries. Journal of Computational Physics. 39(1), 201–225.

Holmes, D.G. and Connell, S.D. (1989) Solution of the 2D Navier-Stokes equations on unstructured adaptive grids. The AIAA 9th Computational Fluid Dynamics Conference, Buffalo, NY, USA.

Howard, J.A. and Walsh, P.A. (2013) Review and extensions to film thickness and relative bubble drift velocity prediction methods in laminar Taylor or slug flows. International Journal of Multiphase Flow. 55, 32–42.

Hua, J., Quan, S., Nossen, J. (2009) Numerical simulation of an intermediate sized bubble rising in a vertical pipe. Computational Methods in Multiphase Flow. 63, 111–121.

Huang, H., Dhir, V.K., Pan, L.M. (2017) Liquid film thickness measurement underneath a gas slug with miniaturized sensor matrix in a microchannel. Microfluidics and Nanofluidics. 21, 159.

Huerre, A., Miralles, V., Jullien, M.C. (2014) Bubbles and foams in microfluidics. Soft Matter. 10(36), 6888–6902.

Huerre, A., Theodoly, O., Leshansky, A.M., Valignat, M.P., Cantat, I., Jullien, M.C. (2015) Droplets in microchannels: dynamical properties of the lubrication film. Physical Review Letters. 115(6), 064501.

Hughes, R.R., Evans, H.D., Sternling, C.V. (1953) Flash vaporization, analysis of fluid mechanical and mass transfer problems. Chemical Engineering Progress. 49, 78–87.

Hyndman, R.J. and Koehler, A.B. (2006) Another look at measures of forecast accuracy. International Journal of Forecasting. 22(4), 679–688.

Inamuro, T., Miyahara, T., Ogino, F. (2001) Lattice Boltzmann simulations of drop deformation and breakup in a simple shear flow. In Computational Fluid Dynamics, Satofuka, N., Ed., Springer, Berlin/Heidelberg, Germany.

Irandoust, S. and Andersson, B. (1989) Simulation of flow and mass transfer in Taylor flow through a capillary. Computers & Chemical Engineering. 13(4–5), 519–526.

Irandoust, S., Ertlé, S., Andersson, B. (1992) Gas-liquid mass transfer in Taylor flow through a capillary. The Canadian Journal of Chemical Engineering. 70(1), 115–119.

Ishii M. and Hibiki, T. (2011) Thermo-fluid dynamics of two-phase flow. Springer-Verlag, New York, USA.

Jabbari, M., Bulatova, R., Hattel, J.H., Bahl, C.R.H. (2014) An evaluation of interface capturing methods in a VOF based model for multiphase flow of a non-Newtonian ceramic in tape casting. Applied Mathematical Modelling. 38(13), 3222–3232.

Jakiela, S., Korczyk, P.M., Makulska, S., Cybulski, O., Garstecki, P. (2012) Discontinuous transition in a laminar fluid flow: a change of flow topology inside a droplet moving in a micron-size channel. Physical Review Letters. 108(13), 134501.

Jayawardena, S.S., Balakotaiah, V., Witte, L.C. (1997) Flow pattern transition maps for microgravity two-phase flows. AIChE Journal. 43(6), 1637–1640.

Jhong, H.R.M., Ma, S., Kenis, P.J. (2013) Electrochemical conversion of CO_2 to useful chemicals: current status, remaining challenges, and future opportunities. Current Opinion in Chemical Engineering. 2(2), 191–199.

Joanny, J.F. (1986) Dynamics of wetting: interface profile of a spreading liquid. Journal of Theoretical and Applied Mechanics. 5, 249–271.

Jose, B.M. and Cubaud, T. (2014) Formation and dynamics of partially wetting droplets in square microchannels. RSC Advances. 4(29), 14962–14970.

Jovanović, J., Zhou, W., Rebrov, E.V., Nijhuis, T.A., Hessel, V., Schouten, J.C. (2011) Liquid-liquid slug flow: hydrodynamics and pressure drop. Chemical Engineering Science. 66(1), 42–54.

Kandlikar, S.G. and Grande, W.J. (2003) Evolution of microchannel flow passages thermohydraulic performance and fabrication technology. Heat Transfer Engineering. 24(1), 3–17.

Karande, R. (2012) Development and application of microreactors for biocatalytic reactions. Ph.D. thesis, the Technical University of Dortmund, Germany.

Kariyasaki, A., Fukano, T., Ousaka A., Kagawa, M. (1992) Isothermal air-water two-phase up-and downward flows in a vertical capillary tube: 1st report, flow pattern and void fraction. Transactions of the Japan Society of Mechanical Engineers Series B. 58, 2684–2690.

Kashid, M.N. and Agar, D.W. (2007) Hydrodynamics of liquid-liquid slug flow capillary microreactor: flow regimes, slug size and pressure drop. Chemical Engineering Journal. 131(1–3), 1–13.

Kashid, M.N., Harshe, Y.M., Agar, D.W. (2007) Liquid-liquid slug flow in a capillary: an alternative to suspended drop or film contactors. Industrial & Engineering Chemistry Research. 46(25), 8420–8430.

Kashid, M.N., Fernández Rivas, D., Agar, D.W., Turek, S. (2008) On the hydrodynamics of liquid-liquid slug flow capillary microreactors. Asia-Pacific Journal of Chemical Engineering. 3(2), 151–160.

Kashid, M.N., Renken, A., Kiwi-Minsker, L. (2011) Influence of flow regime on mass transfer in different types of microchannels. Industrial & Engineering Chemistry Research. 50(11), 6906–6914.

Kataoka, K., Ohmura, N., Kouzu, M., Simamura, Y., Okubo, M. (1995) Emulsion polymerization of styrene in a continuous Taylor vortex flow reactor. Chemical Engineering Science. 50(9), 1409–1416.

Katopodes, N.D. (2018) Free surface flow computational methods. Butterworth-Heinemann, Oxford, UK.

Kawahara, A., Sadatomi, M., Nei, K., Matsuo, H. (2009) Experimental study on bubble velocity, void fraction and pressure drop for gas-liquid two-phase flow in a circular microchannel. International Journal of Heat and Fluid Flow. 30(5), 831–841.

Kawaji, M. and Chung, P.M.-Y. (2003) Unique characteristics of adiabatic gas-liquid flows in microchannels: diameter and shape effects on flow patterns, void fraction and pressure drop. In the ASME 1st International Conference on Microchannels and Minichannels, Rochester, NY, USA, 115–127.

Kelessidis, V.C. and Dukler, A.E. (1989) Modeling flow pattern transitions for upward gas-liquid flow in vertical concentric and eccentric annuli. International Journal of Multiphase Flow. 15(2), 173–191.

Kercher, D.S., Lee, J.B., Brand, O., Allen, M.G., Glezer, A. (2003) Microjet cooling devices for thermal management of electronics. IEEE Transactions on Components and Packaging Technologies. 26(2), 359–366.

Ketabdari, M.J. (2016) Free surface flow simulation using VOF method. In Numerical Simulation-from Brain Imaging to Turbulent Flows, IntechOpen, London, UK.

Kew, P.A. and Cornwell, K. (1997) Correlations for the prediction of boiling heat transfer in small-diameter channels. Applied Thermal Engineering. 17(8–10), 705–715.

Keyes, D.E., McInnes, L.C., Woodward, C., Gropp, W., Myra, E., Pernice, M., Bell, J. (2013) Multiphysics simulations: challenges and opportunities. International Journal of High Performance Computing Applications. 27, 4–83.

Khaledi, H.A., Smith, I.E., Unander, T.E., Nossen, J. (2014) Investigation of two-phase flow pattern, liquid holdup and pressure drop in viscous oil-gas flow. International Journal of Multiphase Flow. 67, 37–51.

Khodaparast, S., Borhani, N., Thome, J.R. (2014) Sudden expansions in circular microchannels: flow dynamics and pressure drop. Microfluidics and Nanofluidics. 17(3), 561–572.

Kim, S.M. and Mudawar, I. (2015) Review of two-phase critical flow models and investigation of the relationship between choking, premature CHF, and CHF in microchannel heat sinks. International Journal of Heat and Mass Transfer. 87, 497–511.

Kirpalani, D.M., Patel, T., Mehrani, P., Macchi, A. (2008) Experimental analysis of the unit cell approach for two-phase flow dynamics in curved flow channels. International Journal of Heat and Mass Transfer. 51(5–6), 1095–1103.

Kiwi-Minsker, L. and Renken, A. (2005) Microstructured reactors for catalytic reactions. Catalysis Today. 110(1–2), 2–14.

Klaseboer, E., Gupta, R., Manica, R. (2014) An extended Bretherton model for long Taylor bubbles at moderate capillary numbers. Physics of Fluids. 26(3), 032107.

Kline, S.J. and McClintock, F.A. (1953) Describing uncertainties in single-sample experiments. Mechanical Engineering. 75, 3–8.

Kohl, M.J., Abdel-Khalik, S.I., Jeter, S.M., Sadowksi, D.L. (2005) An experimental investigation of microchannel flow with internal pressure measurements. International Journal of Heat and Mass Transfer. 48(8), 1518–1533.

Kolb, W.B. and Cerro, R.L. (1993) The motion of long bubbles in tubes of square cross section. Physics of Fluids A: Fluid Dynamics. 5(7), 1549–1557.

Komrakova, A.E., Shardt, O., Eskin, D., Derksen, J.J. (2014) Lattice Boltzmann simulations of drop deformation and breakup in shear flow. International Journal of Multiphase Flow. 59, 24–43.

Kong, R., Kim, S., Bajorek, S., Tien, K., Hoxie, C. (2018) Effects of pipe size on horizontal two-phase flow: flow regimes, pressure drop, two-phase flow parameters, and drift-flux analysis. Experimental Thermal and Fluid Science. 96, 75–89.

Kreutzer, M.T., Du, P., Heiszwolf, J.J., Kapteijn, F., Moulijn, J.A. (2001) Mass transfer characteristics of three-phase monolith reactors. Chemical Engineering Science. 56(21–22), 6015–6023.

Kreutzer, M.T. (2003) Hydrodynamics of Taylor flow in capillaries and monoliths channels. Ph.D. thesis, Delft University of Technology, Delft, The Netherlands.

Kreutzer, M.T., Bakker, J.J.W., Kapteijn, F., Moulijn, J.A., Verheijen, P.J.T. (2005a) Scaling-up multiphase monolith reactors: linking residence time distribution and feed maldistribution. Industrial Engineering and Chemistry Research. 44(14), 4898–4913.

Kreutzer, M.T., Kapteijn, F., Moulijn, J.A., Kleijn, C.R., Heiszwolf, J.J. (2005b) Inertial and interfacial effects on pressure drop of Taylor flow in capillaries. AIChE Journal. 51(9), 2428–2440.

Kreutzer, M.T., Kapteijn, F., Moulijn, J.A., Heiszwolf, J.J. (2005c) Multiphase monolith reactors: chemical reaction engineering of segmented flow in microchannels. Chemical Engineering Science. 60(22), 5895–5916.

Kreutzer, M.T., van der Eijnden, M.G., Kapteijn, F., Moulijn, J.A., Heiszwolf, J.J. (2005d) The pressure drop experiment to determine slug lengths in multiphase monoliths. Catalysis Today. 105(3–4), 667–672.

Kreutzer, M.T., Shah, M.S., Parthiban, P., Khan, S.A. (2018) Evolution of nonconformal Landau-Levich-Bretherton films of partially wetting liquids. Physical Review Fluids. 3(1), 014203.

Kumar, V., Vashisth, S., Hoarau, Y., Nigam, K.D.P. (2007) Slug flow in curved microreactors: hydrodynamic study. Chemical Engineering Science. 62(24), 7494–7504.

Kurimoto, R., Hayashi, K., Tomiyama, A. (2013) Terminal velocities of clean and fully-contaminated drops in vertical pipes. International Journal of Multiphase Flow. 49, 8–23.

Kurimoto, R., Nakazawa, K., Minagawa, H., Yasuda, T. (2017) Prediction models of void fraction and pressure drop for gas-liquid slug flow in microchannels. Experimental Thermal and Fluid Science, 88, 124–133.

Laborie, S., Cabassud, C., Durand-Bourlier, L., Lainé, J.M. (1999) Characterisation of gas-liquid two-phase flow inside capillaries. Chemical Engineering Science. 54(23), 5723–5735.

Ładosz, A. and von Rohr, P.R. (2018) Pressure drop of two-phase liquid-liquid slug flow in square microchannels. Chemical Engineering Science. 191, 398–409.

Landau, L. and Levich, B. (1942) Dragging of a liquid by a moving plate. Acta Physicochimica URSS. 17, 42–54.

Langer, J.S. (1975) Spinodal decomposition. In Fluctuations, Instabilities, and Phase Transitions. NATO Advanced Study Institutes Series (Series B: Physics), Springer: Boston, MA, USA.

Lee, T. and Lin, C.L. (2005) Rarefaction and compressibility effects of the lattice Boltzmann equation method in a gas microchannel. Physical Review, E. 71, 046706.

Li, J., Renardy, Y.Y., Renardy, M. (2000) Numerical simulation of breakup of a viscous drop in simple shear flow through a volume-of-fluid method. Physics of Fluids. 12(2), 269–282.

Li, W. and Wu, Z. (2010a) A general criterion for evaporative heat transfer in micro/mini-channels. International Journal of Heat and Mass Transfer. 53(9–10), 1967–1976.

Li, W. and Wu, Z. (2010b) A general correlation for adiabatic two-phase pressure drop in micro/mini-channels. International Journal of Heat and Mass Transfer. 53(13–14), 2732–2739.

Li, W. and Wu, Z. (2010c) A new predictive tool for saturated critical heat flux in micro/mini-channels: effect of the heated length-to-diameter ratio. International Journal of Heat and Mass Transfer. 54(13–14), 2880–2889.

Li, Q., He, Y.L., Tang, G.H., Tao, W.Q. (2011) Lattice Boltzmann modeling of microchannel flows in the transition flow regime. Microfluidics and Nanofluidics. 10(3), 607–618.

Li, X.B., Li, F.C., Kinoshita, H., Oishi, M., Oshima, M. (2015) Dynamics of viscoelastic fluid droplet under very low interfacial tension in a serpentine T-junction microchannel. Microfluidics and Nanofluidics. 18(5), 1007–1021.

Li, Q., Luo, K.H., Kang, Q.J., He, Y.L., Chen, Q., Liu, Q. (2016) Lattice Boltzmann methods for multiphase flow and phase-change heat transfer. Progress in Energy and Combustion Science. 52, 62–105.

Li, H.W., Wang, Y.C., Hong, W.P., Sun, B., Zhou, Y.L. (2020) Analysis of parallel mini-channels' complex flow boiling and dryout dynamics based on the pressure drop signals. Experimental Thermal and Fluid Science. 110, 109944.

Lilly, D.K. (1992) A proposed modification of the Germano subgrid-scale closure method. Physics of Fluids A. 4(3), 633–635.

Lim, A.E., Lim, C.Y., Lam, Y.C., Lim, Y.H. (2019) Effect of microchannel junction angle on two-phase liquid-gas Taylor flow. Chemical Engineering Science. 202, 417–428.

Liou, T.M. and Lin, C.T. (2014) Study on microchannel flows with a sudden contraction–expansion at a wide range of Knudsen number using lattice Boltzmann method. Microfluidics and Nanofluidics. 16, 315–327.

Liqun, G., Qiang, C., Juanjuan, L., Zhengrong, C., Jianwei, Z., Maohua, D., Chung, M. (2013) Comparison of Ag wire and Cu wire in memory package. ECS Transactions. 52(1), 747.

Lockhart, R.W. and Martinelli, R.G. (1949) Proposed correlation of data for isothermal two phase, two-component flow in pipes. Chemical Engineering Progress. 45, 39–48.

Lopes, R.J.G. and Quinta-Ferreira, R.M. (2009) Volume-of-fluid-based model for multiphase flow in high-pressure Trickle-Bed reactor: Optimization of numerical parameters. AIChE Journal. 55(11), 2920–2933.

Lowe, D.C. and Rezkallah, K.S. (1999) Flow regime identification in microgravity two-phase flows using void fraction signals. International Journal of Multiphase Flow. 25(3), 433–457.

Macchi, A., Plouffe, P., Patience, G.S., Roberge, D.M. (2019) Experimental methods in chemical engineering: micro-reactors. The Canadian Journal of Chemical Engineering. 97(10), 2578–2587.

Machado, R.M., Parrillo, D.J., Boehme, R.P., Broekhuis, R.R. (1999) Use of a monolith catalyst for the hydrogenation of dinitrotoluene to toluenediamine. US Patent 6005143.

Magnini, M., Municchi, F., El Mellas, I., Icardi, M. (2022) Liquid film distribution around long gas bubbles propagating in rectangular capillaries. International Journal of Multiphase Flow. 148, 103939.

Mahady, K., Afkhami, S., Kondic, L. (2015) A volume of fluid method for simulating fluid/fluid interfaces in contact with solid boundaries. Journal of Computational Physics. 294, 243–257.

Mandhane, J.M., Gregory, G.A., Aziz, K. (1974) A flow pattern map for gas-liquid flow in horizontal pipes. International Journal of Multiphase Flow. 1(4), 537–553.

Manz, A., Graber, N., Widmer, H.M. (1990) Miniaturized total chemical analysis systems: a novel concept for chemical sensing. Sensors and Actuators B: Chemical. 1(1–6), 244–248.

Marchessault, R.N. and Mason, S.G. (1960) Flow of entrapped bubbles through a capillary. Industrial and Engineering Chemistry. 52(1), 79–84.

Maruyama, T., Kaji, T., Ohkawa, T., Sotowa, K.I., Matsushita, H., Kubota, F., Kamiya, N., Kusakabe, K., Goto, M. (2004) Intermittent partition walls promote solvent extraction of metal ions in a microfluidic device. Analyst. 129(11), 1008–1013.

McAdams, W.H., Woods, W.K., Bryan, L. (1942) Vaporization inside horizontal tubes II: benzene-oil mixtures. Transactions of ASME. 64, 193–200.

McNamara, G.R. and Zanetti, G. (1988) Use of the Boltzmann equation to simulate lattice-gas automata. Physical Review Letters. 61, 2332–2335.

Mehendale, S.S., Jacobi, A.M., Shah, R.K. (1999) Meso-and micro-scale frontiers of compact heat exchangers, In: Lehner M., Mewes D. (eds) Applied Optical Measurements. Heat and Mass Transfer. Springer, Berlin, Heidelberg, 139–158.

Meller, K., Szumski, M., Buszewski, B. (2017) Microfluidic reactors with immobilized enzymes-characterization, dividing, perspectives. Sensors and Actuators B: Chemical. 244, 84–106.

Meyer, C., Hoffmann, M., Schlüter, M. (2014) Micro-PIV analysis of gas-liquid Taylor flow in a vertical oriented square shaped fluidic channel. International Journal of Multiphase Flow. 67, 140–148.

Mießner, U., Helmers, T., Lindken, R., Westerweel, J. (2020) µPIV measurement of the 3D velocity distribution of Taylor droplets moving in a square horizontal channel. Experiments in Fluids. 61(5), 125.

Mießner, U., Helmers, T., Lindken, R., Westerweel, J. (2021) Reconstruction of the 3D pressure field and energy dissipation of a Taylor droplet from a PIV measurement. Experiments in Fluids. 62(4), 83.

Miki, Y., Matsumoto, S., Kaneko, A., Abe, Y. (2013) Formation behavior of two-phase slug flow and pressure fluctuation in a microchannel T-junction. Japanese Journal of Multiphase Flows. 26(5), 587–594.

Minagawa, H., Asama H., Yasuda, T. (2013) Void fraction and frictional pressure drop of gas-liquid slug flow in a microtube. Transactions of the Japan Society of Mechanical Engineers Series B. 79, 1500–1513.

Mishima, K. and Ishii, M. (1984) Flow regime transition criteria for upward two-phase flow in vertical tubes. International Journal of Heat and Mass Transfer. 27, 723–737.

Mishima, K. and Hibiki, T. (1996) Some characteristics of air-water two-phase flow in small diameter vertical tubes. International Journal of Multiphase Flow. 22, 703–712.

Miyazaki, M. and Maeda, H. (2006) Microchannel enzyme reactors and their applications for processing. Trends in Biotechnology. 24, 463–470.

Mohanty, K.K. (1981) Fluids in porous media: two-phase distribution and flow. Ph.D. thesis, University of Minnesota, MN, USA.

Mohanty, K.K., Davis, H.T., Scriven, L.E. (1981) Thin-films and fluid distributions in porous media. in surface phenomena in enhanced oil recovery (Ed: Shah, D.O.), Springer, Boston, MA, 595–609.

Mohmmed, A.O., Al-Kayiem, H.H., Osman, A.B. (2021) Investigations on the slug two-phase flow in horizontal pipes: past, presents, and future directives. Chemical Engineering Science. 238, 116611.

Morini, G.L., Lorenzini, M., Colin, S., Geoffroy, S. (2007) Experimental analysis of pressure drop and laminar to turbulent transition for gas flows in smooth microtubes. Heat Transfer Engineering. 28(8–9), 670–679.

Moulijn, J.A., Kreutzer, M.T., Nijhuis, T.A., Kapteijn, F. (2011) Monolithic catalysts and reactors: high precision with low energy consumption. Advances in Catalysis. 54, 249–327.

Muzaferija, S. and Peric, M. (1997) Computation of free-surface flows using the finite-volume method and moving grids. Numerical Heat Transfer, Part B: Fundamentals. 32(4), 369–384.

Muzaferija, S., Peric, M., Sames, P., Schelin, T. (1998) A two-fluid Navier-Stokes solver to simulate water entry. In 22nd Symposium on Naval Hydrodynamics. 638–651.

Muzychka, Y.S., Walsh, E., Walsh, P. (2010) Simple models for laminar thermally developing slug flow in noncircular ducts and channels. Journal of Heat Transfer. 132(11), 111702.

Muzychka, Y.S., Walsh, E.J., Walsh, P. (2011) Heat transfer enhancement using laminar gas-liquid segmented plug flows. Journal of Heat Transfer. 133(4), 041902.

Muzychka, Y.S. (2014) Laminar heat transfer for gas-liquid segmented flows in circular and non-circular ducts with constant wall temperature. International Conference on Nanochannels, Microchannels, and Minichannels, Chicago, Illinois, USA.

Nguyen, N.T., Wereley, S.T., Shaegh, S.A.M. (2019) Fundamentals and applications of microfluidics. 3rd Edition, Artech House Inc., Boston, MA, USA.

Ni, D., Hong, F.J., Cheng, P., Chen, G. (2017) Numerical study of liquid-gas and liquid-liquid Taylor flows using a two-phase flow model based on Arbitrary-Lagrangian-Eulerian (ALE) Formulation. International Communications in Heat and Mass Transfer. 88, 37–47.

Nie, X., Doolen, G.D., Chen, S. (2002) Lattice-Boltzmann simulations of fluid flows in MEMS. Journal of Statistical Physics. 107, 279–289.

Nijhuis, T.A., Kreutzer, M.T., Romijn, A.C.J., Kapteijn, F., Moulijn, J.A. (2001) Monolithic catalysts as efficient three-phase reactors. Chemical Engineering Sciences. 56(3), 823–829.

Niu, H., Pan, L., Su, H., Wang, S. (2009) Flow pattern, pressure drop, and mass transfer in a gas-liquid concurrent two-phase flow microchannel reactor. Industrial & Engineering Chemistry Research. 48(3), 1621–1628.

Olbricht, W.L. and Kung, D.M. (1992) The deformation and breakup of liquid drops in low Reynolds number flow through a capillary. Physics of Fluids A: Fluid Dynamics. 4(7), 1347–1354.

Oliveira, P.J., Pinho, F.T., Schulte, A. (1998) A general correlation for the local loss coefficient in Newtonian axisymmetric sudden expansions. International Journal of Heat and Fluid Flow. 19(6), 655–660.

Ong, C.L. and Thome, J.R. (2011) Macro-to-microchannel transition in two-phase flow: part 1–two phase flow patterns and film thickness measurements. Experimental Thermal and Fluid Science. 35(1), 37–47.

Osher, S. and Sethian, J.A. (1988) Fronts propagating with curvature dependent speed: Algorithms based on Hamilton-Jacobi formulations. Journal of Computational Physics. 79, 12–49.

Osher, S. and Fedkiw, R.P. (2001) Level set methods: an overview and some recent results. Journal of Computational Physics. 169(2), 463–502.

Osorio-Nesme, A., Rauh, C., Delgado, A. (2012) Flow rectification and reversal mass flow in printed periodical microstructures. Engineering Applications of Computational Fluid Mechanics. 6(2), 285–294.

Panahi, R., Jahanbakhsh, E., Seif, M.S. (2006) Development of a VoF-fractional step solver for floating body motion simulation. Applied Ocean Research. 28(3), 171–181.

Pang, Z., Zhu, C., Ma, Y., Fu, T. (2020) CO_2 absorption by liquid films under Taylor flow in serpentine minichannels. Industrial & Engineering Chemistry Research. 59(26), 12250–12261.

Pangarkar, K., Schildhauer, T.J., van Ommen, J.R., Nijenhuis, J., Kapteijn, F., Moulijn, J.A. (2008) Structured packings for multiphase catalytic reactors. Industrial and Engineering Chemistry Research. 47(10), 3720–3751.

Papageorgiou, D.T. (1995) On the breakup of viscous liquid threads. Physics of Fluids. 7(7), 1529–1544.

Park, C.W. and Homsy, G.M. (1984) Two-phase displacement in Hele Shaw cells: theory. Journal of Fluid Mechanics. 139, 291–308.

Park, H.S. and Punch, J. (2008) Friction factor and heat transfer in multiple microchannels with uniform flow distribution. International Journal of Heat and Mass Transfer. 51(17–18), 4535–4543.

Park, I.R., Kim, K.S., Kim, J., Van, S.H. (2009) A volume-of-fluid method for incompressible free surface flows. International Journal of Numerical Methods in Fluids. 61(12), 1331–1362.

Parthiban, P. and Khan, S.A. (2013) Bistability in droplet traffic at asymmetric microfluidic junctions. Biomicrofluidics. 7(4), 44123.

Patankar, S.V. (1980) Numerical heat transfer and fluid flow.1st Edition, Taylor & Francis.

Patel, R.S., Weibel, J.A., Garimella, S.V. (2017) Characterization of liquid film thickness in slug-regime microchannel flows. International Journal of Heat and Mass Transfer. 115, 1137–1143.

Pepiot, P. and Desjardins, O. (2012) Numerical analysis of the dynamics of two-and three-dimensional fluidized bed reactors using an Euler-Lagrange approach. Powder Technology. 220, 104–121.

Perot, J.B. (1993) An analysis of the fractional step method. Journal of Computational Physics. 108(1), 51–58.

Petersen, K.E. (1982) Silicon as mechanical material. Proceedings of the IEEE. 70, 420–457.

Prajapati, Y.K. and Bhandari, P. (2017) Flow boiling instabilities in microchannels and their promising solutions—a review. Experimental Thermal and Fluid Science. 88, 576–593.

Qian, D. and Lawal, A. (2006) Numerical study on gas and liquid slugs for Taylor flow in a T-junction microchannel. Chemical Engineering Science. 61(23), 7609–7625.

Qian, J.Y., Chen, M.R., Wu, Z., Jin, Z.J., Sunden, B. (2019) Effects of a dynamic injection flow rate on slug generation in a cross-junction square microchannel. Processes. 7(10), 765.

Qin, F., Mazloomi Moqaddam, A., Kang, Q., Derome, D., Carmeliet, J. (2018) Entropic multiple-relaxation-time multirange pseudopotential lattice Boltzmann model for two-phase flow. Physics of Fluids. 30(3), 032104.

Quan, S. (2011) Co-current flow effects on a rising Taylor bubble. International Journal of Multiphase Flow. 37(8), 888–897.

Queutey, P. and Visonneau, M. (2007) An interface capturing method for free-surface hydrodynamic flows. Computers & Fluids. 36(9), 1481–1510.

Rabinovich, E. and Kalman, H. (2007) Pickup, critical and wind threshold velocities of particles. Powder Technology. 176(1), 9–17.

Radovcich, N.A. and Moissis, R. (1962) The transition from two phase bubble flow to slug flow. Department of Mechanical Engineering, Massachusetts Institute of Technology, Report No. 7–7673–22.

Rajesh, V.M. and Buwa, V.V. (2018) Volume-of-fluid simulations of gas-liquid-liquid flows in minichannels. Chemical Engineering Journal. 345, 688–705.

Ratulowski, J. and Chang, H.C. (1989) Transport of gas bubbles in capillaries. Physics of Fluids A: Fluid Dynamics. 1(10), 1642–1655.

Rauch, R.D., Batira, J.T., Yang, N.T.Y. (1991) Spatial adaption procedures on unstructured meshes for accurate unsteady aerodynamic flow computation. In 32nd Structures, Structural Dynamics, and Materials Conference, Baltimore, MD, USA.

Revellin, R. (2005) Experimental two-phase fluid flow in microchannels. Ph.D. thesis, Federal Institute of Technology Lausanne, Switzerland.

Reynolds, O. (1886) On the theory of lubrication and its applications to Mr. Beauchamp's experiments, including an experimental determination of the viscosity of olive oil. Philosophical Transactions of the Royal Society of London. 177, 157–234.

Richter, H.J. (1983) Separated two-phase flow model: application to critical two-phase flow. International Journal of Multiphase Flow. 9(5), 511–530.

Rodman, J. (1947) Two-phase two-component flow of air and water. M.S. thesis, University of Delaware, USA.

Roudet, M., Loubiere, K., Gourdon, C., Cabassud, M. (2011) Hydrodynamic and mass transfer in inertial gas-liquid flow regimes through straight and meandering millimetric square channels. Chemical Engineering Science. 66(13), 2974–2990.

Rydberg, J. (2004) Solvent extraction principles and practice, revised and expanded. Boca Raton: CRC Press. ISBN 9780429215452.

Saisorn, S. and Wongwises, S. (2008) Flow pattern, void fraction and pressure drop of two-phase air-water flow in a horizontal circular micro-channel. Experimental Thermal and Fluid Science. 32(3), 748–760.

Sarkar, P.S., Singh, K.K., Shenoy, K.T., Sinha, A., Rao, H., Ghosh, S.K. (2012) Liquid-liquid two-phase flow patterns in a serpentine microchannel. Industrial & Engineering Chemistry Research. 51(13), 5056–5066.

Sato, T., Minamiyama, T., Yanai, M., Tokura, T., Ito, Y. (1972) Study of heat transfer in boiling two-phase channel flow part II, heat transfer in the nucleate boiling region. Heat Transfer Japanese Research. 1, 15–30.

Satterfield, C.N. and Ózel, F. (1977) Some characteristics of two-phase flow in monolithic catalyst structures. Industrial & Engineering Chemistry Fundamentals. 16(1), 61–67.

Sauzade, M. and Cubaud, T. (2013) Initial microfluidic dissolution regime of CO_2 bubbles in viscous oils. Physical Review E. 88, 051001.

Schubert, K., Brandner, J., Fichtner, M., Linder, G., Schygulla, U., Wenka, A. (2001) Microstructure devices for applications in thermal and chemical process engineering. Microscale Thermophysical Engineering. 5(1), 17–39.

Schubert, M., Kost, S., Lange, R., Salmi, T., Haase, S., Hampel, U. (2016) Maldistribution susceptibility of monolith reactors: case study of glucose hydrogenation performance. AIChE Journal. 62(12), 4346–4364.

Schwartz, L.W., Princen, H.M., Kiss, A.D. (1986) On the motion of bubbles in capillary tubes. Journal of Fluid Mechanics. 172, 259–275.

Seta, T. and Kono, K. (2004) Thermal lattice Boltzmann method for liquid-gas two-phase flows in two dimension. JSME International Journal Series B Fluids and Thermal Engineering. 47(3), 572–583.

Shah, M.M. (1979) A general correlation for heat transfer during film condensation inside pipes. International Journal of Heat and Mass Transfer. 22(4), 547–556.

Shan, X. and Chen, H. (1993) Lattice Boltzmann model for simulating flows with multiple phases and components. Physical Review A. 47(3), 1815–1819.

Shao, N., Gavriilidis, A., Angeli, P. (2010) Mass transfer during Taylor flow in microchannels with and without chemical reaction. Chemical Engineering Journal. 160(3), 873–881.

Sharp, K.V. and Adrian, R.J. (2004) Transition from laminar flow to turbulent flow in liquid filled microtubes. Experiments in Fluids. 36(5), 741–747.

Shi, Y., Tang, G.H., Lin, H.F., Zhao, P.X., Cheng, L.H. (2019) Dynamics of droplet and liquid layer penetration in three-dimensional porous media: a lattice Boltzmann study. Physics of Fluids. 31(4), 042106.

Sobieszuk, P., Cygański, P., Pohorecki, R. (2010) Bubble lengths in the gas-liquid Taylor flow in microchannels. Chemical Engineering Research and Design. 88(3), 263–269.

Song, Y., Xin, F., Guangyong, G., Lou, S., Cao, C., Wang, J. (2019) Uniform generation of water slugs in air flowing through superhydrophobic microchannels with T-junction. Chemical Engineering Science. 199, 439–450.

Sontti, S.G. and Atta, A. (2017) CFD Analysis of Taylor bubble in a co-flow microchannel with Newtonian and non-Newtonian liquid. Industrial & Engineering Chemistry Research. 56(25), 7401−7412.

Sotowa, K.I., Sugiyama, S., Nakagawa, K. (2009) Flow uniformity in deep microchannel reactor under high throughput conditions. Organic Process Research & Development. 13(5), 1026–1031.

Steegmans, M.L.J., Schroën, K.G.P.H., Boom, R.M. (2009) Characterization of emulsification at flat microchannel Y junctions. Langmuir. 25(6), 3396–3401.

Steijn, V.V., Kreutzerb, M.T., Kleijn, C.R. (2007) μ-PIV study of the formation of segmented flow in microfluidic T-junctions. Chemical Engineering Science. 62(24), 7505–7514.

Steinbrenner, J.E., Hidrovo, C.H., Wang, F.M., Vigneron, S., Lee, E.S., Kramer, T.A., Cheng, C.H., Eaton, J.K., Goodson, K.E. (2007) Measurement and modeling of liquid film thickness evolution in stratified two-phase microchannel flows. Applied Thermal Engineering. 27(10), 1722–1727.

Su, H., Wang, S., Niu, H., Pan, L., Wang, A., Hu, Y. (2010) Mass transfer characteristics of H_2S absorption from gaseous mixture into methyldiethanolamine solution in a T-junction microchannel. Separation and Purification Technology. 72(3), 326–334.

Su, Y., Chen, G., Yuan, Q. (2012) Influence of hydrodynamics on liquid mixing during Taylor flow in a microchannel. AIChE Journal. 58(6), 1660–1670.

Sun, Y., Guo, C., Jiang, Y., Wang, T., Zhang, L. (2018) Transient film thickness and microscale heat transfer during flow boiling in microchannels. International Journal of Heat and Mass Transfer. 116, 458–470.

Suo, M. and Griffith, P. (1964) Two-phase flow in capillary tube. Journal of Basic Engineering. 86, 576–582.

Sur, A. and Liu, D. (2012) Adiabatic air-water two-phase flow in circular microchannels. International Journal of Thermal Sciences. 53, 18–34.

Sussman, M., Smereka, P., Osher, S. (1994) A level set approach for computing solutions to incompressible two-phase flow. Journal of Computational Physics. 114(1), 146–159.

Svetlov, S.D. and Abiev, R.S. (2018) Formation mechanisms and lengths of the bubbles and liquid slugs in a coaxial-spherical micro mixer in Taylor flow regime. Chemical Engineering Journal. 354, 269–284.

Svetlov, S.D. and Abiev, R.S. (2021) Mathematical modeling of the droplet formation process in a microfluidic device. Chemical Engineering Science. 235, 116493.

Taitel, Y., Bornea, D., Dukler, A.E. (1980) Modelling flow pattern transitions for steady upward gas-liquid flow in vertical tubes. AIChE Journal. 26(3), 345–354.

Takada, N., Misawa, M., Tomiyama, A., Fujiwara, S. (2000) Numerical simulation of two- and three-dimensional two-phase fluid motion by lattice Boltzmann method. Computer Physics Communications. 129(1–3), 233–246.

Takeshita, K. (2010) Development of liquid-liquid countercurrent centrifugal extractor with Taylor-Couette flow. Japanese Journal of Multiphase Flow. 24(3), 267–274.

Talimi, V., Muzychka, Y.S., Kocabiyik, S. (2012) Numerical simulation of the pressure drop and heat transfer of two phase slug flows in microtubes using moving frame of reference technique. International Journal of Heat and Mass Transfer. 55(23–24), 6463–6472.

Tan, J., Toh, B.H., Ho, H.M. (2004) Modeling of free air ball for copper wire bonding. In 6th Electronics Packaging Technology Conference, IEEE/CPMT, Singapore, 711–717.

Tan, J., Xu, J.H., Li, S.W., Luo, G.S. (2008) Drop dispenser in a cross-junction microfluidic device: scaling and mechanism of break-up. Chemical Engineering Journal. 136(2–3), 306–311.

Tanna, S., Pisigan, J.L., Song, W.H., Halmo, C., Persic, J., Mayer, M. (2012) Low cost Pd coated Ag bonding wire for high quality FAB in air. In the IEEE Electronic Components & Technology Conference, IEEE/CPMT, San Diego, CA, USA, 1103–1109.

Taylor, G.I. (1961) Deposition of a viscous fluid on the wall of a tube. Journal of Fluid Mechanics. 10(2), 161–165.

Teletzke, G.F. (1983) Thin liquid films: molecular theory and hydrodynamical implications. Ph.D. thesis, University of Minnesota, USA.

Teletzke, G.F., Davis H.T., Scriven, L.E. (1987) How liquids spread on solids. Chemical Engineering Communications. 55, 41–82.

Teletzke, G.F., Davis, H.T., Scriven, L.E. (1988) Wetting hydrodynamics. Revue de Physique Appliquee. 23, 989–1007.

Thomas, S., Esmaeeli, A., Tryggvason, G. (2010) Multiscale computations of thin films in multiphase flows. International Journal of Multiphase Flow. 36(1), 71–77.

Thulasidas, T.C., Abraham, M.A., Cerro, R.L. (1995) Bubble-train flow in capillaries of circular and square cross section. Chemical Engineering Science. 50(2),183–199.

Thulasidas, T.C., Abraham, M.A., Cerro, R.L. (1997) Flow patterns in liquid slugs during bubble-train flow inside capillaries. Chemical Engineering Science. 52(17), 2947–2962.

Tokeshi, M., Minagawa, T., Kitamori, T. (2000) Integration of a microextraction system on a glass chip: ion-pair solvent extraction of Fe(II) with 4,7-Diphenyl-1,10-phenanthrolinedisulfonic acid and Tri-n-octylmethylammonium chloride. Analytical Chemistry. 72(7), 1711–1714.

Trapp, J.A. and Mortensen, G.A. (1993) A discrete particle model for bubble slug two-phase flow. Journal of Computational Physics. 107(2), 367–377.

Triplett, K.A., Ghiaasiaan, S.M., Abdel-Khalik, S.I., Sadowskia, D.L. (1999) Gas-liquid two-phase flow in microchannels part I: Two-phase flow patterns. International Journal of Multiphase Flow. 25(3), 377–394.

Tsaoulidis, D., Dore, V., Angeli, P., Plechkova, N.V., Seddon, K.R. (2013) Flow patterns and pressure drop of ionic liquid-water two-phase flows in microchannels. International Journal of Multiphase Flow. 54, 1–10.

Tsaoulidis, D. and Angeli, P. (2015) Effect of channel size on mass transfer during liquid-liquid plug flow in small scale extractors. Chemical Engineering Journal. 262, 785–793.

Tseng, Y.W., Hung, F.Y., Lui, T.S. (2015a) Tensile and electrical properties of gold-coated silver bonding wire. Microelectronics Reliability. 55(3–4), 608–612.

Tseng, Y.W., Hung, F.Y., Lui, T.S., Chen, M.Y., Hsueh, H.W. (2015b) Effect of annealing on the microstructure and bonding interface properties of Ag-2Pd alloy wire. Microelectronics Reliability. 55(8), 1256–1261.

Turton, R. and Clark, N.N. (1987) An explicit relationship to predict spherical particle terminal velocity. Powder Technology. 53(2), 127–129.

Ubbink, O. (1997) Numerical prediction of two-phase fluid systems with sharp interfaces. Ph.D. thesis, University of London.

Ubbink, O. and Issa, R. (1999) A method for capturing sharp fluid interfaces on arbitrary meshes. Journal of Computational Physics. 153(1), 26–50.

Uno, S. and Kintner, R.C. (1956) Effect of wall proximity on the rate of rise of single air bubbles in a quiescent liquid. AIChE Journal. 2(3), 420–425.

Vaillant, M.P. (1913) Sur un procédé de mesure des grandes résistances polarisables et son application à la mesure de la résistance de liquids. Comptes Rendus de l'Académie des Sciences. 156, 307–310.

Valizadeh, K., Farahbakhsh, S., Bateni, A., Zargarian, A., Davarpanah, A., Alizadeh, A., Zarei, M. (2020) A parametric study to simulate the non-Newtonian turbulent flow in spiral tubes. Energy Science & Engineering. 8(1), 134–149.

van Doormaal, J.P. and Raithby, G.D. (1984) Enhancements of the SIMPLE method for predicting incompressible fluid flows. Numerical Heat Transfer. 7(2), 147–163.

van Oudheusden, B.W., Scarano, F., Roosenboom, E.W.M., Casimiri, E.W.F., Souverein, L.J. (2007) Evaluation of integral forces and pressure fields from planar velocimetry data for incompressible and compressible flows. Experiments in Fluids. 43(2), 153–162.

van Steijn, V., Kreutzer, M.T., Kleijn, C.R. (2007) μ-PIV study of the formation of segmented flow in microfluidic T-junctions. Chemical Engineering Science. 62(24), 7505–7514.

van Steijn, V., Kleijn, C.R., Kreutzer, M.T. (2009) Flows around confined bubbles and their importance in triggering pinch-off. Physical Review Letters.103(21), 214501.

Vasilev, M.P., Rusakov, B.A., Abiev, R.S. (2022) Gas-liquid slug flow in microfluidic heat exchanger: effect of gas hold-up and bubble size on pressure drop and heat transfer. International Journal of Thermal Sciences. 173, 107395.

Versteeg, H.K. and Malalasekera, W. (2007) An introduction to computational fluid dynamics: the finite volume method. 2nd Edition, Pearson/Prentice Hall.

Wacławczyk, T. and Koronowicz, T. (2008) Comparison of CICSAM and HRIC high resolution schemes for interface capturing. Journal of Theoretical and Applied Mechanics. 46(2), 325–345.

Wallis, G.B. (1962) The transition from flooding to upwards concurrent annular flow in a vertical pipe. UKAEA Report, AEEW–R–142, United Kingdom Atomic Energy Authority, Abingdon, UK.

Walsh, E., Muzychka, Y.S., Walsh, P., Egan, V., Punch, J. (2009) Pressure drop in two phase slug/bubble flows in mini scale capillaries. International Journal of Multiphase Flow. 35(10), 879–884.

Wang, T., Wang, J., Jin, Y. (2005) Theoretical prediction of flow regime transition in bubble columns by the population balance model. Chemical Engineering Science. 60(22), 6199–6209.

Wang, C.C., Tseng, C.Y., Chen, I.Y. (2010) A new correlation and the review of two-phase flow pressure change across sudden expansion in small channels. International Journal of Heat and Mass Transfer. 53(19–20), 4287–4295.

Wang, X., Sun, X., Doup, B., Zhao, H. (2012) Dynamic modeling strategy for flow regime transition in gas-liquid two-phase flows. Journal of Computational Multiphase Flows. 4(4), 387–397.

Wang, Z.L. (2015) Speed up bubbling in a tapered co-flow geometry. Chemical Engineering Journal. 263, 346–355.

Wangfeng, C.A.I., Jiao, Z., Xubin, Z., Yan, W., Xiangjuan, Q.I. (2013) Enhancement of CO_2 absorption under Taylor flow in the presence of fine particles. Chinese Journal of Chemical Engineering. 21(2), 135–143.

Warnier, M.J.F., Rebrov, E.V., de Croon, M.H.J.M., Hessel, V., Schouten, J.C. (2008) Gas hold-up and liquid film thickness in Taylor flow in rectangular microchannels. Chemical Engineering Journal. 135S, S153–S158.

Warnier, M.J.F., de Croon, M.H.J.M., Rebrov, E.V., Schouten, J.C. (2010) Pressure drop of gas-liquid Taylor flow in round micro-capillaries for low to intermediate Reynolds numbers. Microfluidics and Nanofluidics. 8, 33–45.

Watts, P. and Haswell, S.J. (2005) The application of micro reactors for organic synthesis. Chemical Society Reviews. 34(3), 235–246.

Weisman, J. and Kang, S.Y. (1981) Flow pattern transitions in vertical and upwardly inclined lines. International Journal of Multiphase Flow. 7(3), 271–291.

White, F.M. (2006) Viscous Fluid Flow, 3rd ed., McGraw–Hill: New York, NY, USA.

White, F.M. (2011) Fluid mechanics. McGraw–Hill.

White, F.M. (2016) Fluid Mechanics, 8th ed., McGraw-Hill: New York, NY, USA.

Wong, H., Radke, C., Morris, S. (1995) The motion of long bubbles in polygonal capillaries. part 1. thin films. Journal of Fluid Mechanics, 292, 71–94.

Wörner, M. (2012) Numerical modeling of multiphase flows in microfluidics and micro process engineering: a review of methods and applications. Microfluidics and Nanofluidics. 12(6), 841–886.

Wright, R. (1934) Jamin effect in oil production. AAPG Bulletin. 18, 548–549.

Wu, Z. and Li, W. (2010) A new predictive tool for saturated critical heat flux in micro/mini-channels: effect of the heated length-to-diameter ratio. International Journal of Heat and Mass Transfer. 54(13–14), 2880–2889.

Wu, Z., Li, W., Ye, S. (2011) Correlations for saturated critical heat flux in microchannels. International Journal of Heat and Mass Transfer. 54(1–3), 379–389.

Wu, J., Rockey, T., Yauw, O., Shen, L., Chylak, B. (2012) Bonding of Ag-alloy wire in LED packages. In 35th IEEE/CPMT International Electronics Manufacturing Technology Conference (IEMT), Ipoh, Perak, Malaysia, 1–4.

Wu, C., Tang, K., Gu, B., Deng, J., Liu, Z., Wu, Z. (2016) Concentration-dependent viscous mixing in microfluidics: modelings and experiments. Microfluidics and Nanofluidics. 20(6), 90.

Wu, Z. and Sundén, B. (2019) Liquid-liquid two-phase flow patterns in ultra-shallow straight and serpentine microchannels. Heat and Mass Transfer. 55(4), 1095–1108.

Xu, J.H., Li, S.W., Tan, J., Wang, Y.J., Luo, G.S. (2006) Controllable preparation of monodisperse O/W and W/O emulsions in the same microfluidic device. Langmuir. 22(19), 7943–7946.

Xu, H., Liu, C., Silberschmidt, V.V., Pramana, S.S., White, T.J., Chen, Z., Acoff, V.L. (2011) New mechanisms of void growth in Au-Al wire bonds: volumetric shrinkage and intermetallic oxidation. Scripta Materialia. 65(7), 642–645.

Xu, B., Cai, W., Liu, X., Zhang, X. (2013) Mass transfer behavior of liquid-liquid slug flow in circular cross-section microchannel. Chemical Engineering Research and Design. 91(7), 1203–1211.

Xu, C. and Xie, T. (2017) Review of microfluidic liquid-liquid extractors. Industrial & Engineering Chemistry Research. 56(27), 7593–7622.

Xu, F., Yang, L., Liu, Z., Chen, G. (2021) Numerical investigation on the hydrodynamics of Taylor flow in ultrasonically oscillating microreactors. Chemical Engineering Science. 235, 116477.

Yagodnitsyna, A.A., Kovalev, A.V., Bilsky, A.V. (2016) Flow patterns of immiscible liquid-liquid flow in a rectangular microchannel with T-junction. Chemical Engineering Journal. 303, 547–554.

Yagodnitsyna, A., Kovalev, A., Bilsky, A. (2021) Liquid-liquid flows with non-Newtonian dispersed phase in a T-junction microchannel. Micromachines. 12(3), 335.

Yao, X., Zhang, Y., Du, L., Liu, J., Yao, J. (2015) Review of the applications of microreactors. Renewable and Sustainable Energy Reviews. 47, 519–539.

Yao, C., Zheng, J., Zhao, Y., Zhang, Q., Chen, G. (2019) Characteristics of gas-liquid Taylor flow with different liquid viscosities in a rectangular microchannel. Chemical Engineering Journal. 373, 437–445.

Yao, C., Ma, H., Zhao, Q., Liu, Y., Zhao, Y., Chen, G. (2020) Mass transfer in liquid-liquid Taylor flow in a microchannel: local concentration distribution, mass transfer regime and the effect of fluid viscosity. Chemical Engineering Science. 223, 115734.

Ye, M., Van Der Hoef, M.A., Kuipers, J.A.M. (2005) From discrete particle model to a continuous model of Geldart a particles. Chemical Engineering Research and Design. 83(7), 833–843.

Yin, X. and Koch, D.L. (2007) Hindered settling velocity and microstructure in suspensions of solid spheres with moderate Reynolds numbers. Physics of Fluids. 19(9), 093302.

Yokoi, K. (2013) A practical numerical framework for free surface flows based on CLSVOF method, multi-moment methods and density-scaled CSF model: numerical simulations of droplet splashing. Journal of Computational Physics. 232(1), 252–271.

Youngs, D.L. (1982) Time-dependent multi-material flow with large fluid distortion, In K.W. Morton and M.J. Baines, editors, Numerical Methods for Fluid Dynamics. Academic Press. 273–285.

Yu, Z. (2010) Process research on improving bonding strength of hot-pressed ultrasonic ball solder joint. Master's thesis, Southwest Jiaotong University, Chengdu, China.

Yue, J., Chen, G., Yuan, Q., Luo, L., Gonthier, Y. (2007) Hydrodynamics and mass transfer characteristics in gas-liquid flow through a rectangular microchannel. Chemical Engineering Science. 62(7), 2096–2108.

Yue, J., Luo, L., Gonthier, Y., Chen, G., Yuan, Q. (2008) An experimental investigation of gas-liquid two-phase flow in single microchannel contactors. Chemical Engineering Science. 63(16), 4189–4202.

Yue, J., Luo, L., Gonthier, Y., Chen, G., Yuan, Q. (2009) An experimental study of air-water Taylor flow and mass transfer inside square microchannels. Chemical Engineering Science. 64(16), 3697–3708.

Yue, J., Rebrov, E.V., Schouten, J.C. (2014) Gas-liquid-liquid three-phase flow pattern and pressure drop in a microfluidic chip: similarities with gas-liquid/liquid-liquid flows. Lab on a Chip. 14(9), 1632–1649.

Yun, J., Lei, Q., Zhang, S., Shen, S., Yao, K. (2010) Slug flow characteristics of gas-miscible liquids in a rectangular microchannel with cross and T-shaped junctions. Chemical Engineering Science. 65(18), 5256–263.

Zhan, C., Sardina, G., Lushi, E., Brandt, L. (2014) Accumulation of motile elongated micro-organisms in turbulence. Journal of Fluid Mechanics. 739, 22–36.

Zhang, Q. and Prosperetti, A. (2010) Physics-based analysis of the hydrodynamic stress in a fluid-particle system. Physics of Fluids. 22(3), 033306.

Zhang, D., Jiang, C., Liang, D., Chen, Z., Yang, Y., Shi, Y. (2014) A refined volume-of-fluid algorithm for capturing sharp fluid interfaces on arbitrary meshes. Journal of Computational Physics. 274, 709–736.

Zhang, M., Pan, L.M., Ju, P., Yang, X., Ishii, M. (2017) The mechanism of bubbly to slug flow regime transition in air-water two phase flow: a new transition criterion. International Journal of Heat and Mass Transfer. 108, 1579–1590.

Zhang, D. and Goharzadeh, A. (2019) Effect of sudden expansion on two-phase flow in a horizontal pipe. Fluid Dynamics. 54(1), 123–136.

Zhang, J.Z., Chen, W.K., Zhou, N.X., Lei, L., Liang, F.S. (2020a) Experiment study on formation and length of droplets in T-junction microchannels. Journal of ZheJiang University (Engineering Science). 54(5), 1007–1013.

Zhang, J., Lei, L., Liang, F., Li, H., Sundén, B., Wu, Z. (2020b) An improved method to visualize two regions of interest synchronously in microfluidics. Flow Measurement and Instrumentation. 72, 101715.

Zhang, J., Lei, L., Li, H., Xin, G., Wang, X. (2021) Experimental and numerical studies of liquid-liquid two-phase flows in microchannel with sudden expansion/contraction cavities. Chemical Engineering Journal. 433, 133820.

Zhao, T.S. and Bi, Q.C. (2001) Co-current air-water two-phase flow patterns in vertical triangular microchannels. International Journal of Multiphase Flow. 27(5), 765–782.

Zhao, Y., Chen, G., Yuan, Q. (2006) Liquid-liquid two-phase flow patterns in a rectangular microchannel. AIChE Journal. 52(12), 4052–4060.

Zhao, Y., Chen, G., Yuan, Q. (2007) Liquid-liquid two-phase mass transfer in the T-junction microchannels. AIChE Journal. 53(12), 3042–3053.

Zitouni, H., Arabi, A., Salhi, Y., Zenati, Y., Si-Ahmed, E.K., Legrand, J. (2021) Slug length and frequency upstream a sudden expansion in gas-liquid intermittent flow. Experimental and Computational Multiphase Flow. 3(2), 124–130.

Zuber N. and Findlay, J.A. (1968) Average volumetric concentration in two-phase flow systems. Journal of Heat Transfer. 87(4), 453–468.